Christian Pauritsch, BSc

Acquisition of Selected Physiological Parameters with Spectral Optical Sensors

MASTER'S THESIS

to achieve the university degree of

Diplom-Ingenieur

Master's degree programme: Biomedical Engineering

submitted to

Graz University of Technology

Supervisor

ao. Univ.Prof. DI. Dr. Hermann Scharfetter

Institute of Medical Engineering
Stremayrgasse 16/III, A-8010 Graz

Graz, January 2019

Acknowledgments

First and foremost, I would like to thank Dipl.-Ing. (FH) Bernhard Gruber, who made this master thesis possible and gave me the chance as well as his trust for realizing this thesis at the ams AG.

Especially, I like to thank Dr. Ernst Haselsteiner, who set the whole thing up, and who was there from the first ideas to the concept of this thesis.

I am grateful for the support of Dipl.-Ing. Martin Dedek and his team during the realization of this thesis as well as the master practical.

Moreover, I want to mention Prof. Dr. Hermann Scharfetter for his supervision and help during the completion of this thesis as well as Prof. Dr. Rudolf Stollberger for giving me the opportunity to write this master thesis at the Institute of Medical Engineering.

Nobody has been more important and helpful for me during the work on this thesis than my family. So, I would like to point out my huge appreciation for my fiancé Kerstin and my sons, Finn and Mika, in terms of their personal and mental support as well as for their huge patience.

Graz, January 2019 Christian Pauritsch

Affidavit

I declare that I have authored this thesis independently, that I have not used other than the declared sources/resources, and that I have explicitly indicated all material which has been quoted either literally or by content from the sources used. The text document uploaded to TUGRAZonline is identical to the present master's thesis.

Date

Signature

Abstract

According to the Word Health Organization (WHO) cardiovascular diseases (CVDs) are the number one cause of death globally, where CVD patients need an early detection and management. The field of optical and spectral biosensors contains a huge and highly potential amount of methods and approaches, which could enable the possibility of measuring these health indicators by spectral biosensor solutions.

This master thesis summarizes and reviews the commonly used methods in the field of optical blood glucose, heart rate, and blood pressure measurement. It also gives a review of non-invasive and optical biosignal acquisition using spectral sensors.

Moreover, for describing the complex optical behavior of human tissue, a summarization of the most important optical parameters as well as a description of the interactions between light and matter is given, where care is taken to describe the basic ways of optical tissue characterization for biooptical applications and in-vivo measurements.

Considering optical blood glucose determination, spectral methods, containing near- and mid-range infrared, and Raman spectroscopy are reviewed as well as other optical- and non-optical methods are summarized. The results show that no optical method for non-invasive glucose level prediction is available on the market today, although some approaches have a huge potential for detecting trends of the glucose concentration.

The described photoplethysmography (PPG) represents the origin of optical heart rate monitoring (HRM), where a focus is placed on choosing the best wavelength, resulting in a preference of green light, but a persisting dependency on the target application. Moreover, next to major influences as well as limitations of HRM, heart rate variability (HRV), and pulse oximetry are discussed.

Based on the PPG signal, optical blood pressure estimation methods are evaluated, considering the physiological and biomechanical properties of vessels, which were based on the measurement of the pulse wave velocity (PWV), the pulse transit time (PTT), and pulse arrival time (PAT) approaches. The results are an indicator for the possibility of a fully optical blood pressure measurement, whereas several drawbacks must be overcome.

Table of Contents

1 Introduction

1.1 Motivation

Cardiovascular diseases (CVDs) are the most common causes for death globally, for instant, approximately 17.9 million people died in 2016 [1]. According to the Word Health Organization (WHO), people with hypertension or diabetes are at a higher risk of CVD and need an early detection and management [2, 3].

Optical and spectral biosensors contain a huge and highly potential amount of methods, techniques, and approaches, enabling the possibility of detecting and measuring signals, which are related to different diseases or health indicators. Due to the available photonics technologies, miniature CCDs and spectrometers can be build as well as integrated into low cost diagnostic systems, where especially the transformation of the massive available amount of smartphones into an useful diagnostic imaging or spectroscopy device, was researched by Global Health programs at NIH and the Bill & Melinda Gates Foundation [4, 5]. The growing interest as well as research in wearable and mobile devices for consumer and health applications, enables the possibility of continuous biosignal monitoring, resulting in additional diagnostic data as well as relevant clinical information.

1.2 Assignment of Tasks

The aim of this master thesis is the literature research of non-invasive and optical biosignal acquisition, where the following tasks shall be fulfilled:

- A review of biological and optical basics, building the basis for the development of optical biosensors with attention paid to spectral measurement.

- A summary and discussion of optically measured biosignals as well as derived parameters, which provide diagnostic information of the human body.

- A review of biological properties of the human skin and blood as well as the underlying tissue with the focus placed on their optical behavior.
- An identification of suitable areas of the human body for biosignal measurement with respect to the signal quality and a summary of optical principles, which bring biological properties in context with spectrally resolved signals.

To recapitulate, all of the mentioned tasks shall be related to three selected biosignals, which are optical glucose, heart rate, and blood pressure measurement. This master thesis is commissioned by ams AG[1].

1.3 Outline

The present thesis is organized as follows:

Chapter 2: Biological and Optical Basics give an overview of biological and optical basics, describe the interaction between light and tissue, and summarize the most important tissue types for optical investigation.

Chapter 3: Optical Glucose Measurement reviews optical approaches of non-invasive glucose measurement, containing NIR, MIR, and Raman spectroscopy, and summarizes other optical and non-optical methods.

Chapter 4: Optical Heart Rate Measurement describes the method of photoplethysmography (PPG) and its application in heart monitoring (HRM), heart rate variability (HRV) as well as pulse oximetry.

Chapter 5: Optical Glucose Measurement summarizes current approaches of optical blood pressure estimation and pulse wave velocity (PWV) measurement, with its focus placed on pulse transit time (PTT) and pulse arrival time (PAT) models.

Chapter 6: Conclusion summarizes the main results and concludes the present thesis.

---

[1] ams AG, Tobelbader Strasse 30, A-8141 Premstaetten, Austria, https://ams.com/

2 Biological and Optical Basics

Since optical sensors represent a major part of non-invasive biosensors, it is necessary to understand the optical as well as the biological point of view. The optical properties of human tissue affect the diagnostic and the therapeutic applications of light [6]. In this case, the focus will be on the diagnostic part of biomedical applications. First, the optical principles, which are necessary to understand the interactions between light and human tissue, are summarized. Second, the optical properties of skin and its components are analyzed. Last but not least, the light transport in tissue as well as the optically detectable parameters are mentioned.

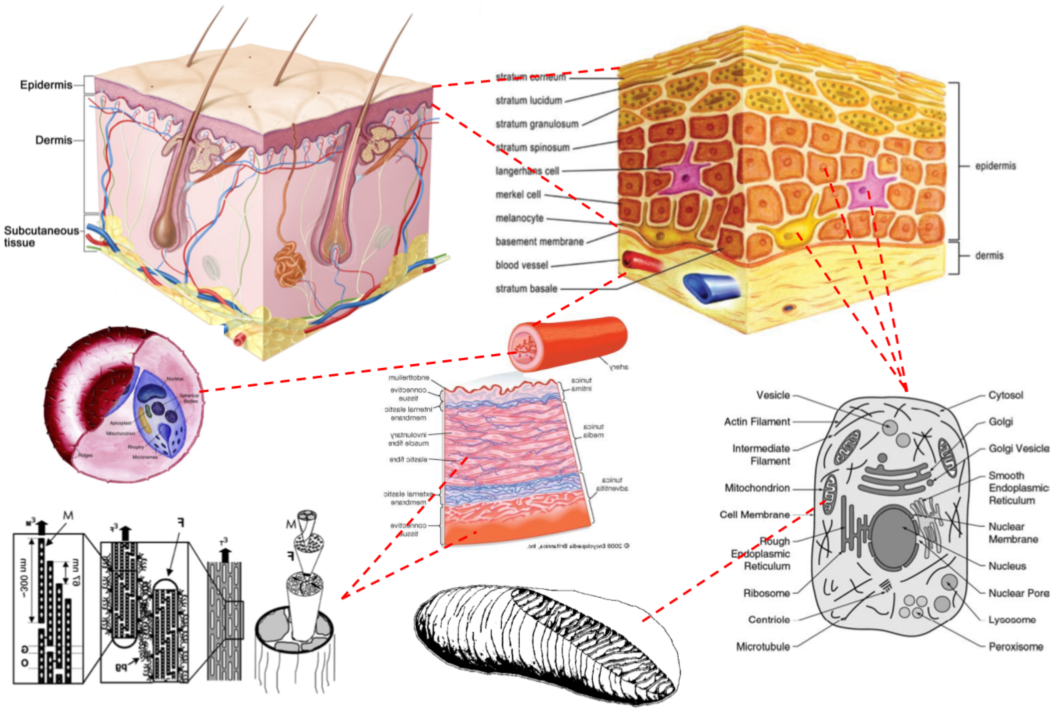

Figure 2.1: Human skin and its tissue layers as well as its components (adapted from [7–10]).

An overview of different tissue types and their consisting components are illustrated in Fig. 2.1, where the considered parts are summarized in Tab. 2.1. Each of them is described and characterized by its biological and optical information for a diagnostic application of biosensors.

Tissue Type:	***Skin***	***Blood Vessels***	***Blood***	***Human Cells***
Components:	Epidermis	Tunica Intima	Plasma	Cell Membrane
	Dermis	Tunica Media	Leucoytes	Nucleus
	Subcutaneous Tissue	Tunica Adventica	Erythrocytes	Cell Organelles

Table 2.1: Overview of selected tissue types.

It is necessary to define parameters to characterize these properties due to the complex optical behavior of the human tissue. A summary of the most important optical parameters as well as a description of the interactions between light and matter is given, which encompass descriptions for the basic ways of optical tissue characterization for biosensor-applications and in-vivo measurements.

2.1 Light and Optical Parameters

The term ”light” means the portion of the electromagnetic spectrum with the vacuum wavelengths λ_{vac} in the range of 1 μm to 100 nm, including the near infrared (NIR), the visible (VIS), and the ultraviolet (UV) regions [8], illustrated in Fig. 2.2 as part of the whole electromagnetic spectrum. The relationship between frequency and wavelength is defined in Eq. 2.1, where f is the frequency and c means the speed of light. Considering the quantum-mechanical point of view, light consists of energy-packets (”quanta”), called photons, which have an energy proportional to the frequency of the electromagnetic wave [8]. This relationship between the energy E and the wavelength, respectively the frequency, is shown in Eq. 2.2, where h refers to Planck‘s constant.

$$f = \frac{c}{\lambda} \tag{2.1}$$

$$E = hf = \frac{hc}{\lambda} \tag{2.2}$$

Due to the wave-particle duality, light can be treated as a particle, which is shown in Fig. 2.3a, or as a wave, which is illustrated in Fig. 2.3b, where light consists of an electric field E and a perpendicular magnetic field H. Thus, several interactions between light and tissue can be described by different approaches, which are either based on the particle-

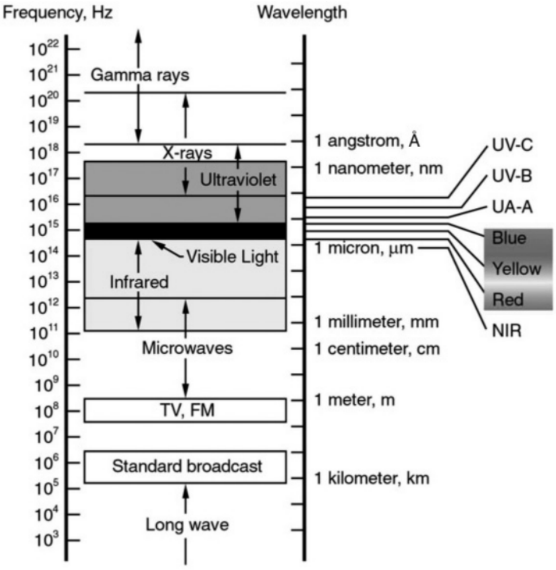

Figure 2.2: The regions of light in the whole electromagnetic spectrum [8].

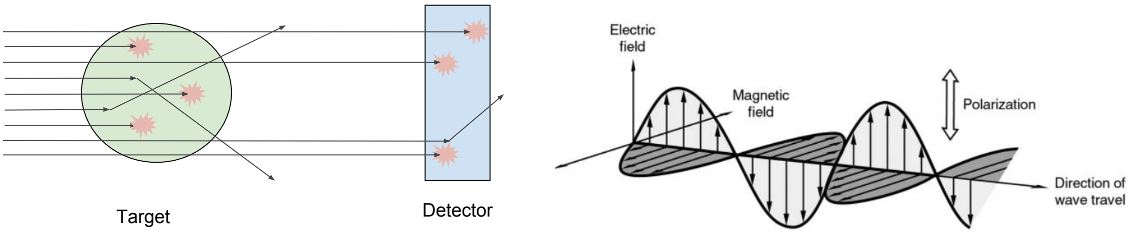

a) Light as particle.

b) Light as wave [8].

Figure 2.3: Different views of light due to wave-particle duality.

or wave-model of light. Also, optical parameters must be defined in oder to characterize the different tissue types and to describe the appearing interactions. The main optical properties, which are commonly used to describe human tissue, are summarized in Tab. 2.2, where θ is defined as the deflection angle and ψ represents the azimuthal angle of scattering [6].

Optical Parameter	Symbol	Unit
Absorption coefficient	μ_a	cm^{-1}
Scattering coefficient	μ_s	cm^{-1}
Scattering function	$p(\Theta, \Psi)$	sr^{-1}
Real refraction index	n'	1

Table 2.2: Optical parameters for tissue characterization.

2.2 Interactions between Light and Tissue

The possibility of tissue penetration, the interrogation of tissue parts, and the detection of the escaped light are major components of the diagnostic use of light [6]. Several events take place during the interaction of light and human tissue as shown in Fig. 2.4, where these can be divided generally into two groups, differentiated into the two major viewpoints of light, the wave and the particle model. Some of these processes can be explained by both models, while some can only be described in one of the two. However, the most important processes to consider for the application of optical biosignal acquisition are the following ones:

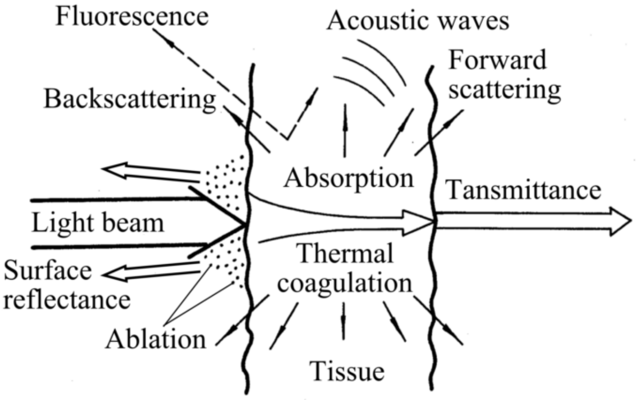

Figure 2.4: Light interacting with tissue [11].

- Refraction
- Reflection
- Transmission
- Attenuation
- Scattering
- Absorption
- Polarization
- Fluorescence
- Interference

Thus, when the light reaches the skin, it is partly absorbed, reflected, scattered, and transmitted [12]. These four possible events can be described by assuming the particle-model of light. Moreover, an overview of these interactions are illustrated in Fig. 2.5, where each of these processes is depicted, considering a single incident photon interacting with the surface of the human skin. At the same time, other optical parameters are changing, for instance, the state of polarization at a scatter event, considering the wave-properties of light, or other optical phenomena, such as the interference pattern, which are used to describe and visualize human tissue, by applying diagnostic methods like optical coherence tomography

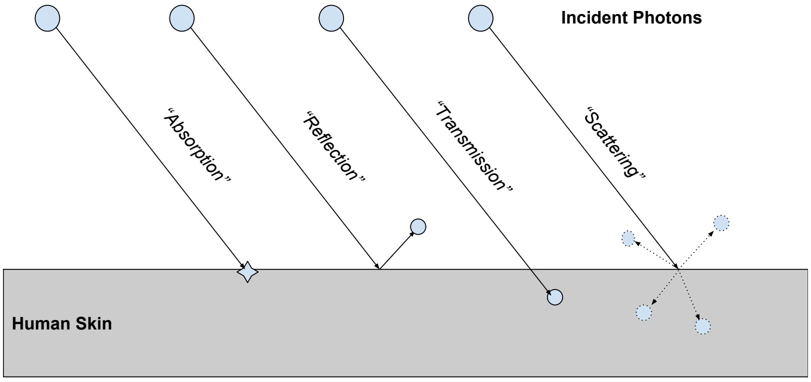

Figure 2.5: Interactions between light and human tissue from the particle point of view.

(OCT). However, the most important optical interactions as well as the derived parameters for tissue description are considered in the next sections.

2.2.1 Refraction

The refraction appears as a process, which can occur when a photon crosses the boundary between two media with different properties (refractive index), and can be described by the complex index of refraction $\tilde{n}(\lambda)$, which is represented in Eq. 2.3 for a homogeneous medium, describing its linear optical properties [6, 8].

$$\tilde{n}(\lambda) = n' + jn'' \tag{2.3}$$

The real refractive index $n' = \Re(\tilde{n}(\lambda))$, which is commonly referred to the general term "index of refraction" $n(\lambda)$, describes the lossless part of the diffraction process, affects the speed of light in a medium [6], and is represented in Eq. 2.4 in respect of the phase velocity of light in a medium $c_m(\lambda)$ and the speed of light in vacuum c as well as the wavelength of light in a medium λ_m and the vacuum wavelength λ, where the index of refraction in vacuum is n_v = 1 [8].

$$n'(\lambda) = \frac{c}{c_m(\lambda)} = \frac{\lambda}{\lambda_m} \tag{2.4}$$

When light travels through two materials, which have different indices of refraction, then the path of light is redirected. This event is illustrated in Fig. 2.6a, where light incidents on a planar boundary and undergoes refraction because of the different refraction indices n_1 and n_2 of the two media. The relationship between the angle of incidence θ_1 and the angle of refraction θ_2 is defined by the Snell's law, shown in Eq. 2.5, which presents

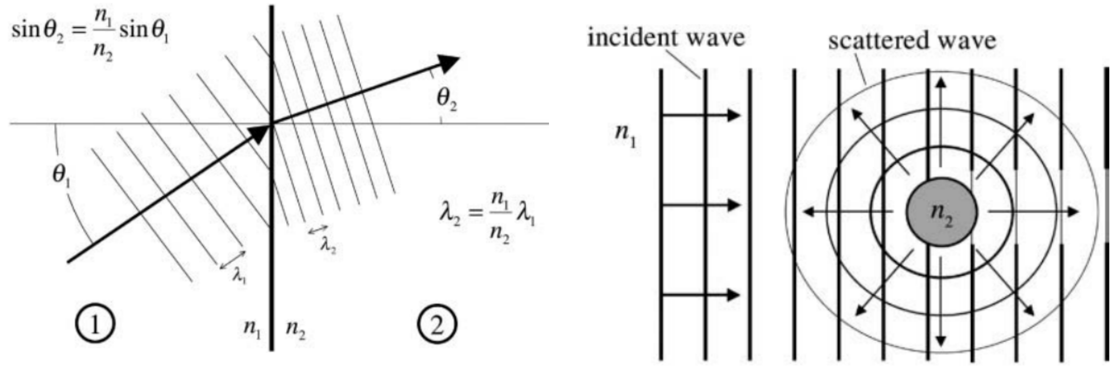

a) Refraction on a planar boundary [8]. **b)** Partially scattered light on a particle [8].

Figure 2.6: Refraction and scattering due to different indices of refraction.

the refraction indices of the two media as well as the wavelength of the initial and the redirected light beam. (cf. [8, 13])

$$\frac{\sin\theta_2}{\sin\theta_1} = \frac{n_1}{n_2} = \frac{\lambda_2}{\lambda_1} \tag{2.5}$$

Another situation, where two different indices of refraction lead to a partial redirection of the incident light, is shown in Fig. 2.6b, in which light is scattered partially on a localized particle that has a different index of refraction than the surrounding medium.

The imaginary refractive index $n'' = \Im(\tilde{n}(\lambda))$ describes the energy dissipation, specifies the absorption coefficient μ_a, and is shown in Eq. 2.6 [6]. Thus, for a medium with low absorption, the imaginary index of refraction can be neglected [14].

$$n''(\lambda) = \frac{\lambda\mu_a}{4\pi} \tag{2.6}$$

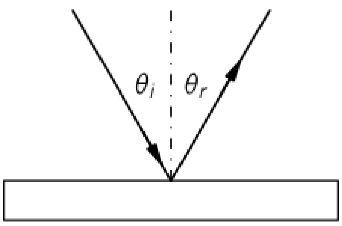

Figure 2.7: Reflection of light [15].

Next to refraction, where a part of the incoming light is transmitted through the medium, reflection occurs. According to the law of reflection, illustrated in Fig. 2.7, the angle of

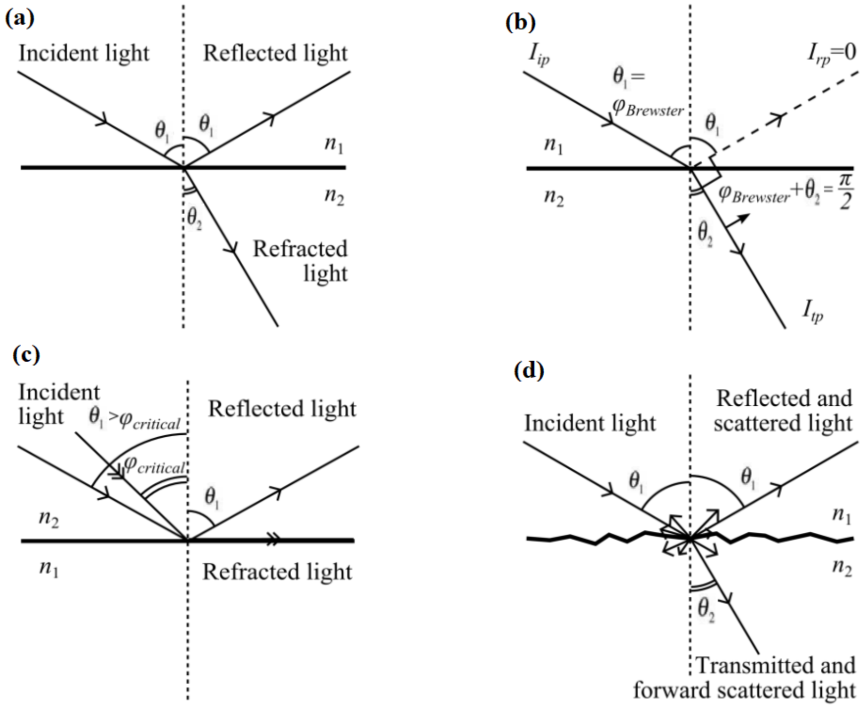

Figure 2.8: Light interaction scenarios: Reflection and transmission of a non-scattering tissue (a), considering the Brewster-angle (b), considering total internal reflection (c), and reflection and transmission of a scattering tissue and its surrounding media (d) (modified from [11]).

incidence θ_i is equal to the angle of reflection θ_r, defined in Eq. 2.7 [15].

$$\theta_r = \theta_i \tag{2.7}$$

An overview of four different scenarios between light interacting with tissue surfaces is illustrated in Fig. 2.8. First, the interaction of light and a non-scattering tissue is shown in (a), assuming that $n_2 > n_1$, where n_2 is the refraction index of the tissue and n_1 is the one of the surrounding medium. The amount of incident energy of light is split into a refracted, respectively transmitted part T and a reflected part R. Furthermore, the relationship between the reflected and transmitted part of light is described by the Fresnel equations, defined in Eq. 2.8, for the reflected energy R and, according to the conversation of energy, in Eq. 2.9, for the transmitted one. Considering the wave-model of light, R_p and T_p mean the reflected and transmitted energy of the parallel polarization state (p-polarized), representing the component of the electric field, which is parallel to the plane of incidence. R_s and T_s correspond to the perpendicular polarization component (s-polarized), which is normal to the plane of incidence. (See Sec. 2.2.5 (p. 22) for more information about polarization.) A special case, setting the incident angle $\theta_1 = 0°$, is leading to a normal incidence on a planar boundary and results in $R_\text{s} = R_\text{p} = R$ as well as $T_\text{s} = T_\text{p} = T$, shown in Eq. 2.10 [13].

$$\begin{aligned} R_\text{s} &= \left| \frac{n_1 \cos\theta_1 - n_2 \cos\theta_2}{n_1 \cos\theta_1 + n_2 \cos\theta_2} \right|^2 && (2.8) \\ R_\text{p} &= \left| \frac{n_1 \cos\theta_2 - n_2 \cos\theta_1}{n_1 \cos\theta_2 + n_2 \cos\theta_1} \right|^2 \\ T_\text{s} &= 1 - R_\text{s} && (2.9) \\ T_\text{p} &= 1 - R_\text{p} \\ R &= 1 - T = \frac{(n_1 - n_2)^2}{(n_1 + n_2)^2} && (2.10) \\ T &= \frac{4 n_1 n_2}{(n_1 + n_2)^2} \end{aligned}$$

In Fig. 2.8 (b), the incident angle is set to the Brewster-angle, which is defined in Eq. 2.11, and therefore produces a rectangular angle between the reflected and the refracted part of light, shown in Eq. 2.12, causing the amount of reflected parallel polarized light to vanish (R_p = 0) [13]. As a result, the incident parallel polarized light is fully transmitted, setting $\varphi_\text{Breswter} \approx 57°$ for n_1 = 1 and n_2 = 1.5 (stratum corneum) [11]. Otherwise, only the perpendicularly polarized (s-polarized) part of light will be reflected, using incoming unpolarized light [13].

$$\varphi_\text{Breswter} = \arctan \frac{n_2}{n_1} \tag{2.11}$$

$$\theta_2 + \varphi_\text{Breswter} = \frac{\pi}{2} \tag{2.12}$$

Using an incident angle higher than the critical angle, as shown in Fig. 2.8 (c), leads to the total internal reflection, which means that the total amount of light gets reflected (T=0). This angle is defined in Eq. 2.13 and is determined again for n_1 = 1 and n_2 1.5 (stratum corneum) to $\varphi_\text{Critical} \approx 47$ ° [11]. This happens only, when the light travels from the optically denser to the optically less dense material, which means out of the stratum corneum towards the air. (cf. [13])

$$\varphi_\text{Critical} = \arcsin \frac{n_2}{n_1} \tag{2.13}$$

The last three scenarios are only valid considering two homogeneous media with flat interface between them, which means they only represent a limited amount of tissues, such as healthy eye cornea, lens, and vitreous body [11]. However, the most realistic scenario is illustrated in Fig. 2.8 (d), where the light interacts with a scattering tissue. Since most of the tissue types are inhomogeneous and absorptive multi-layered media with rough interfaces, multi-scattering will influence the transmission and the reflection of light [11].

2.2.2 Scattering

The scattering process provides important diagnostic informations, depending on the size, morphology, and structure of the components in human tissue [8]. Scattering occurs, when a guest material occupies only a localized region in a host material, which is the case in biological tissue, where the mismatch in refraction indices between different tissue parts (e.g. cell organelles) and the surrounding medium (e.g. cytoplasm) represents a source of scattering [8]. Thus, light scattering in tissue occurs due to the mismatch between refraction indices of different tissue components or layers, for example, cell membrane and extracellular fluid in case of tissue [16] as well as between hemoglobin solution inside the cell and its plasma environment in case of blood [17].

Generally, scattering can be described by either assuming the incident light as single particles, photons, which leads to a redirection of the photon trajectory or as wave, resulting in a change of the polarization. The interactions during a scattering event, from particle point of view, are illustrated in Fig. 2.9a, where an incident photon travels along the direction $\hat{\mathbf{s}}$ and is scattered in the new direction $\hat{\mathbf{s}}'$. Another point of view is additionally shown in Fig. 2.9b, where the incident light wave consists of a parallel and perpendicular polarized part $\mathbf{E}_{\perp,i}$ and $\mathbf{E}_{\|,i}$ before, and $\mathbf{E}_{\perp,s}$ and $\mathbf{E}_{\|,s}$ after the scattering event, representing a change of the polarization state.

Also scattering can be be quantified by the scattering cross section σ_s, which is defined in Eq. 2.14, where a monochromatic plane wave is assumed and P_{scatter} means the amount of power which gets scattered spatially, as well as I_0 the intensity encountering with the scattering object [8]. The interactions during a scattering event as well as the construction of the cross section is illustrated in Fig. 2.10, where an incident beam is shown before (A) and after (B) interacting with a scatterer. Thus, the scattered power is then equal to product

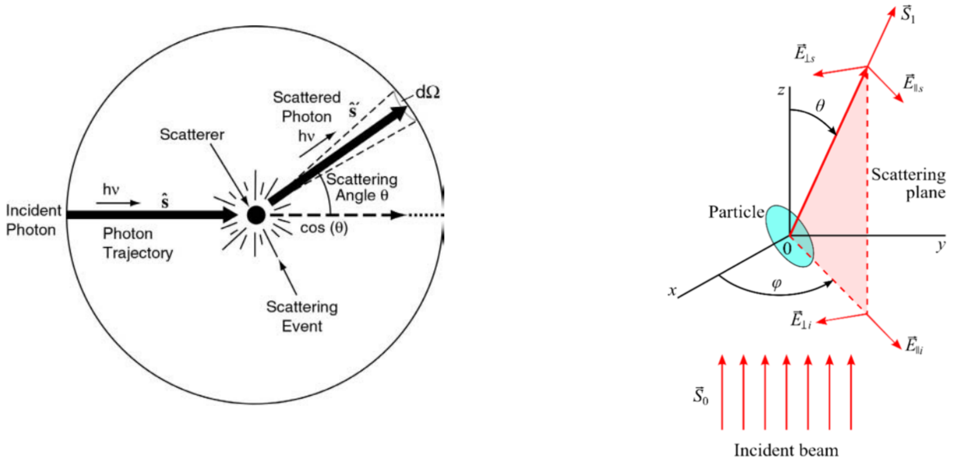

a) Scattering process thought as particle model, resulting in change of the trajectory [8].

b) Scattering light in the wave model, resulting in a change of the polarization [18].

Figure 2.9: Scattering of light considering wave or particle model of light.

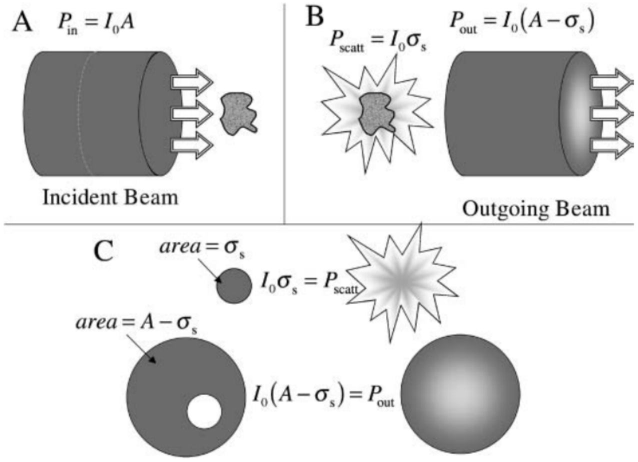

Figure 2.10: Interactions during scattering considering a scattering cross section area σ_s [8].

of the incoming intensity I_0 with the scattering cross section σ_s (C) [8].

$$\sigma_s(\hat{\mathbf{s}}) = \frac{P_{\text{scatter}}}{I_0} \tag{2.14}$$

The intensity or irradiance of a planar wave can be seen as time averaged energy density and is defined in Eq. 2.15, in which E means the electric field, n the index of refraction, c

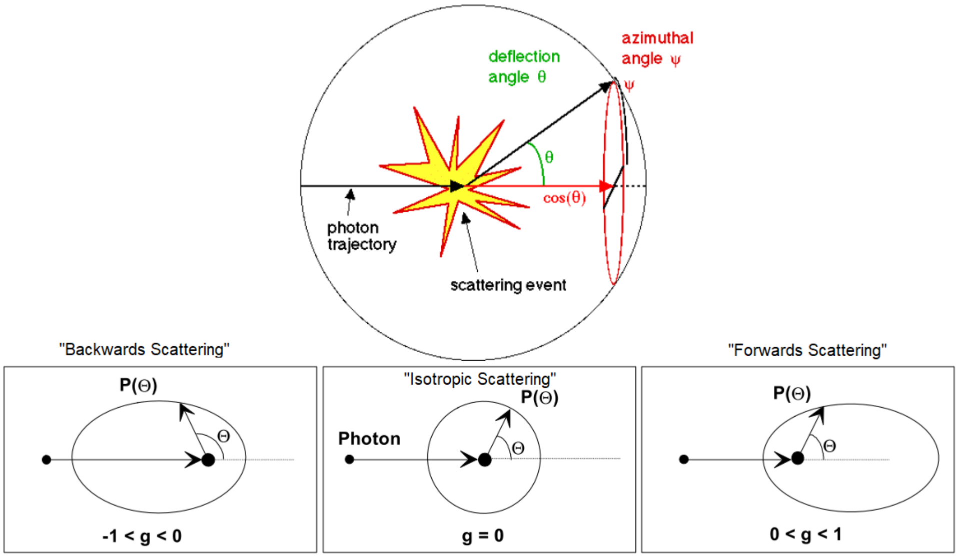

Figure 2.11: Scattering event and anisotropy (modified from [9, 19]).

the speed of light and ε_0 the permittivity in vacuum.

$$I = \frac{cn\varepsilon_0}{2}|E|^2 \tag{2.15}$$

In a uniform medium of identical scatterers, the scattering coefficient μ_s is defined as in Eq. 2.16, where ρ is the volume density of scatterer, and determines the average distance a photon can travel between two scattering events, as so called ”scattering mean free path” l_s, defined in Eq. 2.17 [8].

$$\mu_s = \rho\sigma_s \tag{2.16}$$

$$l_s = \frac{1}{\mu_s} \tag{2.17}$$

The new direction of the scattered photon can be described by two angles, illustrated in Fig. 2.11 (top), where Θ means the scattering or deflection angle, and Ψ means the azimuthal angle [9]. Since the scattered irradiance E_{scatter} is defined in Eq. 2.18, in which I_0 is a specific constant, the differential power dP_{scatter} of a differential surface element dA of a sphere, defined in Eq. 2.19, with a radius r, can be calculated in Eq. 2.20.

$$E_{\text{scatter}}(\Theta, \Psi) = E_0 \frac{r_0^2}{r^2} f(\Theta, \Psi) = \frac{I_0}{r^2} f(\Theta, \Psi) \tag{2.18}$$

$$dA = d\Theta \sin \Theta d\Psi \tag{2.19}$$

$$\begin{aligned} dP_{\text{scatter}}(\Theta, \Psi) &= E_{\text{scatter}} dA \\ &= \frac{I_0}{r^2} f(\Theta, \Psi) r^2 d\Theta \sin \Theta d\Psi \end{aligned} \tag{2.20}$$

Dividing the differential power dP_{scatter} by the total power P_{scatter} and considering the unit sphere (r = 1), results in Eq. 2.21,where the resulting normalized differential power, shown in Eq. 2.22, represents the differential probability of deflecting a photon into a specific angle. Finally, the function $f(\Theta, \Psi)$ can be written as $f(\Theta, \Psi) = p(\Theta, \Psi)$, representing the angular distribution by assuming Eq. 2.23. (cf. [20])

$$\frac{dP_{\text{scatter}}(\Theta, \Psi)}{P_{\text{scatter}}(\Theta, \Psi)} = \frac{I_0 f(\Theta, \Psi) d\Theta \sin \Theta d\Psi}{I_0 \int_{\Theta=0}^{\pi} \int_{\Psi=0}^{2\pi} f(\Theta, \Psi) d\Theta \sin \Theta d\Psi} \tag{2.21}$$

$$\frac{dP_{\text{scatter}}(\Omega)}{P_{\text{scatter}}(\Omega)} = \frac{f(\Theta, \Psi) d\Omega}{\int_{\Omega=0}^{4\pi} f(\Theta, \Psi) d\Omega} \tag{2.22}$$

$$\int_{\Omega=0}^{4\pi} f(\Theta, \Psi) d\Omega = 1 \tag{2.23}$$

Thus, the normalized angular distribution of the scattered irradiance $p(\Theta, \Psi)$ gives the probability density function, which is also called scattering phase function and gives a full description of the scattering event [14]. The scattering phase function can only be used to describe a single or a few scattering events, for example, during transmission microscopy of a thin tissue section. Considering thicker tissues with randomly oriented structures, multiple scattering occurs and, thus, the dependence of the azimuthal angle Ψ is only averaged or neglected. (cf. [6])

A parameter, called anisotropy factor g, describes tissue scattering in terms of relative forward and backward directions of scattering [6]. Considering scattering as anisotropic, the scattered intensity is not the same in all directions. The anisotropy factor is defined in Eq. 2.24 in terms of the deflection angle Θ and is illustrated in Fig. 2.11 (bottom), showing backwards ($-1 < g < 0$), isotropic ($g = 0$), and forwards scattering ($0 < g < 1$).

$$g = \langle \cos \Theta \rangle = 2\pi \int_0^{\pi} p(\Theta, \Psi) \cos \Theta \sin \Theta d\Theta \tag{2.24}$$

An isotropic scattering function is defined in Eq. 2.25, resulting in the same probability of scattering in each possible direction, so that Eq. 2.26 is true [9].

$$p(\Theta) = \frac{1}{4\pi} \tag{2.25}$$

$$2\pi \int_0^{\pi} p(\Theta) \cos\Theta \sin\Theta d\Theta = 0 \tag{2.26}$$

Depending on the size of the scatterer, the terms Rayleigh and Mie scattering are commonly used in biomedical optics [6]. If the scatterer is small in comparison to the wavelength of incident light, the Rayleigh theory is applicable under the condition of

$$\frac{n_s}{n_m}\frac{2\pi d}{\lambda} \ll 1, \tag{2.27}$$

where n_s means the refraction index of the scatterer, n_m the refraction index of the surrounding medium, d the radius of the scatterer, and λ the wavelength of the incident light [11]. The Rayleigh formula is shown in Eq. 2.28, describing the dependence of the scattered irradiance E_{scatter} from the distance of the detector r, the deflection angle Θ as well as the wavelength λ, and the irradiance of unpolarized incident light E_0, for N randomly distributed particles with a mean distance between each particle greater than the wavelength λ and for unpolarized light [8, 11]. The angular distribution of Rayleigh scattering is shown in Fig. 2.12a for linear polarized and unpolarized light in 2D and 3D view, in Fig. 2.12b, where a donut-shaped scattering phase function is achieved by parallel and perpendicular polarized incident light, while unpolarized light results in a dumbbell-shaped distribution [11].

$$E_{\text{scatter}}(r,\Theta,\lambda) = E_0 \frac{1+\cos^2\Theta}{2r^2}\left(\frac{2\pi}{\lambda}\right)^4 N \left(\frac{(\frac{n_s}{n_m})^2 - 1}{(\frac{n_s}{n_m})^2 + 2}\right)^2 \left(\frac{d}{2}\right)^6 \tag{2.28}$$

In case of larger scatterers, which are in the order of the wavelength or higher, meaning the size of each scatterer

$$x = \frac{2\pi d}{\lambda} \approx 1, \tag{2.29}$$

scattering is described by the Mie theory [6, 8, 11]. The Mie scattering phase function is defined in Eq. 2.30, where $S_1(\Theta)$ and $S_2(\Theta)$ depend on the polar scattering angle and can be determined from Mie theory [11]. The angular distribution of Mie scattering compared to Rayleigh, depending on the size of the scatterer, is illustrated in Fig. 2.13, in which a

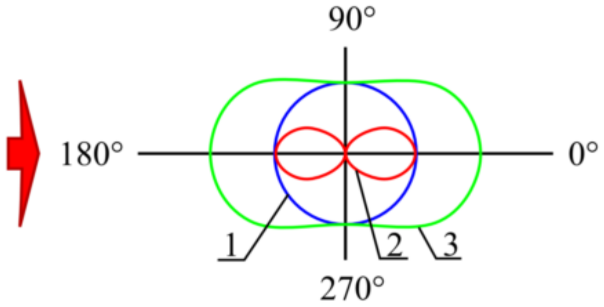

a) 2D view of angular distribution of perpendicular polarized (1), parallel polarized (2) and unpolarized light (3) [11].

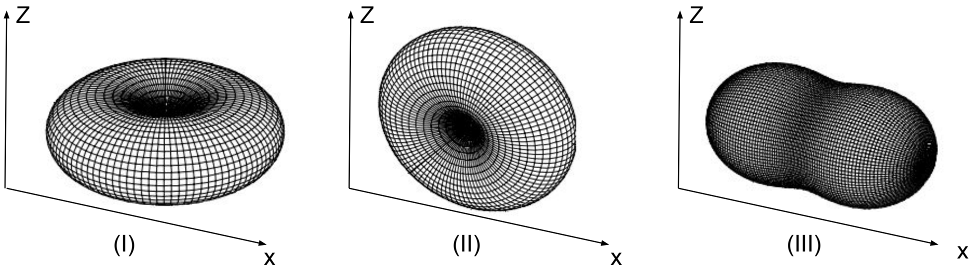

b) 3D view of parallel (I), perpendicular polarized (II) and unpolarized light (III) (modified from [21, 22]).

Figure 2.12: Angular distribution of Rayleigh scattering.

total forward scattering occurs in terms of being scattered by large particles.

$$p(\Theta)_{\text{Mie}} = \frac{\lambda_0^2}{2\pi n_0^2 \sigma_{s,\text{Mie}}} \left(|S_1(\Theta)|^2 + |S_2(\Theta)|^2 \right) \tag{2.30}$$

Tissue usually consists of smaller and larger scatterers, as shown in Fig. 2.14a, for the human cell and its components. An overview of the valid scattering regimes is illustrated in Fig. 2.14b, where different ultra-structures of biological tissue parts are summarized, and the fields of Rayleigh and Mie scattering are marked.

Also scattering can be divided into different types of energy conversion, meaning elastic and inelastic scattering. If the scattered wavelength is the same as the incident one, the scattered photon will have the same amount of energy as before the interaction. This one is called elastic scattering, which is the case for Rayleigh and Mie scattering. Otherwise, when the scattered radiation has a different wavelength than the incident one, the scattering is called inelastic because a part of the energy is transmitted to the scatterer, which is the case in Raman scattering or fluorescence.

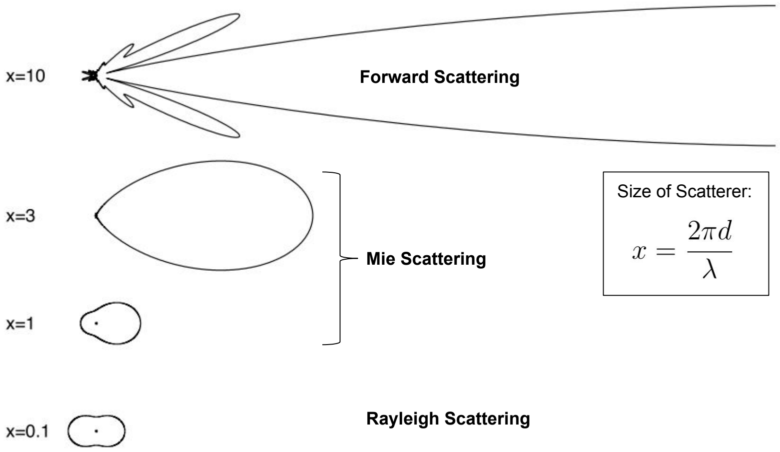

Figure 2.13: Angular distribution depending on scatterer size (modified from [22]).

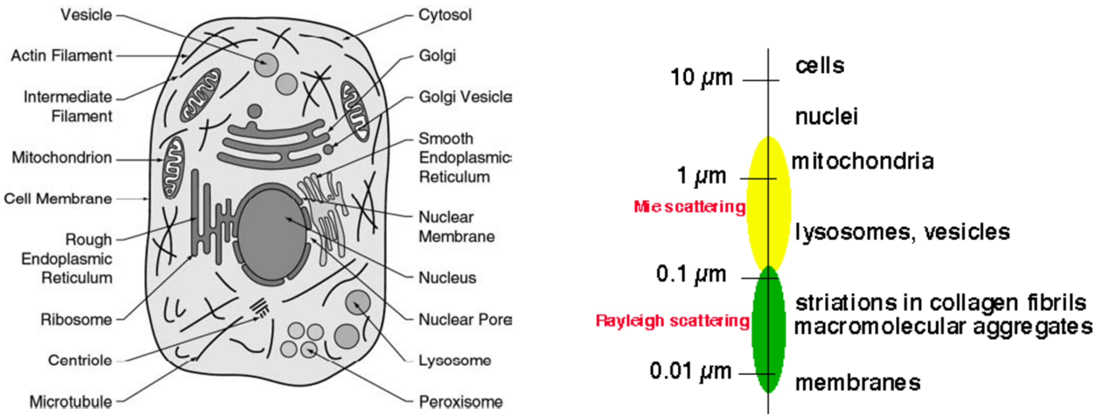

a) Components of human cell [8]. **b)** Scattering in human tissue [9].

Figure 2.14: Rayleigh and Mie scattering in human tissue.

In terms of Raman scattering, the amount of energy is either less (Stokes-Raman) or more (Anti-Stokes-Raman) than before the scattering event. In Stokes-Raman scattering, the energy of the photon is transfered on the scattered molecule and, thus, is lower after the scatter event. The opposite is happening in case of Anti-Stokes-Raman scattering, in which the photon is getting energy transfered from the scattering molecule. An overview of these energy conversions is illustrated in Fig. 2.15, where both cases of Raman scattering and, for comparison's sake only, Rayleigh scattering is shown where the scattered equals the incident energy ($hf_s = hf_i$). When the incident photon (hf_i) is absorbed, it raises the system to some virtual (intermediate) state, making a Stokes transition resulting in $hf_s < hf_i$) or in case of an excited initial state, an Anti-Stokes transition resulting in

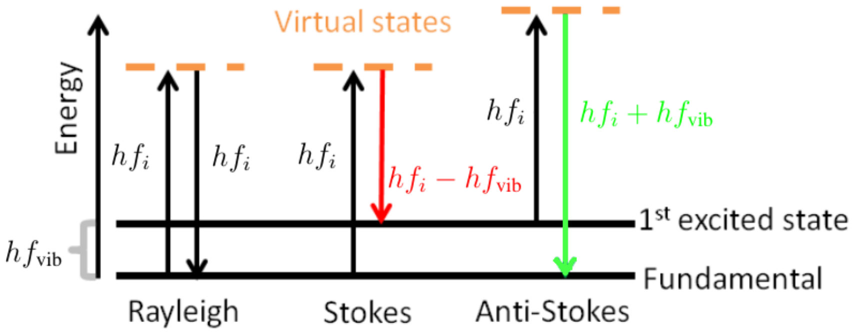

Figure 2.15: Comparison of Rayleigh (elastic) (left), Stokes-Raman (inelastic) (middle) and Anti-Stokes-Raman (inelastic) (right) scattering (modified from [23]).

$hf_s > hf_i$. Thus, in terms of Raman scattering, the energy is converted into vibrational energy with a frequency f_{vib}. (cf. [13])

2.2.3 Absorption

Absorption means converting the energy of photons into internal energy, resulting in the extraction of energy from light by different groups of molecules [8]. The energy of light and, thus, the type of absorption depends on the individual wavelength [9, 24, 25].

At equilibrium, a molecule is in the ground or fundamental state S_0, meaning the lowest vibrational and rotational energy level, shown in Fig. 2.16a. By absorbing excitation energy, the molecule is risen from S_0 to some vibrational level of the excited singlet states S_1 to S_n. This process is called electronic transition, in which transition generally means the shift of an atom or molecule from one energy state to another. The transition from a lower to a higher energy level requires the absorption of photon energy hf, which is equal to the energy difference between two energy levels ΔE, shown in Eq. 2.31. (cf. [8, 13])

$$\Delta E = hf \tag{2.31}$$

The drop from a higher energy level to a lower one can result in heating or in the emission of photons, which is the case in luminescence [8]. The process of absorption, meaning excitation, and the relaxation, for example, in case of fluorescence, is illustrated in Fig. 2.16b. An overview of the different types of absorption is summarized in Tab. 2.3, in which also the regions, where these transitions occur (absorption band), are mentioned. The transition between two energy levels of a molecule and, moreover, the specific wavelengths are used as spectral fingerprint for diagnostic purposes [8].

Absorption Band	**Type of Absorption**	**Appearance**
UV, VIS, NIR	Electronic Transition	Atoms, Molecules
IR	Vibrational Transition	Molecules
Far IR, Microwaves	Rotational Transition	Molecules

Table 2.3: Different types of absorption and the concerned wavelength region (adapted from [8]).

The vibrational levels describe the different states of vibration of an atom in a molecule [8] and are considered as an approach of metabolic fingerprinting in case of IR [26]. The vibrational transition as well as the rotational transition are illustrated in Fig. 2.16c.

The parts of human tissue absorbing the photons or, more specific, the parts of the molecule that gives rise to the electronic transition, are called chromophores [8, 12]. The most common biological chromophores are represented by hemoglobin and its deviates, melanin, water, and foreign pigmented tattoos [12].

However, considering the same cross section area as in case of scattering, illustrated in Fig. 2.10 (p. 12), the absorption can be characterized in a similar way. The absorption cross section is defined as

$$\sigma_a = \frac{P_{\text{absorption}}}{I_0}, \tag{2.32}$$

where, again, I_0 is the incoming intensity and $P_{\text{absorption}}$ is the power of absorption [8]. Furthermore, the absorption coefficient is defined in Eq. 2.33, in which ρ means the density of the absorber, and the average distance, a photon is able to travel without getting absorbed, is defined in Eq. 2.34 and is the so called, "absorption mean free path" l_a [8].

$$\mu_a = \rho\sigma_a \tag{2.33}$$

$$l_a = \frac{1}{\mu_a} \tag{2.34}$$

The absorption coefficient of a homogeneous medium can be defined by Eq. 2.35, where a differential intensity dI changes by traveling an infinitesimal path dL. The integration over the thickness leads to the, well known, Beer-Lambert law, defined in Eq. 2.36 and illustrated in Fig. 2.17, where $\varepsilon = \frac{\mu_a}{c}$ means the molar extension coefficient and c stands for the molar concentration. Another commonly used quantity, which considers the length L as the path-length of the photon, is the transmission T, defined in Eq. 2.37, where also the relation to the imaginary index of refraction n'' can be recognized. The attenuation, also called absorbance A or optical density OD, defined in Eq. 2.38, is also used [8]. As will be discussed later, the absorption spectrum arises from the variation of ε.

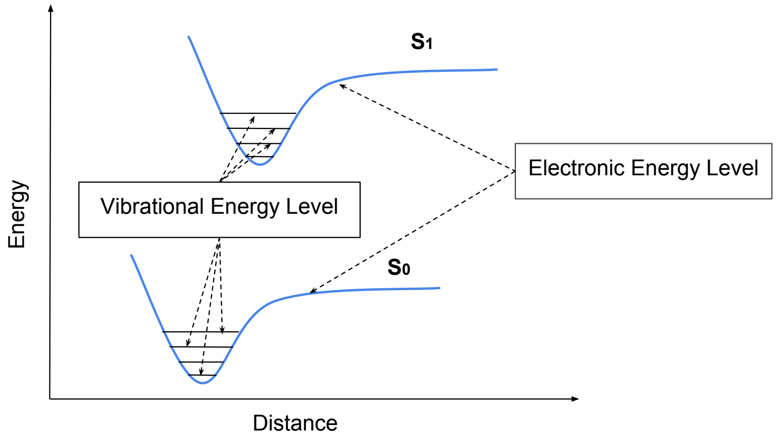

a) Vibrational and electronic energy levels of fundamental state S_0 and excited state S_1.

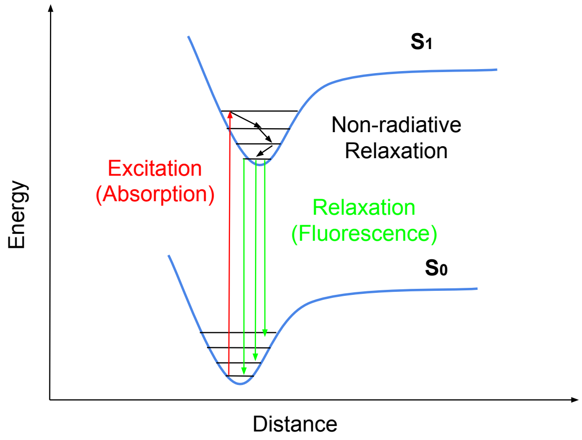

b) Electronic transition, showing absorption as excitation and fluorescence as relaxation.

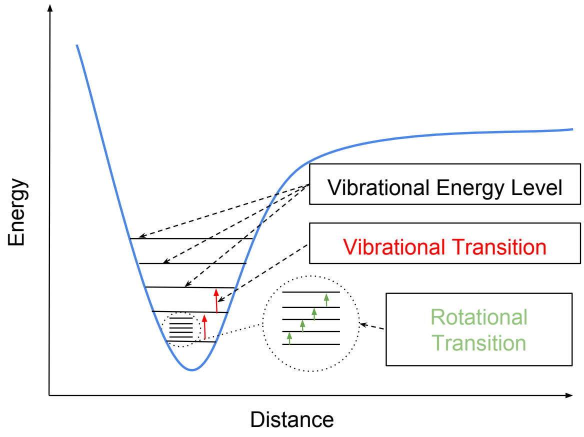

c) Vibrational and rotational transition, demonstrated at a single electric energy level.

Figure 2.16: Energy conversion during absorption with different transition types.

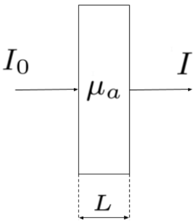

Figure 2.17: Illustration of Beer-Lambert law.

$$\frac{dI}{I} = -\mu_a dL \tag{2.35}$$

$$I = I_0 e^{-\mu_a L} = I_0 e^{-\varepsilon c L} \tag{2.36}$$

$$T = \frac{I}{I_0} = e^{-\varepsilon c L} = e^{\frac{-4\pi n'' L}{\lambda}} \tag{2.37}$$

$$A = OD = \log_{10} \frac{I}{I_0} = -\log_{10} T = \varepsilon c L \tag{2.38}$$

2.2.4 Fluorescence

The absorbed energy can be converted optically by emitting a photon or non-radiatively by exchanging kinetic energy, which can result in heating. Predominantly, both conversions occur together, where a small amount of energy is dissipated non-radiatively, and the major amount optically [8].

The emission of photons from the electronic state is called luminescence and can be divided into two types, fluorescence and phosphorescence, where the former one means the relaxation from a singlet state and the latter one from a triplet excited state (cf. [13]). An illustration of these two types of emission are shown in Fig. 2.18a, the so called Jablonski diagram, where the relaxation from an excited vibrational level to S_1 is called internal conversion (IC) and the following conversion to the ground level S_0 is referred to as fluorescence, while the intersystem crossing (ISC) from the singlet state S_1 to the triplet state $T2$ results, after additional IC, in phosphorescence. In fluorescence, a prompt emission occurs with a typical delay between absorption and emission on the order of nanoseconds, while in phosphorescence the emission is delayed on the order of milliseconds or longer [8, 13].

Human cells contain molecules, which are getting fluorescent by excitation with UV or VIS radiation, where fluorescence, caused by endogenous fluorophores, is an essential property of human cells and also called auto-fluorescence [27]. The Stokes shift is the reason for the emitted photons to have a lower energy, resulting in a longer wavelength

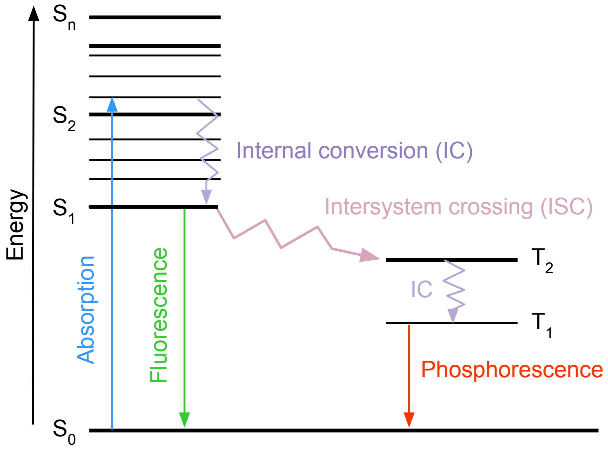

a) Jablonski diagram of energy levels.

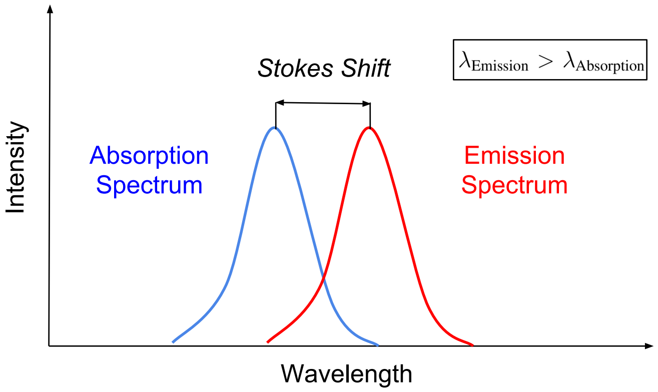

b) Stokes Shift.

Figure 2.18: Illustration of fluorescence by Jablonski diagram and Stokes shift.

compared to the absorbed photons, $\lambda_{\text{Emission}} > \lambda_{\text{Absorption}}$, illustrated in Fig. 2.18b. Thus, an absorption in the ultraviolet spectrum results in the radiation in the visible spectrum, which is usually used for dermatological diagnostics [28].

2.2.5 Polarization

As already mentioned, light can be characterized either by the particle or the wave model. The latter one describes light as electromagnetic wave, composed of two vectors, the electric field $\mathbf{E}$ and the magnetic field or magnetic field strength $\mathbf{H}$, shown in Fig. 2.19, where $\mathrm{B} = \mu\mathrm{H}$ is referred to as the magnetic flux density.

The relationship between the electric and magnetic field can be described by Maxwells equations, consisting of the Gauss law (Eq. 2.39), Gauss law of magnetism (Eq. 2.40), the

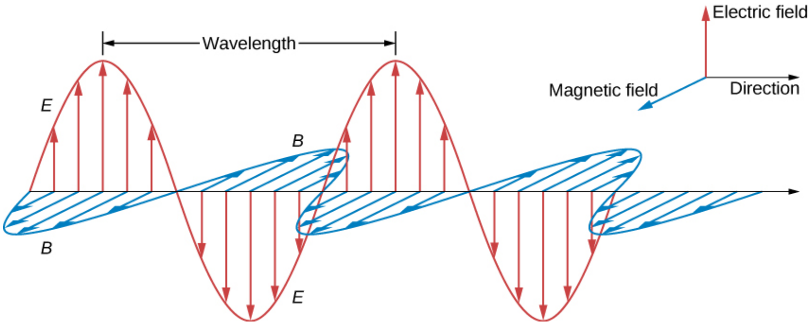

Figure 2.19: Light considered as transverse electromagnetic wave [29].

Maxwell-Faraday equation (Eq. 2.41), and Ampere's law with Maxwell's addition, shown in Eq. 2.42, where ρ is the charge density and $\mathbf{J}$ means the current density [15].

$$\nabla \cdot \mathbf{E} = \frac{\rho}{\varepsilon_0} \tag{2.39}$$

$$\nabla \cdot \mathbf{B} = 0 \tag{2.40}$$

$$\nabla \times \mathbf{E} = -\frac{\partial \mathbf{B}}{\partial t} \tag{2.41}$$

$$c^2 \nabla \times \mathbf{B} = \frac{\mathbf{J}}{\varepsilon_0} + \frac{\partial \mathbf{E}}{\partial t} \tag{2.42}$$

Both notations of the magnetic field, $\mathbf{B}$ and $\mathbf{H}$, have different units and are linked together by Eq. 2.43, where $\mathbf{M}$ is the magnetism [15], and in case of vacuum, $\mathbf{B} = \mu_0 \mathbf{H}$ is valid.

$$\mathbf{H} = \frac{1}{\mu_0}\mathbf{B} - \mathbf{M} \tag{2.43}$$

Faradays law (Eq. 2.41), written as integral equation in Eq. 2.44, leads to the term of a time-dependent field $\mathbf{B}$, produced by the spatial-dependent field $\mathbf{E}$, shown in Eq. 2.45, while considering the Ampere's law (Eq. 2.42), Eq. 2.46 results, where the spatially-dependent field $\mathbf{B}$ and the time-dependent field $\mathbf{E}$ can be recognized [29].

$$\oint \mathbf{E} \cdot d\mathbf{s} = -\frac{d}{dt}\int_S \mathbf{B} \cdot \mathbf{n} dA \tag{2.44}$$

$$\frac{\partial B_z(x,t)}{\partial t} = -\frac{\partial E_y(x,t)}{\partial x} \tag{2.45}$$

$$\frac{\partial B_z(x,t)}{\partial x} = -\varepsilon_0 \mu_0 \frac{\partial E_y(x,t)}{\partial t} \tag{2.46}$$

However, as a solution a planar wave is considered for the electric field in Eq. 2.47 and for the magnetic field in Eq. 2.48, traveling in positive x-direction, where $k = \frac{2\pi n}{\lambda}$ is the wave number of a medium with a refraction index n [13, 29]. Thus, $\mathbf{B}$ and $\mathbf{E}$ are in the same ratio, which equals the speed of light c, shown in Eq. 2.49 [29].

$$E_z(x,t) = E_0 \cos\left(kx - \omega t\right) \tag{2.47}$$

$$B_z(x,t) = B_0 \cos\left(kx - \omega t\right) \tag{2.48}$$

$$\frac{E_y}{B_z} = \frac{E_0}{B_0} = c \tag{2.49}$$

The plane of this transverse wave is called polarization, which can have different orientations of oscillations [29] and which is indicating the direction of the electric field [8]. Assuming a sinusoidal uniform plane wave as a complex function, leads to Eq. 2.50, where $\mathbf{k}$ is the propagation vector and $\mathbf{r}$ the coordinate vector. A propagating wave in z-direction can then be written as in Eq. 2.51, leading to the definition of the Jones formalism, which gives an easier description of the state of polarization [15, 29]. The polarization, defined by the Jones vector, is shown in Eq. 2.52, where an oscillation in x-direction (direction of the electric field) is called parallel polarized (p-polarized), while the direction of the magnetic field (y-direction) is termed as perpendicular polarized (s-polarized) [13]. Linear polarization, in which each angle between the plane and the direction of polarization is possible, is shown in Fig. 2.20, for an angle of 60°.

$$\mathbf{E} = \mathbf{E}_0 e^{j(\omega t - \mathbf{kr})} \tag{2.50}$$

$$\mathbf{E}(z,t) = \begin{bmatrix} e_x \\ e_y \\ 0 \end{bmatrix} e^{i(kz - \omega t)} \tag{2.51}$$

$$\mathbf{J} = \begin{bmatrix} e_x \\ e_y \end{bmatrix} = \begin{bmatrix} e_p \\ e_s \end{bmatrix} \tag{2.52}$$

The plane of polarization of incident linearly polarized light can be rotated by the presence of chiral molecules such as glucose [31]. However, the state of polarization also changes by the interaction with matter, and therefore, by scattering. The fast loss of polarization in tissues occurs because of multiple scattering, due to the randomness of tissue structures and thus, polarization effects are usually ignored, but in certain tissues like eye tissue, cellular mono-layers, muscous membrane, or superficial skin layers, the degree of polarization remains measurable [8, 31].

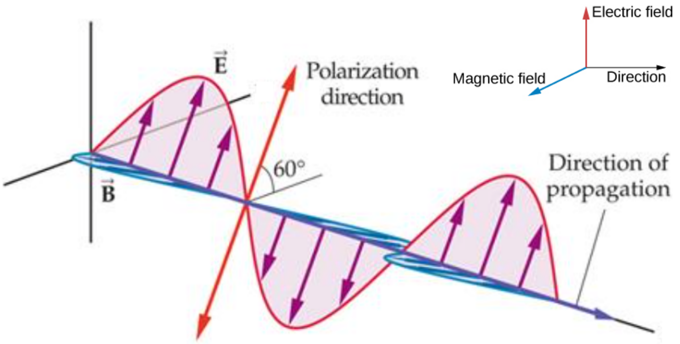

Figure 2.20: Linear polarized light of 60° (modified from [30]).

2.3 Human Tissue

The light propagation in a tissue depends on the optical properties of the tissue's components, meaning size, shape, and density of tissue parts and structures like cells, cell organelles, and various fiber structures, and mentioned properties like index of refraction, absorption, and scattering coefficient as well as the polarization of light, which all have an influence on the optical characteristic of a tissue [11].

Considering non-invasive optical biosensors for consumer and personal-health application in everyday use, a main focus is set on the interaction between light and the body surface, meaning the human skin.

Strongly or multiple scattering tissue, such as skin, brain tissues, or vessel walls, can be described by the radiation transport equation (RTE) or Monte Carlo simulation, and high transparent, and thus, weakly scattering tissues, such as eye tissues (cornea and lens), can be modeled by the assumption of Rayleigh and Mie scatterers [32], for most purposes even by ray optics. Since the direct application of electromagnetic theory to the tissue is complicated, due to multiple scattering effects, radiation transport theory is used, which ignores the wave-model of light, and thus, phenomena like polarization or interference [8]. Generally, the light transport through tissue is analyzed by Monte Carlo simulation [33].

A commonly used scattering function for biological material is the Henyey-Greenstein phase function [34], shown in Eq. 2.53, while the Reynold-McCormick scattering function [35], shown in Eq. 2.54, is usable for human blood [14].

$$p_{\mathrm{HG}}(\Theta) = \frac{1}{2}\frac{1-g^2}{(1+g^2-2g\cos\Theta)^{\frac{2}{3}}} \tag{2.53}$$

$$p_{\mathrm{RM}}(\Theta) = \alpha\hat{g}\frac{1}{\pi}\frac{(1-\hat{g})^{2\alpha}}{((1+\hat{g})^{2\alpha}-(1-\hat{g})^{2\alpha})(1+\hat{g}^2-2\hat{g}\cos\Theta)^{\alpha+1}} \tag{2.54}$$

Since the scattering phase function is only appropriate for a small number of scattering events, the anisotropy of scatter characterizes tissue in terms of their scattering directions [6]. For a simplified description of scattering properties, the reduced scattering coefficient μ_s' can be used, shown in Eq. 2.55, which links the anisotropy g and the scattering coefficient μ_s together, since the independent determination of these factors is not always possible [6, 14]. Finally, the interaction between radiation and biological tissue can be described by the light transport theory, shown in Eq. 2.56, where the effective attenuation coefficient μ_{eff} is defined in Eq. 2.57 in terms of reduced scattering and absorption coefficient [16, 36, 37], and which is valid for a Beer-Lambert-like situation.

$$\mu_s' = \mu_s(1-g) \tag{2.55}$$

$$I = I_0 e^{-\mu_{\text{eff}} L} \tag{2.56}$$

$$\mu_{\text{eff}} = \sqrt{3\mu_a(\mu_a+\mu_s')} \tag{2.57}$$

2.3.1 Skin

The human skin represents the major part of interaction with optical sensors, and consists of different components, resulting in a multi-layered structure. An overview of a normal human skin is shown in Fig. 2.21a, where the two main layers of the skin are mentioned as epidermis and dermis. The epidermis, representing the external skin surface, has a typical thickness of 30 to 100 μm [38], consists mainly of keratinocytes and melanocytes, and is a dynamic system, whose major functions are performed by their outermost layer, the stratum corneum, which consists of 60 $\%$ structural proteins, 20 $\%$ water, and 20 $\%$ lipids [7, 39, 40]. The dermis has a thickness of 1 mm to 2 mm, while the subcutaneous tissue, illustrated in Fig. 2.21b, contains larger vessels and nerves, compared to the dermis, in which only capillaries supply the non-vascular epidermis with nutrition, demonstrated as glucose diffusion via the interstitial fluid (ISF) [38]. The influence of aging is illustrated in Fig. 2.22, where major changes in all three layers can be recognized, considering a younger

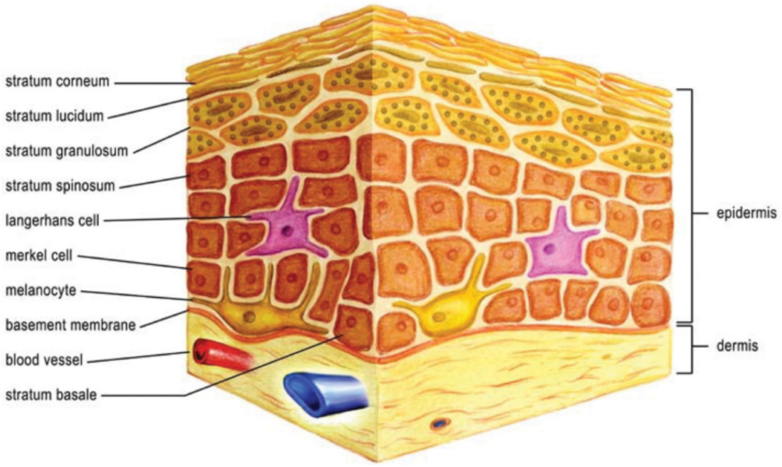

a) Human skin showing epidermis and dermis [7].

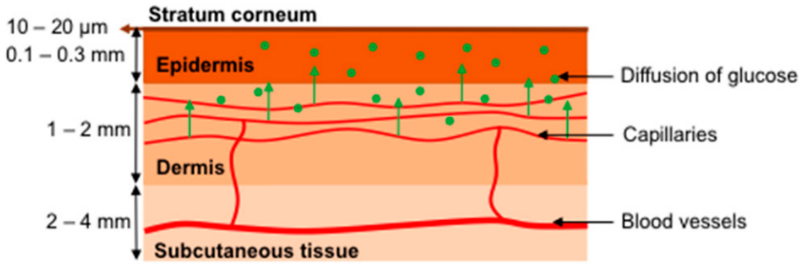

b) Another view of human skin, considering diffusion of glucose [38].

Figure 2.21: Illustration of human skin with its main layers and components.

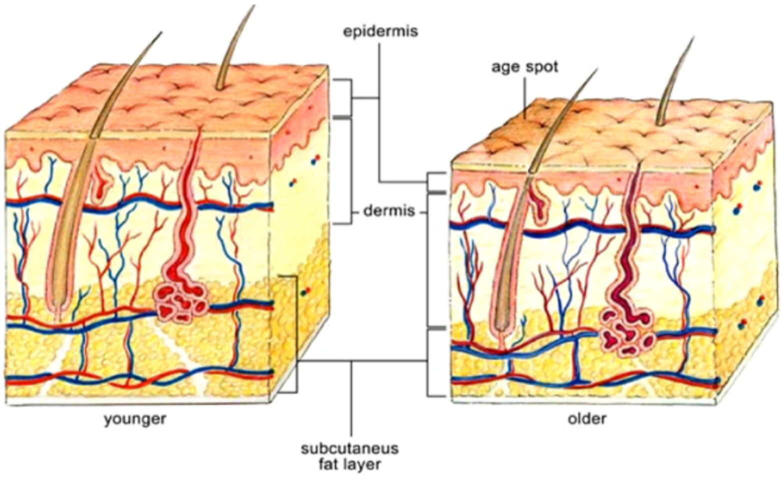

Figure 2.22: Influence of aging on skin structures, showing a normal (left) and an aged skin (right), in which changes in skin thickness and its layers can be recognized [7].

(left) and an older (right) human skin. (See [7] for a structural characterization of the aging skin.)

2.3.2 Spectral Aspects of Human Tissue

The possibility of tissue penetration by light depends strongly on its absorption, although, a preponderance of scattering over absorption in the range of 600 nm to 1600 nm and an increase of reflected radiation from 35 % to 70 % of total incident light due to backscattering occur [8]. An overview of different absorptions or scattering by a tissue is shown in Fig. 2.23, in which UV or mid-range (MIR), and far-range (FIR) infra-red light lead to a domination of absorption (left), while a radiation with NIR light results in approximately the same amount of scattering and absorption (middle), and NIR and VIS light cause a prevail of scattering [11]. Thus, the applied wavelength influences the absorption of light as well as the depth of tissue penetration, as demonstrated in Fig. 2.24, where different wavelengths can be recognized that reach different depths in tissue [12].

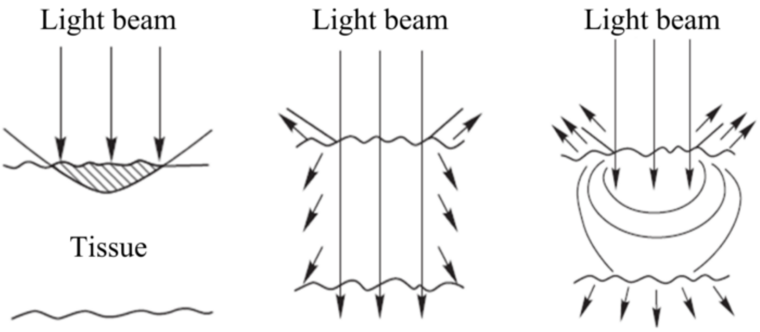

Figure 2.23: Absorption and scattering of a light beam, considering UV, MIR or FIR (left), NIR (middle), and NIR or VIS (right) light radiation (modified from [11]).

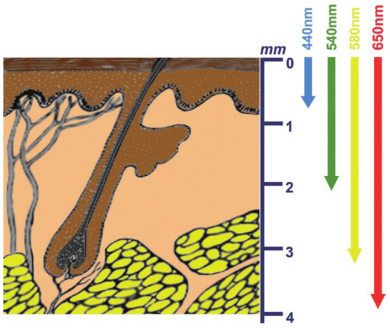

Figure 2.24: Different wavelengths and penetration depths of light in human tissue [12].

An overview of typical cutaneous melanosomes, showing their absorption coefficients over a spectral range from 200 nm to 1200 nm, was proposed by [6], and is illustrated in Fig. 2.25, where the mentioned dependency of the wavelength and the penetration depth can be seen. The absorption spectra of the aorta, whole blood, melanosome, epidermis, and water are illustrated in Fig. 2.26, where their absorption coefficients of the whole UV, VIS, NIR, and IR range are mentioned, and the, so-called, therapeutic or diagnostic window between 600 nm and 1400 nm, meaning the orange part of VIS to the NIR region, where most tissues are sufficiently weak absorbers and, thus, enable a significant penetration of light, is marked [8]. The absorption coefficient of the whole blood, which is used in different optical sensing solutions, is illustrated in Fig. 2.27, for oxygenated (top) and deoxygenated blood.

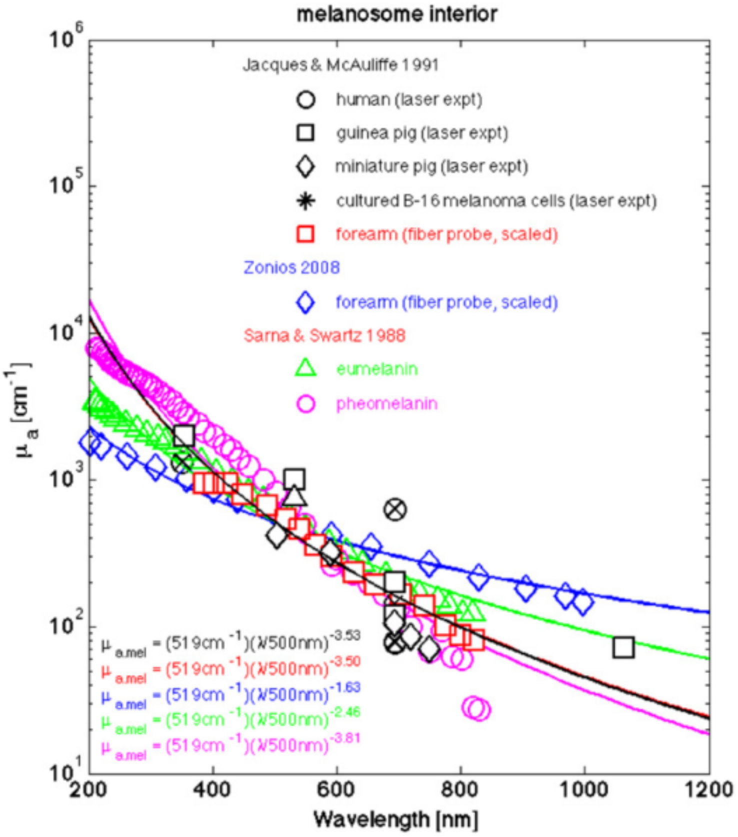

Figure 2.25: Absorption coefficient of typical cutaneous melanosomes [6].

The human skin also consists of several endogenous chromophores, which are absorbed in the UV region of light [12]. Some of them are illustrated in Fig. 2.28, where also other biological components and tissue chromophores are compared.

Next to absorption, scattering and the index of refraction represent also optical properties of human tissue. For example, the main scatters in human blood are the red blood cells (RBC), which have an refractive index of $n = 1.42$ for a hemoglobin (Hb) concentration of

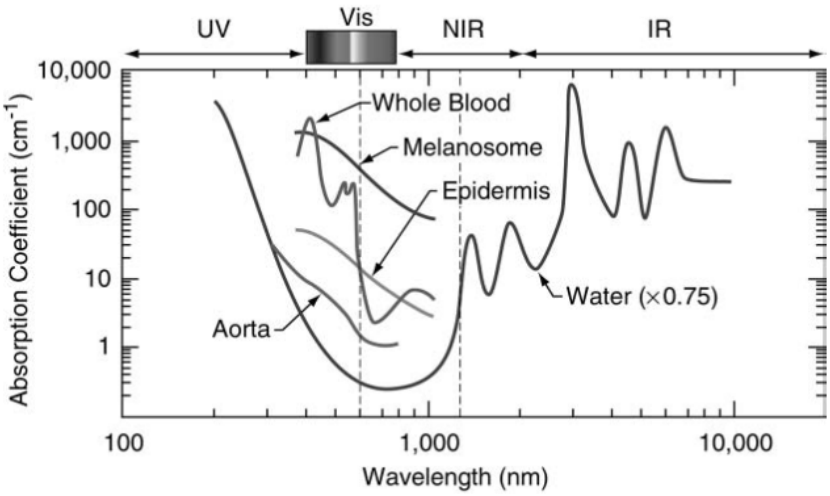

Figure 2.26: Absorption sepctra of the aorta, whole blood, melanosome, epidermis, and water, indicating the therapeutic window (dashed lines) between 600 nm to 1400 nm [8].

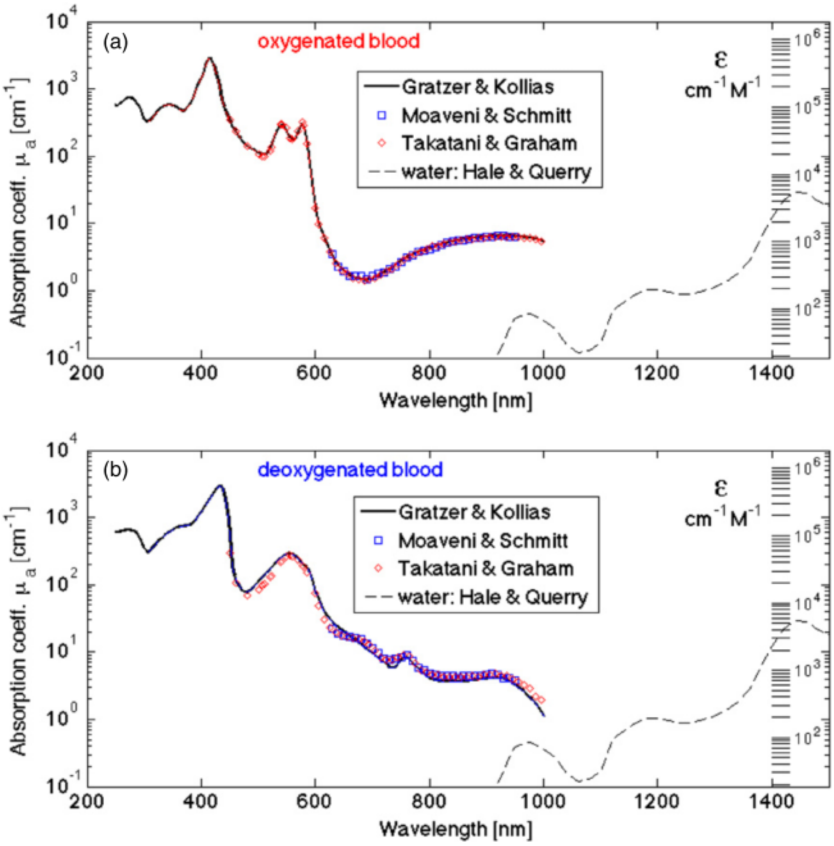

Figure 2.27: Absorption spectra of oxygenated (top) and deoxygenated (bottom) blood [6].

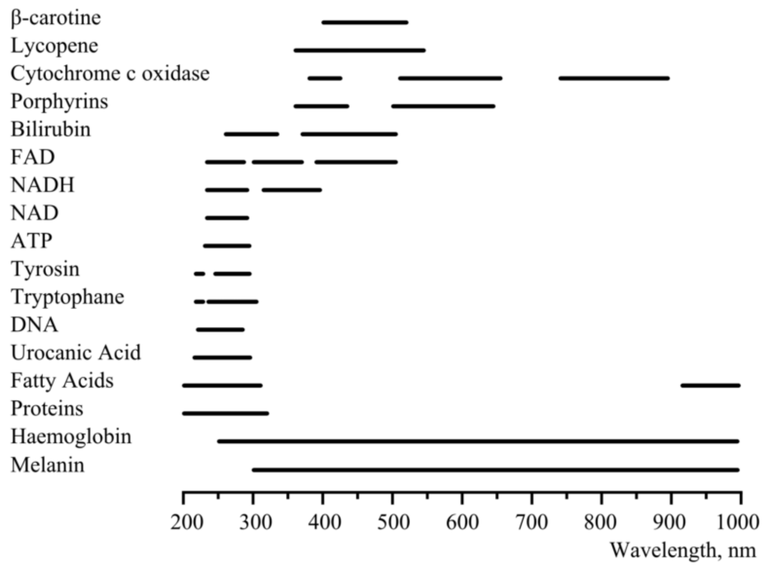

Figure 2.28: Comparison of spectral range of skin and tissue chromophores [11].

32 g/dl, while the index of refraction of the whole blood, depending on the wavelength, is between 1.36 and 1.40 [11].

Considering the real index of refraction n', it can be assumed as first approximation that the value of n' scales with the water content W of a tissue, which is specified in Eq. 2.58, where n'_{dry} stands for the refraction index of the tissues dry mass and n'_{water} = 1.33 refers to the one of water [6].

$$n' = n'_{\text{dry}} - (n'_{\text{dry}} - n'_{\text{water}})W \tag{2.58}$$

This assumption is shown in Fig. 2.29, where different refraction indices of biological tissues of the brain are compared. The water content was measured by [41] using MRI and thus, the dry mass density was determined as ρ_{dry} = 1.53 g/cm^3 as well as n'_{dry}= 1.514 [6]. The corresponding data of Fig. 2.29 is summarized in Tab. 2.4, where the density ρ, the water content W, and the real refraction index n' are compared.

An overview of refraction indices of common tissue types and cell structures is shown in Fig. 2.30, where the huge amount of different values as well as the high variation can be recognized, resulting in the property of multi-scattering tissue.

Taking scattering into consideration, the authors of [6] presented two models for approximating the reduced scattering coefficient μ'_s by fitting data from literature. They mentioned that both approaches are not exhaustive, but sufficient to characterize the behavior of seven tissue groups (skin, brain, breast, bone, other soft tissues, other fibrous tissues

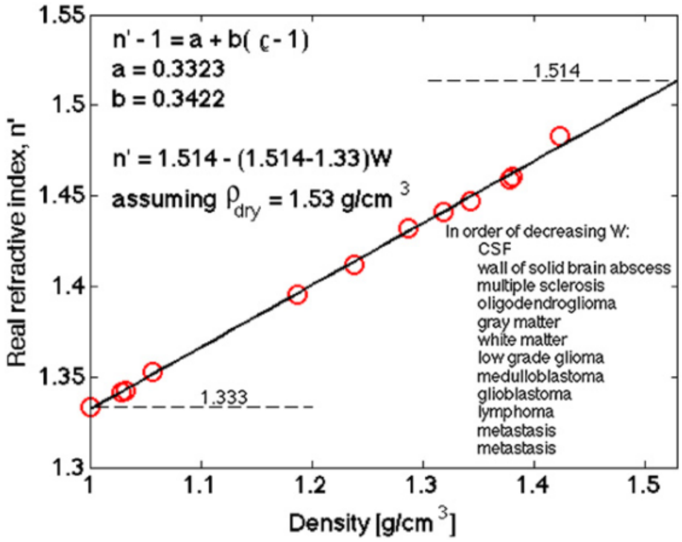

Figure 2.29: Real refraction index of biological tissues in order of decreasing water content [6] (data from [41] shown in Tab. 2.4).

Tissue	Density ρ (g/cm^3)	Water Content W (%)	Real Refraction Index n'
CSF	1.000	100	1.3333
Wall of solid brain abscess	1.028	97	1.3412
Multiple sclerosis	1.031	96	1.3425
Oligodendroglioma	1.056	94	1.3531
Gray matters	1.186	80	1.3951
White matters	1.237	70	1.4121
Low grade glioma	1.286	58	1.4320
Medulloblastoma	1.318	53	1.4412
Glioblastoma	1.343	49	1.4470
Lymphoma	1.378	42	1.4591
Metastasis	1.381	40	1.4602
Metastasis	1.423	29	1.4833

Table 2.4: Tissues types of human brain in order of decreasing water content (modified from [41]).

and fat tissues). The first model is shown in Eq. 2.59, where the wavelength is normalized by a reference value of 500 nm, b means a term, which shows the wavelength dependency of μ_s', and the factor a equals to $\mu_s'(\lambda = 500nm)$. The second model, shown in Eq. 2.60, is described by contributions of Rayleigh and Mie scattering at the reference wavelength,

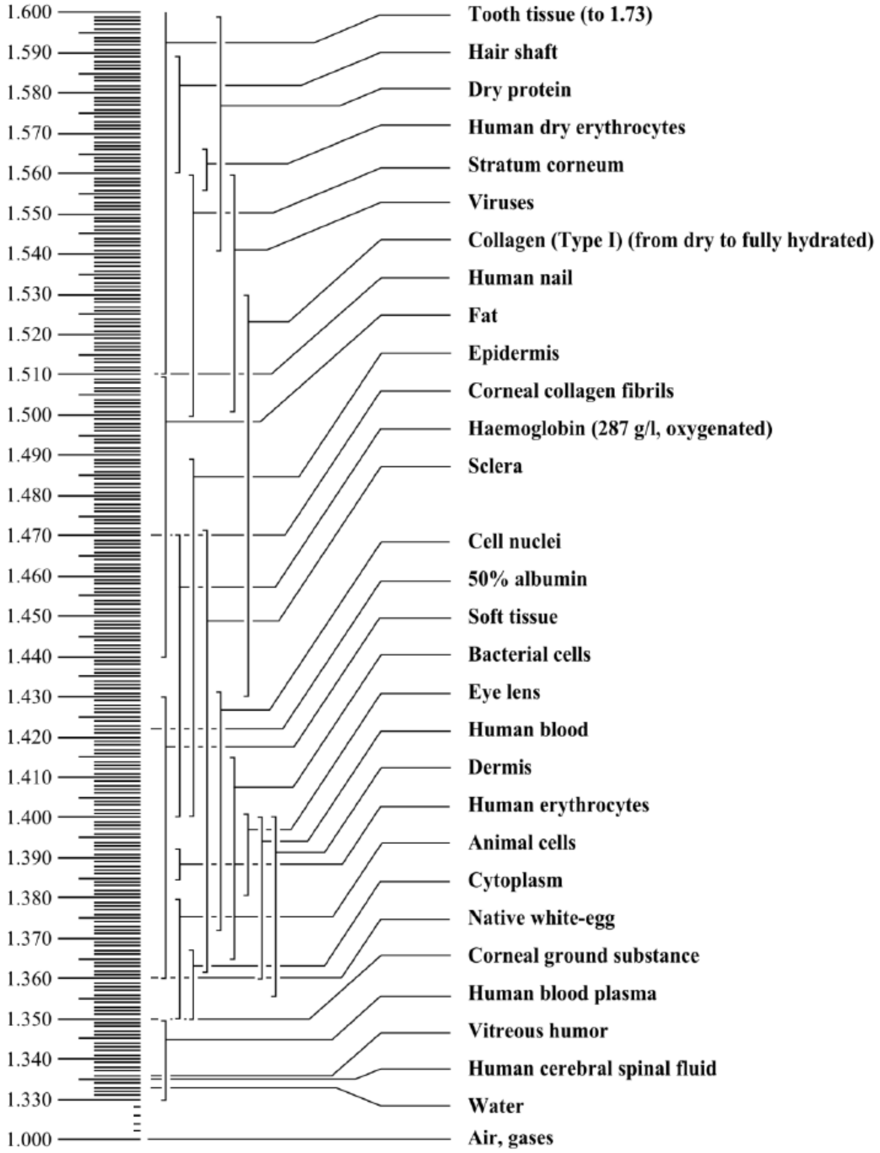

Figure 2.30: Index of refraction of common tissue types and cell structures [11].

where, according to the authors, $1 - f_{\text{Ray}}$ indicates the fraction of Mie scattering.

$$\mu_s' = a\left(\frac{\lambda}{500\text{nm}}\right)^{-b} \tag{2.59}$$

$$\mu_s'(\lambda) = a\left(f_{\text{Ray}}\left(\frac{\lambda}{500\text{nm}}\right)^{-4} + (1 - f_{\text{Ray}})\left(\frac{\lambda}{500\text{nm}}\right)^{-b_{\text{Mie}}}\right) \tag{2.60}$$

A comparison of both models as well as their reference data are shown in Fig. 2.31, where

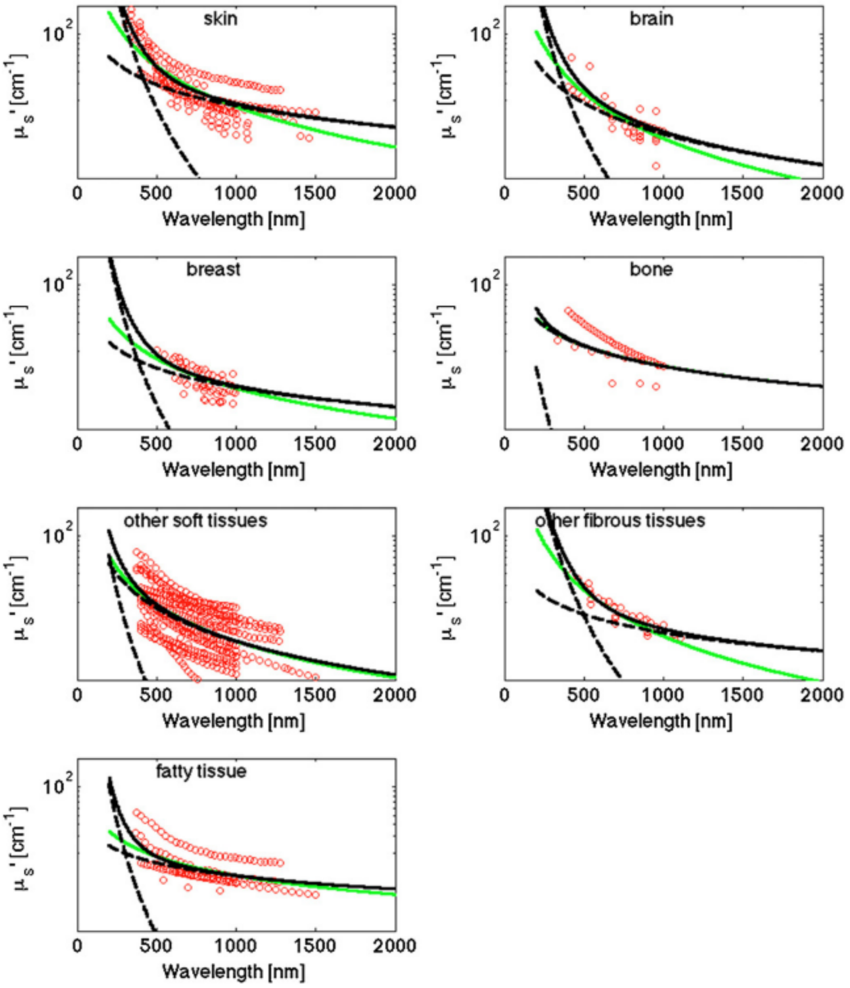

Figure 2.31: Comparison of two models for the reduced scattering coefficient μ_s', considering the first model (Eq. 2.59, green), the second model (Eq. 2.60, black solid) with Rayleigh and Mie components (black), and the reference data (red) (modified from [6]).

the authors mentioned a equally good usage for routine prediction of tissue scattering within 400 nm to 1300 nm, and a divergence of both models outside this range, meaning UV and longer IR.

Since the variability of a in Eq. 2.59 and 2.60 scales the wavelength-dependent term, a ranking of the different tissue types is given in Fig. 2.32, showing that skin and fibrous tissue result in higher a-values, while breast tissue can be seen as both, low and high scattering, which might depend on the specific content of fibrous and fat tissue of a particular breast [6].

As mentioned before, the type of scattering depends on the size of the scatterer. Therefore, a comparison of the most common tissue and cell structures, considering their size

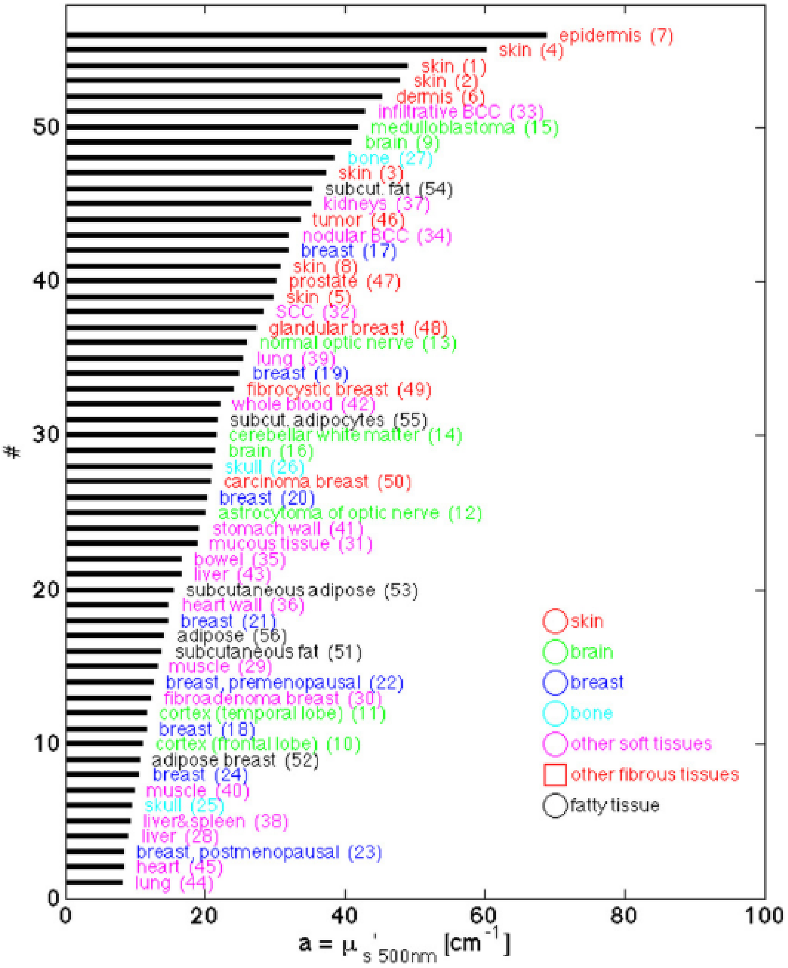

Figure 2.32: Different tissue types ranked by their scattering at 500 nm (Eq. 2.59) (modified from [6]).

range as well as their scattering regime, are illustrated in Fig. 2.33, where many tissues can be seen as a system of discrete scattering particles [11].

Finally, it should be mentioned that autofluorescence is caused by several fluorophores such as collagen, elastin, and tryptophan, which is a component of most proteins, nicotinamide adenine dinucleotide (NAD), representing a coenzyme in all living cells, which all have different fluorescence lifetimes, varying between short (0.2 ns to 0.4 ns) lifetimes for collagen as well as melanin, and long (3.5 ns to 5.2 ns) lifetimes for flavin [28].

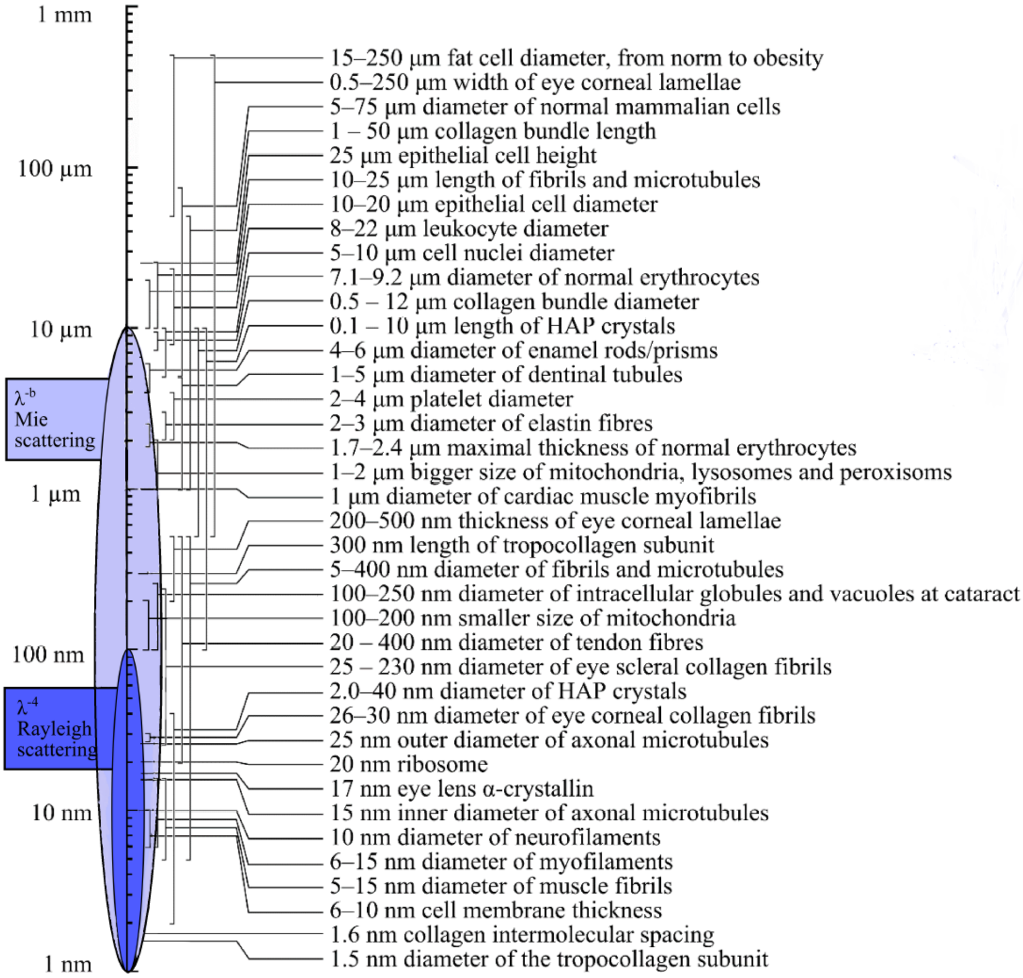

Figure 2.33: Size of different tissue and cell structures, where Mie and Rayleigh scattering are marked [11].

2.4 Spectral Measurement of Human Tissue

Spectroscopy provides the possibility to compensate unwanted signal variations due to interfering analytes by multi-wavelength measurement, where in different biological applications the tissue of interest can either be measured in transmission or diffuse reflectance mode, or sometimes in both, shown as a comparison of these two modes, illustrated in Fig. 2.34 [42]. Considering wearable applications like watches, wristbands, or smartphones, the reflectance mode would be the preferred measurement mode.

The most basic measurement of diffuse reflectance from a tissue is represented by diffuse optical spectroscopy (DOS) [43] or, also called diffuse reflectance spectroscopy (DRS), where a broadband light source (eg. thermal lamp, white LEDs, or laser diodes)

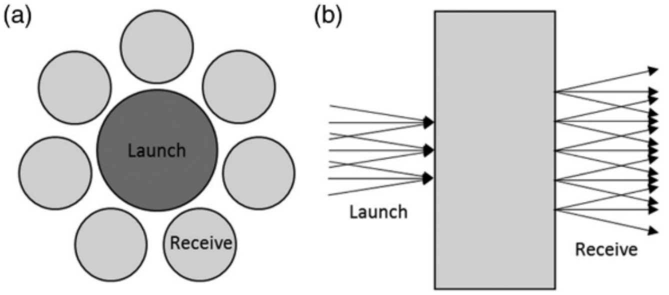

Figure 2.34: Comparison between reflectance (a) and transmission measurement geometry (b) [42].

penetrates into a tissue, often realized as multi-mode optical fibers, and the emitted photons interacting with the tissue, which might result in elastic or Raman scattering, absorption, or fluorescence, before the reflected portion of photons is detected by an optical spectrometer [4]. This process is illustrated in Fig. 2.35, where the reflectance spectrum is analyzed by an analytical method like diffusion equation, Monte Carlo simulation, or an empirical model to extract absorption and reduced scattering information [4].

Another method is called diffuse correlation spectroscopy (DCS), which detects blood flow by temporal fluctuations of light fields from tissue surface, with a typical setup illustrated in Fig. 2.36, where a long-coherent-length source is coupled with a multi-mode fiber, and, after its detection by a photon-count detector, the autocorrelation function is calculated [44].

Also, other measurement geometries are applied in the field of biomedical optics. An overview of typical spectral measurement geometries, used in different in-vivo as well as in-vitro studies, was given by [11], summarized and compared in Fig. 2.37, where measurements of back- and forward-scattering, collimated transmittance, and specular reflectance can be recognized in (a), while total transmittance shown in (b), diffuse reflectance in (c) with in-vivo integrating sphere detection in (d), spatially-resolved fiber in (e) and CCD in (f), are mentioned.

Generally, optical spectroscopy can be differed by their measurement geometry, the applied wavelength range, or the measured optical quantity. A comparison of these most general distinguishing features is given in Fig. 2.38, representing a rough overview of the predominantly used methods for the considered fields of spectral biosignal acquisition.

As reviewed in this thesis, human tissue has different optical properties at different wavelengths as well as it is possible to penetrate tissue to different depths. Due to increasing photonics technologies, which provide the production of miniature CCDs and spec-

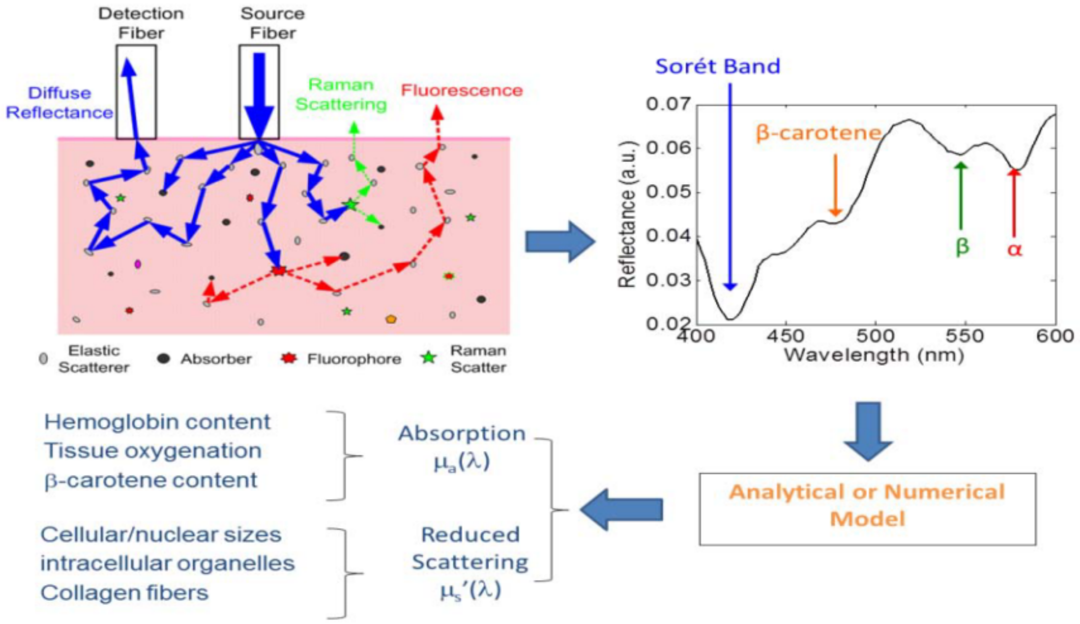

Figure 2.35: Principle of diffuse reflectance spectroscopy (DRS) [4].

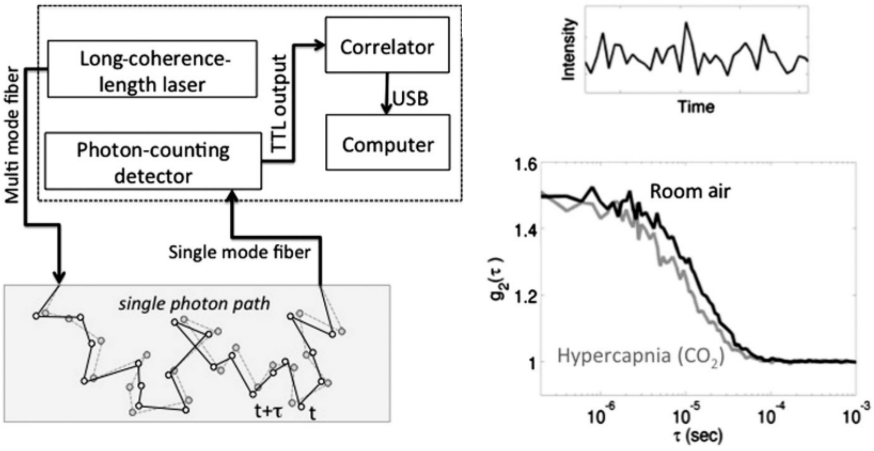

Figure 2.36: Typical schematic of diffuse correlation spectroscopy (DCS) (modified from [44]).

trometers, [45] the availability of multi-spectral health and costumer devices is enabled, representing potential diagnostic systems for different areas of biomedical applications.

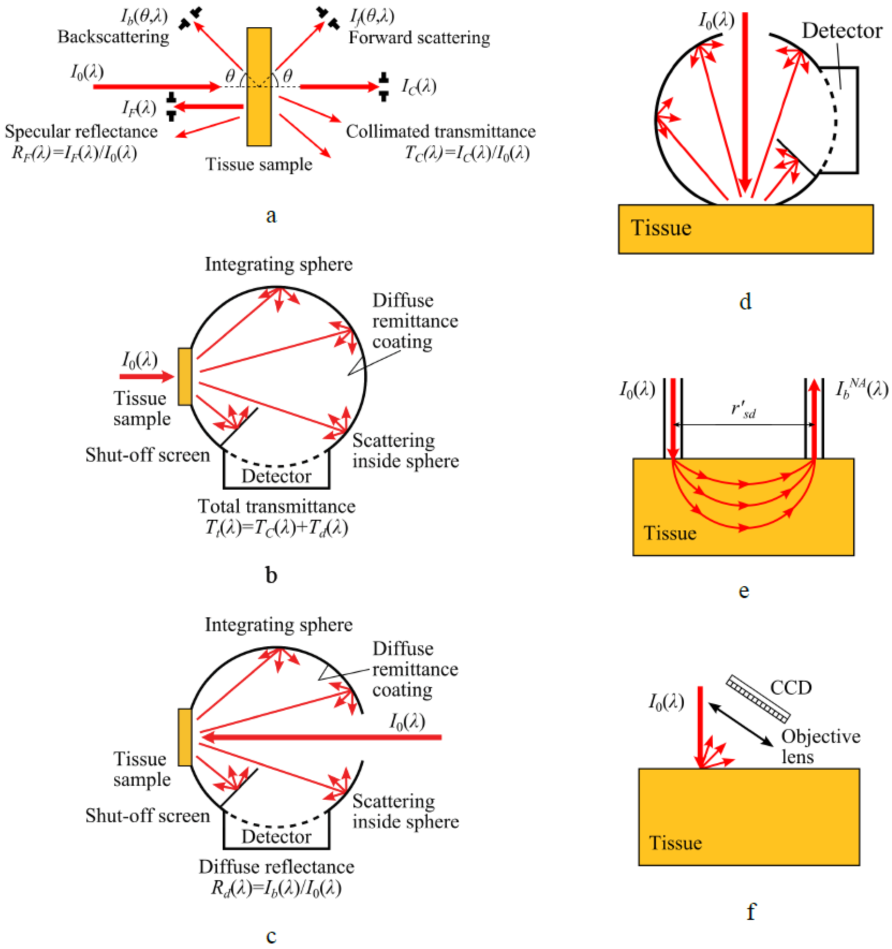

Figure 2.37: Typical geometries for spectral measurement, showing back and forward scattering, collimated transmittance as well as specular reflectance (a), total transmittance (b), and diffuse reflectance (c) to (f) (modified from [11]).

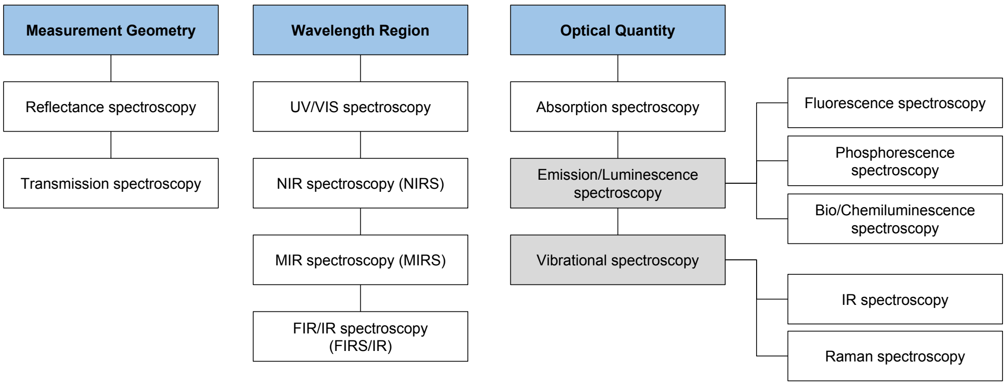

Figure 2.38: Different types of optical spectroscopy, differed by measurement geometry, applied wavelength region, and optical quantity.

3 Optical Glucose Measurement

3.1 Introduction

Diabetes is a chronic disease of metabolism [46] that occurs when the pancreas does not produce enough insulin or the body can not use it effectively [2]. Insulin is the only hormone which is able to decrease the blood glucose level by an increasing absorption of glucose in human cells, especially, muscle and fat cells [46]. A raised level of blood glucose may lead to serious damage of the heart, blood vessels, eyes, kidneys, and nerves [2]. According to the Word Health Organization (WHO) [2], in 2014 approximately 422 million adults were living with diabetes worldwide. Diabetes also caused 1.5 million deaths in 2012 and an additional 2.2 millions deaths by increasing the risks of cardiovascular and other diseases as a result of higher-than-optimal blood glucose [47].

Generally, two types of diabetes exist, which are type 1 and type 2 diabetes. The first one is also known as insulin-dependent diabetes and is characterized by an insufficient production of insulin, while the second one results from the ineffective use of insulin and is therefore called non-insulin-dependent diabetes. A differentiation between both types requires sophisticated laboratory tests for pancreas function [2].

The control of the blood glucose level is an important part of diabetes management. Moreover, the treatment of diabetes needs a periodically measurement of the blood glucose level [46]. Especially, the success of treating type 1 diabetes requires, next to a precise insulin delivery system, a reliable glucose monitoring [48]. The self-monitoring is an essential part of the treatment, which can identify and prevent periods of hypo- and hyperglycemia [49]. Furthermore, a raised glucose level can cause permanent damages in tissues and organs [50].

Today, there are two common methods of detecting the blood glucose level, classical self-monitoring of blood glucose, and real-time continuous glucose monitoring [48]. Both methods are invasive measurements. The first one determines the glucose level by pricking the finger and testing the blood with a glucometer, while the other one delivers the concentration of glucose in the subcutaneous tissue about every five minutes [48].

The detection of blood glucose by an optical sensor solution would increase the quality of patient's life by replacing the finger-pricking with a non-invasive method, which could also allow a continuous monitoring of the glucose concentration. Also, this might be the reason why so many different approaches of non-invasive blood glucose measurement were highly discussed topics in the past. This chapter has a focus on optical approaches of in-vivo glucose measurement and will summarize the principle, advantages, and disadvantages as well as the limitation of these non-invasive glucose detection methods.

3.2 Glucose in Human Body

Carbohydrates represent the essential source of energy for human cells, where glucose, or also called blood sugar ($C_6H_{12}O_6$), is the most important one. The human body does not store glucose by itself, because a higher concentration of glucose inside the cell would make the cell hypotonic, which would lead to an influx of water into the cell. Instead of glucose, the body uses glycogen as a buffer of carbohydrates. Glycogen is an insoluble polysaccharide, which will not become osmotic in comparison to glucose. The liver is able to store glycogen or transform it into energy. Also, the regulation of the blood glucose level is done by a group of hormones, where insulin is the only one which is able to decrease the blood glucose level. The interplay of these hormones makes it possible to keep the blood glucose level constant at a state of fasting, which is necessary to secure the energy supply of the central nerve system (CNS). (See [46, 51] for a more detailed description of these metabolic and physiological processes.)

As already mentioned, diabetes means that the pancreas does not produce enough insulin or the human body can not use it effectively. Next to type 1 and type 2 diabetes, impaired glucose tolerance (IGT) and impaired fasting glycaemia (IFG) exist as a intermediate state between normal blood glucose level and diabetes (especially type 2), causing a higher risk of heart attacks as well as strokes [2]. Also, gestational diabetes (GDM) can occur as a temporary condition during pregnancy and increases the risk of developing type 2 diabetes [52].

A diagnose of diabetes can be done either by measuring the fasting plasma glucose (FPG), meaning the glucose level of blood after eight hours of fasting [53], or by the oral glucose tolerance test (OGTT), also called 2-h plasma glucose, where the glucose level is measured two hours after an oral intake of 75 g glucose [2]. The WHO recommended different threshold values of blood glucose, taken from venous plasma. These values are summarized for diabetes in Tab. 3.1, where values from capillary blood samples are also mentioned. (See [46, 47] for the diagnostic criteria of IGT, IFG and GDM.) These criteria for diabetes and hyperglycemia were set by the WHO in 1999 and differ from the, also commonly used, cut-off values from the American Diabetes Association (ADA), defined in 1997 [54].

	Venous Plasma (mmol/l)	**Cappilary Blood (mmol/l)**
FPG	≥ 7.0	≥ 6.1
OGTT	≥ 11.1	≥ 11.1

Table 3.1: Diagnostic criteria for diabetes taken from venous plasma [47] and capillary blood [46].

Next to the venous plasma level, four other blood sample types to measure the blood glucose concentration are routinely used [55], which are venous, arterial, and capillary whole blood as well as venous serum [55, 56]. The concentration measured by the whole blood, which is the case by glucose meters, can differ from plasma glucose level up to 11 %, where plasma has the higher value [57]. It has been shown by [56], that measurements, based on the venous whole blood, give results 0.5 mmol/l lower than other methods. In addition to that, the use of capillary blood has shown a very large variability compared to other methods. According to [58], the difference between capillary and venous glucose concentration was similar before and 120 min to 180 min after an intake of glucose, while the mean difference after 15 min to 90 min was 1.8 mmol/l. In a study from [59], the relationship between venous and capillary glucose measurement was investigated by measuring both simultaneously on random samples of 609 people, fasting samples of 685 people and two hours after oral glucose intake of 463 people. The results also show a variability between venous and capillary blood glucose, with venous plasma being higher at the random and fasting samples, but lower after the two hours after the glucose intake [59].

Thus, for an accurate interpretation of the measurement results, it is important to know the type of blood sample [55]. A general overview of the blood supply of the human tissue, respectively the tissue cells, is illustrated in Fig. 3.1.

In the study from [61], the trend of the venous and capillary whole blood glucose concentrations were compared of 75 healthy subjects by measuring the OGTT. The results are shown in Fig. 3.2, where a significant higher glucose level in capillary whole blood as in venous blood can be recognized. Comparing the relationship between different blood sample types, the authors used the HK-G6PD method as a reference, where the lowest

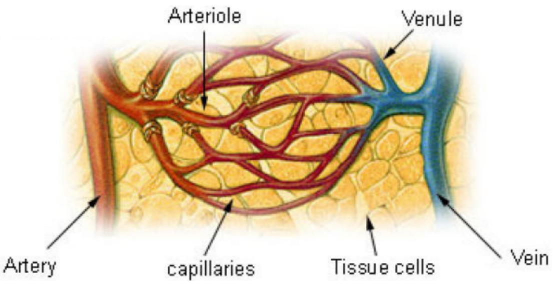

Figure 3.1: Overview of humans tissue blood supply (modified from [60]).

concentration of 9.58 mmol/l was obtained in venous whole blood. The other results show 10.50 mmol/l for capillary whole blood and 10.84 mmol/l for venous plasma level. These relations are summarized in Fig. 3.3, where the authors additionally mentioned that it was also possible to estimate the capillary plasma value to 11.58 mmol/l.

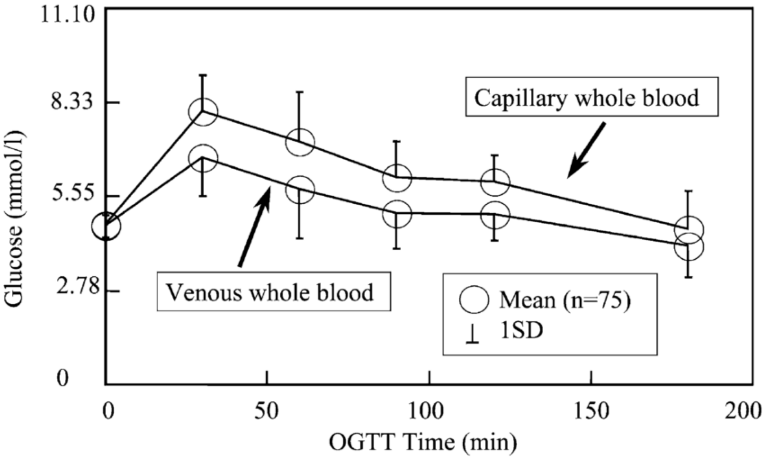

Figure 3.2: Venous whole blood vs. capillary whole blood glucose concentration [61].

However, the arterial blood concentration approximates closely to the capillary blood glucose concentration [55, 62]. Generally, it is agreed that in the state of fasting, the level of the arterial blood is between 0.167 and 0.278 mmol/l higher than the venous level [63], while in a postprandial state, the arterial blood glucose concentration is almost higher due to the glucose diffusion from the plasma to the interstitial fluid (ISF) [57].

The interstitial fluid (ISF) connects the cells with the capillaries and supplies them with nutrition like glucose, so plasma and IF have different characteristics and should be handled as separate glucose compartments [57]. Since the measurement of IF glucose represents one of the most effective methods for continuous blood glucose monitoring (CGM) [64], it is important to define a relationship between IF and blood glucose mathematically.

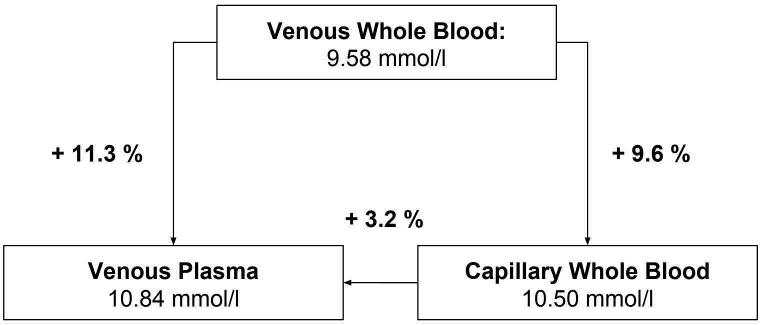

Figure 3.3: Relationship of different blood sample types for blood glucose measurement (adapted and modified from [61]).

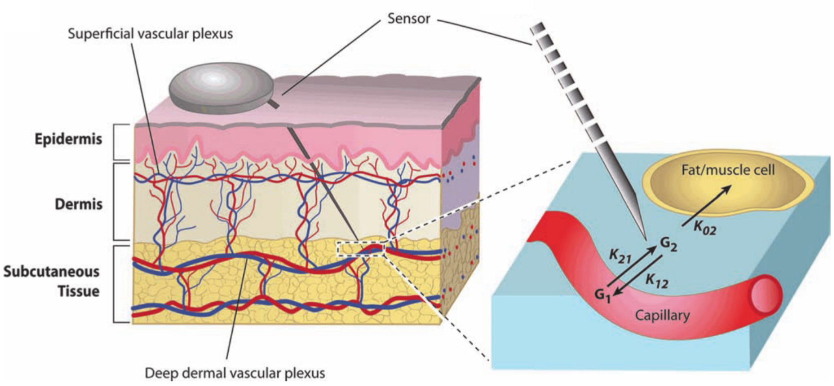

Figure 3.4: ISF and blood glucose as two different compartments (adapted by [57] from [65]).

An overview of these two compartments is illustrated in Fig. 3.4, where for this subcutaneous measurement, the sensing part is implanted under the skin to detect the IF glucose level [33]. On the left side, different skin layers with the inserted sensor of a continuous glucose monitoring (CGM) are shown, while the right site shows the detailed view of the ISF and blood glucose compartments [57]. The indicated glucose dynamic was described by [65] as a two-compartment-model, shown in Eq. 3.1, where G_1 and G_2 are the plasma and IF glucose concentration, K_{12} the forward and K_{21} the reverse flux rate of the glucose transport across the capillary, K_{02} is the glucose uptake into the tissue, and V_1 and V_2 are the volumes of plasma and IF compartments.

$$\begin{aligned} \frac{dV_2G_2}{dt} &= K_{21}V_1G_1 - (K_{12}+K_{02})V_2G_2 \\ \rightarrow \frac{dG_2}{dt} &= K_{21}\frac{V_1}{V_2}G_1 - (K_{12}+K_{02})G_2 \end{aligned} \tag{3.1}$$

According to [64], the results of this model may not accurately represent the true ISF glucose values due to the easy clotting of the electrode and the resulting potential drift. They combined the mentioned model with real-time measurements of glucose dynamics in blood and ISF compartments, meaning that they included the kinetic analysis of glucose movement from capillaries to the surrounding tissue by considering the concentration gradient differences and blood pressure-driven forces, involving capillary, ISF, and the diffusion process with the interstitial space. Thus, they developed a theoretical model, which is based on Starling equation and Fick's laws, to accurately describe the glucose transport in microcirculation, which also considers the diffusion distance that describes how far the glucose molecules diffuse from capillary into tissue. They concluded that it is possible with the developed model to monitor the dynamic change of blood glucose concentration with high accuracy by measuring glucose changes in ISF.

However, the glucose concentration in the ISF also depends on blood flow, metabolic rate, and the rate of change of the glucose concentration [66]. Moreover, the ISF glucose concentration depends more on the local conditions, meaning that ISF glucose is measured in relatively small volumes of tissue which undergoes slow changes, while the glucose concentration in the blood can rapidly change, since it is in a state of instant ”mixing” [67]. Thus, there is a time lag of 2 min to 45 min between the peak glucose concentration in the blood and the concentration in the ISF, which is the reason why an ISF sensor has to be calibrated to blood glucose value regulatory [66]. This calibration of the IF glucose level by means of the blood glucose measurements may have influence on the maximal recorded glucose level [67] and, thus, a frequent calibration is needed [33]. (See [68] for a summary of the estimated time lag values of several studies using different sampling methods as well as different measurement principles.) Since complications by hypo- and hyperglycemia depend on the blood glucose, an ISF glucose sensor may not ideally be suitable for closed-loop insulin delivery systems due to the mentioned time lag [69]. The time lag between blood and ISF glucose is also a major challenge, considering the non-invasive glucose measurement by different spectral methods [70].

A common assumption is that the difference between blood and ISF glucose is short-lived and not of significant therapeutic relevance [67]. According to [67], this assumption is not true all the time. As an example, the authors mentioned the refilling of glycogen store, which takes some time and, thus, the ISF glucose is lower than the one in blood. They declared that in this case, the blood glucose level does not represent the correct therapeutic target glucose value. Furthermore, they showed that the ISF glucose level uncovers clinically relevant differences, considering physical activity, hypoglycemic episodes, and meal-related differences of glucose level, and that it would be risky, from a therapeutic point of view, to use blood glucose values instead for therapeutic decisions. Based on that, they mentioned that it may be reasonable to switch from blood to ISF glucose measurement as the appropriate therapeutic target in diabetes management.

3.3 Optical & Non-Invasive Glucose Measurement

Several different approaches were developed detecting the glucose level in human blood optically. All of them are applied directly onto the human skin and act like a non-invasive glucose measurement without the need of a blood sample. The following methods represent only a selected amount of optical techniques, which are discussed in detail:

- Near infrared spectroscopy (NIRS)
- Mid infrared spectroscopy (MIRS)
- Raman spectroscopy
- Other methods

Generally, they all follow the same principle of measurement, illustrated in Fig. 3.5, where an individual light source (e.g. LED or laser) acts on different parts of the human body (measurement site). A detector measures the optical response and the glucose concentration results after applying individual signal processing and analyzing methods.

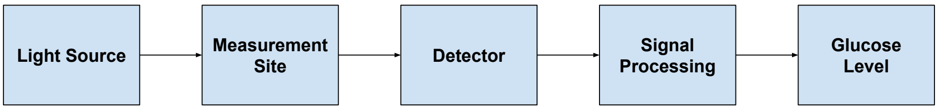

Figure 3.5: General overview of optical glucose measurement methods (adapted from [33]).

Before discussing each method in detail, the target accuracy should be considered. To do so, care should be taken to the accuracy of current invasive blood glucose monitoring systems. Since July 2017, the standard EN ISO 15197:2015 adapted from the international standard ISO 15197:2003 is obligatory in the European Union, replacing the former standard EN ISO 15197:2003 and containing stricter requirements for the system accuracy of blood glucose meter systems for self-testing [71]. According to this new standard, an error of at most ± 15 % of the measured glucose concentration above 5.6 mmol/l and at most ± 0.8 mmol/l for concentrations under 5.6 mmol/l are allowed and has to be fulfilled at 95 % of all measurement results [72]. These requirements are summarized in Tab. 3.2.

Glucose Concentration (mmol/l)	Maximum Error
≥ 5.6	$\pm$ 15 %
<5.6	$\pm$ 0.8 mmol/l

Table 3.2: New system accuracy of blood glucose measurement system for self-testing according to EN ISO 15197:2015 [72].

In order to perform an evaluation of the mentioned techniques, a comparison with a reference method should be done to determine the accuracy of the described methods. Many possibilities to determine the accuracy (correctness) and precision (degree of reproducibility) of a glucose sensor exist [69]. For clinical measurement comparison, the use of correlation is often misleading [73]. Therefore, for a better interpretation of compared measurement results the Bland-Altman plot can be used (cf. [73, 74]). A frequently used method to compare a measured and a reference blood glucose value is the Clarke error grid analysis (EGA), illustrated in Fig. 3.6a. The error grid is divided into five regions, where the Zone A shows the clinical accurate zone with 20 % error, Zone B, C, and D represent an inappropriate, unnecessary, and a potential dangerous treatment, while resulting measurement values in Zone E lead to confusion and a mix-up in treatment between hyperglycemia and hypoglycemia [33]. In 2000, the ”consensus error grid” was proposed by [75], based on the answers of 100 diabetologists and diabetes experts, asking to assign the risk of self-monitoring blood glucose error [66]. This, also called ”Parkes error grid”, is illustrated in Fig. 3.6b for type 1 diabetes patients, where in comparison to the Clark error grid, the risk groups of the Parkes error grid are continuous.

3.3.1 Near Infrared Spectroscopy (NIRS)

Near-infrared spectroscopy (NIRS) uses light in the region of 750 nm to 2500 nm, where the C−H, O−H and C=O bonds of glucose molecules cause absorptions of NIR light in different bodily fluids (e.g. blood) [77]. The NIR region can be divided into three bands, which are the combination overtone band (2000 nm to 2500 nm), the first overtone band (1400 nm to 2000 nm), and the second or higher overtone band (750 nm to 1400 nm) [33]. In the combination overtone band, bending and stretching vibrations of C−H, O−H and N−H occur, while the regions of 1000 nm to 1800 nm primarily correspond to stretching vibrations of C−H bonds [78]. Additionally, the radiation of NIRS has several optical windows [8], which allow a penetration of a few millimeters into human tissue due to a

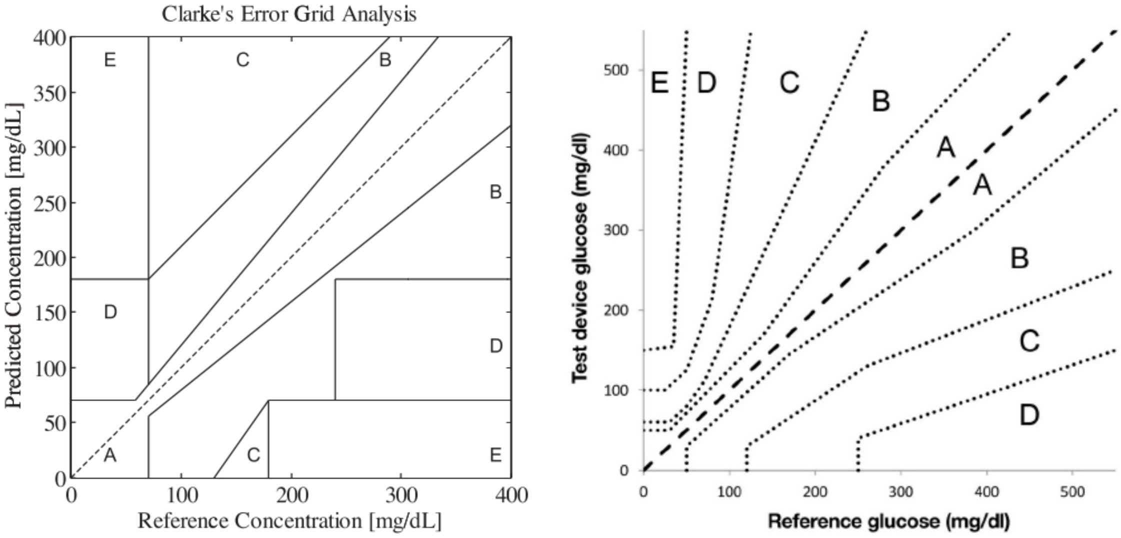

a) Clarke's error grid analysis [33]. **b)** Consensus (Parkes) error grid [76].

Figure 3.6: Overview of common glucose evaluation methods: Clarks and Parkes error grid.

lower absorption of the light by hemoglobin, lipid, and water [33]. (See Sec. 2.3.2 (p. 28))

The measurement of glucose level by NIRS is generally done as it is illustrated in Fig. 3.5 (p. 47). Usually, a broad-band spectrum source is used for in-vivo glucose sensing, but also a laser could be used as light source [33]. As already mentioned, the measurement of optical parameters can be done in different measurement geometries. The two most common modes of NIRS are reflectance or transmittance mode [66]. Each mode has different measurement sites, on which they can be used on, where for example, the reflectance mode is applied to the human arm or palm, while the transmission mode is used for measurements on the finger, earlobe, or tongue. Thus, NIRS collects absorption or reflectance spectra, which partially scatters or absorbs light due to the chemical interaction with the tissue [69], since the combination and first overtone band are dominated by absorption, and the second overtone band provides more scattering information [78].

In order to quantify the concentration of glucose, which represents a single solute in a complex solution, several wavelengths are used and multivariate analysis including calibration is done [66].

3.3.1.1 Optical Influence of Glucose in NIR

As already mentioned, the interaction of light and human tissue is influenced by scattering and absorption. Scattering occurs because of mismatch between the refraction indices of the different tissue types. (See Sec. 2.2.2 p. 11))

Since glucose is a chiral molecule, meaning it is optically active and has the ability to rotate the plane of linear polarized light proportional to its concentration, it also changes the optical path-length, the refraction index as well as the scattering coefficient of a medium, in which the magnitude of each is related to the concentration of glucose [49]. As illustrated in Fig. 3.7a, the Beer-Lambert law, defined in Eq. 2.36 (p. 21), clearly establishes a correlation between the absorbance of light in a media and its concentration [77].

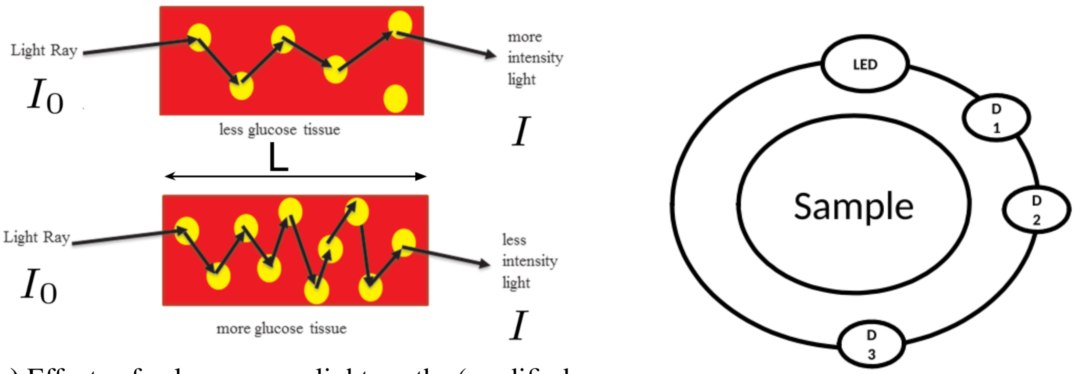

a) Effect of glucose on light path (modified from [16]).

b) In-vitro test setup [49].

Figure 3.7: Influence of glucose on the optical properties of a media.

The optical behavior of glucose was investigated by [49], who setup an in-vitro test, shown in Fig. 3.7b, where three photodiodes (D1 to D3) were placed on 45°, 90°, and 180° around a LED (940 nm) surrounding a sample solution. The path-length was 20 mm and the glucose concentration of the solution was increased from 40 to 400 mg/dl (2.2 to 22 mmol/l). The resulting variation of glucose concentration, indicated by the measured voltages of the photodiodes, is summarized in Tab. 3.3, where an increase of glucose level in photodiode 1 and 2 can be noticed due to an increase of scattering as a result of the increasing refraction index. As another consequence of the glucose increase, a decrease of the transmittance, resulting in a lower voltage of the photodiode 3, placed on the opposite side of the LED, can be observed.

It was shown by [78] that glucose has also a great impact on the optical properties of the whole blood, mainly, by the scattering properties of the whole blood matrix. To demonstrate its influence, they measured single-beamed NIR spectra of the blood in-vitro, while increasing the glucose level. The resulting spectra are illustrated in Fig. 3.8, where a successive increase of the glucose concentration led to a lower transmission of light, observed in the combination (A) as well as in the first and second overtone band (B).

Glucose (mg/dl)	Photodiode 1: 45° (mV)	Photodiode 2: 90° (mV)	Photodiode 3: 180° (mV)
0	256.0	258	257.8
40	256.2	258.3	257.56
80	256	259	256.06
120	256.07	260.6	255.09
160	257.08	261.4	255.05
200	257	261.8	254.08
240	257.06	262.01	254.01
280	257	262.9	253.06
320	257.02	262.8	252
360	257.6	263.1	252.1
400	258	263.6	252.06

Table 3.3: Variation of glucose concentration on different angles, demonstrated in in-vitro setup by [49].

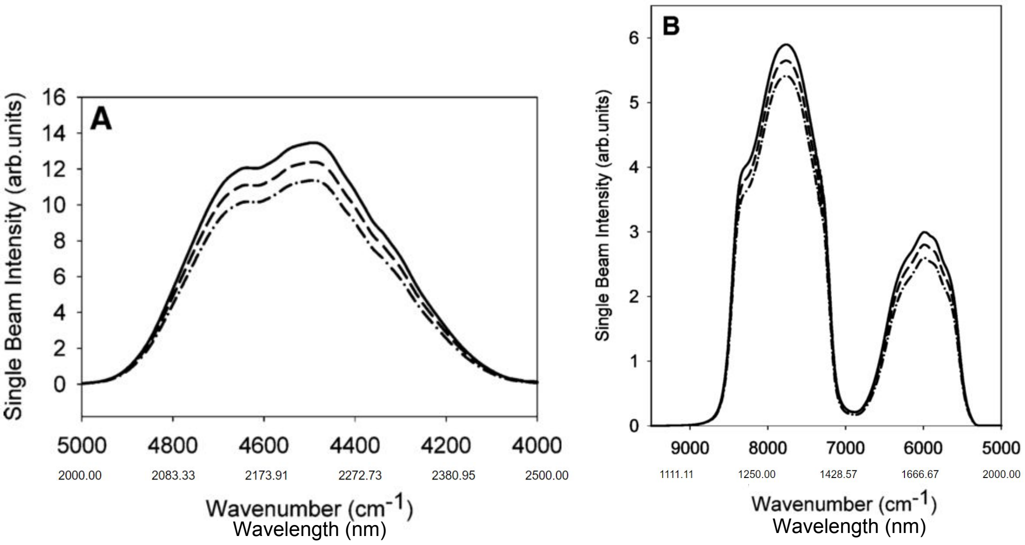

Figure 3.8: Single-beam NIR intensity spectra of whole blood (in-vitro) with glucose concentrations: 9.6 mmol/l (solid), 19.2 mmol/l (dash) and 27.4 mmol/l (dash-dot) in combination overtone region (A), and in first and second overtone region (B) (modified from [78]).

They concluded, that scattering, depending on the glucose concentration, is caused by a mismatch of the refraction index between red blood cells and plasma as well as by the changes in the dimensions of the red blood cells.

3.3.1.2 NIR Spectra of Glucose

A measured in-vivo spectrum contains not only the required absorbance information of glucose, but also information of other analytes, representing an overlapping of all spectra [79]. Several components of human tissue and blood represent potential interferences with non-invasive in-vivo glucose measurement [36]. As a result, it is difficult to prevent these disturbances, caused by other components as glucose, and secure clinical prediction accuracy [80].

Thus, there is usually no single wavelength which is only influenced by glucose, but it exists several variables which are weakly correlated to it [79]. To demonstrate these circumstances, the spectra of five components of living tissue, proposed by [80], are illustrated in Fig. 3.9, where next to glucose (yellow marked), water, protein, fat, and a baseline are shown in the first overtone region. All spectra were adjusted to 1400 nm and the baseline represents the scattering properties of the epidermis. In respect to the combination overtone region, the absorbance spectra of water, collagen, elastin, triolein, decorin, ethanol, and glucose (yellow marked) were collected by [42]. The resulting absorption spectra are illustrated in Fig. 3.10, where an offset was applied for clarity.

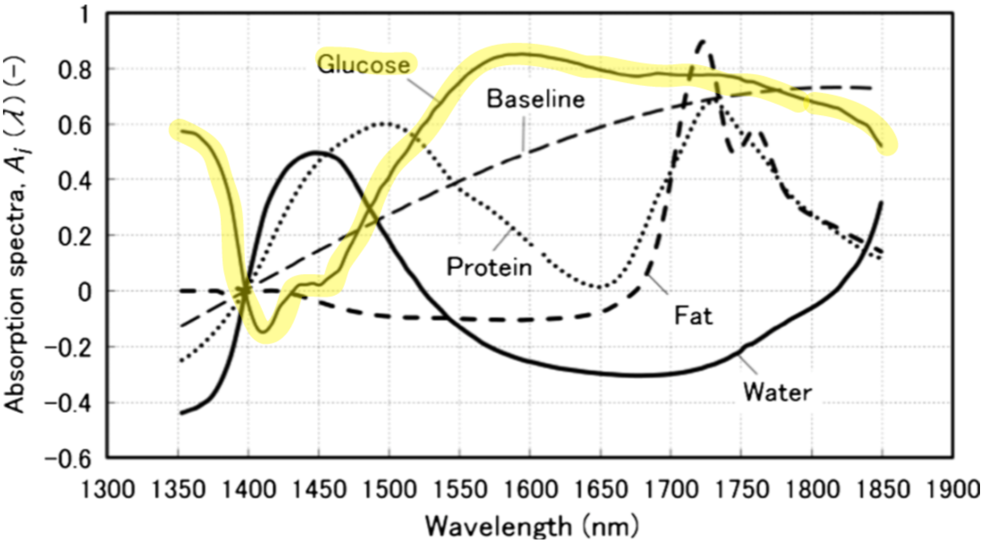

Figure 3.9: NIR spectra at first overtone region with absorption spectra of water, glucose, protein, fat, and base line (modified from [80]).

Both examples clearly show the possibility of glucose getting corrupted by other in-vivo measured components. As an overview, the most significant absorption peaks of glucose, water, fat, protein, and hemoglobin are summarized in Tab. 3.4. Furthermore, the absorption spectrum of glucose is illustrated in Fig. 3.11 for the second and in Fig. 3.12 for the

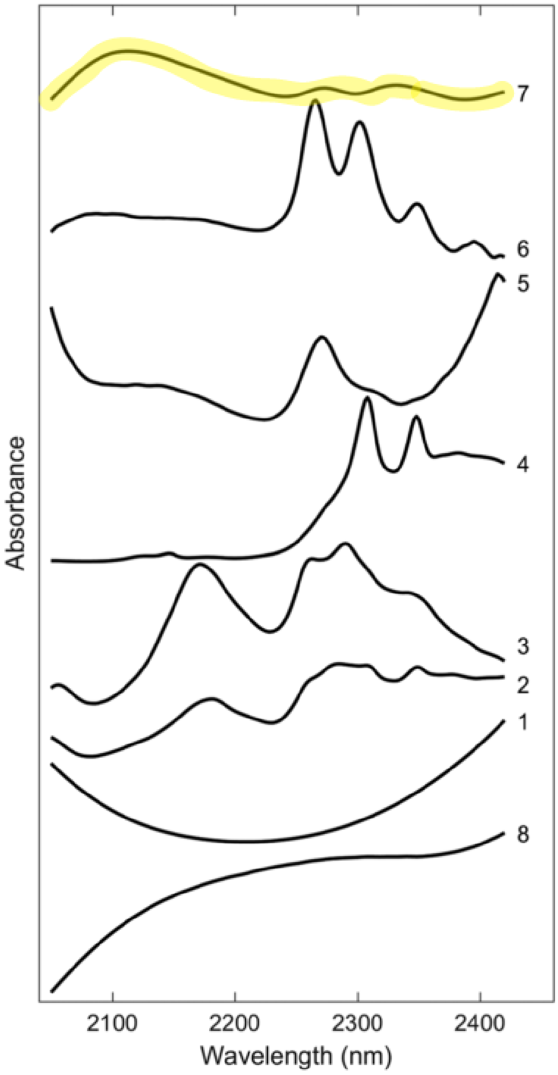

Figure 3.10: NIR spectra at combination overtone region with absorption spectra of water (1), collagen (2), elastin (3), triolin (4), decorin (5), ethanol (6), and glucose (7) in water with water temperature (8) (modified from [42]).

first and combination overtone region as well as in Fig. 3.13 for the combination overtone band. Additionally, the transmission spectrum of glucose is shown in Fig. 3.14a for the second and in Fig. 3.14b for the first overtone region, while the whole NIR spectrum of water is shown in Fig. 3.15 and the one of fat is represented in Fig. 3.16.

Since on-chip spectrometers measure only a limited amount of wavelengths, the most informative combination of variables should be selected [79]. In a study of [79], it was investigated which wavelength region or combination of them contains the most information

Analyte	Absorbtion Peaks (nm)								
Glucose	714	939	1126	1408	1536	1688	2100	2261	2326
Water	749	880	980	1211	1450	1787	1934		
Fat	770	920	1040	1727	2299	2342			
Protein	910	1020	1510	2174	2288				
Hemoglobin	760	805	820	910	1020				

Table 3.4: Absorption peaks of glucose, water, fat, protein, and hemoglobin in NIR region [8, 36, 80–82] (adapted and modified from [36]).

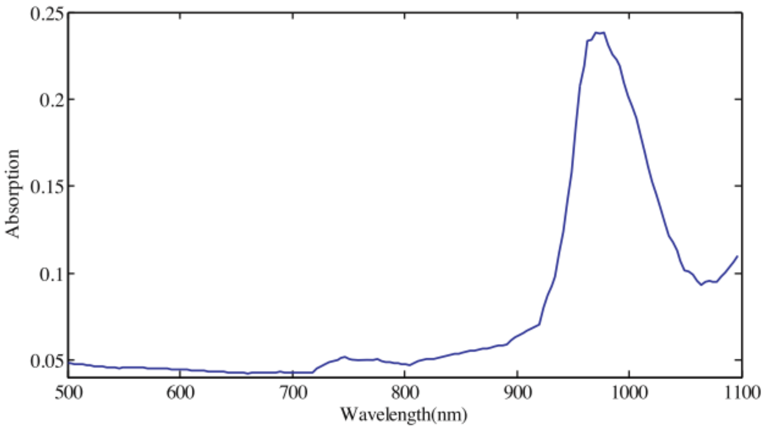

Figure 3.11: NIR absorption spectrum at second overtone region of glucose in water [33].

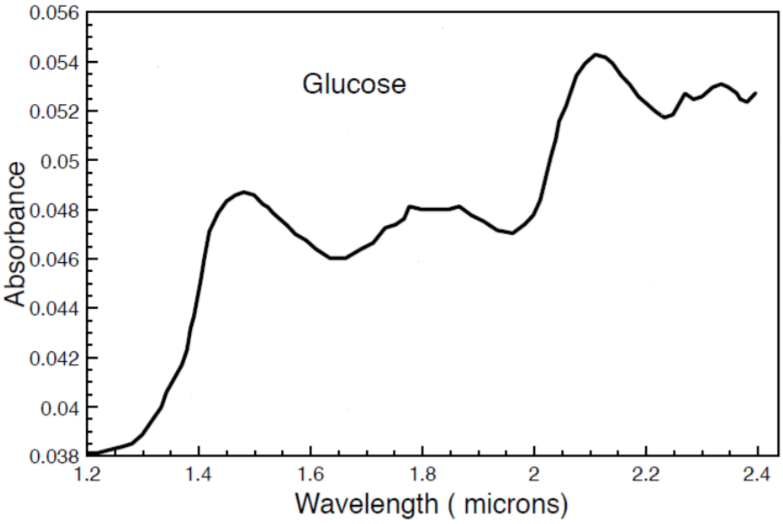

Figure 3.12: NIR absorption spectrum at first and combination overtone region of glucose [83].

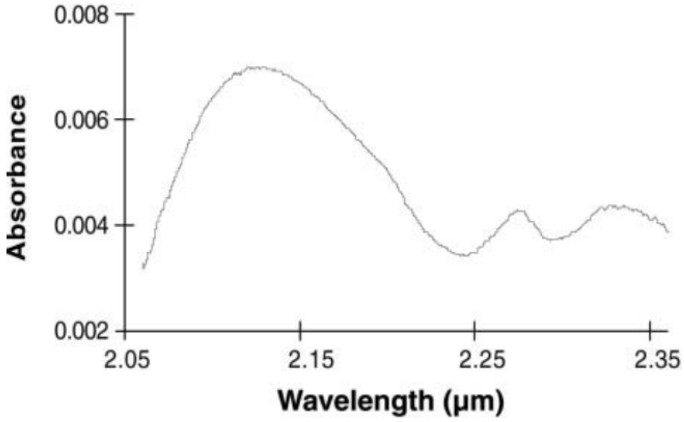

Figure 3.13: NIR absorption spectrum at combination overtone region of glucose [8].

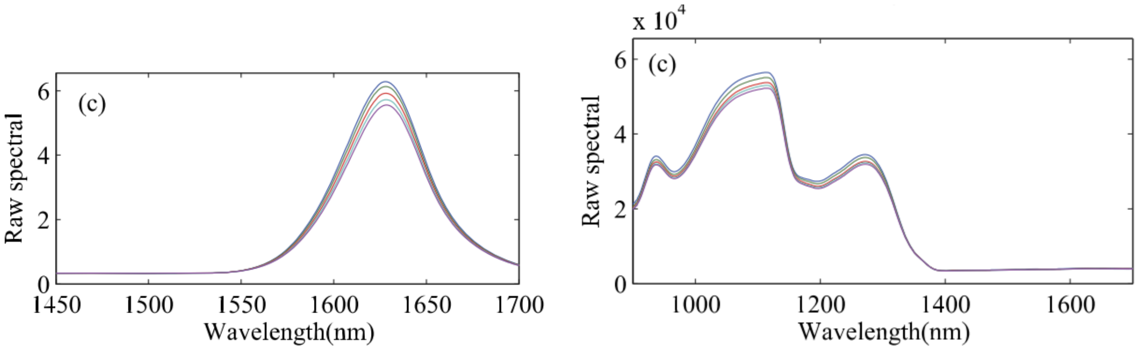

a) Second overtone region.

b) First overtone region.

Figure 3.14: Processed NIR transmission spectra at first and second overtone region of glucose in water [84].

for continuous glucose measurement. In order to do this, they applied different statistical methods (Interval PLS (iPLS), Variable Importance in Projection (VIP), Uniform Variable Elimination (UVE), Bootstrap PLS coefficients, Moving window, CorXyPLS, Interval Random Frog-PLS), and combinations of them. They found out that for aqueous glucose solutions the first overtone band (1500 nm to 1800 nm) is the most informative one, while for glucose measurement in serum samples the combination band (2050 nm to 2300 nm) should be preferred. However, they also mentioned that many researches have aimed to find the most informative wavelength region, resulting in different conclusions.

3.3.1.3 Modeling of Glucose Level in NIR

As already mentioned, the light transport through tissue is generally analyzed by Monte-Carlo simulation. Since the determination of physiological parameters from spectral data

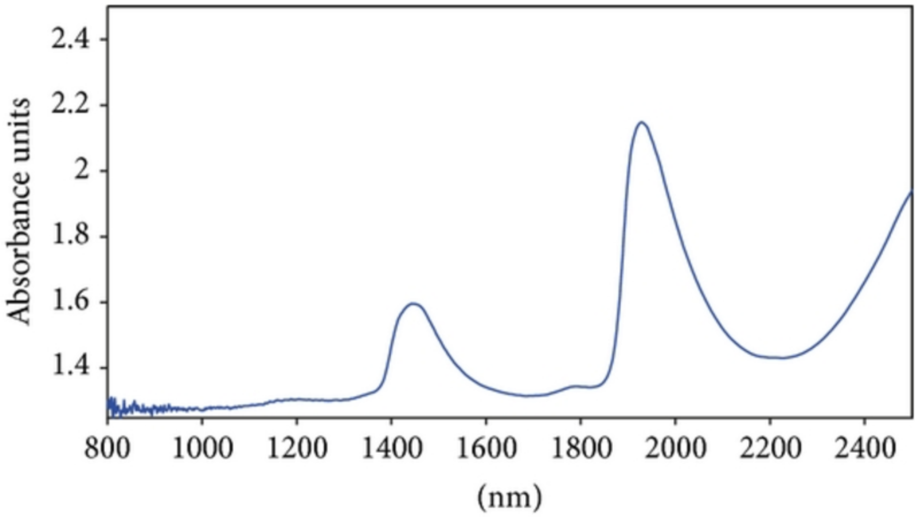

Figure 3.15: NIR absorption spectra at whole NIR region of water [85].

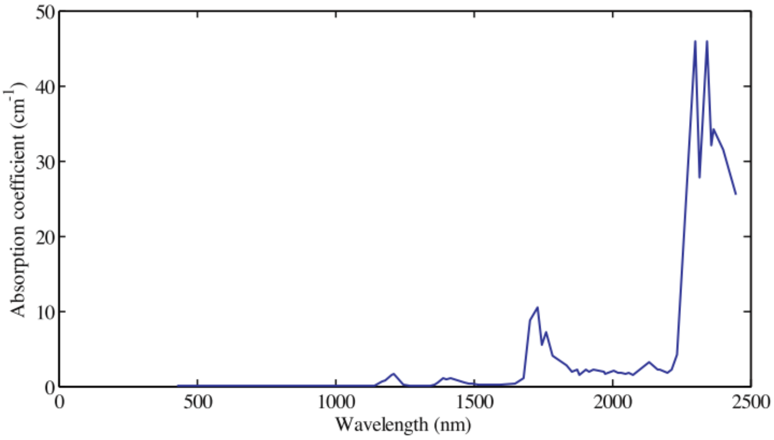

Figure 3.16: NIR absorption spectra at whole NIR region of fat [86].

by Monte-Carlo simulation is not always possible or too time-intensive, multivariate statistic methods or neuronal networks can be utilized instead when relationships as well as dependencies between the measured spectra are known [14]. Since the absorption peaks of glucose are relativity weak and highly overlapping, and thus, no single wavelength in NIR, which is only influenced by glucose, is available, there is a need for multivariate analysis techniques in order to extract the glucose information of the NIR spectra [79], remove underlying spectral noise, and compensate the physiological events, which are not related to glucose [33].

One of the most important aspects of the non-invasive glucose sensing is selectivity, which can not be produced by physical separations or selective chemical reactions due to no direct access of the sample, and thus, all selective analytical information must be from the in-vivo spectra [87]. Thus, selectivity is the possibility to determine a partial amount of glucose in a complex matrix without any interaction of other analytes [69], or more general, the recommended term in analytical chemistry to show the amount to which a partial method is able to determine an analyte of interest under given conditions in the presence of similar behaving components [88].

Generally, two methodologies for non-invasive glucose measurement are used, the empirical approach and the physical model, where the first one means the collection of glucose concentrations by invasive and non-invasive methods and computing a model, based on the correlation between them, whereas the physical model measures glucose in a matrix, increases its complexity to include the influence of human tissue, and correlates the data with a model for light propagation in tissue [36]. The first one is also called black-box model, in which a calibration model is automatically build by multivariate analysis and predict an object variable by removing the influence of other components [80].

Calibration models, which are generated by using glucose concentration values from invasive measurements [33], can be developed by a linear approach, using partial least squares (PLS), or by artificial neural networks (ANN) as a non-linear regression method [89]. These models can be used to extract glucose related information from the measured NIR spectra [33] by correlating the intensity of the measurements at different wavelengths to the relevant components by using mathematical methods like principal component regression (PCR) or multi linear regression (MLR) [89]. The general steps after the measurement of the spectra are visualized in Fig. 3.17.

Figure 3.17: Steps after raw data processing for optical glucose measurement [33].

Since the spectrum is measured from skin, it is not only influenced by biological components, but also from environmental factors like temperature and vapor level [90], and thus, next to different preprocessing techniques like moving average filter [33], several spectral pretreatment methods exist which are applied before building a model.

In case of PLS modeling, the authors of [89] used the following 10 different methods of spectral pretreatment: Multiplicative Scatter Correction (MSC), Constant Offset Elimination (COE), Vector Normalization (VN), First Derivative, Second Derivative, Min Max Normalization (MMN), Straight Line Subtraction (SLS), First Derivative + SLS, First Derivative + VN and First Derivative + MSC. The model with the best prediction was chosen by the highest R-value of calibration and validation, the residual predictive deviation (RPD) as well as the lowest root mean square errors of cross validation (RMSECV) and validation (RMSEP). In comparison to that, three ANN models were compared using MMN, VN, and no spectral treatment. They were ranked according to calibration and validation R-value as well as lowest MSE and RMSEP, where the results are discussed in the next section. However, to prevent under- or overfitting in PLS models, it is important to find the optimal number of model factors [89].

Next to the black-box approach, also grey-box models were used for optical glucose measurements. For example, the authors of [80] used the modified Beer-Lambert law for predicting the blood glucose concentration without multivariate analysis, purposing the development of a method, which considers the origins and magnitudes of the disturbances by tracing and predicting the changes of blood glucose content. They applied a method, similar to conventional classical least square (CLS) methods, where NIR absorbance spectra were measured periodically from reflectance spectra at human skin. The absorption spectra were determined by the subtraction of the basis spectra (first measured spectra), every five minutes, where the absorbance difference was assumed to by synthesized by a linear combination of five components of the human tissue (water, protein, glucose, fat, and a baseline (Fig. 3.9 (p. 52)) using Beer-Lambert's law, shown in Eq. 3.2, where the absorbance difference spectrum $\Delta OD(\lambda, t)$, the absorption spectra of a component i $A_i(\lambda)$, and the content index of a component i $N_i(t)$ can be recognized. The characteristic wavelengths of the different components were selected as their peak points, meaning 1450 nm for water (W), 1510 nm for protein (P), 1600 nm for glucose (G), 1727 nm for fat (F), and 1650 nm for the baseline (S). The predicted glucose content was determined using Eq. 3.3, where the glucose content index $\Delta N_G(t)$, a conversation factor r, and the true initial measured glucose concentration $G_m(t = 0)$ are used. Since this approach failed, they combined fat with the baseline in order to receive one component in a new approach, which was able to reduce the error of blood glucose prediction. They concluded that the main factor of large prediction errors are the change in scattering of human skin as well as the similarity between glucose and the baseline, which was improved by using the second approach, providing a possible tool for simple, real-time glucose prediction, by using NIRS.

$$\Delta OD(\lambda, t) = \sum_i A_i(\lambda) \Delta N_i(t) \tag{3.2}$$

$$\begin{bmatrix} \Delta OD(1450, t) \\ \Delta OD(1510, t) \\ \Delta OD(1600, t) \\ \Delta OD(1650, t) \\ \Delta OD(1727, t) \end{bmatrix} = \begin{bmatrix} A_W(1450) & A_P(1450) & A_G(1450) & A_S(1450) & A_F(1450) \\ A_W(1510) & A_P(1510) & A_G(1510) & A_S(1510) & A_F(1510) \\ A_W(1600) & A_P(1600) & A_G(1600) & A_S(1600) & A_F(1600) \\ A_W(1650) & A_P(1650) & A_G(1650) & A_S(1650) & A_F(1650) \\ A_W(1727) & A_P(1727) & A_G(1727) & A_S(1727) & A_F(1727) \end{bmatrix} \begin{bmatrix} \Delta N_W(t) \\ \Delta N_P(t) \\ \Delta N_G(t) \\ \Delta N_S(t) \\ \Delta N_F(t) \end{bmatrix}$$

$$G(t) = r \Delta N_G(t) + G_m(t = 0) \tag{3.3}$$

3.3.1.4 In-Vivo NIR Glucose Measurement

Non-invasive in-vivo glucose measurement determines the level of blood glucose without the need of a blood sample [69]. Many approaches of in-vivo NIR blood glucose measurement were developed in the past, varying in measurement site and mode, used wavelength region and detection as well as signal processing and statistical modeling.

A method of non-invasive and fast blood glucose assay in-vivo using NIR spectroscopy on rats was developed by [89]. An overview of their measurement process as well as the measured spectra are illustrated in Fig. 3.18, where spectra and plasma samples of the rats were collected 0 min, 15 min, 30 min, 45 min, 60 min, 90 min, 120 min, 180 min, and 360 min after a glucose injection. The resulting change in the blood glucose level of the normal group (n=12) and the hyperglycemia group (n = 18) is illustrated in Fig. 3.19. They followed two multivariate strategies, PLS and ANN, where the first one was optimized individually by spectral range, pretreatment, and number of model factors. Whereas the latter one was developed by spectral treatment methods, parameter of network topology, number of hidden neuron, and times of epoch. Additionally, they selected four regions in the NIR spectra: 833.68 nm to 1332.98 nm (A), 1332.98 nm to 1639.88 (B), 1639.88 nm to 2173.20 nm (C), and 2173.20 nm to 2354.757 nm (D). The use of the pretreatment method Constant Offset Elimination (COE) and the combination of the wavelength regions B, C, and D showed the best performance. The resulting scattering plot of the validation is illustrated in Fig. 3.20, showing the best ANN and PLS model. The performance of the PLS was R^2 = 96.22 and the one of the ANN model was R^2 = 92.79 %. Thus, they concluded that both model types are robust, accurate, and repeatable, where especially, the

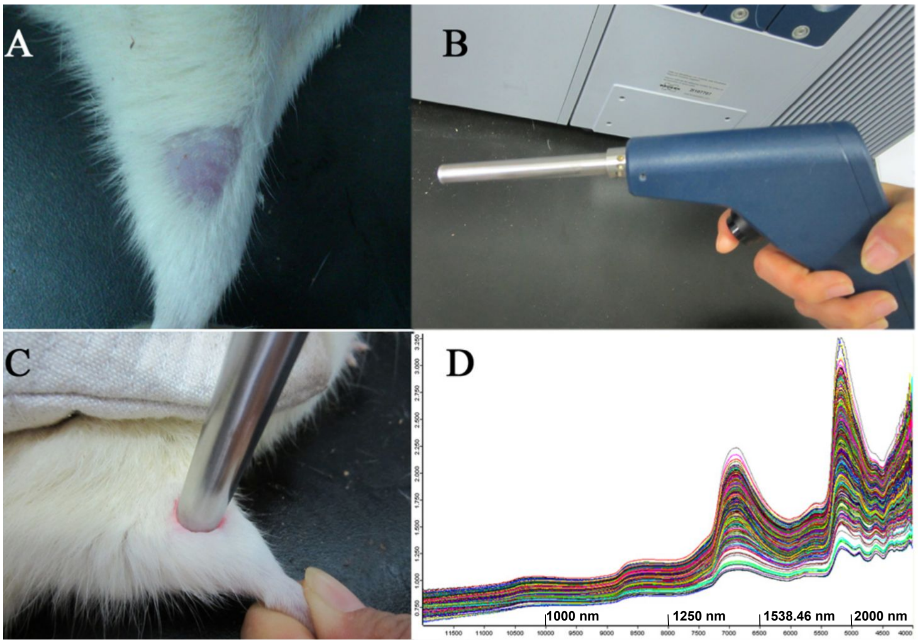

Figure 3.18: Measuring NIR spectra of rats, where rats leg shaved (A), NIR optical probe (B), measurement process (C), and NIR spectra from 869.57 nm to 2500 nm (D) can be recognized (modified from [89]).

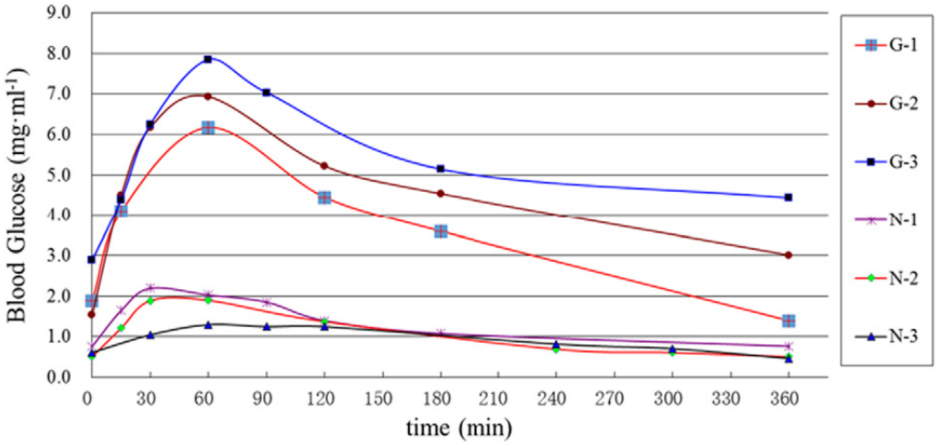

Figure 3.19: Change of the rats blood glucose level after glucose injection (G: hyperglycemia group, N: normal group) [89].

PLS model showed a good performance and will be used in further human in-vivo studies.

The authors of [91] investigated the influence of glucose in the second overtone (short-wavelength) region between 700 nm and 1050 nm, measured on the right-hand palm of 34 healthy subjects, shown in Fig. 3.21, where five tungsten halogen lamps (1 W) were placed in a circle around the light guide of the the spectrometer (S-2930, Soma Optics),

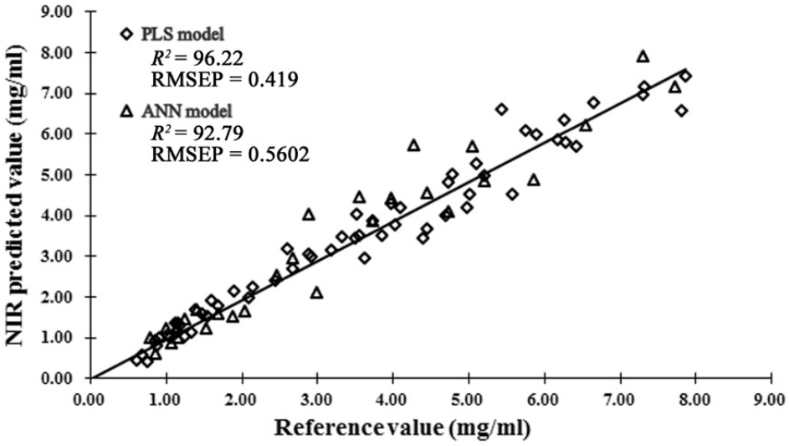

Figure 3.20: Validation of predicted and reference glucose concentration, showing the best PLS and ANN model [89].

and the temperature during measurement was maintained at 36.0 ± 0.1 ° C. Also, they applied six carbohydrate tolerance tests (CTT) on each subject, where on each test, 50 g carbohydrates were eaten in the morning after a night of fasting and the blood glucose concentration was measured with a conventional invasive method 15 min, 30 min, 45 min, 60 min, 90 min, and 120 min after the meal, simultaneously to the acquisition of the NIR spectra. The NIR spectra of one subject after one CTT is shown in Fig. 3.22, where the raw and the second-order derivative spectra can be recognized. For each wavelength, the absorbance $A = \log(\frac{1}{R})$ was calculated, and the derivative intensity $I = -\frac{d^2A}{d\lambda^2}$ was defined. Next, the correlation between the blood glucose level and the light intensity difference $\Delta I_{\lambda t} = I_{\lambda t} - I_{\lambda_0}$, meaning the difference between the intensity at the mentioned time steps and the one at the fasting state (t = 0), was determined for each CTT, where the highest correlated wavelength was named as glucose-linked wavelength λ^*. Using this wavelength, the authors applied a simple linear regression (SLR) model to the blood glucose level and the difference intensity at the glucose-linked wavelength, resulting in the error grid, shown in Fig. 3.23, where the predicted values, calculated by $\Delta I_{\lambda^* t}$, were compared to the reference values, and a histogram of standard error of prediction can be recognized, where the mean value as well as the SD were 11.70 mg/dl (0.649 mmol/l) and 5.03 mg/dl (0.279 mmol/l), respectively. Additionally, they showed that the mentioned glucose-linked wavelength was different at each CTT. The distribution of the probability of the occurrence of the correlation coefficient between the glucose concentration and $\Delta I_{\lambda^* t} \geq$ 0.70 are shown in Fig. 3.24, in which also the intensity spectra of all CTTs are illustrated. In conclusion, the authors mentioned the existence of a glucose-linked wavelength within a two-hour win-

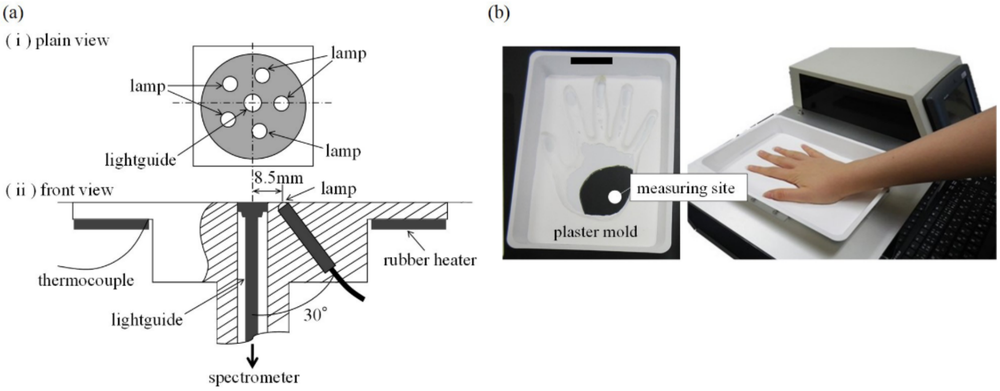

Figure 3.21: Measurement setup for glucose measurement in NIR region with a detailed view of the probe (left) and the placement for measurement site (right) [91].

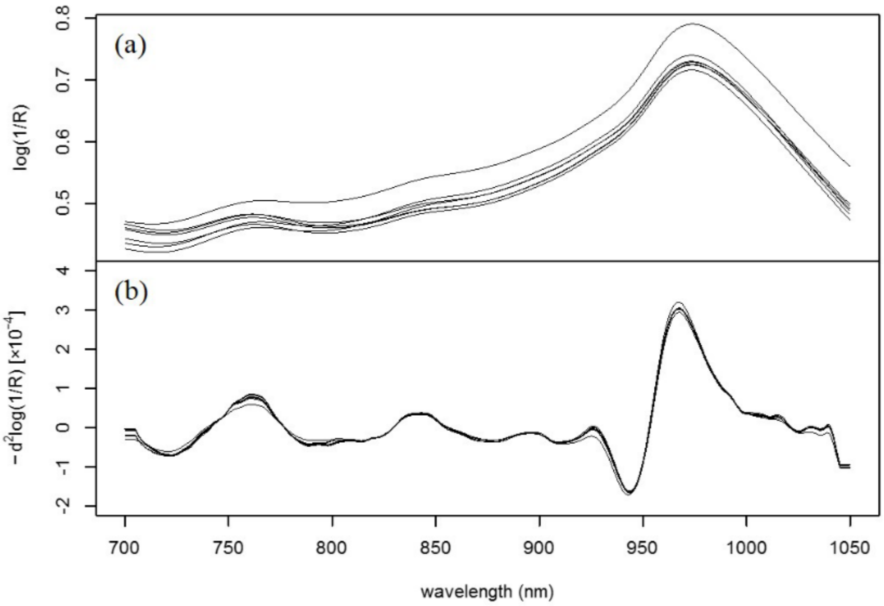

Figure 3.22: NIR spectra of one patient measured after one CTT with the raw spectra (top) and the second-order derivate spectra (bottom) [91].

dow, although, this wavelength is fluctuating daily even on the same subject.

In the study of [84], the short-wave band (900 nm to 1450 nm) as well as the first overtone region (1450 nm to 1700 nm) were investigated, using NIR Fourier transform spectroscopy, where the glucose-characteristic wavelengths were determined by using in-vivo spectra, measured from the middle fingertip of OGTT subjects, and applying SLR and correlation, meaning 21 datasets for seven patients, which were split into a calibration set of 14 samples and a test set of seven samples. The characteristic absorption peaks

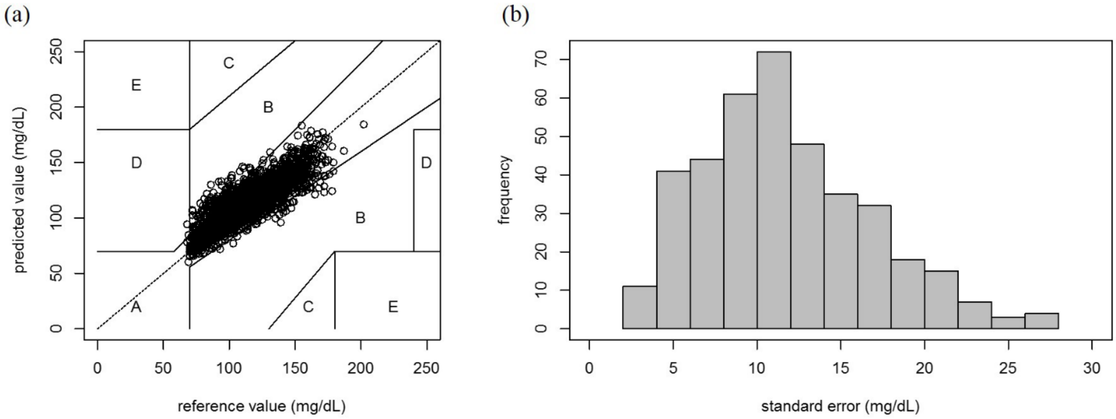

Figure 3.23: Error grid of reference and predicted values calculated from $\Delta I_{\lambda^* t}$ of 391 CTTs in sets of seven samples (left) and histogram of standard error of prediction of all CTTs (right) [91].

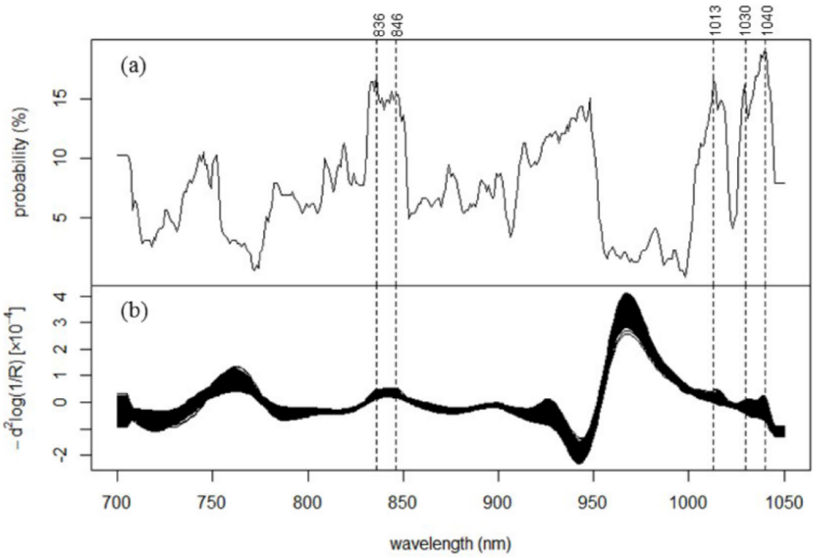

Figure 3.24: Fluctuation of glucose-linked wavelengths, represented by correlation coefficient between the glucose concentration and $\Delta I_{\lambda^* t} \geq 0.70$ (top), and intensity spectra of all CTTs (bottom) [91].

were delivered from the second-derivate processing of an aqueous glucose solution. Moreover, the scatter plot of the reference and estimated blood glucose concentration, using the wavelengths 950 nm and 1280 nm, is shown in Fig. 3.25. The authors mentioned that the characteristic peaks of the fingertip were only found in the short-wave band between 930 nm to 970 nm, 1040 nm to 1100 nm, and 1280 nm to 1300 nm, where a high correlation between intensity difference and reference glucose level were observed (r = 0.82 for 950 nm

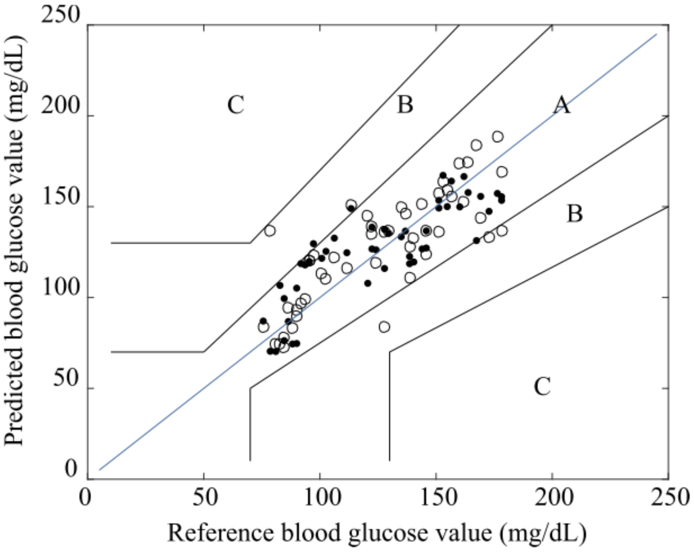

Figure 3.25: Scatter plot of reference and estimated blood glucose concentration, using $\lambda = 950$ nm (filled circles) and $\lambda = 1280$ nm (open circles) [84].

and r = 0.79 for 1280 nm for all patients). Thus, it was concluded that the SLR model from seven OGTTs in seven patients enabled the estimation of a glucose-linked wavelength.

A review study from [33] compared several methods of non-invasive glucose measurement, using NIRS. The adapted results are summarized in Tab. 3.5, where different measurement sites, methods[1], and errors[2] can be recognized.

3.3.2 Mid Infrared Spectroscopy (MIRS)

Mid-infrared spectroscopy (MIRS) uses the same principles as NIRS by applying light, ranging from 2500 nm to 10000 nm [69]. The MIR region, also known as ”fingerprint” region, provides strong vibrational resonances of many molecules, among other things glucose [107], which has a target wavelength region between 8000 nm and 10000 nm [108]. The peaks in the MIR spectra are much sharper as they are in case of NIRS [33]. However, the absorption spectrum of glucose in the MIR region is illustrated in Fig. 3.26, where the most significant peaks are indicated.

The major challenge of in-vivo application of MIR light is the limited penetration into the skin because of the high absorption of water [38, 107], which means the fundamental vibrational resonances in the target region of glucose are overlapped by no other biological

---

[1] DT . . . diffuse transmittance, DR . . . diffuse reflectance, T . . . transmittance, R . . . reflectance

[2] MEP . . . mean error percent, SEP . . . standard error of prediction, RMSEP . . . root mean square error of prediction

Measurement Site	Method	Error	Wavelength Region	Source
Finger	DT	1.1 to 2.1 mmol/l (MEP)	800 - 1300 nm	[92]
Oral mucosa membrane	DR	2.4 mmol/l (SEP)	1111 - 1835 nm	[93]
Finger and cuticle	DR	90 % prediction in clinical range	900 - 1200 nm	[94]
Finger	DR	1.02 to 1.88 mmol/l (RMSEP)	800 - 1350 nm	[95]
Middle Finger	DR	2.0 mmol/l (RMSEP)	800 - 1350 nm	[96]
Arm	DR	1.03 mmol/l (SEP)	1050 - 2450 nm	[97]
Cheek, lips, nasal septum, tongue, tissue between thumb and forefinger	T	3 mmol/l (SEP)	1520 - 1850 nm	[98]
Tongue	T	3 mmol/l (SEP)	First overtone region	[99]
Forearm	R	< 1.5 mmol/l (SEP)	590, 660, 890, 935 nm	[100]
Forearm	DR	1.787 mmol/l (SEP)	1500-1600 nm	[101]
Finger	DR	0.904 mmol/l (RMSEP)	900 nm to 1700 nm	[102]
Palm	DR	0.8 - 1.1 mmol/l (RMSEP)	1100-1800 nm	[103]
Forearm	DR	77.7 % Sensitivity	1250-2500 nm	[104]
Nail bed	DR	± 0.729 mmol/l (SEP)	First overtone region	[105]
Finger	DR	7.96 % (MEP)	1500-1800 nm	[106]

Table 3.5: Different NIRS glucose monitoring methods (adapted and modified from [33]).

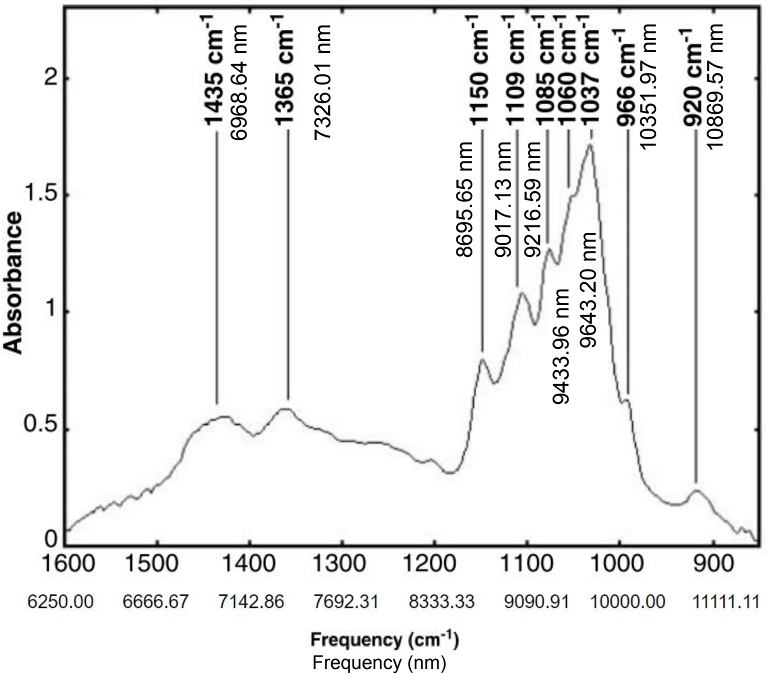

Figure 3.26: MIR absorption spectra of glucose from 6250 nm to 11000 nm (modified from [8]).

absorber except water [109]. Moreover, the specific wavelength region for glucose reaches only a depth less than 50 μm, which is represented by the upper layer of skin (stratum cornuem and stratum spinosum) [110]. Thus, MIRS is only applicable in the reflectance mode [33] as well as solely used for glucose measurement in the ISF space.

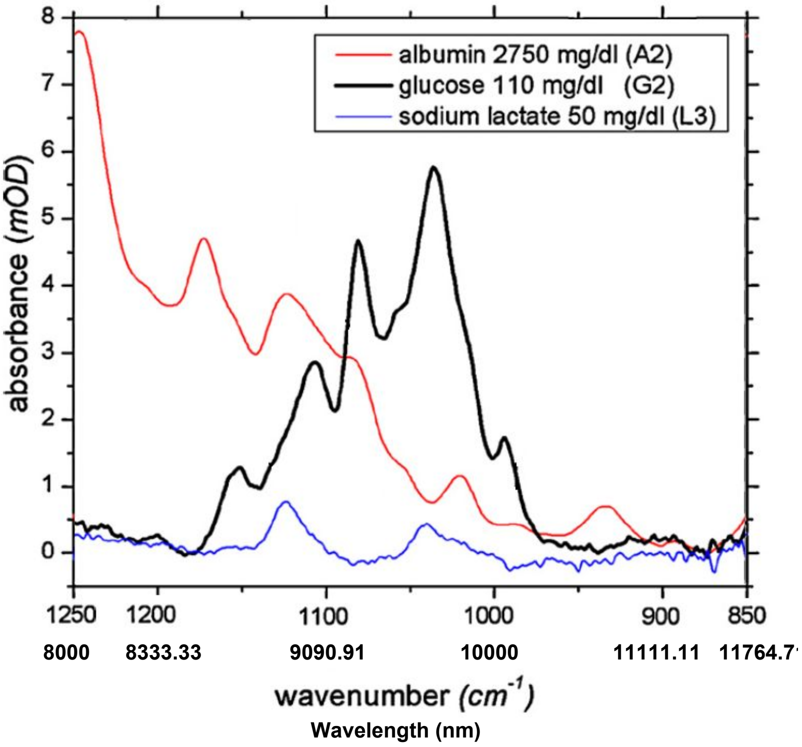

Figure 3.27: MIR absorption spectra of albumin, glucose, and sodium lactate in a physiological buffer solution (modified from [110]).

In a study from [110], the in-vitro spectra of glucose, albumin, and sodium lactate in a physiological buffer solution were reviewed, shown in Fig. 3.27, where an overlap of these three components can be recognized. Additionally, they presented the in-vitro spectra of real ISF samples, taken from a bulla of three volunteers, which are illustrated in Fig. 3.28, showing two dominant peaks at approximately 6060 nm and 6452 nm due to the strong presence of protein in ISF. The absorption region of glucose is shown on the right side (8000 nm to 11111 nm). They mentioned, that the absorption spectra of the volunteers can be modeled directly and that the albumin and lactate can be neglected because of selected wavelength regions.

However, for an in-vivo application, a powerful and stable MIR source is needed, which is represented by a quantum cascade (QC) laser [107]. In the study from [107], a method for in-vivo glucose sensing, using a pulsed QC laser, was proposed. The setup is shown in Fig. 3.29, where the light was applied on a region of the human palm between thumb and index finger. Moreover, the backscattered light was measured by a bundle of six fibers coupled with a liquid nitrogen cooled mercury cadmium telluride (MCT) detector. The glu-

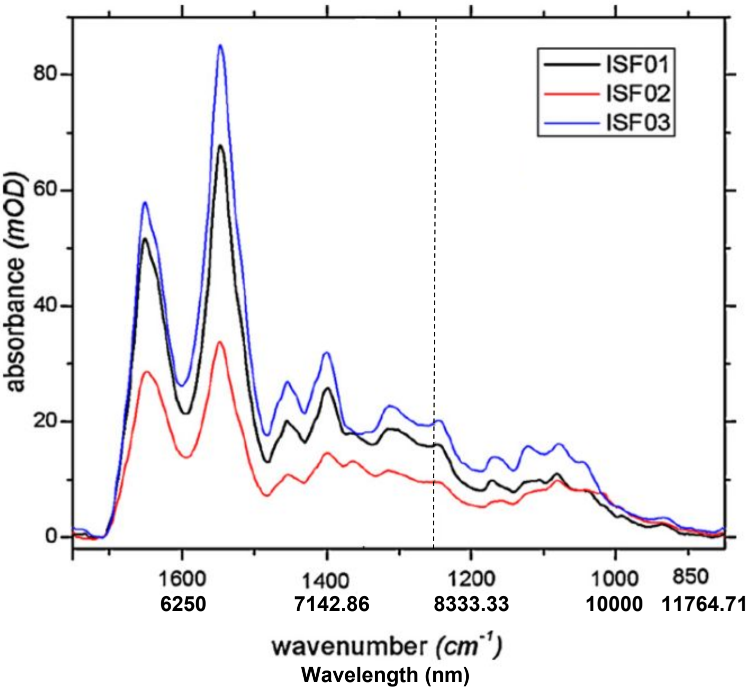

Figure 3.28: MIR spectra of three ISF samples from three volunteers (ISF01, ISF02, ISF03) (modified from [110]).

cose concentration was measured by three healthy subjects, taking spectra between the start point (empty stomach) and after eating 20 jelly beans to rise their glucose level. The spectra were calibrated with a commercial electrochemical glucometer, using partial least square regression (PLSR) and derivative spectroscopy methods. They used linear regression for 1080 cm^{-1} (9259.26 nm), which represents a prominent absorption feature of glucose, since it is present in the in-vivo as well as in the in-vitro spectrum, shown in Fig. 3.30a. The variation of the glucose concentration at this region is illustrated in Fig. 3.30b. Also, the resulting Clarke-Error grids of the three subjects are shown in Fig. 3.31, where an average clinically accurate prediction of 84 % can be recognized.

In the study of [111], a significant correlation between wavelength peaks about 7142.9 nm to 7693.3 nm, measured on the lips of 28 subjects, using FTIR spectroscopy and partial least square regression (PLS), and the blood glucose as well as hemoglobin A1c levels were reviewed. They concluded that the FTIR-ATR technique has the potential to measure and monitor metabolic disregulation (glycemic and lipidomic) in-vivo.

The authors of [112] reported a method for glucose measurement in the MIRS region, using only three wavelengths (9523.81 nm, 9345.79 nm, and 9090.91 nm), showing that the correlation between the measured wavelengths and the reference values of different

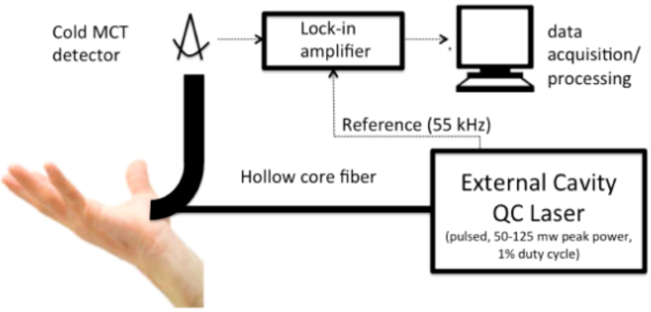

Figure 3.29: In-vivo MIRS setup for glucose sensing reviewed by [107].

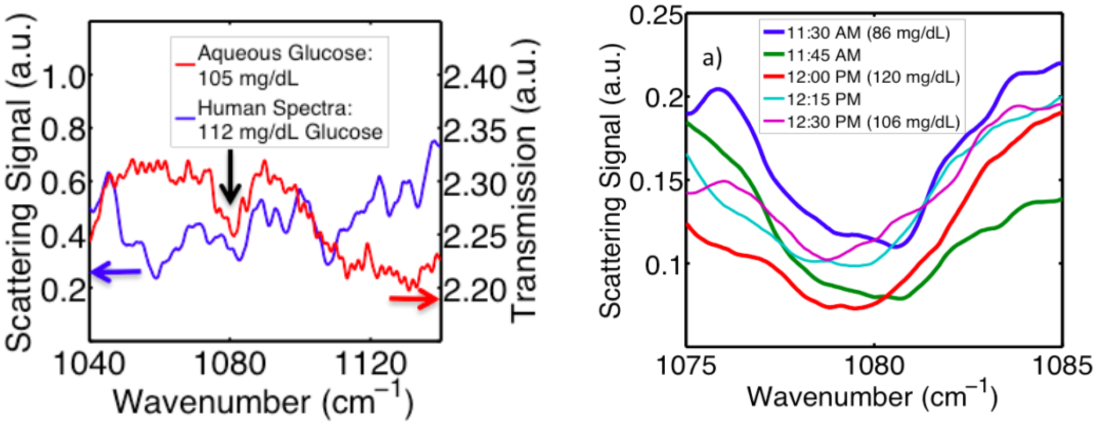

a) Back-scattered in-vivo spectrum (blue) and transmission in-vitro spectrum (red) [107].

b) Fluctuation of glucose concentration after intake of 20 jelly beans [107].

Figure 3.30: In-vivo and in-vitro glucose concentration in MIR.

subjects, seasons, and meals, without calibration, could be improved by the use of only three wavelengths (multi linear regression) compared to more wavelengths by using PLS models. Thus, the authors aimed for future work to verify the accuracy by the use of a laser as light source.

The authors [113] used MIR ATR spectroscopy by applying a multi-reflection prism on the human inner lip mucosa for in-vivo glucose measurement. They measured a calibration plot at 8658.01 nm, which originates from the pyranose ring structure of glucose, resulting in a measurement error less than 20 %, and thus, the conclusion of a need to improve the SNR of the system by a stronger light source as QCL.

However, although the MIR region contains sharper and stronger absorption, and lower scattering compared to NIR spectroscopy, the poor penetration of a few micrometers, the absorption by water as well as the influence of body temperature, and contact pressure

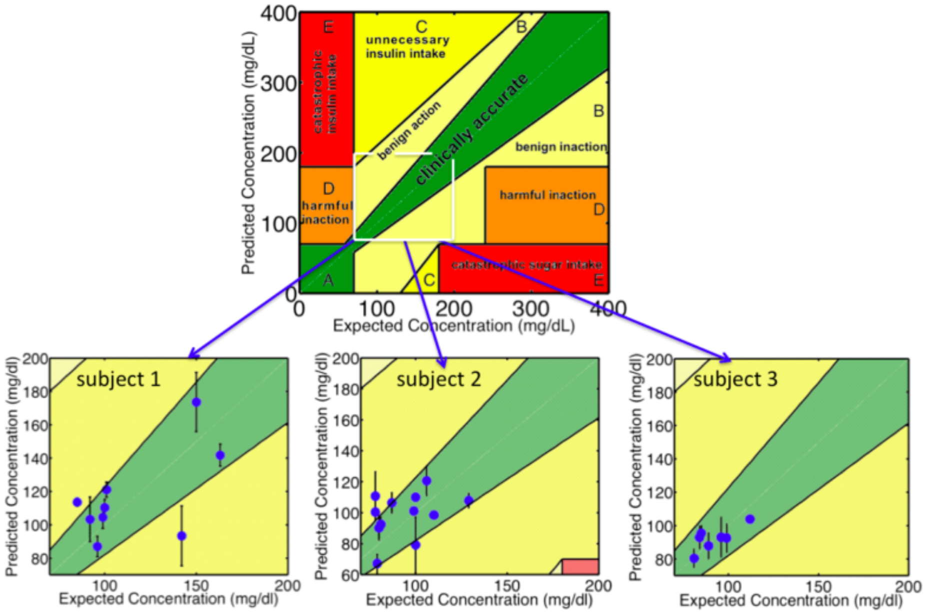

Figure 3.31: Results of in-vivo glucose measurement of three volunteers using MIRS [107].

represent significant limitations of this detection method for glucose measurement [114].

3.3.3 Raman Spectroscopy

Raman spectroscopy uses the inelastic scattering of photons to characterize molecules by their vibrational transitions, meaning that the initial and final vibrational state forms a characteristic pattern, the so-called Raman fingerprint [70]. In contrast to infrared spectroscopy, the spectral signature of glucose is not disguised by water [115]. A Raman spectrum of aqueous glucose, measured in a quartz cuvette, is shown in Fig. 3.32 as well as in Fig. 3.33 for different glucose concentrations. A typical Raman spectrum of the tissue of the human skin is shown in Fig. 3.34

A clearly linear relationship (R^2 = 0.91) between the Raman intensity and the glucose concentration was concluded by [117]. They proposed a Raman spectroscopy method for measuring in-vivo blood glucose concentration non-invasively applied on mice, shown in Fig. 3.35. In order to observe the change in the glucose concentration, each mouse was given a glucose injection after 24 hours without food, and the spectra were measured 30 min afterwards, in intervals of 15 min for 2 hours. The best peak was observed at 1125 cm^{-1} (8888.89 nm), resulting from the best SNR. The measured Raman spectra are shown in Fig. 3.36, where next to the mouses blood vessels, the spectra normalized to 1549 cm^{-1}

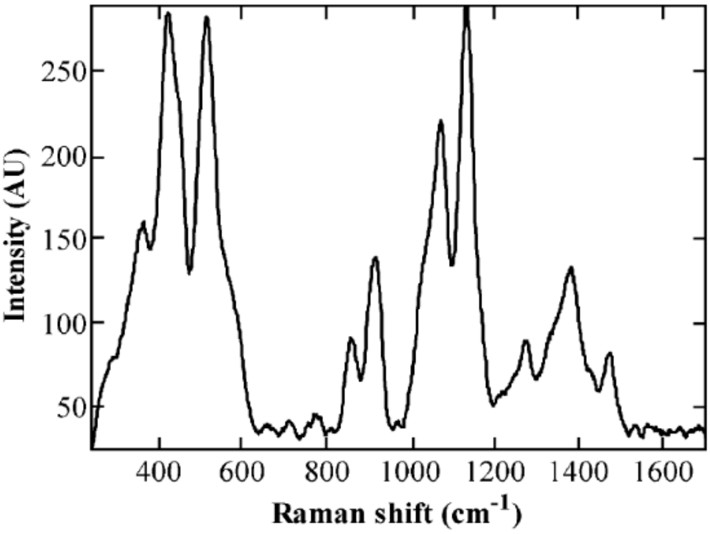

Figure 3.32: Raman spectra of an aqueous glucose solution measured in a quartz cuvette [116].

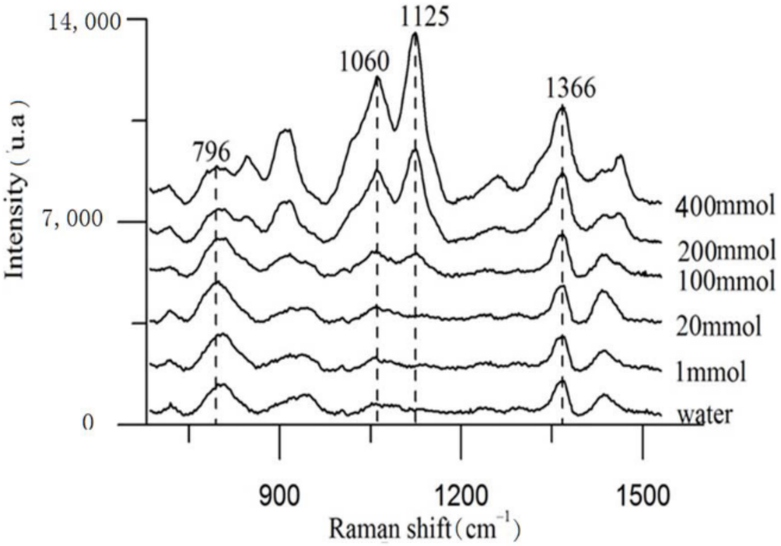

Figure 3.33: Raman spectra of glucose solution at different glucose concentrations [117].

(6455.78 nm) can be recognized.

The authors of [118] used a custom-made Raman spectrometer system on 111 subjects, where blood reference values, based on mean-centered data, were used to correlate the Raman data by PLS, shown in Fig. 3.37. They also presented a relationship of $R^2 = 0.83$ correlating independent Raman-based predictors on reference values of all subjects, resulting in the error grids of Fig. 3.38, where the results of male ($R^2 = 0.94$) and female subjects ($R^2 = 0.88$) can be recognized.

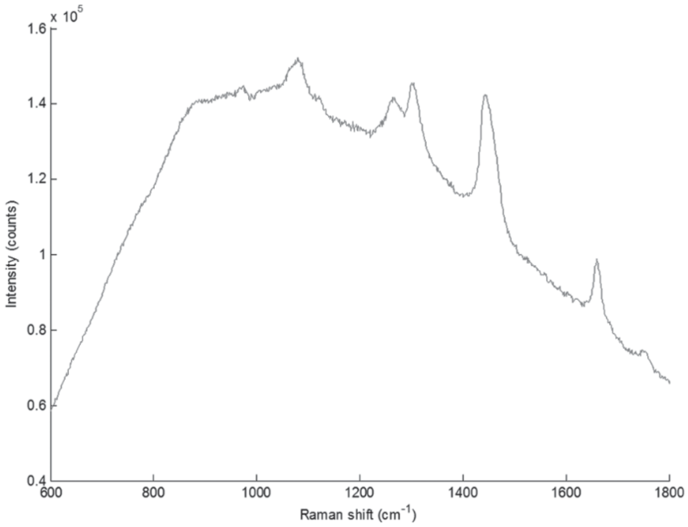

Figure 3.34: Typical Raman spectrum of human skin [118].

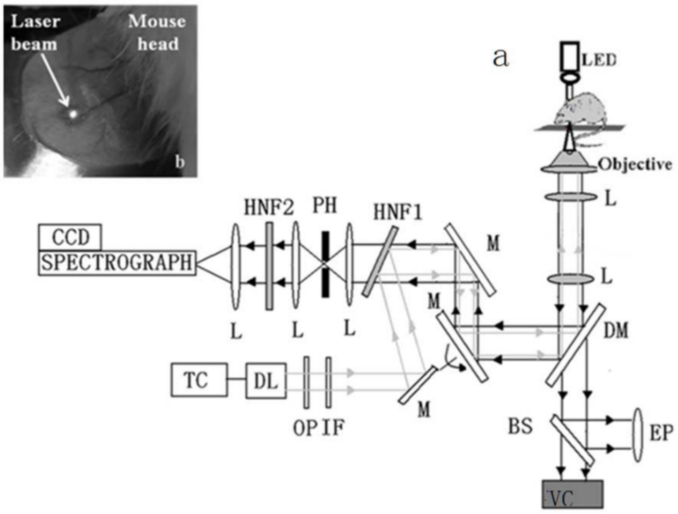

Figure 3.35: Measurement setup for blood glucose measurement using Raman spectroscopy on mice [117].

In the study from [119], critical-depth Raman spectroscopy (CD-Raman) was used to analyze the ISF, in a depth of about 2.5 mm below the skins surface, of 35 patients of diabetes over 60 days. They achieved a stable calibration for more than 10 days. The portable Raman spectrometer is illustrated in Fig. 3.39, where a 300 mW continuous diode laser at 830 nm is collimated and filtered, before it is redirected and focused on the surface of the skin. As a result, the measured Raman spectra of 14 patients, showing the spectra of skin and aqueous glucose as well as a regression vector from PLS calibration model, are

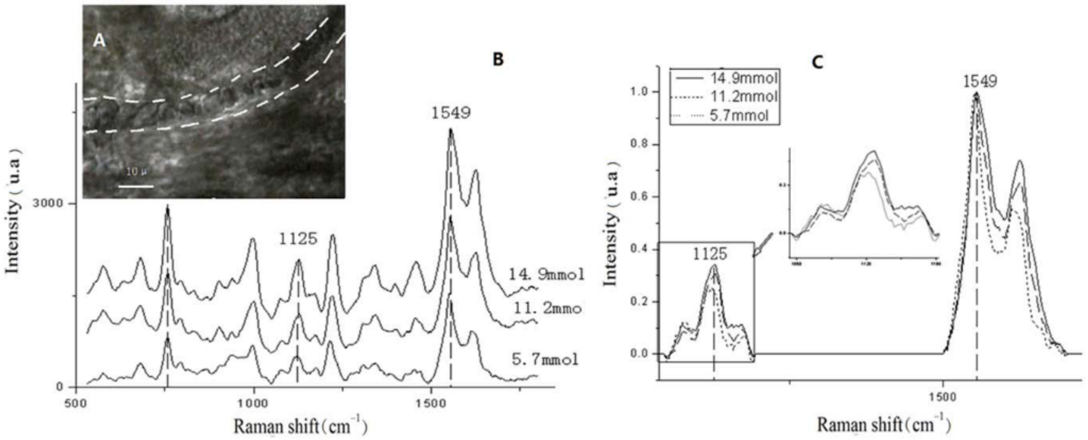

Figure 3.36: Raman spectra of blood with different glucose concentrations (left, B), blood vessel in the ear of a mouse (left, A), and the normalized Raman spectra at 1549 cm^{-1} (6455.78 nm) (right, C) [117].

Figure 3.37: Measurement of Raman spectra for blood glucose determination [118].

shown in Fig. 3.40, where significant glucose peaks at 514 cm^{-1} (19455.25 nm) and 1123 cm^{-1} (8904.72 nm) can be noticed. The data was analyzed and evaluated using MATLAB, where a calibration set (25 days of analysis) was used for PLS regression. The independent validation as a function of time is illustrated in Fig. 3.41, in which the estimated glucose level by Raman spectroscopy was compared to the reference value for 14 patients over at least five days, since calibration. The resulting error grid of 15 patients, considering the last five days of analysis after calibration, is illustrated in Fig. 3.42.

Although Raman spectroscopy is an effective method to measure glucose, the detection process is very complex and, thus, it is not suitable for everyday use [50].

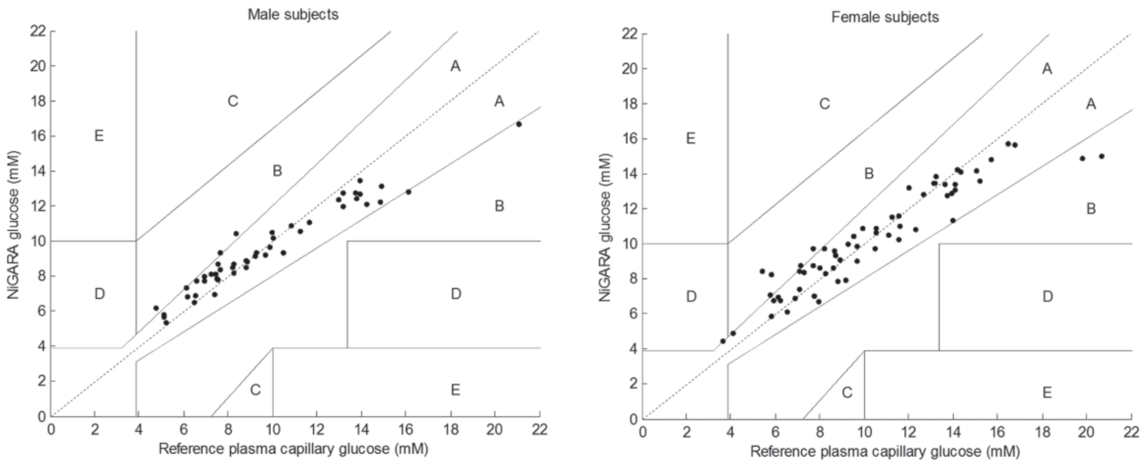

Figure 3.38: Error grid of predicted glucose values by Raman spectroscopy and reference values for male (n=49) (left) and female (n = 62) (right) subjects [118].

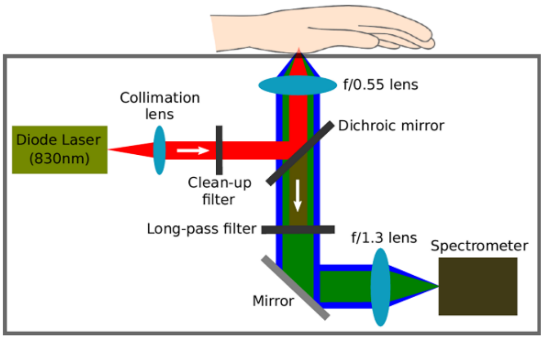

Figure 3.39: Portable Raman spectrometer proposed by [119].

3.3.4 Other Methods

Next to NIR, MIR, and Raman spectroscopy several other optical and non-optical methods as well as a combination of them for non-invasive glucose monitoring were developed and investigated in the past. Also, many review studies [33, 50, 66, 69, 114, 120–123] were published in the last years, demonstrating the multiplicity as well as the great general interest in approaches for non-invasive blood glucose measurement. Next to methods, which use the contact of human skin, and thus, the electro-osmotic flow, in reverse iontophoresis (GlucoWatch Biographer, Gygnus Inc., USA) [124], methods, which measure glucose concentrations in tears via electro-chemical methods [125, 126], were developed. Moreover, approaches, using bio-impedance spectroscopy [127] or tattoo-based techniques [128], were considered in the past. A major amount of reviewed devices are combining

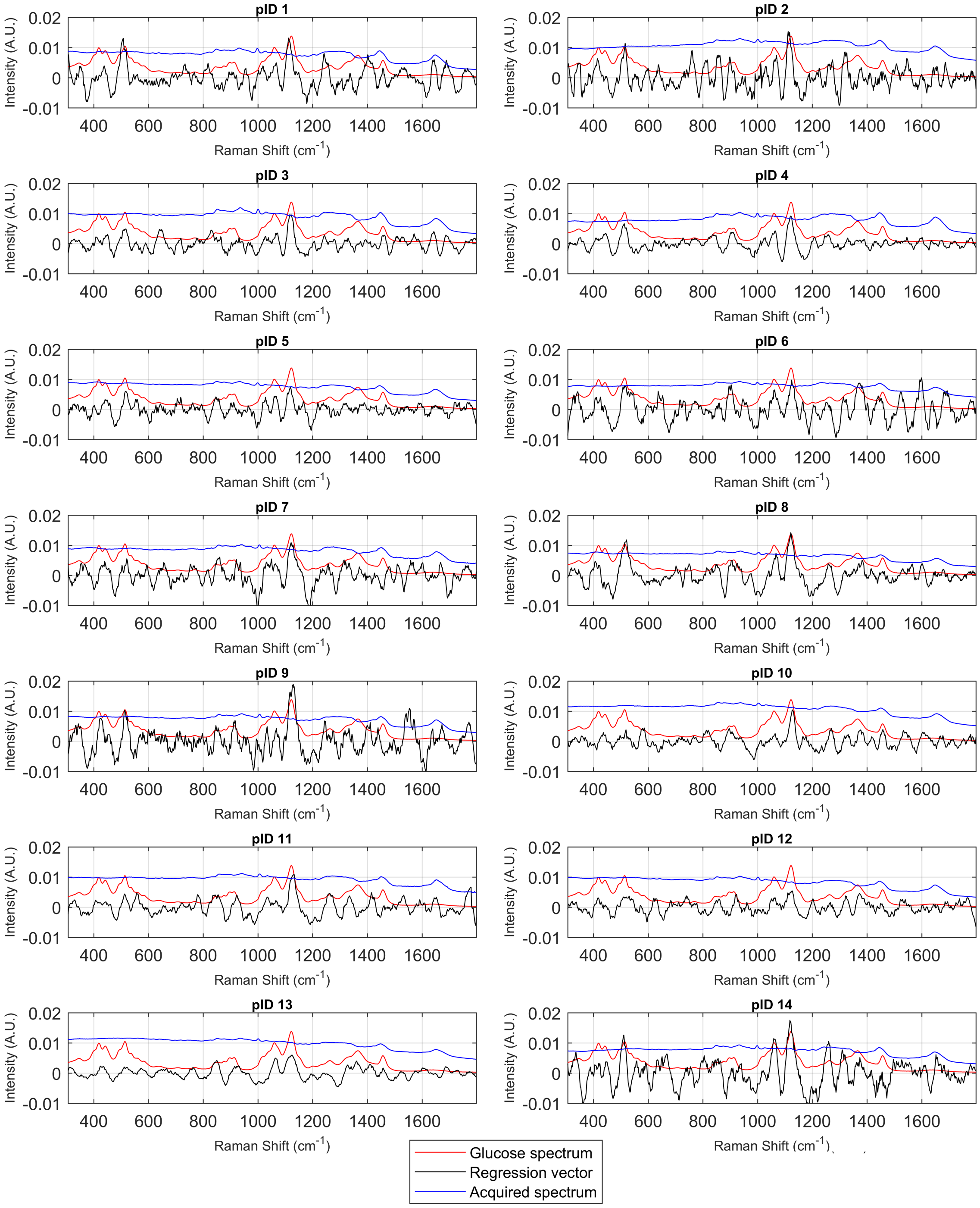

Figure 3.40: Raman spectrum of the thenar region (blue) and glucose in aqueous solution (red), and the regression vector for PLS calibration model (black) for 14 patients [119].

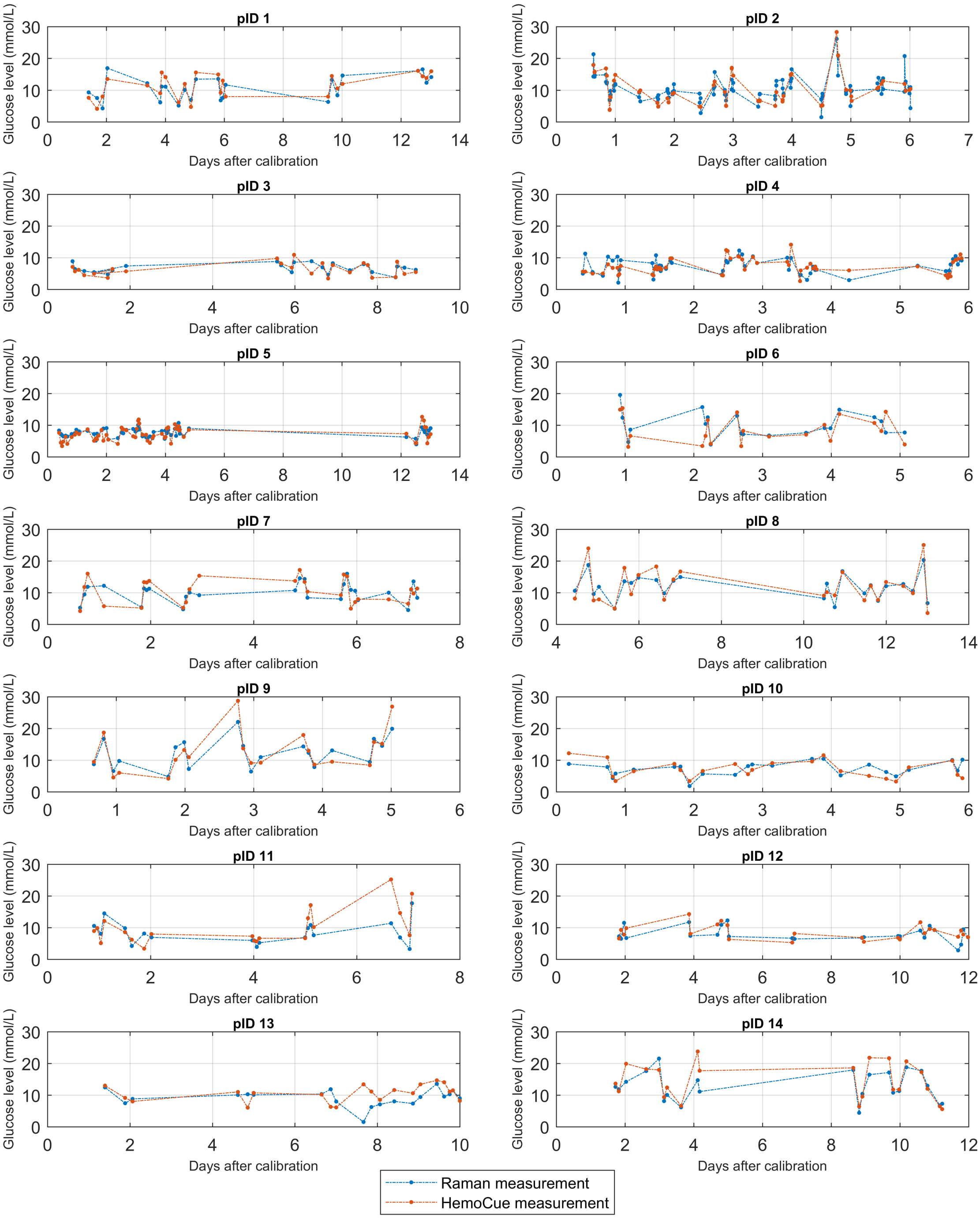

Figure 3.41: Independently predicted and reference glucose values, which start at the last day of calibration of 14 patients [119].

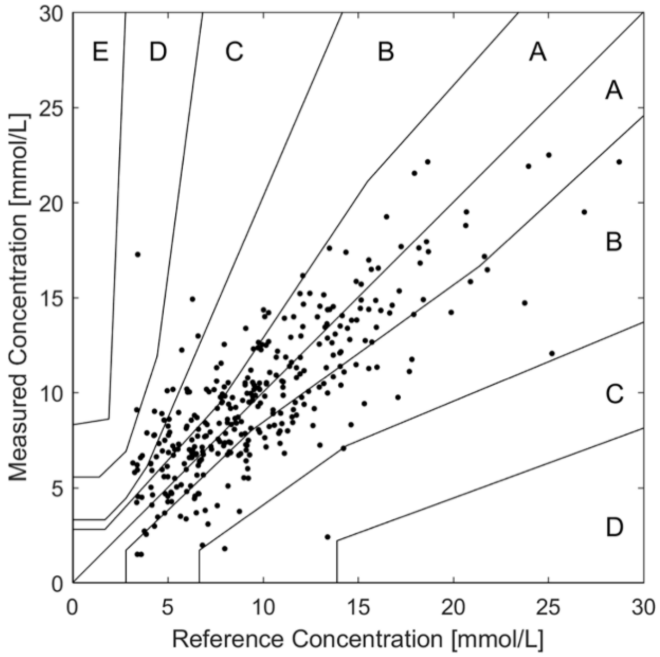

Figure 3.42: Error grid of 15 patients during the last five days of analysis after calibration [119].

different variables, resulting in multi-sensor methods for blood glucose estimation. For example, a combination of galvanic skin response, temperature, and PPG measurement was applied by [129], while GlucoTrack [130] combines ultrasonic, electromagnetic, and thermal technologies for measurement on the earlobe, and a wrist-worn multi-sensor device, proposed by [131], uses impedance spectroscopy, temperature, humidity, and photoelectric sensors.

However, an overview of other optical methods for the detection of blood glucose as well as a short description is summarized in Tab. 3.6.

3.4 Discussion

Since diabetes may lead to serious damage in the human body, an important part of diabetes management is done by periodical measurement of the blood glucose concentration. It was shown that different types of blood samples, which are all used for blood glucose measurement, may lead to different results. Thus, different diagnostic criteria must be considered, where varying threshold values for the different specimen types exist, and therefore, for an accurate interpretation of the measurement results, the used blood sample type must be known. When glucose is used for a diagnose of diabetes or screening of high-risk individ-

Method	**Description**	**Source**
FIRS, thermal emission spectroscopy	Radiation contains spectral information of glucose	[132, 133]
Photo-acoustic spectroscopy (PAS)	Linear dependence between photo-acoustic intensity and progression of skin glycation, absorption peaks at 9671.18 nm and 9259.26 nm (MIR), 540 nm and 620 nm (NIR)	[38, 134–136]
Fluorescence spectroscopy	Measurement of fluorescence markers of mitochondrial metabolism or cell autoflourescence by NAD(P)H, *Application:* glucose-sensing contact lenses	[137–139]
Secondary speckles, polarization	Change of skin vibration profile and in magnetic medium due to variation in glucose concentration	[53, 140, 141]
Optical coherence tomography (OCT)	Correlation (r = 0.78 to 0.91) of the OCT signal slope and blood glucose	[142, 143]
Polarimetry	Rotation of the polarization plane of linearly polarized light in proportion of glucose concentration	[144–147]
Metabolic heat conformation (MHC)	Relates glucose concentration to body heat and oxygen supply	[148]

Table 3.6: Overview of other optical methods for non-invasive glucose measurement.

uals, it is recommended to use venous plasma that is measured in an accredited laboratory [149]. It should also be considered that plasma and serum glucose is not the same, and that differences between both are not clearly revealed, but each hospital or screening center should establish the same diagnostic method [150].

Considering continuous glucose monitoring (CGM), the measured ISF glucose should be also kept in mind, since it represents one of the most effective ways for CGM. A major challenge between blood and ISF glucose is represented by the time lag, which is created by the diffusion from blood to the interstitial space, where the ISF glucose level may not ideally be suitable for closed-loop insulin delivery systems, but can, on the other hand side, deliver additional data and uncover clinically relevant information [67]. Different minimal-invasive methods for CGM are available commercially, employing a subcutaneous sensor, where state-of-the-art CGM devices, like Freestyle Libre Pro[3] (Abbott, USA), need no calibration and can be used for 14 days [114].

Several methods for non-invasive optical glucose measurement were mentioned, where especially the optical approaches of NIR, MIR, and Raman spectroscopy were reviewed. All of them use a spectral dependency on glucose, which shows a statistical relation between spectral information and the glucose content in the blood. Since on-chip spectrometers for wearable and mobile applications have only a limited amount of wavelength-channels as well as a limited resolution compared to an optical spectrometer, it is important to know the most informative region for the target of interest.

---

[3] https://www.freestyle-diabetes.at/produkte/freestyle-libre/

Considering NIRS, it was shown by [91] that a glucose-linked wavelength fluctuates daily, even at the same person, which is, according to the authors, one reason why an universal calibration model for individual subjects does not exist at the moment. Thus, it is not clear, which wavelength region keeps the most information for glucose monitoring at NIRS, since it is disturbed by several other tissue component like, among other things, water, fat, or protein. Although, it was observed by [49] that the ear lobe resulted in higher changes of the glucose signal compared to arm and finger, because its boneless structure and its shorter path-length, due to the disturbance of other analytes, multivariate methods or neuronal network are necessary to extract the glucose relevant information, resulting in a calibration of the optical method, where also grey-box approaches were mentioned, assuming a modified Beer-Lambert law. Thus, as mentioned by [91], an individual prediction method must be based on time-limited conditions, but it could decrease the frequency of blood sampling for invasive glucose measurement.

Considering MIRS and Raman spectroscopy, the target wavelength regions are much clearer, since they are applied in the ”fingerprint” region, where in the case of MIRS, only water represents a major disturbance. In case of Raman spectroscopy, also the influence of water is omitted, resulting in characteristic peaks in the spectra with a clear linear relation to glucose. Especially at MIRS, a drawback of poor penetration depth was considered as a major limitation of this method, next to influences of temperature change of the body and contact pressure. A possible solution for the problem of the limited penetration is represented by attenuated total reflection (ATR), which is applied by using flexible hollow infrared fibers with diamond (ATR) prism [69]. Although it was concluded that Raman spectroscopy represents an effective method for glucose measurement, since a clear linear relationship between Raman intensity and glucose concentration exists as well as a huge potential for detecting a trend of the glucose level is present, the detection itself is very complex and not suitable for everyday usage.

The importance and great general interest of a non-invasive solution for blood glucose monitoring is demonstrated by the huge amount of other methods and approaches, which were developed in the past and consider different optical and non-optical measurement methods as well as combinations of them.

Although an optical method for blood glucose measurement could reduce the temporal intervals between invasive measurements, and thus, increase the quality of a patient’s life, no optical method for non-invasive blood glucose measurement is available on the market today.

4 Optical Heart Rate Measurement

4.1 Introduction

Personal health care is important to prevent lifestyle diseases like hypertension, dyslipidemia and diabetes with exercise, sleep, and nutrition, where especially exercise needs an estimation of magnitude and duration for a safe and effective training [151]. In case of athletes, trainings like triathlon, cycling, and long-distance running, are more effective within a specific range of heart rate [152]. The recent improvement of battery life and miniaturization of hardware for real-time biosignal acquisition as well as the interpretation of the measured data led to the development of wrist worn devices for physiological monitoring, providing a consumer model for health and fitness [153].

Heart rate monitoring (HRM) also represents a diagnostic tool for many different applications in the field of cardiovascular diseases (CVD) and is general determined by the electrocardiogram (ECG). The common surrogated pulse rate (PR) is measured by the photoplethysmography (PPG) and represents the optical detection of the pulse pressure wave. The PPG forms the basis for other applications like the measurements of the pulse wave velocity (PWV) for vascular diagnostics of arterial stiffness or optical blood pressure estimation. Also, common known medical and clinical implementations like blood oxygenation monitoring (SpO_2) or the measurement of the heart rate variability (HRV), representing the physiological phenomenon of time difference between sequential heartbeats, which is widely used in medical and psychological applications [154], can be realized by the use of the PPG.

This chapter gives an overview of optical heart rate measurement, delivered from PPG, where also other applications and influences next to HRM are discussed.

4.2 Heart and Pulse Rate

Generally, the activity of the human heart is measured by the electrocardiogram (ECG), which represents the heart rate (HR). The optical detection of the pulse, more precisely, the dispersion of the pulse pressure wave, measured by photoplethysmography (PPG), is the so-called pulse rate (PR). The pulse and heart rate tend to be the same under normal conditions, but may differ in conditions that affect either only the heart or only the blood vessels [155]. This might be the reason why the term ”heart rate monitoring (HRM)” is often mixed up and commonly used for both methods.

Although the pulse rate depends on the heart rate [155], the ECG prevents other diagnostic features as the PPG does. To clarify the relationship between those, the origin of the ECG is illustrated in Fig. 4.1, where the electric impulse of the heart leads to contraction of the heart muscles. These impulses produce an electrical current, which can be measured by electrodes on the skin, representing the ECG, a record of the impulses of the cardiac muscle [156].

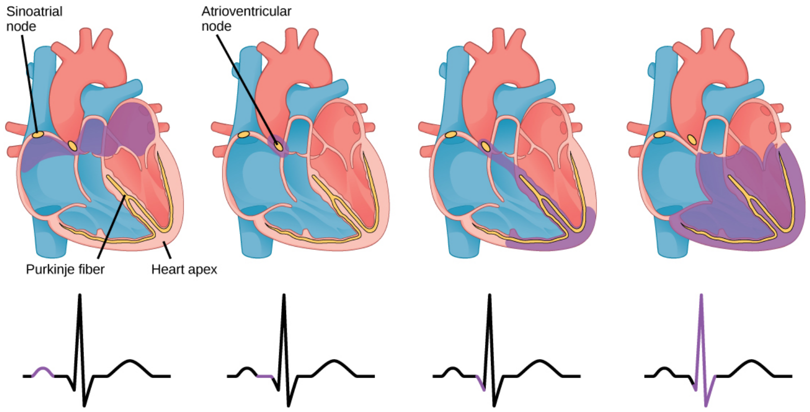

(a) An electrical impulse travels from the sinoatrial node to the walls of the atria, causing them to contract.

(b) The impulse reaches the atrioventricular node, which delays it by about 0.1 second.

(c) Bundle branches carry signals from the atrioventricular node to the heart apex.

(d) The signal spreads through the ventricle walls, causing them to contract.

Figure 4.1: Origin of the ECG signal [156].

As a function of the heart muscle, the pumping of the heart allows the blood to flow through the body by repeated contractions of the cardiac muscle and is called cardiac cycle [156]. The heart can be mentioned as two pumps, which are connected serially, where the venous blood is pumped out of the body into the lung on the right side of the heart, while on the left side the oxygenated blood from the lung is pumped into the human body [46]. This process is illustrated in Fig. 4.2, where the state of relaxation (diastole) and the contraction (systole) of the cardiac muscle build the pump function of the heart, characterized by the cardiac output (CO), defined in Eq. 4.1, in terms of the heart rate (HR) and the stroke volume (SV) [46].

$$CO = HR \cdot SV \tag{4.1}$$

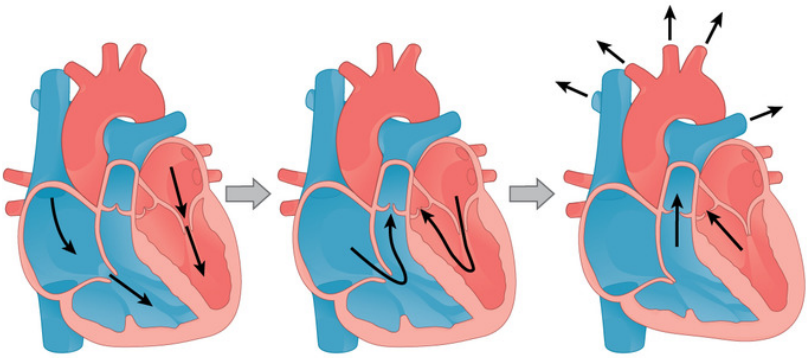

(a) **Cardiac diastole**: all chambers are relaxed, and blood flows into the heart.

(b) **Atrial systole, ventricular diastole**: atria contract, pushing blood into the ventricles.

(c) **Atrial diastole, ventricular systole**: after the atria relax, the ventricles contract, pushing blood out of the heart.

Figure 4.2: Systole and diastole of human heart [156].

This intermittently pump function of the heart causes a pulse pressure wave, which is propagating along the arteries with the so-called pulse wave velocity (PWV), differing due to the elasticity variations of the arteries between 3 m/s to 5 m/s on the aorta and 5 m/s to 12 m/s on the aorta radial artery [157].

This pulse wave can be detected by placing the finger on the wrist or neck, and can be used to determine the heart rate by counting the recognized pulse for ten seconds and multiply the result by the factor of six. Since the heart rate is usually indicated in ”beats per minute” (bpm), a normal resting heart rate of a healthy adult lies between 60 to 100 bpm and between 40 to 60 bpm for a well-trained athlete, while the maximum heart rate can be estimated by $\mathrm{HR}_{max} = 220 - \mathrm{age}$ [158]. A comparison of the heart rate measured by ECG and the pulse wave, determined by the photoplethysmography (PPG), is illustrated in Fig. 4.3, where the latter one will be described in detail in the next section.

4.3 Photoplethysmography (PPG)

Photoplethysmography (PPG) plays a major role in heart rate monitoring, since it is a non-invasive optical method to determine changes in the blood volume [160]. It delivers features that are used for further clinical application like heart rate variation (HRV), blood oxygenation, vascular diagnostics as well as blood pressure measurement [161]. An often

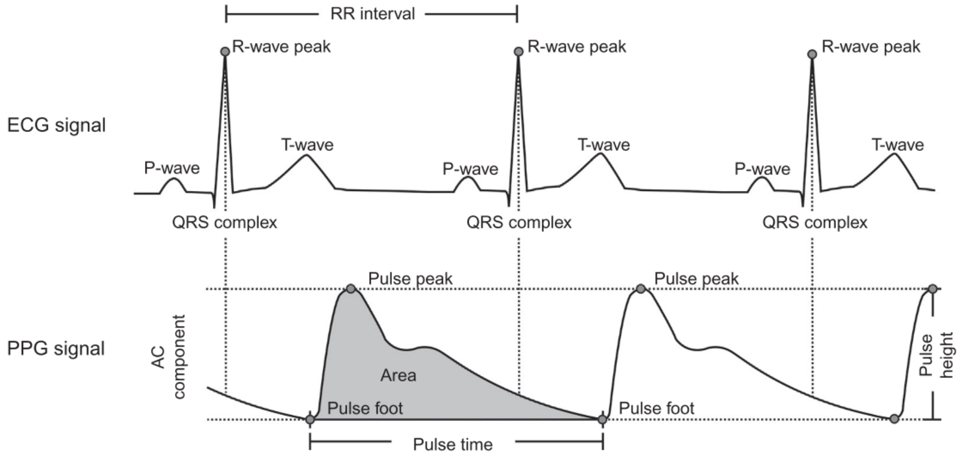

Figure 4.3: Comparison of typical ECG and PPG waveforms [159].

used acronym in literature is digital volume pulse (DVP) [160, 162]. (See [162] for more information of the standard terminologies for PPG signals.)

The principle of PPG is the detection of changes in the light intensity in the microvascular bed of tissue due to changes of the blood flow volume [163]. Since blood absorbs more light as the surrounding tissue, the detected change in light intensity is caused by a reduction of the amount of blood [163]. For the acquisition of a PPG signal, a light source, commonly realized as LED, and a photo-detector, are needed. The attenuation of light is typically modeled by Beer-Lambert's law [159], defined in Eq. 2.36 (p. 21). The application of PPG in wearable devices is possible in two modes, the transmission and the reflectance mode [163]. An overview of these two modes is illustrated in Fig. 4.4a, in case of fingertip PPG, and in Fig. 4.4b in detailed view, showing the pathway of light. The transmission mode is effective on body sites, where the light can reach the detector through the tissue, like fingertip, nasal septum, cheek, tongue, or earlobe [163].

The typical waveform of a fingertip PPG signal is illustrated in Fig. 4.5a, representing only the pulsatile (AC) component of the whole detected signal. The whole measured signal is illustrated in Fig. 4.5b, where the AC component represents changes in blood volume during the systolic and diastolic phase of the cardiac cycle [163] and is defined as the heart-beat-related signal from arterial blood flow [151]. The DC component corresponds with the optically detected signal from the tissue, depending on the tissue structure as well as the average volume of arterial and venous blood, and changes slowly with the respiration [163].

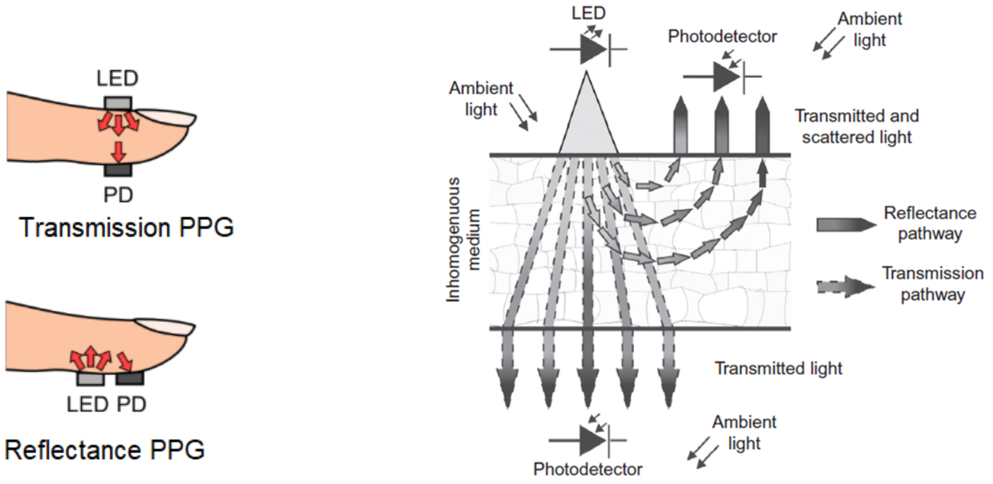

a) Measurement mode of fingertip PPG (modified from [163]). **b)** Overview of PPG modes (adapted by [159] from [164]).

Figure 4.4: Reflectance and transmission mode for the acquisition of a PPG signal.

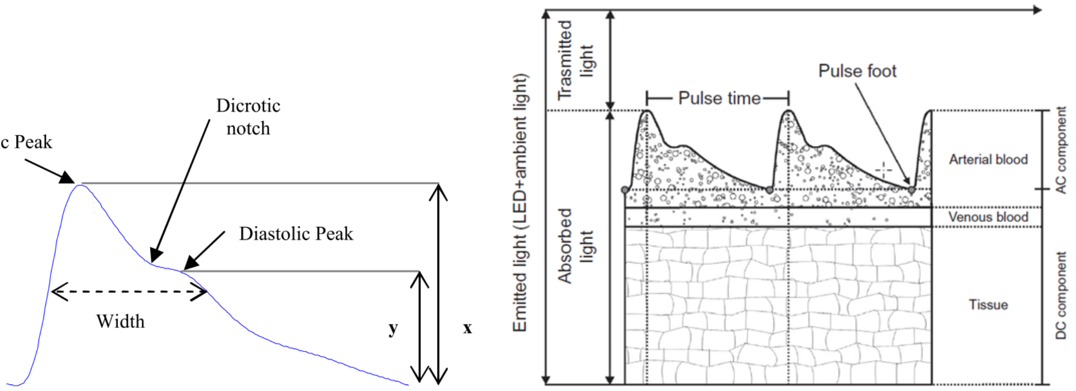

a) Typical waveform of a fingertip PPG [160]. **b)** AC and DC component of a PPG signal [159].

Figure 4.5: Characteristics of a PPG signal.

4.3.1 PPG Features

As already mentioned, PPG is used for different medical applications. In order to do so, a PPG diagnostic structure has to be followed, illustrated in Fig. 4.6. Since the PPG signal represents the blood movement in a vessel, and thus, it is affected by the heartbeat, haemodynamics, and physiological conditions, which are caused by changes in the arterioles, it is possible to observe these effects as a deformation of the PPG wave form [160]. An overview of the typical features, extracted of the PPG curvature and their related applica-

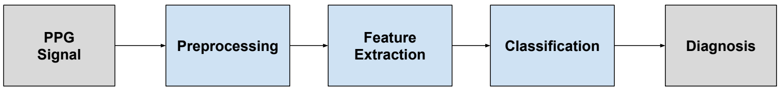

Figure 4.6: Common structure of PPG diagnostic system (adapted from [160]).

PPG Feature	Feature-related Application	Source
Systolic amplitude	Indicator of pulsatile blood volume changes	[159, 163, 165]
	Determination of ankle-brachial pressure index (ABPI)	[166, 167]
	Determination of pulse arrival/transit time (PAT, PTT) in blood pressure estimation	See Sec. 5.3.1 (p. 123)
	Determination of blood oxygenation (SpO_2)	See Sec. 4.6 (p. 102)
Pulse width	Correlates with systemic vascular resistance (SVR) (r = 0.56 at finger PPG, r = 0.62 for ear PPG)	[168]
Peak to peak distance	Correlates closely with R-R-interval	[160]
	Determination of hear rate (HR)	See Sec. 4.4 (p. 94)
	Determination of rate variability (HRV)	See Sec. 4.5 (p. 98)
Stiffness index (SI)	Related to large artery stiffness, age and pulse wave velocity (PWV)	[169, 170]
Reflection index (RI)	Related to compliance, vascular tone and systolic blood pressure (SBP)	[169, 170]
Areas under PPG curve	Related to total peripheral resistance (TPR) and cardiac output (CO)	[171, 172]

Table 4.1: Summary of PPG curve features and related applications (adapted from [160]).

tions, are summarized in Tab. 4.1.

The systolic and diastolic amplitude as well as the the pulse width can be recognized in Fig. 4.5a. As the first feature, the systolic peak represents an indicator of change in the pulsatile blood volume caused by the arterial blood flow, since it represents the AC part of the PPG signal [159, 163, 165]. The systolic amplitude was also used for the determination of the ankle-brachial pressure index (ABPI) [166, 167], which is associated with an increased risk of cardiovascular diseases (CVD) in case of decreased ABPI [173–175]. It is also used to measure the pulse arrival (PAT) and pulse transit time (PTT), which both play a central role in optical blood pressure estimation and will be discussed in Sec. 5.3.1 (p. 123). Furthermore, the systolic amplitude of two PPG curves is used to determine the blood oxygenation (SpO_2), which will be described in Sec. 4.6 (p. 102).

It was shown by [168] that the pulse width of finger and ear PPG curves are more sensitive to changes of the systemic vascular resistance (SVR) than other PPG features,

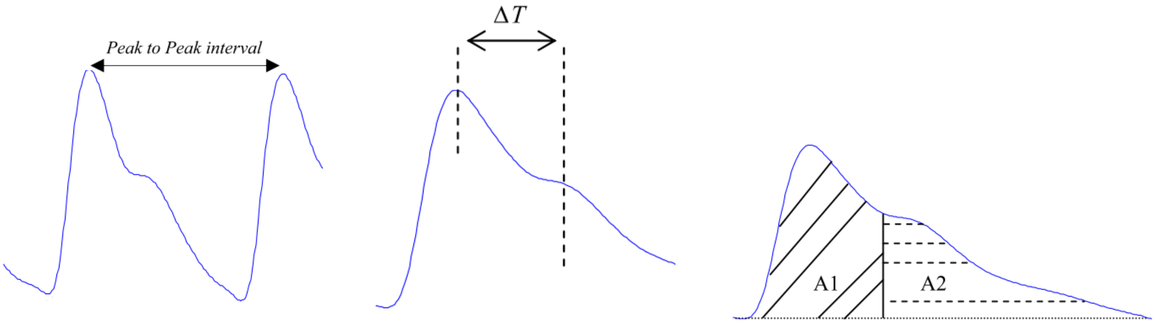

a) PPG interval. **b)** Definitoin of ΔT. **c)** PPG areas.

Figure 4.7: Definition of typical features of the PPG curve (modified from [160]).

resulting in a correlation of r = 0.56 in case of finger PPG and r = 0.62 for PPG measured on the ear.

The peak-to-peak distance, indicated in Fig. 4.7a, closely correlates with the R-R interval of the ECG and represents a whole heart cycle [160]. Thus, it is possible to determine the heart rate by this or another equal distance, which is measured between two significant points of the curve which occur in each period, as it will be described in Sec. 4.4 (p. 94). The other major application derived from the periodic duration of the PPG signal, is the heart rate variability (HRV) which will be described in Sec. 4.5 (p. 98).

As a simple assumption, the PPG waveform can be thought as a superposition of two approximately Gaussian shaped waves, the systolic and diastolic wave [176]. The systolic part of the PPG waveform is mainly caused by the pressure wave going forward from the left ventricle to the finger, while the diastolic part is produced by the reflected pressure wave from the small arteries in the lower body back and further to the fingers, generating a time-shifted second peak in the PPG curve shape, where the distance ΔT between these two peaks is defined in Fig. 4.7b [160]. Based on that time delay, the authors of [169] formulated a stiffness index of large arteries SI, shown in Eq. 4.2, where they mentioned that the unknown traveling path of the reflected wave h can be assumed to be proportional to the subjects height (measured in m) [169, 170]. The proposed index, which is actually a velocity, is measured in m/s, and linearly correlated to the mean pulse wave velocity [169, 170]. They showed that the time delay ΔT decreases with age as a consequence of increased artery stiffness and increased pulse wave velocity (PWV) of the pressure wave in large arteries, and concluded that the SI also increases with age and correlates with the carotid-femoral pulse wave velocity (PWV$_{cf}$) (r = 0.65, P $<$ 0.001).

$$SI = \frac{h}{\Delta T} \tag{4.2}$$

Next to the SI, [169] used the reflection index (RI), which is also called augmented index (AI), to determine the relation between diastolic and systolic peak height. The definition of RI is shown in Eq. 4.3, where the systolic x and diastolic height y are indicated in Fig. 4.5a.

$$RI = \frac{y}{x} \tag{4.3}$$

They showed a reduction of RI from 64 $\pm$ 3 % to 29$\pm$ 6 % (P $<$ 0.001) by decreasing the blood pressure of healthy subjects by using glyceryl trinitrate (GTN), while the change in SI was relatively modest.

The last feature of PPG, described here, is represented by the areas under the PPG curve, which are illustrated in Fig. 4.7c. In the study from [171], they introduced the so-called inflection point area ratio (IPA), shown in Eq. 4.4, which is, according to the authors, a very good indicator of the total peripheral resistant (TPR). The same authors presented in [172] a modified ratio called inflection and harmonic area ratio (IHAR), which had been shown to trace changes of cardiac output (CO) over a wide dynamic range before and after exercise. The IHAR is defined in Eq. 4.5, where NHA means the normalized harmonic area, shown in Eq. 4.6, where $FFT^2(f_n)$ means the squared magnitude of the n^{th} harmonic of the PPG signal in the frequency domain. The NHA was introduced by the same authors before and is related to pulse reflection and, according to the authors, strongly correlates with systolic and diastolic blood pressure [172].

$$IPA = \frac{A_2}{A_1} \tag{4.4}$$

$$IHAR = \frac{NHA}{IPA} \tag{4.5}$$

$$NHA = 1 - \frac{\sum_{n=2}^{N} FFT^2(f_n)}{\sum_{n=1}^{N} FFT^2(f_n)} \tag{4.6}$$

Next to the original PPG signal, its first and second derivation is also used to extract diagnostic informations, since it is difficult to detect changes in the simple form of the original PPG wave [177, 178]. As reviewed by [160, 179], the first derivation, also called velocity photoplethysmogram (VPG) [162], delivers the systolic and diastolic peak point as well as the points of maximum slope in original PPG. Furthermore, they mentioned that the VPG is used to determine the mentioned time delay ΔT and the crest time CT, which was related by [180] to be useful in a CVD classification in combination with ΔT and the SI. The authors of [180] achieved as the best classification of the PWV a result of 87 %. The VPG is shown in Fig. 4.8a.

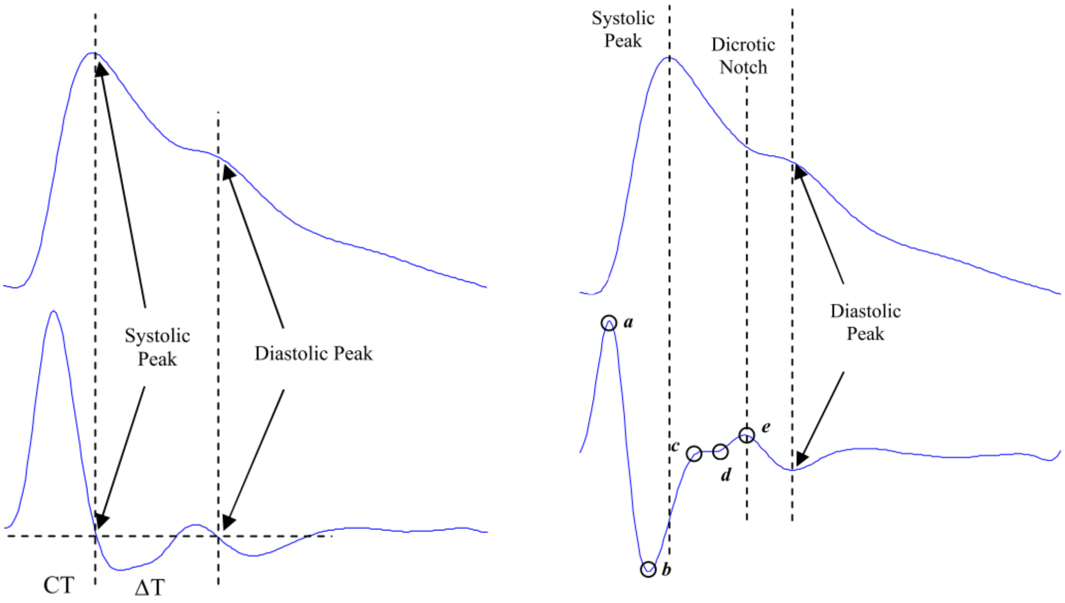

a) PPG (top) and VPG (bottom). **b)** PPG (top) and APG (bottom).

Figure 4.8: Original PPG waveform (top) and the first derivation, velocity photoplethysmogram (VPG) (bottom, left), and the second derivation, acceleration photoplethysmogram (APG) (bottom, right), (modified from [160]).

The second derivation, which represents the acceleration of the blood in the finger, is thus, also known as acceleration photoplethysmogram (APG) and more commonly used as the VPG [160, 162]. The APG is illustrated in Fig. 4.8b, where five significant points (a to e) in the curvature are marked. The ratios of the heights of these points can also be used for wave form analysis. The ratios $\frac{b}{a}$, $\frac{c}{a}$, $\frac{d}{a}$ and $\frac{e}{a}$ were concluded by [177] to represent an indicator of arterial stiffness since the ratio $\frac{b}{a}$ increases and the ratios $\frac{c}{a}$, $\frac{d}{a}$ and $\frac{e}{a}$ decrease with age. The authors of [181] related the ratio $\frac{b}{a}$ to be proportional to the thickness of the intima-media complex of the carotid artery and thus, to be related to atherosclerosis and altered arterial distensibility.

However, more details of vessel mechanics and vascular dynamics will be described in the next chapter (Chap. 5, (p. 109)), using PPG for the application of cuff-less optical blood pressure estimation.

4.3.2 Influence of the Wavelength

Since a PPG needs a light source and a detector, the choice of the wavelength is a trade-off and depends on the target application [159]. As already mentioned, the interaction of tissue and light is complex and involves scattering, absorption, and reflection [163]. A variety of wavelengths is used for common PPG applications, including light sources from red to near-infrared and green light [159, 163]. The typical wavelength range, used in PPG measurement, is marked in Fig. 4.9, showing the absorption and molar extinction coefficients of the main biological components. It can be recognized that shorter wavelengths are more absorbed by melanin and hemoglobin than longer ones, such as near-infrared and red, resulting in a higher tissue penetration depth for longer wavelengths [163]. This circumstances are illustrated in Fig. 4.10, where a blue and a red light source, applied on human skin, were simulated and the resulting path-lengths of light were indicated. Thus, for PPG applications in the transmission mode, an infra-red light source (600 nm to 1300 nm) is generally used [151]. For the reflectance mode, which is commonly used in wearable devices, the question of the best wavelength is not definitely clear. Several PPG applications are available on the market today, using green light [163]. Considering the application of heart rate monitoring (HRM), different approaches were made to assess the pros and cons of commonly used wavelengths.

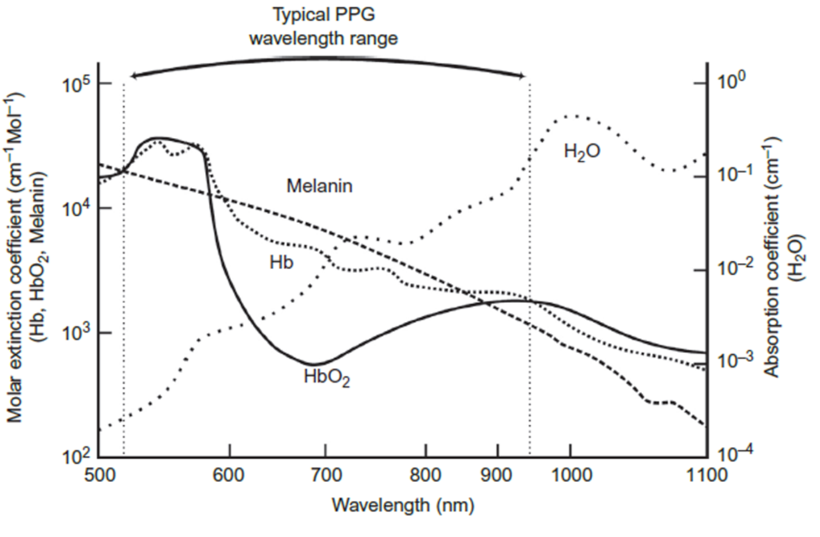

Figure 4.9: Typical PPG wavelength range with the molar extinction and absorption coefficients of main biological tissue components [159].

Green light has a much higher extinction coefficient for hemoglobin in comparison to red and infrared light, which means that hemoglobin absorbs green much better than red

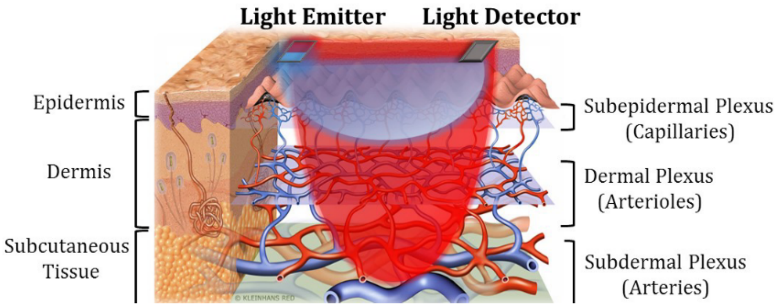

Figure 4.10: Simulation of PPG usage in case of a blue and a red LED on typical skin vasculature, indicating regions of high sensitivity [182].

light, but penetrates tissue deeper than blue light. Thus, the change of reflected green light is higher than that of infrared light, leading to a better signal-to-noise ratio (SNR) [163].

It was shown by [151] that differences in wavelengths affect the component ratio (CR), which influences the correlation between heart and pulse rate. The CR is defined in Eq. 4.7 and represents the ratio of the AC component to the whole measured signal. Since the AC part of the PPG signal is based on the heartbeats and contains the pulsatile information and the DC component depends on reflected and scattered light from tissue, the PPG in reflectance mode should contain a small DC and a large AC part [151], which would result in a high CR. Furthermore, the DC component depends on breathing and sympathetic nerve activity, meaning a variation for each subject, and resulting in low frequency signals about 0.3 Hz due to respiratory-induced vascular volume changes [183]. The authors of [151] suggested that reflected green light (525 nm) has an advantage over reflected infrared light (880 nm) in PPG, especially, at temperatures over 38°C. According to them, the correlation coefficients between the pulse rate, measured with PPG on the fingertip, and the heart rate, measured with ECG, were $r = 0.934 \pm 0.081$ for cold (below 20°C) and $r = 0.988 \pm 0.016$ for warm (over 38°C) conditions of green light. In comparison to that, infra-red light achieved correlation coefficients of $r = 0.731 \pm 0.266$ for cold and $r = 0.903 \pm 0.145$ for warm conditions. Additionally, they showed that green light has the larger CR in all environments.

$$CR = \frac{AC}{AC + DC} \tag{4.7}$$

In the study of [184], blue (470 nm), green (530 nm), and red (645 nm) light were compared for HRM during motion. They measured the PPG on the hand of twelve healthy subjects by horizontal and vertical motion of the hand. The resulting Bland-Altman plots between the ECG and the three PPG measurements are illustrated in Fig. 4.11, where limits of agreement (1.96 SD) of ± 3.2 bpm for red, ± 0.61 bpm for green, and ± 1,96 bpm for blue light, can be recognized. Furthermore, they compared the change in signal-to-noise ratio (SNR) from steady to motion state. Their results show that green and blue light have a significant smaller change in vertical and horizontal motion than red light, resulting in a change of -7.41 ±3.64 dB, -7.49 ±3.69 dB and -13.60 ±4.19 dB for horizontal and -8.64 ±4.39 dB, -7.49 ±3.75 dB and -13.43 ±5.09 dB for vertical motion, using green, blue, and red light, respectively. Thus, they concluded a relative freedom from motion artifacts for green compared to red and blue light, and that green light is more suitable for monitoring the heart rate under everyday life conditions.

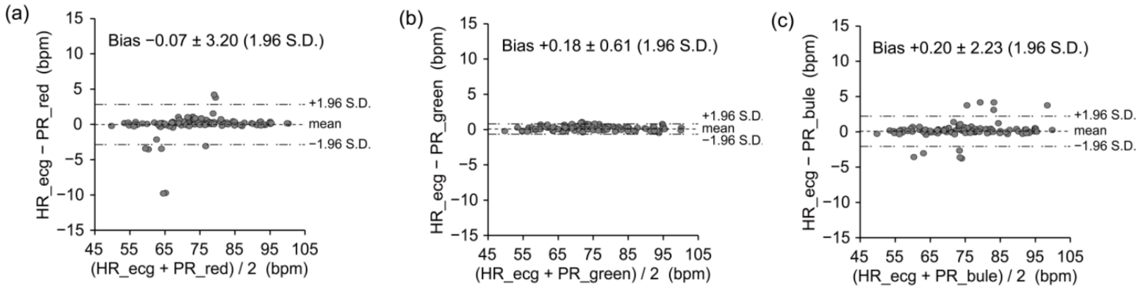

Figure 4.11: Bland-Altman plots between heart rate measured by ECG and pulse rate measured with (a) red, (b) green and (c) blue light PPG (modified from [184]).

Next to motion artifacts, the pigmentation of human skin should be kept in mind, since the pigmentation in various human skin types could also affect the quality of a PPG signal and could even make the measurement invalid [185]. The skin color characterizes the increase of melanin pigmentation and results from the interplay of solar radiation and hormones, depending on the genetically endowed melanogenesis of the individual subject [186]. The human skin tone is commonly categorized by using six different types (Type I to Type VI), which were defined by Fitzpatrick in 1975 [187]. These types are shown in Tab. 4.2, where the color and the ancestry of each skin type is mentioned.

In the study of [189], PPG measurements, using four different wavelengths (470 nm, 520 nm, 630 nm and 880 nm), were compared in terms of their AC/DC ratio for subjects with different skin types (Type I to Type V). Their results indicate, that in resting condition, green light (520 nm) shows a better performance in terms of AC/DC compared to the other wavelengths, independent of the skin type, but that the ratio was significant lower in type V skin type (dark brown). They concluded that it is possible with PPG to detect the pulsation across all skin types and achieving a higher resolution with green light at rest and blue or green light during exercise.

Type	Skin Color (unexposed)	Ancestry
I	bright white	Northern Europe, Britain
II	white	European, Scandinavian
III	fair	Southern or Central Europe
IV	light brown	Mediterranean, Asian, Latino
V	brown	East Indian, Native American, Latino, African
VI	black	African, Aboriginal

Table 4.2: Fitzpatrick skin types and corresponding skin color and ancestry (adapted from [188]).

Since infrared light has a much higher penetration-depth into human tissue, it can reach blood vessels in deeper skin regions, while green light can only interact with surface near tissue layers. This produces a more complex reflected signal in the case of infra-red light [159] and could be seen as a disadvantage. On the other hand, the authors of [159] mentioned that reaching deeper tissues could change into an advantage on cold ambient conditions with dramatically decreased microcirculation, where infra-red light would be the better choice of wavelength. They also mentioned that infra-red light is the desired light source for dark skin pigmentation with a high melanin content and a strong absorption of wavelengths, shorter than 650 nm.

Next to using only one specific wavelength, also, multi-wavelength PPG sensors are used for analysis of the peripheral blood volume pulsation by getting parallel informations of tissue layers from different vascular depth [190, 191].

In the study from [185], a multi-wavelength PPG sensor, shown in Fig. 4.12a, was used to perform a better measurement for different types of skin pigmentation and overcome drawbacks of present PPG sensors. They build a four channel sensor, where each channel has the same four peak wavelengths (green (525 nm), yellow (590 nm), red (650 nm), and infra-red (870 nm)). 33 healthy subjects were divided into four groups, according to their skin type (Type I and Type II (n=11), Type III (n=10), Type IV (n = 7), and Type V (n=5)), and compared in terms of their SD, using the multi-wavelength PPG sensor on the palm during exercise. In order to do this, they applied an auto-adaption of the LED illumination intensity by comparing each channel with a lower and an upper threshold, where the illumination current is adapted, when the signal of a channel is either smaller than the lower value or higher than the upper one. Their results showed that there is no significant difference between the five skin types across four different activities (resting, walking, jogging, and running).

In the case of blood pressure estimation, the authors of [182] used a multi-wavelength

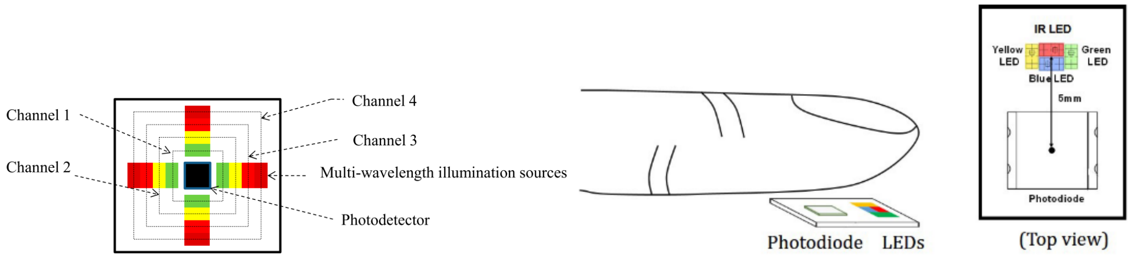

a) Multi-wavelength PPG sensor using four colors (green, yellow, red, and IR) for each of the four channels [185].

b) Multi-wavelength PPG sensor using four colors (green, yellow, blue, and IR) for blood pressure estimation [182].

c) Six-channel forehead mounted PPG sensor [192].

Figure 4.12: Examples of different PPG sensors, using multiple wavelengths.

sensor, shown in Fig. 4.12b, to achieve depth resolution of the blood pulsation in the skin. They used blue (470 nm), green (570 nm), yellow (590 nm), and infra-red (940 nm) light on the PPG sensor, which was attached to the left fingertip. They build a multilayer light-skin interaction model to remove capillary pulsation (short wavelengths) from the longer ones and to calculate the blood pressure, which will be discussed in the next chapter.

In the study of [192], a multi-wavelength PPG sensor, shown in Fig. 4.12c, was used to investigate the performance between multi- and single-wavelength approaches in terms of motion tolerance. The sensor contains six photodiodes, which were symmetrically mounted around a pair of red (660 nm) and a pair of infra-red (940 nm) LEDs, and were worn as a headband on the forehead. They collected data of 15 healthy subjects, using the multi-wavelength sensor and a transmission pulse oximeter as reference, which was kept motionless. In order to do this, they used a multichannel template-matching algorithm, where six IR PPG waveforms create a template, used as input, and an automatic selection of the best signal of the different PPG channels is done. Their results showed that using a multi-wavelength instead of a single-wavelength solution, leads to a much better performance in motion tolerance, signal quality, and pulse rate error.

4.3.3 Other Influences on PPG

The measurement side as well as the property of the subjects skin, including skin structure, blood oxygenation, blood flow rate, skin temperature as well as the environment have an influence on the quality of the PPG signal [160]. The authors of [159] summarized the major elements, which have an influence on PPG measurement, shown in Fig. 4.13, where three main factors (sensing, biological, and cardiovascular factors) can be recognized. They mentioned that sensor geometry and the distance between light source and detector are important factors, where the sensor geometry has an influence on the amount of light, traveling from the emitter directly to the detector without any interaction with human tissue, while the optical distance between the light source and the detector is a trade-off, which depends on the desired penetration depth and achievable light intensity. The authors pointed at empirical studies, which indicate that the optimal separation distances are 6 mm to 10 mm for infra-red light [193] and approximately 2 mm for green light [194].

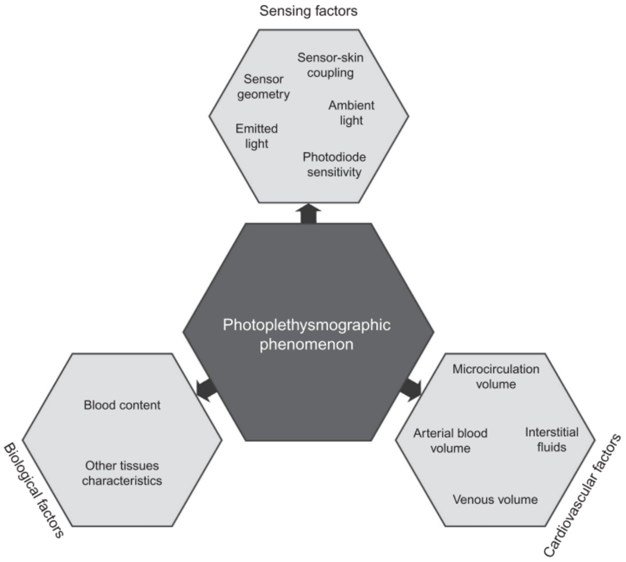

Figure 4.13: Major influences on PPG measurement [159].

Additionally, the authors of [163] mentioned that the PPG waveform may be affected by the contact pressure on the sensor device. They summarized that a moderate pressure on the sensor can improve the PPG signal, while the best results can be achieved by applying the transmural pressure, meaning the pressure difference between inside and outside the blood vessel. They also mentioned, that thus, an insufficient contact force results in a low AC amplitude. These results were also observed by heart rate measurement with ams Moonlight (18-channel spectral sensor solution), which was used in a separated project

(”Master Practical”), shown in Fig. 4.14, where a low and high contact pressure was applied on the sensor and changes in the PPG amplitude can be recognized.

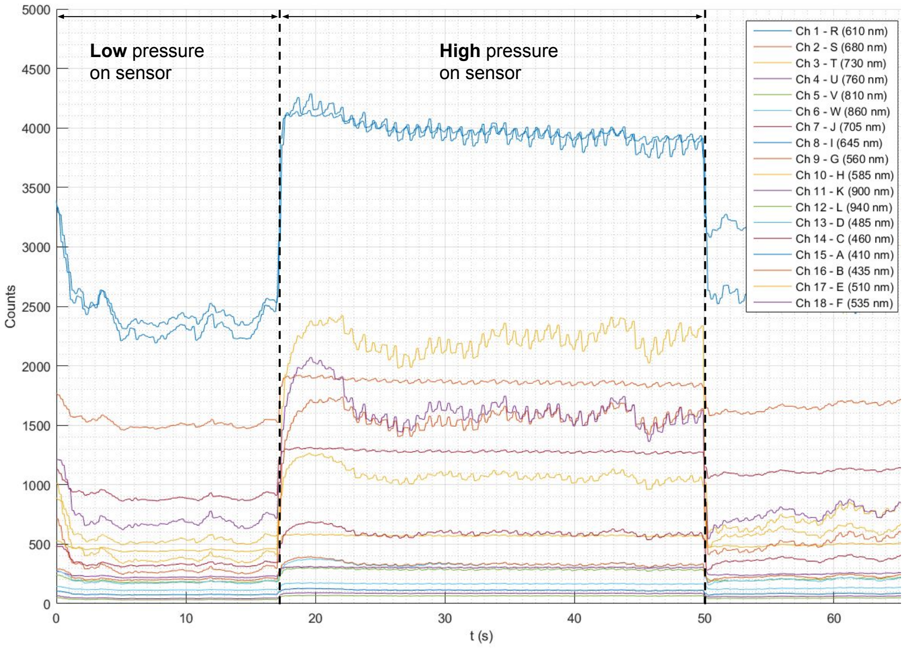

Figure 4.14: Influence of contact pressure on PPG wave form applying HRM, using ams Moonlight (18-channel spectral sensor solution).

4.4 Heart Rate Monitoring (HRM)

As already mentioned, the PPG signal itself represents the heart rate. In terms of heart rate monitoring (HRM), it is necessary to extract the heart-beat-relevant information from the measured signal. Generally speaking, two approaches exist to do this. The first one is based on the time domain and measures the beat-to-beat interval T_{b2b} between two significant points of the PPG curve, which represents the period duration of a cardiac circle. The commonly used detection points are illustrated in Fig. 4.15a, where the peak point (A), the valley point (B), the maximum of the first (C) and the second derivative (D) as well as the tangent intersection (E) can be recognized [195]. After the determination of this distance, which involves several signal processing methods, the heart rate f_{HR}, measured in bpm, is determined as $f_{\text{HR}} = \frac{1}{T_{b2b}} \cdot 60$.

However, the second method to estimate the HR from a PPG signal is based on the frequency domain. For example, it is possible to determine the power spectral density

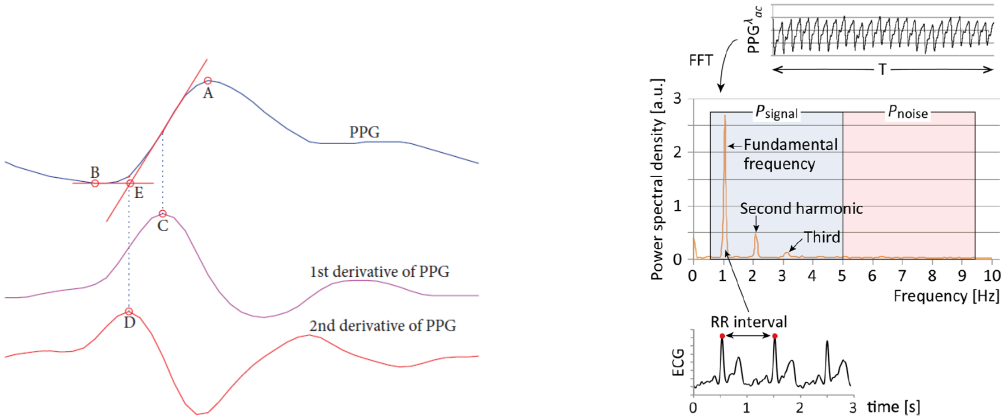

a) Five characteristic points of PPG curve [195]. **b)** Power spectra of PPG [183].

Figure 4.15: Time vs. frequency domain of heart rate estimation.

(PSD) of a signal by calculating its Fourier transform (FFT). The highest peak of the PSD spectrum corresponds to the heart rate under motion-free conditions [196]. This process is shown in Fig. 4.15b. Since the Fourier transform is only applicable for periodic signals, the use of FFT to detect the frequency of quasi-periodic or non-stationary signals is only limited useful because biological signals are often non-stationary and changing their properties over time [163].

As for HRM during motion, several techniques for motion artifact reduction exist, since the PPG signal is sensitive to motion artifacts (MA) [159]. These are usually realized by signal processing and basically assume that the PPG signal has only power at certain frequencies and the rest is noise, since motion artifacts mainly consist of random low-frequency interferences [163]. The authors of [159] named the three main causes of MA as tissue modifications due to movements, relative motion of the sensor-skin interface, and changes in the pressure between optical probe and skin. For example, according to [163], moving average filters are commonly used to remove MA, which are suitable for a limited artifact range, but do not handle sudden changes. They also mentioned the use of Fourier analysis, which can also be applied to non-stationary and quasi-periodic signals by applying cycle-by-cycle Fourier series and a former removing of high frequencies with Savitzky-Golay smoothing. When the noise frequency is similar to the pulse rate, it is not possible to separate the noise from the signal and thus, conventional signal filtering is not effective anymore, when MA have no predetermined frequency band [192]. Adaptive noise cancellation (ANC) is often used as an alternative to selective MA filters, where the signal corrupted by noise or interferences is estimated, based on a reference signal

[159, 163, 192] like an on-board accelerometer [197]. An overview of adaptive filtering, illustrated as motion-tolerant bio-sensor, is shown in Fig. 4.16, where next to the measured signal, a reference signal is required as input for the adaptive filter [198]. Adaptive filtering can be realized by methods like least mean square adaptive algorithm, Kalman filter, wavelet transform as well as principal component analysis (PCA) and independent component analysis (ICA), which are often applied as a method, called blind source separation (BSS) [163].

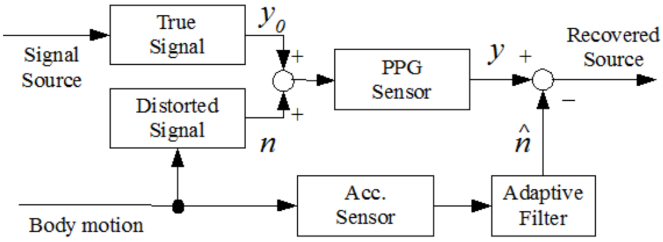

Figure 4.16: Motion-tolerant bio-sensor realized as adaptive filter with an accelerometer (adapted by [163] from [198]).

Next to motion artifacts, respiration effects and low perfusion are also resulting in a baseline drift and wandering of the PPG curve, where these effects are also caused by physiological conditions, like drowsiness, movement, or sympathetic activities, resulting in a fluctuation of the PPG signal [199].

However, as already mentioned, for the calculation of the HR in the time domain, the distance between two significant points of the PPG curve has to be determined. Generally, several methods for peak detection exist, which were summarized by [200] and include, among other things, traditional window-threshold techniques, wavelet transform, artificial neural networks, or techniques, which use templates. A simple and commonly used approach is the maximum or minimum value detection of the PPG signal, which could be realized by applying a knowledge-based approach that uses fixed thresholding [201], or by using an adaptive threshold method [199]. The former one is illustrated in Fig. 4.17, where the tangent intersection point (shown as ”E” in Fig. 4.15a) is detected by calculating the second derivate of the PPG signal (”b wave” means the minimum of the second derivate). Considering the mentioned adaptive threshold method, the detection of maximum (top) and minimum values (bottom) of a measured PPG signal are illustrated in Fig. 4.18a, where the detection threshold is indicated as red dashed line. This adaptive threshold method was presented by [199] to improve the PPG peak detection as well as to overcome the respiration effect, and is shown in Fig. 4.18b in detail, where a virtual threshold is increased or decreased by fixed slope parameters and an additionally selected refraction period was set with 0.6 seconds for the initial value and 0.6 times of the previous average pulse interval for the next periods.

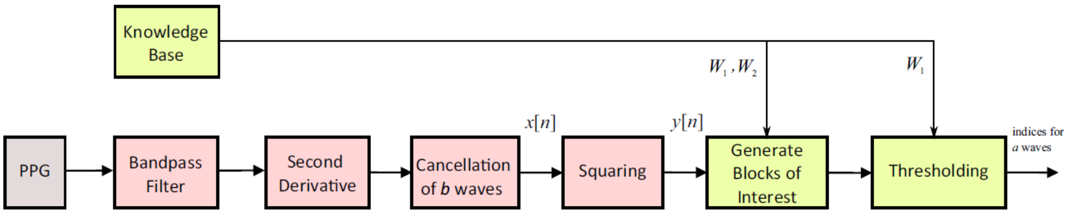

Figure 4.17: Knowledge-based peak detection using fixed thresholding [201].

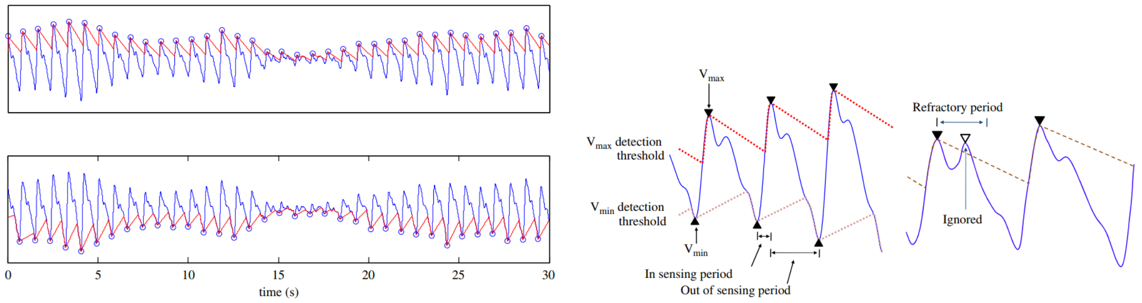

a) Detection of maximum (top) and minimum values (bottom) of a PPG signal.

b) Peak detection using adaptive threshold method.

Figure 4.18: Adaptive thresholding for PPG peak detection [199].

One possibility to simplify the detection of pulse peaks is to transform a low-pass filtered PPG signal y_k to a slope sum function (SSF) z_i, which is defined in Eq. 4.8, where $\Delta y_k = y_k - y_{k-1}$ and w means the length of the analyzing window [202, 203]. The relationship between the original PPG signal and the transformed SSF signal is shown in Fig. 4.19, where the upslope of the PPG signal is enhanced and the remainder is suppressed [203, 204].

$$z_i = \sum_{k=i-w}^{i} \Delta u_k \, , \Delta u_k = \begin{cases} \Delta y_k : & \Delta y_k > 0 \\ 0 : & \Delta y_k \leq x \end{cases} \tag{4.8}$$

As already mentioned, in a separated project ("Master Practical"), the ams Moonlight, an 18-channel spectral identification solution with a central optical filter range from 410 nm to 940 nm, illustrated in Fig. 4.20, was used for HRM by reflectance PPG measurement. To do so, an offline analysis using MATLAB was done, where the mentioned threshold peak detection method as well as a modification of SSF was applied for peak detection.

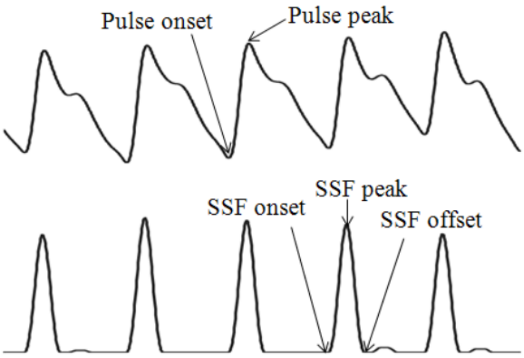

Figure 4.19: Simplifying of PPG curve by slope sum function (SSF): Original PPG signal (top) and SSF (bottom) (modified from [204]).

An overview of the implemented steps is shown in Fig. 4.21, where the measured PPG signal is used as an input to estimate the HR as well as the resulting error between the calculated and reference value. Using a white LED, 18 spectra were measured, analyzed, and compared with a commercial pulse oximeter (Medisana PM 100). A resulting HR measurement of about 180 seconds is illustrated in Fig. 4.22, where the estimated values (blue) were compared to the reference values (red).

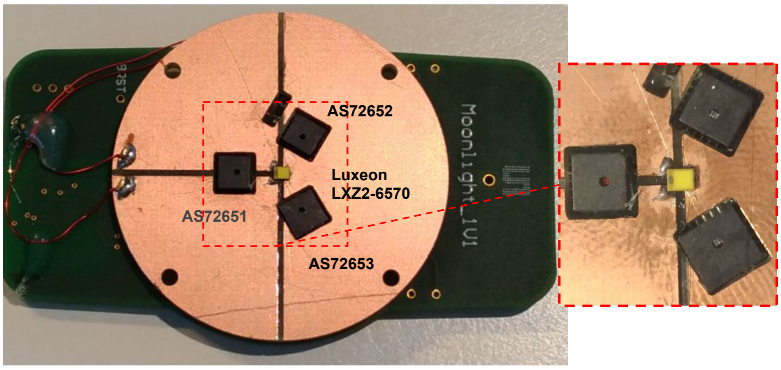

Figure 4.20: Modified setup using ams Moonlight for HRM measurement.

4.5 Heart Rate Variability (HRV)

Since the human heart rate is not constant and varies with each heartbeat, this physiological phenomenon of tiny fluctuations in the time interval is called heart rate variability (HRV), which is of significant importance and widely used in clinical applications [195, 205]. Thus, HRV determines the variation in time duration between continuous heartbeats [206],

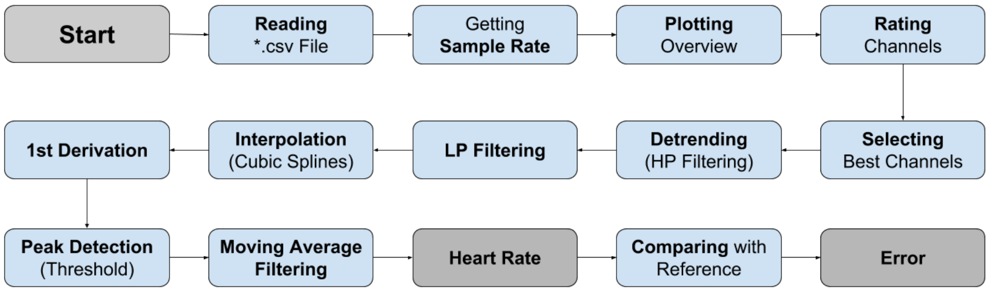

Figure 4.21: Overview of HRM using ams Moonlight and MATLAB.

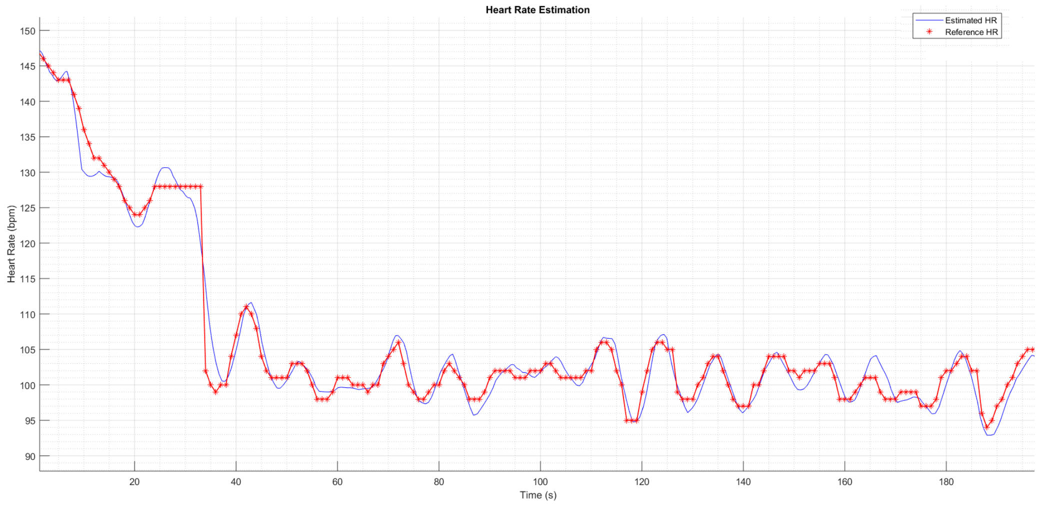

Figure 4.22: Estimated HR with ams Moonlight (blue) and reference signal from pulse oximeter (red).

where too much instability, like arrhythmias or nervous system chaos is harmful for the efficient physiological function and energy utilization [207].

A continuous HRM can show the net effect of the neural output of parasympathetic nerves, which decreases the HR and increases HRV, while the sympathetic nerves let the HR increase and the HRV decrease [154, 207]. HRV can be determined in several ways, but the most common ones are based on time- and frequency-domain analysis [207], while the most common form of observing changes in the HR is the HR tachogram, representing the sequences of time intervals between heartbeats, illustrated in Fig. 4.23, where an eight hour period was measured of a 36-year-old male subject between 11:45 and 17:45, and two significant changes, named as high stress during public speaking and high energy expenditure during exercise, can be recognized [207]. Thus, the HRV can be thought as biofeedback, where, for instance, a sudden drop in HRV could be seen as an indicator of

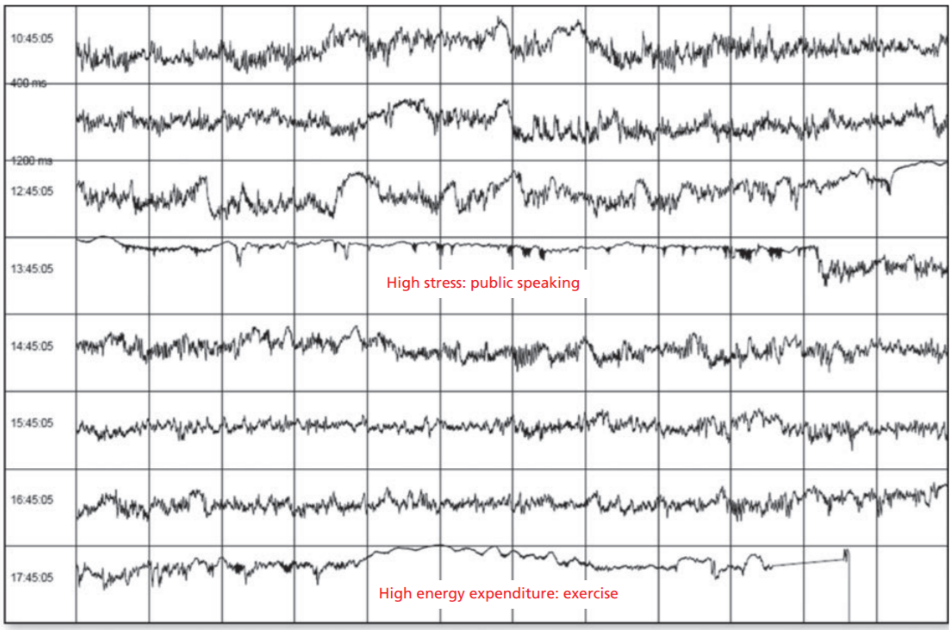

Figure 4.23: HR tachogram, showing an eight hour period of a 36-year-old male [207].

over-training and fatigue [154].

Generally, heart rhythm oscillations can be divided into four primary frequency bands: high frequency (HF), low frequency (LF), very low frequency (VLF), and ultra low frequency (ULF) [208]. According to [207], most HRV analysis is done in segments of five minutes of 24 hour recordings, but also other recording lengths are often used, which should, as recommend by the authors, be reported, since the recording length has a huge influence on frequency- and time-domain values of HRV analysis. The most commonly used HRV parameters in frequency-domain are summarized in Tab. 4.3, where the HF band is associated with parasympathetic or vagal activities and also known as the ”respiratory band”, while the LF band reflects baroreceptor activities [207]. Additionally, the authors of [195] mentioned the ratio of LF/HF as well as the LF and HF, normalized by the total power as an additional parameter for HRV analysis. The HRV signal is then separated by the power spectral analysis into its components and provides frequency and amplitude information of specific rhythms, which are contained in the main signal [207]. For instance, the authors [207] showed a typical HRV recording over a 15 minute period during the rest condition in Fig. 4.24, where the original wave form as well as the separated bands, and the corresponding frequency analysis can be recognized.

The commonly used parameters of HRV in time-domain were summarized by [195], shown in Tab. 4.4, where all parameters are related to the term NN, meaning ”normal-

Frequency Band	Frequency Range (Hz)	Description
HF	0.15 to 0.4	High frequency power
LF	0.04 to 0.15	Low frequency power
VLF	0.0033 to 0.04	Very low frequency power
ULF	< 0.0033	Ultra low frequency power

Table 4.3: Overview of frequency bands of heart rhythm oscillations (adapted from [195, 207, 208]).

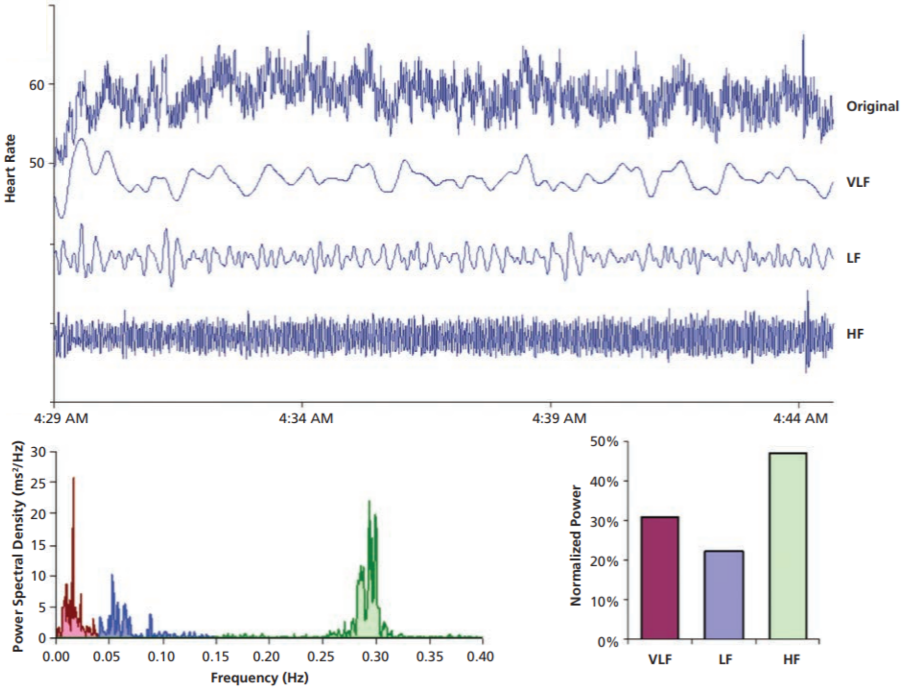

Figure 4.24: Typical HRV recording during rest condition (top) and HRV analysis considering the frequency domain (bottom) [207].

to-normal interval" and representing all intervals between adjacent QRS complexes from sinus node depolarization [208]. Furthermore, time-domain parameters can also be used for HRV, considering geometric measurement, where the series of NN intervals can be illustrated as a geometric pattern, like sample density distribution of NN intervals or sample density distribution of differences between adjacent NN intervals, realized as distribution histogram, or Lorenz plot of NN intervals [208]. In addition to that, the authors [195] mentioned two non-linear parameters, SD1 and SD2, which are commonly used for HRV analysis and represent the SD of the short (SD1) and long (SD2) diagonal axis in the Poincare plot, a diagram of each R-to-R interval against its previous one [208, 209].

Parameter	**Description**
AVNN	Average of all NN intervals
CV	Coefficient of variation of NN intervals
SDNN	SD of NN intervals
SDANN	SD of all NN intervals in all five minute segments of the whole recording
RMSSD	Root mean square of successive differences between adjacent NN intervals
SDSD	SD of successive differences between adjacent NN intervals
NN50	Number of pairs of successive NN intervals that differs by more than 50 minutes
pNN50	Proportion of NN50 divided by total number of NN intervals

Table 4.4: Commonly used time domain parameter for HRV (adapted from [195, 208]).

However, HRV is usually measured by digital signal processing of the ECG, where QRS complexes and thus R-to-R intervals are determined [195]. Common ECG recording systems use sample frequencies between 100 Hz and 1 kHz, meaning a time resolution of 1 ms to 10 ms [210]. But the measurement of HRV is also possible by using single-sensor devices, such as PPG sensors [154]. The authors of [195] extracted 16 HRV related values, consisting of time- and frequency-domain as well as non-linear parameters, from the PPG signal, measured by a smartphone on 30 healthy subjects, compared the results with ECG measurements and achieved a correlation of $r > 0.7$ for 14 parameters between PPG and ECG measurements of HRV. Their resulting HRV, using ECG as well as PPG with five different characteristic points for interval detection, are shown in Fig. 4.25, where the R-to-R interval is delivered from ECG (a), while (b) to (f) represent pulse-to-pulse intervals, using PPG with peak point, valley point, maximum of first and second derivate as well as tangent intersection, respectively. (See Fig. 4.15a (p. 95) for description of characteristic points.)

4.6 Pulse Oximetry

The arterial blood oxygen saturation (SaO_2) has major clinical and physiological significance, since it represents, next to the arterial oxygen partial pressure (PaO_2), the oxygen supply of the organs, depending on the respiratory function [211]. Pulse oximetry is an optical and non-invasive method for estimating the SaO_2 by measuring the peripheral oxygen saturation (SpO_2), as both are sufficiently correlated [212]. The oxygen transfer from the lungs to the tissue is mostly done by hemoglobin molecules in the red blood cells (97 % to 98 %), while only 2 % of the total oxygen content is dissolved in plasma [213]. The oxygen saturation in arterial blood is defined in Eq. 4.9 as a ratio of the oxygenated hemoglobin

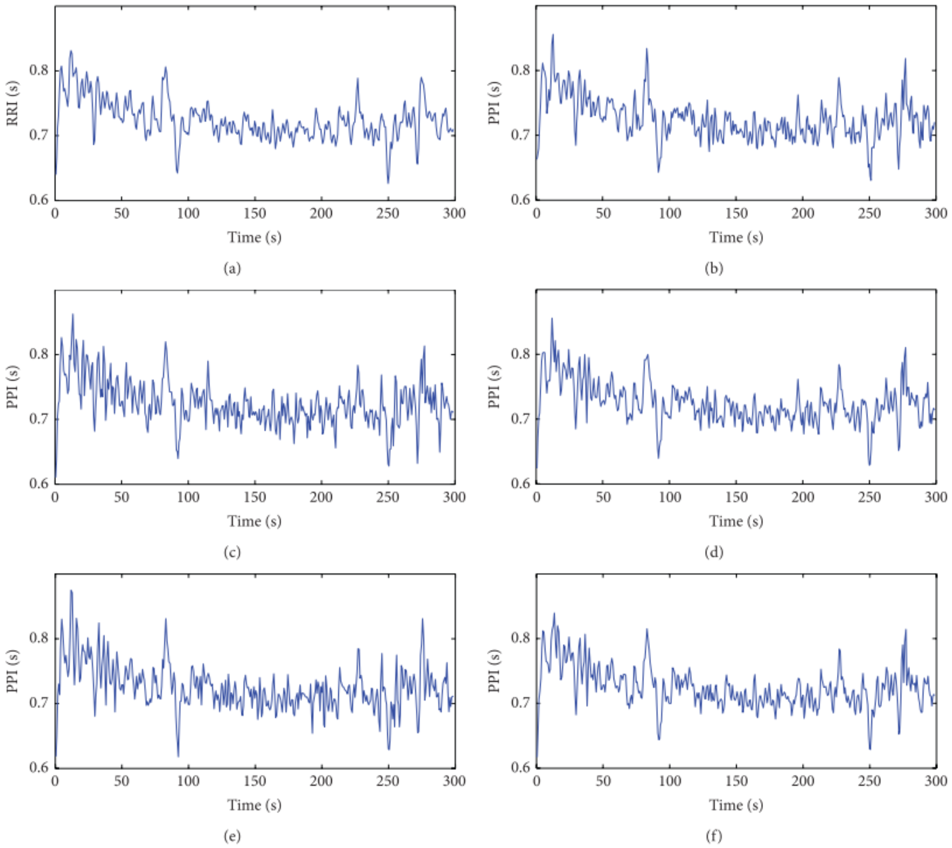

(a) (b) (c) (d) (e) (f)

Figure 4.25: Comparison of HRV, using R-to-R intervals (RRI) from ECG (a) and pulse-to-pulse intervals (PPI) from PPG, using different characteristic points (b) to (f) [195].

concentration $c_{\mathrm{HbO_2}}$ and the total hemoglobin concentration $c_{\mathrm{HbO_2}} + c_{\mathrm{Hb}}$ [211].

$$\mathrm{SaO_2} = \frac{c_{\mathrm{HbO_2}}}{c_{\mathrm{HbO_2}} + c_{\mathrm{Hb}}} = \frac{[\mathrm{HbO_2}]}{[\mathrm{HbO_2}] + [\mathrm{Hb}]} \tag{4.9}$$

The estimation of $\mathrm{SaO_2}$ is done by measuring two PPG curves in two different wavelengths, which deliver the ratio of ratios R in terms of the AC and DC component of each wavelength [211], and is shown in Eq. 4.10 for the usual choice of wavelength for pulse oximetry, red (660 nm), and infra-red (880 nm to 940 nm) [214], which are used because of their relatively large difference in light absorption [211], shown in Fig. 4.26.

$$R = \frac{\mathrm{AC_{Red}}/\mathrm{DC_{Red}}}{\mathrm{AC_{IR}}/\mathrm{DC_{IR}}} \tag{4.10}$$

A direct determination of $\mathrm{SaO_2}$ from multiple PPG measurements by using Beer-Lambert's law is not possible, since light scattering in tissue and blood also affects the light attenu-

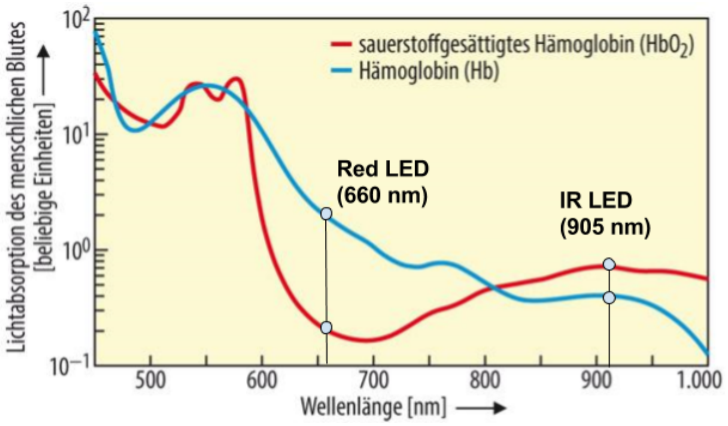

Figure 4.26: Light absorption of oxyhemoglobin (HbO_2, red) and deoxyhemoglobin (Hb, blue) at different wavelengths, where the marked wavelengths red (660 nm) and IR (905 nm) are usually used for pulse oximetry (modified from [215]).

ation of the tissue, and thus, the scattering constant and optical path length between red and infrared light differ significantly [211]. Thus, the relation between R and SaO_2 is determined by calibration [216, 217], where R is measured in healthy subjects invasively by in-vitro measurement of SaO_2, resulting in Eq. 4.11, where the values k_1 to k_4 are obtained by best-fit analysis of the determined parameter in the calibration process for a specific pulse oximeter [211]. The estimated value from pulse oximetry is usually called SpO_2 [211] and can be determined by the use of empirical derived calibration curves as shown in Fig. 4.27 [212].

$$SaO_2 = \frac{k_1 - k_2 R}{k_3 - k_4 R} \tag{4.11}$$

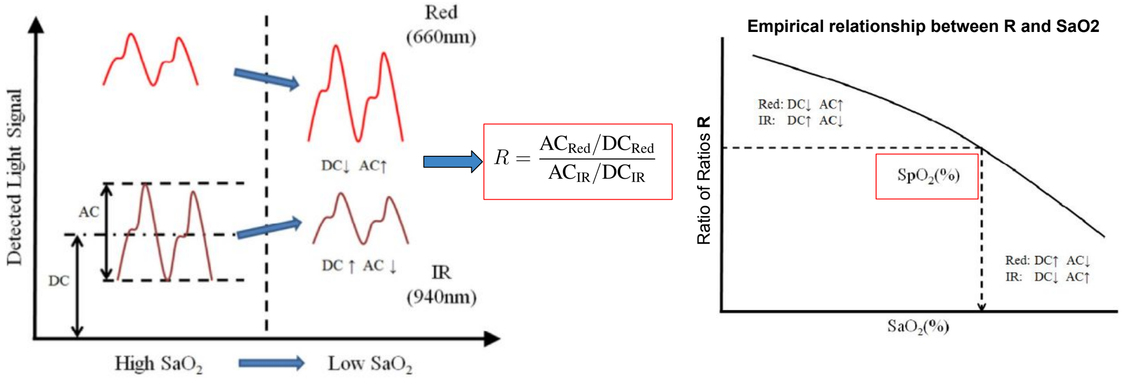

Figure 4.27: Estimation of SaO_2 using pulse oximetry (left) and empirical relationship between R and SaO_2 (right), resulting in SpO_2 (modified from [212]).

A possible way to determine SaO_2 without calibration is shown in Eq. 4.12 [218, 219], where ε_o and ε_d refer to the extinction coefficient of HbO_2 and Hb of the first and second used wavelength (indicated as 1 and 2) [211, 213], respectively, and it is assumed that the used wavelengths are sufficiently close, so that the difference between both path lengths can be neglected [218]. For example, this was realized by [213], using a multiple PPG with the wavelengths 780 nm, 785 nm, and 808 nm for SpO_2 measurement on healthy subjects, resulted in the normal range. However, although it is possible to determine SpO_2 without calibration, both methods are based on models that match tissue circulation only in terms of approximations [211].

$$SaO_2 = \frac{\varepsilon_{d1} - \varepsilon_{d2} R}{R(\varepsilon_{o2} - \varepsilon_{d2}) + (\varepsilon_{d1} - \varepsilon_{o1})} \tag{4.12}$$

The authors of [214] build and reviewed a low cost reflective PPG system for HR and SpO_2 determination, using a red and an infra-red LED, realized as SoC, and shown in Fig. 4.28. They used Eq. 4.11 for the estimation of the SaO_2 and obtained their values from calibration. An overview of all the implemented modules is illustrated in Fig. 4.29, where the signal processing methods are realized as low power high performance MCU, and real time software routines are delivered to a workstation. They investigated the influence of the LED current range on the signal quality, considering the highest and lowest ADC resolution as well as the the trade-off between power consumption and signal quality, resulting in two designs, which have been summarized in Tab. 4.5.

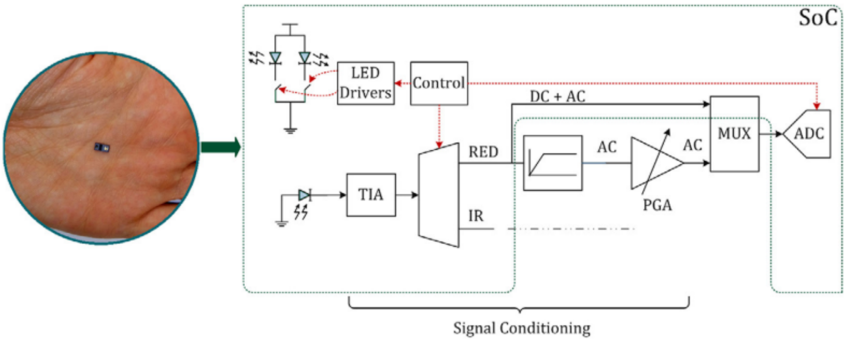

Figure 4.28: Typical reflectance pulse oximeter implemented on SoC [214].

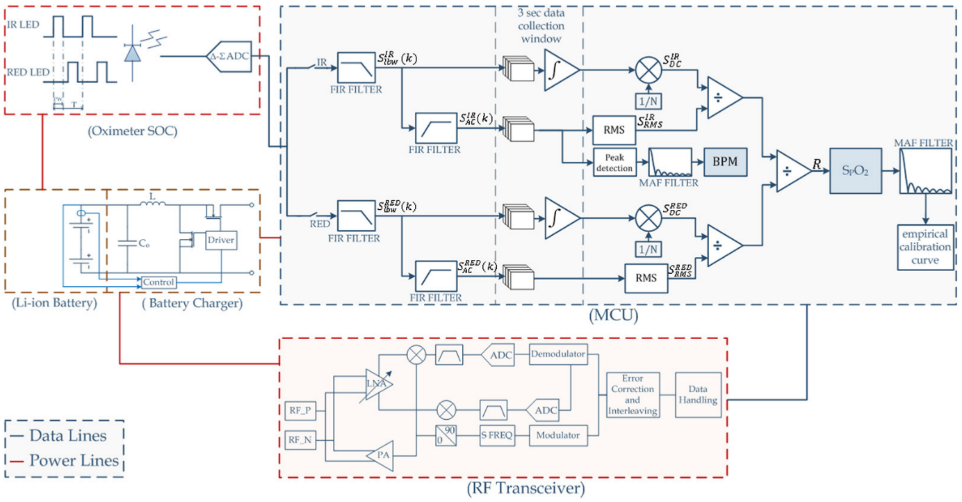

Figure 4.29: Functional modules of pulse oximeter [214].

Low Power Design		**High Performance Design**	
Pros:	**Cons:**	**Pros:**	**Cons:**
Low energy consumption	Low accuracy	High accuracy	High energy consumption
Small batter size	Low dynamic range	High dynamic range	Increased batter size and regulatory complexity
High autonomy	PPG low sampling rate	PPG high sampling rate	Low autonomy

Table 4.5: Overview of two designs, representing a trade-off between low power and high performance (adapted from [214]).

4.7 Discussion

The pulse rate (PR) detected by PPG as well as the measured curve form contain important cardiovascular information like vessel stiffness [220] and have a wide field of clinical and consumer applications in medical and fitness devices. It was shown that the PPG provides information about the age and thus, about the state of the arteries, which is used in the determination of arterial stiffness by measuring the PWV [221, 222].

Since the simplest form of PPG has only two components, the question of the light color, more precisely the choice of the best wavelength, is of particular importance. It can be concluded that the usage of green light in the reflectance mode has some advantages in comparison to infra-red and blue light, since infra-red light delivers a too complex signal due to its higher penetration and blue may not reach deep enough into the tissue, but in general, it is a trade-off and the wavelength depends on the target application [159].

However, the detection of the PPG is a complex interplay of different factors, which all have an influence on the performance. First, a major challenge for PPG sensors is the sensitivity to movements which have influence on the accuracy of this measurement [223]. To prevent these influences, different methods for motion artifacts removal were mentioned, where for instance, the movement could be detected by an on-board accelerometer. Next to MA, the authors of [151] showed that the PPG signal also changes in different environments. They reviewed that the AC component of green and infra-red light decreases significantly in cold exposure due to vasoconstriction, while the DC components were almost similar. Also, other factors like contact pressure or the distance between light source and detector have an influence on the PPG signal, where a moderate pressure could alloy the signal quality and the spacing of emitter and detector depends on the used wavelength and should be considered in the sensor design.

The major application of PPG is the usage as HRM, where the beat detection can either be done in time- or frequency-domain. For the first one, common detection methods as well as characteristic points in PPG curvature were mentioned. In a separated project (”Master Practical”), the ams Moonlight was used for HRM, where a beat detection was realized in time-domain, using a modified threshold-method and the maximum of the first derivate as characteristic point in PPG curve shape. The outcome of this project was a possible heart rate estimation, using the ams Moonlight with a mean absolute error (MAE) lower than 2 bpm in comparison to a commercial pulse oximeter.

Also, other medical applications for clinical and personal use, measuring a PPG signal, were mentioned. As an extension of HRM, HRV represents an important and useful indicator to evaluate the response of the autonomic nervous system [224]. It was shown by [195] that next to the traditional ECG recordings, also technologies like smartphones, have the potential for HRV measurement at resting and would represent a low-cost health care application without the need of body attached electrodes and specially trained medical staff. The authors of [224] showed that trends in PPG signals affect HRV analysis and must be removed before HRV analysis. Since HRV measures fluctuations in the time interval, the used sample frequency of PPG should be kept in mind. Moreover, the authors of [225] investigated the influence of the sample frequency on HRV analysis, using a 10 kHz-sampled PPG signal, which was down-sampled to 5000, 2500, 1000, 500, 250, 100, 50, 25, 20, 15, 10, and 5 Hz, and used to derive common time- and frequency-domain parameters for HRV. They compared them to values from a 10 kHz sampled ECG signal and concluded that the minimal sampling rate depends on the analyzed parameter, but that similar results for ECG and PPG-based HRV can be reached, using a sample frequency greater than 25 Hz, certainly, the authors indicated to the usage of a perfectly detected PPG peak position.

As another application of PPG, pulse oximetry was discussed, where the arterial blood oxygen saturation (SaO_2) can either be estimated with a calibration curve, using usually a red and infra-red LED, or without calibration, using two or more wavelengths, which are close together. According to [211], empirical calibration assumes that the relationship between R and the physiological parameter SaO_2 is not influenced by inter-subject variability in the circulatory system and thus, a resulting inaccuracy occurs, if the path-length ratio between the two wavelengths changes between the subjects of the calibration and those, whom the clinical examination is applied to. Otherwise, the authors of [213] mentioned, that calibration-free pulse oximetry, meaning the use of two or more nearby wavelengths, is more challenging, but has the potential to provide more accuracy than pulse oximeter, using red and infra-red lights as well as an initial calibration.

Considering a reflectance pulse oximeter, the authors of [214] mentioned that a fully wearable PPG SpO_2 monitoring can be challenging, since a small design size and other constraints should be realized, while their main contribution was, that there exists a trade-off between power consumption and signal quality.

5 Optical Blood Pressure Measurement

5.1 Introduction

Hypertension or high blood pressure represents circumstances in which blood vessels are under increased stress due to raised pressure, which lead to a higher risk of damage for the heart and blood vessels in major organs (e.g. brain and kidney) [3]. Next to hypertension, arterial stiffness is an important index and a potential therapeutic target for patients with hypertension, independent from blood pressure [226, 227] and is associated as a major contribution to cardiovascular events, like myocardial infarction or stroke [221].

According to the WHO [1], cardiovascular diseases (CVDs) are the number 1 cause of death globally, where estimated 17.9 million people died in 2016. Complications from hypertension result in 9.4 million deaths worldwide every year [3]. It was mentioned that people with CVD or people with a high risk of CVD, which is the case, among other things, in the presence of hypertension, diabetes, or hyperlipidaemia, need an early detection and management. Since the blood pressure depends on the arterial properties, it represents an indicator of the health state of the cardiovascular system, which is therefore important to measure [228].

Today, the currently used gold standard methods for blood pressure control are the well known auscultatory and oscillometric method [228]. Both are measuring a discrete value the blood pressure and need a cuff for applying a pressure on the vessel. The reviewed optical approaches of blood pressure measurement in this chapter seek a cuff-less and continuous blood pressure measurement, which could be used in personal health or consumer devices.

5.2 Arterial Blood Pressure and Vascular System

As already mentioned, a pulse pressure wave is caused by the periodical pump function of the human heart [157]. This pressure wave carries the blood into the body by pumping it into the vessels, and creating a force on the wall of the arteries [3]. So, the term ”blood pressure” (BP) is commonly used as a synonym for arterial blood pressure [157] and is generally defined as a pressure, which is applied on the wall of the blood vessels by the blood. In case of arterial BP, it is exerted upon the walls of arteries. For a higher BP, the human heart has to pump much harder as in case of a lower one [3]. Generally, the arterial BP depends on several factors and varies with the muscular efficiency of the heart, the blood volume and viscosity, the age and health of the individual as well as the state of the vascular wall [228].

The blood pressure is measured in mmHg and alters periodically between two extreme values, the maximum of the systolic value or systolic blood pressure (SBP), and the minimum of the diastolic value or diastolic blood pressure (DBP) as well as it changes these values over time [228]. A typical example of a blood pressure curve is shown in Fig. 5.1, where next to the mentioned values SBP and DBP, which represents the minimum and the maximum of the curve, the pulse pressure (PP), which is defined as the difference of systolic and diastolic pressure, and the mean arterial pressure (MAP), representing the average pressure value over time, can be recognized during a period of 0.8 s (75 bpm).

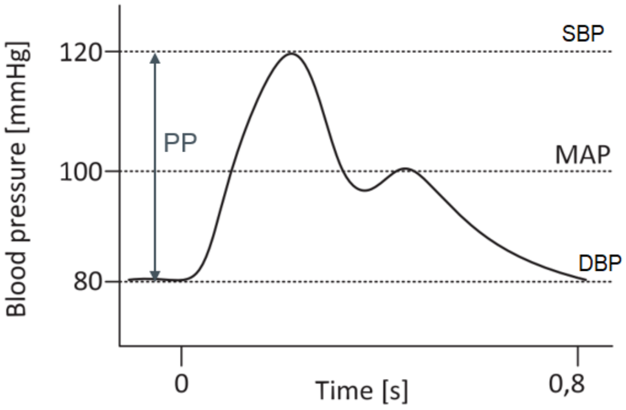

Figure 5.1: Curve of blood pressure during a cardiac cycle and its significant points (modified from [228]).

While a too low SBP leads to a bad perfusion of the tissue, which causes a poor distribution of nutrition and oxygen, a too high DBP creates the risk of a vessel rupture as well as a damage of major organs like liver, kidney, brain, or heart [228]. The classification of blood pressure as well as the definitions of hypertension grade are summarized in Tab. 5.1 according to the guidelines for arterial hypertension management of the European Society of Cardiology (ESC) and the European Society of Hypertension (ESH) from 2018.

Classification	**SBP (mmHg)**		**DBP (mmHg)**
Optimal	< 120	and	< 80
Normal	120 to 129	and/or	80 to 84
High normal	130 to 139	and/or	85 to 89
Grade 1 Hypertension	140 to 159	and/or	90 to 99
Grade 2 Hypertension	160 to 179	and/or	100 to 109
Grade 3 Hypertension	≥ 180	and/or	≥ 110
Isolated systolic hypertension	≥ 140	and	< 90

Table 5.1: Classification of blood pressure and definition of hypertension grade according to ESC/ESH guidelines 2018 (adapted from [229]).

5.2.1 Arterial Wall Mechanics

Since the blood pressure acts on the wall of vessels, it is important to understand the structure and compositions of these as well as the difference between them for further blood pressure modeling. The system of cardiovascular circulation can generally be split into a high and low pressure system, represented by arteries and veins, respectively [157]. A comparison of these two major types of blood vessels is illustrated in Fig. 5.2. Arteries and arterioles have thicker walls than veins and venules due to their closer location to the heart and the higher receiving pressure [230]. The relationship between the systemic blood pressure and the different types of blood vessels is illustrated in Fig. 5.3, where the mentioned high and low pressure system can be recognized.

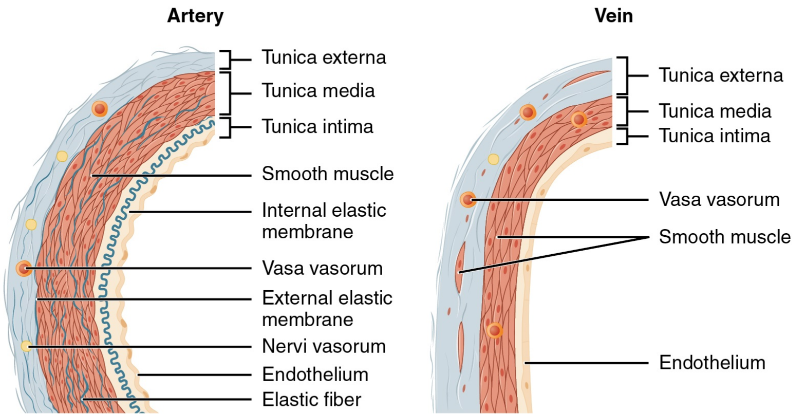

Figure 5.2: Comparison of artery and vein wall [230].

As already mentioned, in terms of the arterial blood pressure the main focus is on arteries. Generally, the wall of an artery and also of a vein has three main layers, the Tu-

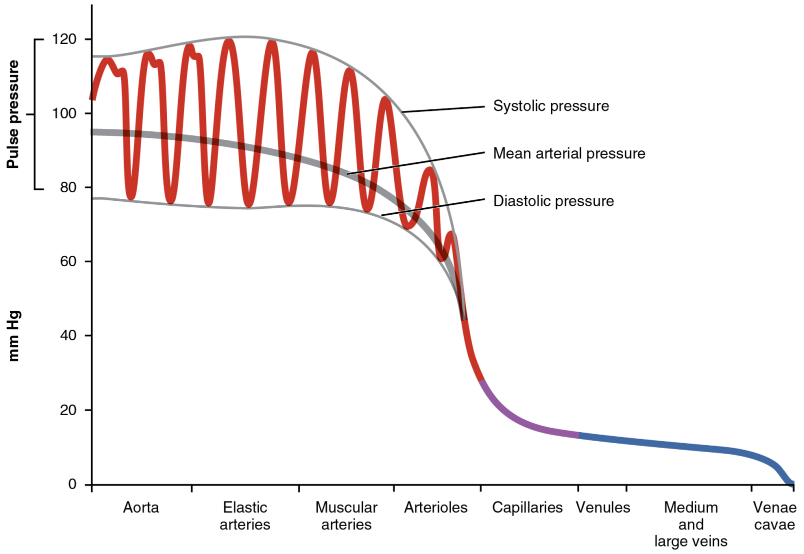

Figure 5.3: Systemic blood pressure throughout different types of blood vessels [230].

nica adventitia (externa), Tunica media, and Tunica intima, where the Tunica media is the functional layer of the artery [231]. The Tunica intima (inner layer) is a mono-layer of endothelial cells, which are biologically very active and able to produce a host of molecules as response of chemomechanical stimuli, and is primarily composed of type IV collagen and laminin [231]. The Tunica media (middle layer) is generally the thickest layer in the artery and is composed of smooth muscle cells, which are mostly arranged in circular sheets and also responsible for vasodilation and vasoconstriction, and supported by connective tissue, made by elastic fibers [230, 232]. The outer layer, called the Tunica adventitia, represents the envelope of the artery, made of connective tissue, which is primary composed of collagen fibers [230], where collagen is the key ingredient of the arterial structure [232].

Collagen, which is relatively inextensible, represents the main load-carrying element in the arterial wall and is a stiffness reinforcing structural element [233]. So, if the Tunica adventitia does not hold the vessel tight, any movement would disturb the blood flow [230]. Arteries are deformable with a highly non-linear stress-strain response, which is characterized by stiffening at higher pressure [233]. This behavior can be recognized in Fig. 5.4, where an untreated human illiac artery (control) is compared to two arteries in which elastin and collagen had been digested, resulting in a change of the stress-strain relationships. It can be seen that a lower amount of collagen (collagen-digested) in the artery leads to a more elastic behavior, while a higher amount of collagen (elastin-digested) makes the arteries stiffer.

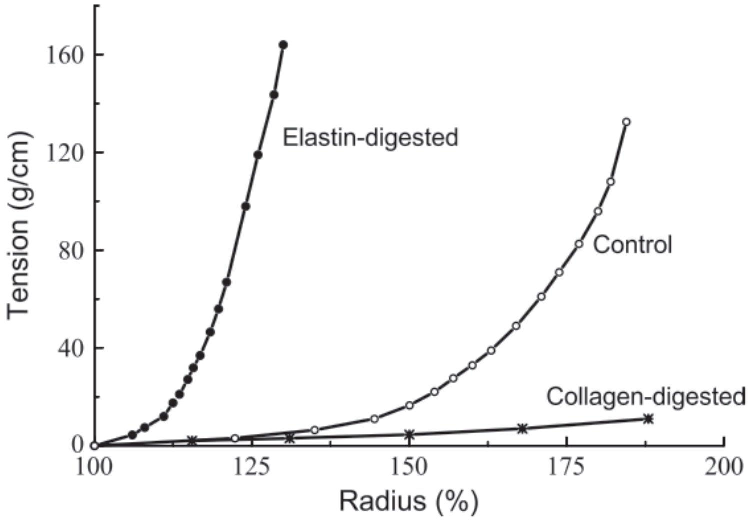

Figure 5.4: Relationship of tension and radius of human illiac arteries (modified by [233] from [234]).

Thus, the elasticity of the arterial wall is mainly caused by elastin, collagen, and smooth muscle cells [235]. To clarify the effect of elastin and collagen, the structure of collagen is illustrated in Fig. 5.5a, where collagen fibrils build collagen fibers, which are finally connected together to collagen fiber bundles, whereas elastin, shown in Fig. 5.5b, has a clew shaped structure which is cross-linked, but has no ordered macromolecular structure [236]. Therefore, the stiffness of the vascular wall is determined by these two predominant scaffolding proteins, collagen, and elastin, which means that an overproduction of collagen or a minor production of elastin would lead to vascular stiffness [221].

Generally, the relationship between tensile stress σ and strain ε of a linear medium is described by Young‘s modulus E, defined in Eq. 5.1, as the property of elastic material, which is often approximated by the ratio of load and deformation [238]. As illustrated in Fig. 5.6, the stress is defined as force F, acting on the area A, while the strain is the ratio between initial length L and the resulting length difference ΔL. Since the load transfer from elastin to collagen is strain-related, a higher blood pressure leads to a shift of load from elastin to collagen, resulting in stiffening, and it also leads to an anisotropic mechanical behavior of the arteries [233].

$$E = \frac{\sigma}{\varepsilon} = \frac{F \cdot L}{A \Delta L} \tag{5.1}$$

In contrast to Young’s modulus, the compliance C is a structural parameter and not a material parameter [235]. The compliance is the ability of each compartment to increase

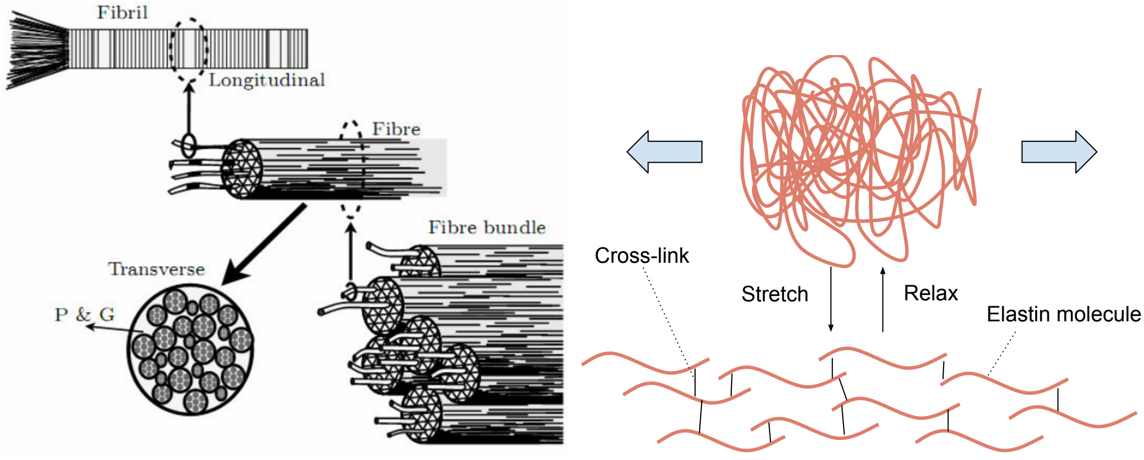

a) Collagen Structure [237]. **b)** Elastin structure.

Figure 5.5: Comparison of the structure of collagen and elastin.

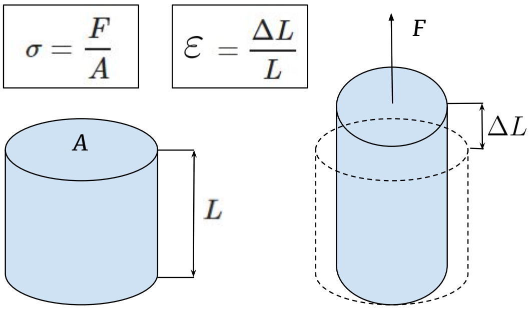

Figure 5.6: Components of stress and strain.

its volume [230] and is defined in Eq. 5.2, as ratio between the volume change ΔV and the change of arterial blood pressure ΔP [236]. The normalized compliance is called distensibility D, shown in Eq. 5.3, and represents the inverse of the bulk modulus K [235]. The flow resistance R is defined by the Hagen-Poiseuille law, shown in Eq. 5.4, assuming a pipe with a length L, a radius r, and the viscosity of blood η [157, 230] as well as a Newtonian behavior of the fluid. As shown in Fig. 5.7a, an analogy to an electrical circuit can be recognized, comparing the peripheral resistance of the arterial system to an electrical resistor. The resulting relationship with the blood flow Φ (also called Q) is shown in Eq. 5.5.

$$C = \frac{\Delta V}{\Delta P} \tag{5.2}$$

$$D = \frac{C}{V} = \frac{\Delta V}{V \Delta P} = \frac{1}{K} \tag{5.3}$$

$$R = \frac{8L\eta}{\pi r^4} \tag{5.4}$$

$$\Phi = \frac{dV}{dt} = \frac{\Delta P}{R} = \frac{\pi r^4 \Delta P}{8\eta L} \tag{5.5}$$

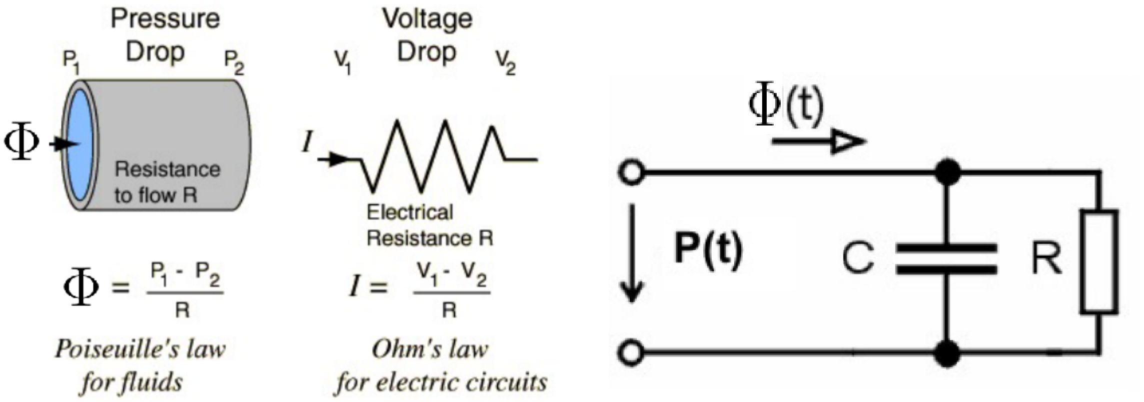

a) Fluid-dynamics vs. electrical circuit (modified from [239]).

b) 2-element Windkessel model (modified from [239]).

Figure 5.7: Windkessel model and relationship to electrical circuit.

The blood flow is only continuous because of the compliance of the aorta, although the human heart acts as a pulsatile pump. The description of the human heart and the systemic arterial system as closed hydraulic circuit is done by the Windkessel model, which is commonly used to represent the load of the heart by the vascular system [239]. For instance, the simplest form of the Windkessel model, the 2-element model, is illustrated in Fig. 5.7b, where the peripheral circulation, which is assumed to be a pure flow resistance (peripheral resistance) [236], is modeled as a resistor R and the arterial compliance is represented as a capacitor C. The model can be described by Eq. 5.6 [145]. Two major limitations of the Windkessel model are the assumption of infinite pulse-wave velocity (PWV) and the separation of conduit and cushioning function [221]. However, as discussed later, the Windkessel model is also been used in several approaches for blood pressure estimation.

$$\Phi(t) = \frac{dP(t)}{dt} C + \frac{P(t)}{R} \tag{5.6}$$

An overview of the main systemic arteries in the human body is illustrated in Fig. 5.8. Since no single artery segment has exactly the same viscoelastic properties, it is impossible to describe the whole arterial tree by a single segment [221]. In Fig. 5.9, the muscular and elastic artery as well as the arterioles are compared by their different composed vessel walls, representing, next to the aorta, the three major types of arteries. Elastic arteries are close to the heart, containing a high amount of elastic fibers in all three tunics and are typically larger than 10 mm in diameter, while muscular arteries are farther from the heart (arms and legs) with a decreased content of elastic fibers, but a thick Tunica media for vasoconstriction, with a typically size between 0.1 mm to 10 mm in diameter [230, 236]. According to [221], the most accepted model of the arterial tree is the propagative model, which assumes a visco-elastic tube in which a forward pressure wave travels along this tube and generates retrograde waves by numerous branch points and high level resistance of the tubes end.

5.2.2 Arterial Stiffness and Pulse Wave Velocity

Arterial stiffness is an important prognostic index as well as a potential therapeutic target in patient with hypertension, and plays a major role, next to arterial pulse wave reflection, for cardiovascular outcome, independently from blood pressure [226, 227]. It is associated as a major contribution to cardiovascular events, like myocardial infarction or stroke [221]. It is generally accepted that an increased arterial stiffness causes a premature return of the reflected wave in the late systole, and thus, increases the central pulse pressure and the systolic blood pressure [221]. Additionally, a decreased vascular compliance of the large arteries results also in an increased PP, with higher SBP and lower DBP [240].

Thus, arterial stiffness has an influence on the Windkessel effect and on the arterial blood pressure. Furthermore, it leads to an acceleration of the pulse wave, which increases the pulse wave velocity (PWV). As indicated by [241], using the title ”Arterial Stiffness and Hypertension: Chicken or Egg?”, it is not always clear which event comes first. For example, age related arterial stiffness is mainly caused by the degeneration of elastin fibers, which are responsible for compliance, and the deposition of collagen [226], while hypertension can be seen as an accelerated form of vascular aging, which leads to aortic stiffness [241]. A higher pulse pressure at any age as well as an advanced age is predominantly associated with a larger forward pressure wave [242].

However, several methods for determination of arterial stiffness exist [226]. For example, the earlier mentioned stiffness index SI, derived from the PPG curve shape, is related

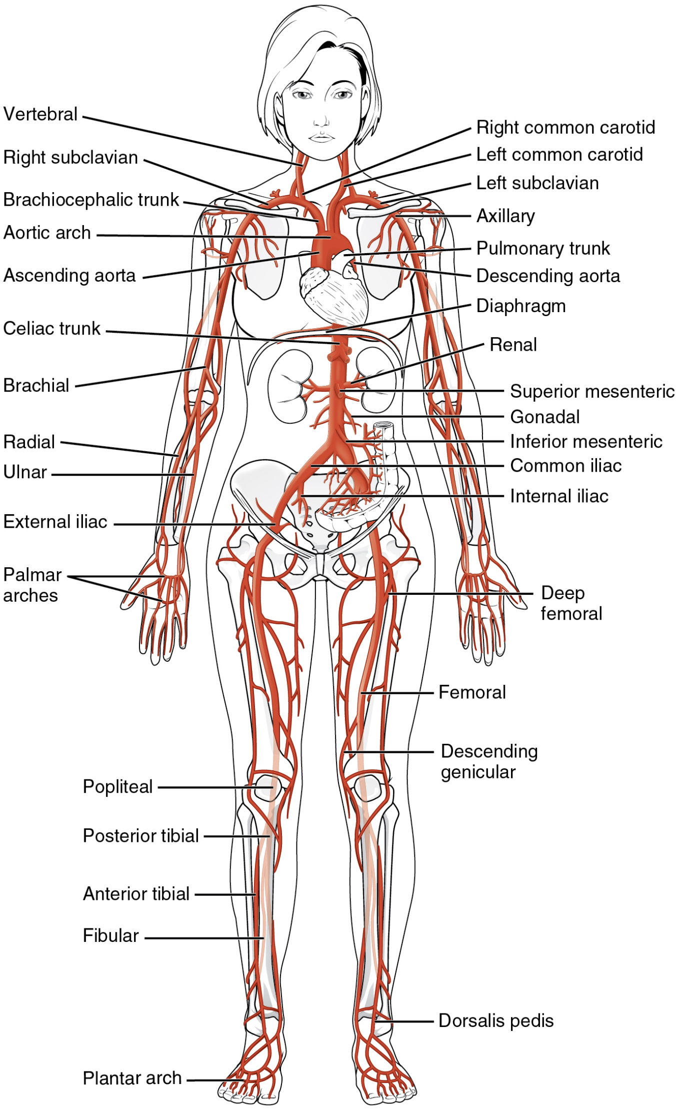

Figure 5.8: Overview of major systemic arteries of the human body [230].

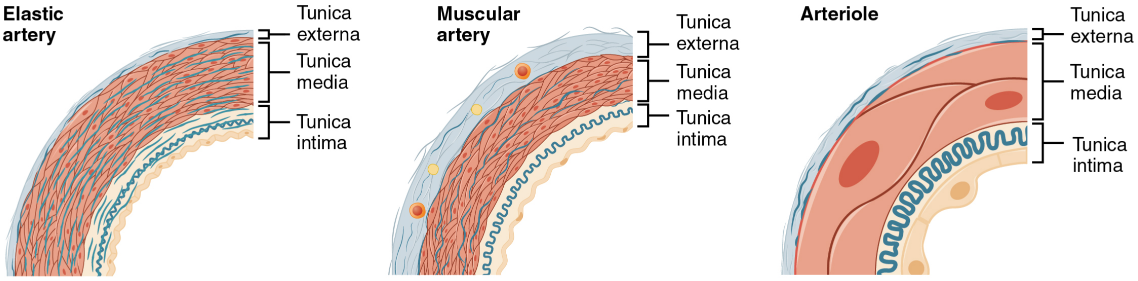

Figure 5.9: Comparison of elastic and muscular artery as well as arteriole [230].

to the larger arterial stiffness (See Sec. 4.3.1, (p. 83)). The gold standard for determining arterial stiffness is the measurement of the carotid-femoral pulse wave velocity (cf-PWV), which is usually done by the foot-to-foot method, meaning the foot of the wave and illustrated in Fig. 5.10, where a time delay between the wave forms of the two used arteries (carotid and femoral) is measured, indicated as Δt [221, 222]. This time delay is also called pulse transit time PTT and means the time that the pulse wave requires to travel a length L between two points in the artery tree, and thus, leads to the general definition of the PWV in Eq. 5.7.

$$PWV = \frac{L}{PTT} \tag{5.7}$$

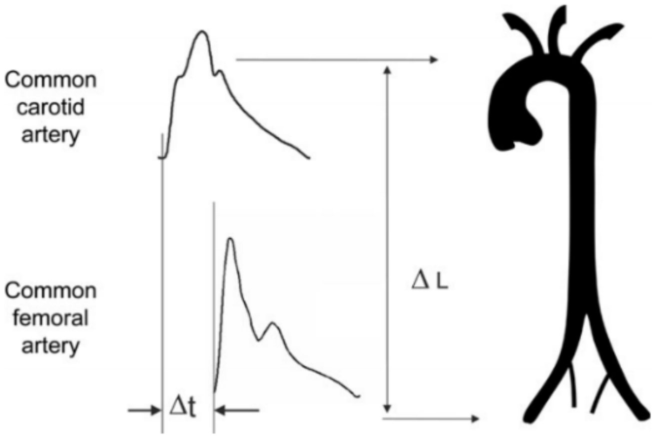

Figure 5.10: Measurement of cf-PWV by foot-to-foot method [221].

A higher aortic stiffness, measured by PWV, is generally associated with the increased risk of the first CVD [243]. The PWV increases appreciable with age, especially, after midlife [241]. This circumstance is also shown in Fig. 5.11, where the normal values of the PWV are illustrated. These values were derived in a study from [222], where reference and normal values of PWV were established in an extensive amount of 16867 subjects in the European population. They also presented the PWV reference values of different blood pressure categories, shown in Fig. 5.12, where an increased PWV due to increasing age as well as increasing blood pressure can be recognized. Thus, the PWV represents a source of information for arterial stiffness and arterial blood pressure.

The measurement of the cf-PWV represents a method of regional PWV determination [244], which only provides the average PWV over a long measurement length, consisting of segments with different mechanical characteristics, and can not evaluate biomechanical

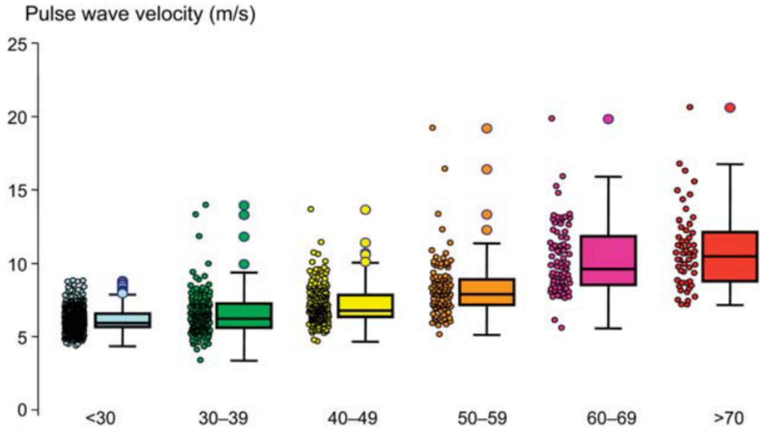

Figure 5.11: Normal values of PWV (average according to age) of 1455 subjects [222].

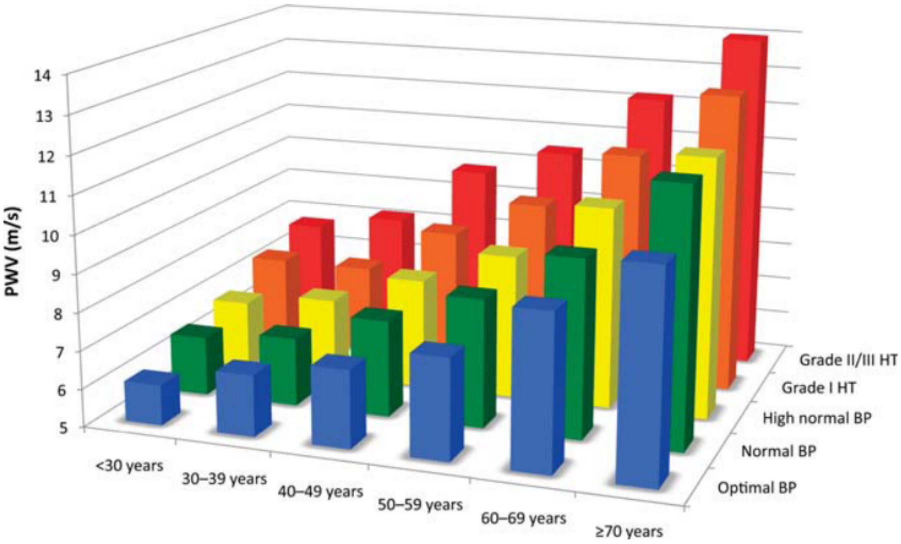

Figure 5.12: Reference values for PWV (mean values according to age and blood pressure (bp) categories) of 11092 subjects [222].

properties in small segments as well as information about the local of arterial abnormalities [245]. Next to the regional PWV, another method is known as local PWV measurement and represents the detection of the PWV over a small arterial segment, which avoids the approximation of the distance, done in the regional measurement [221, 244]. As mentioned before, no single segment of the whole artery tree can be used to describe them all. It should be considered that peripheral arteries in healthy subjects are significant stiffer as central arteries, which leads to an increase of the amplitude of the pressure wave from the heart to the periphery, which is also known as pressure amplification [221]. Considering the regional PWV measurement, this circumstance misrepresents the values of the local PWV due to the large heterogeneity of the arterial wall at different sites [244]. Furthermore, the local arterial stiffness is used for mechanical analyses in pathophysiology, pharmacology, therapeutic, and epidemiological studies [221] and plays a major role in optical blood pressure estimation.

Next to the former definition, the PWV can also be described by the Moens-Korteweg equation, shown in Eq. 5.8, where the velocity with which the pressure wave is propagating, is related to the Young‘s modulus E of the vessel wall, the wall thickness h, the inner radius of the vessel r, and the density of blood ρ, and thus, the PWV depends on the elastic properties of the artery and blood [246].

$$PWV = \sqrt{\frac{Eh}{2r\rho}} \tag{5.8}$$

Next to the Moens-Korteweg equation, the Bramwell-Hill model describes the PWV in terms of the vessel distensibility, is shown in Eq. 5.9, and thus, connects the PWV to the vessel strain, pulse pressure, and blood density [247, 248] as well as the compliance C [235, 248]. The arterial distensibility D, earlier defined in Eq. 5.3 (p. 115), can also be described by Eq. 5.10 [221, 247], where the systolic and diastolic diameter D_s and D_d are illustrated in Fig. 5.13a, while the relationship between the BP and the diameter as well as between the BP and the volume change is shown in Fig. 5.13b. Furthermore, D is related to the change of the stroke volume ΔA and the pulse pressure PP [221].

$$PWV = \sqrt{\frac{1}{\rho D}} = \sqrt{\frac{V}{\rho C}} \tag{5.9}$$

$$D = \frac{D_s^2 - D_d^2}{D_d^2 \cdot PP} = \frac{\Delta A}{A \cdot PP} \tag{5.10}$$

5.2.3 Blood Pressure Measurement

This section should only give a short overview about currently used non-invasive blood pressure measurement methods, since the main focus of this chapter is on the optical blood pressure estimation. First of all, the currently used gold standard methods for standard blood pressure control and for the use of a pressure holster are the well known auscultatory and oscillometric method [228]. Both are measuring the BP discrete in time and are illustrated in Fig. 5.14, where the auscultatory method is based on Korotkoff‘s sounds, in

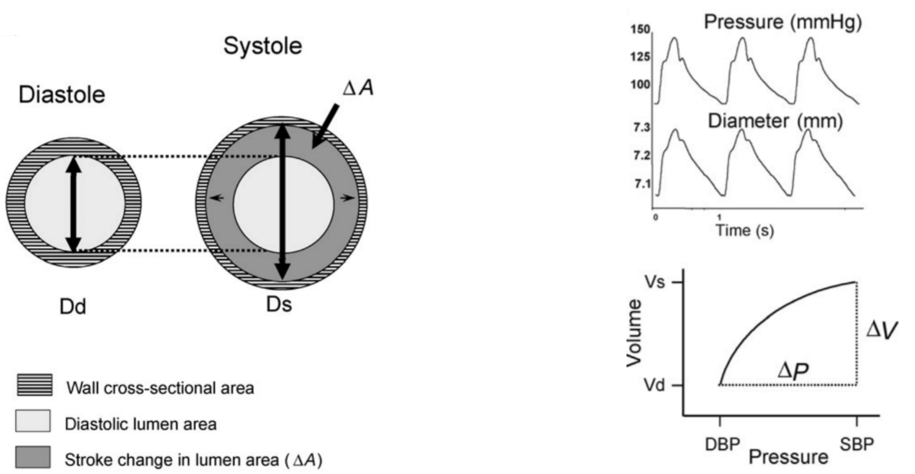

a) Representation of stroke change ΔA in lumen cross section.

b) Relationship between BP and diameter, and BP and volume.

Figure 5.13: Definition of the local arterial distensibility D (modified from [221]).

which their beginning (first heart sound) represents the SBP value and their ending (last heart sound) represents the value of the DPB [228, 230]. This method is also known as Riva-Rocci‘s method [157]. The oscillometric method measures the pressure oscillations, which are transmitted onto the cuff [228]. At the beginning, the artery is fully closed by the cuff and only small oscillations are recognized, while after an automatical decrease of the cuff-pressure, which leads to an opening of the blood vessel, higher oscillations are detected after a decrease of the cuff-pressure under the SBP value, where the maximum amplitude appears, when the cuff-pressure equals the mean arterial blood pressure (MAD) and the DBP value is reached by a further drop of the cuff-pressure, when the oscillations stay constant [249].

By the way, a not commonly used method, called tonometry, also exists, where a controlled force is applied orthogonally on the wall of the artery against the bone, and which is highly sensitive to motion and ideally used at a resting position [228].

A continuous and non-invasive measurement method is represented by the volume clamp method, also called vascular upload technique, which was introduced by Penaz in 1973 [250, 251] and further developed and made commercially available in different implementations, for example, provided by CNSystems Medizintechnik GmbH (Graz, Austria)[1]. As shown in Fig. 5.15, a PPG signal is measured on the finger and a pressure controller is regulating the pressure on the cuff until the PPG wave stays constant [249]. So, the

---

[1] https://www.cnsystems.com

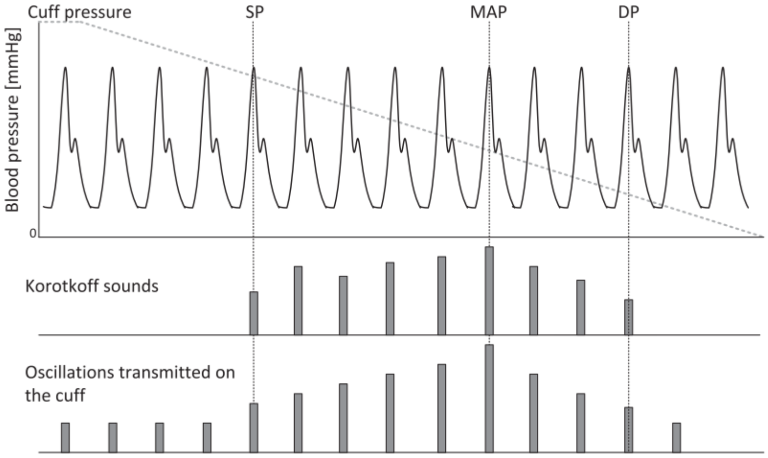

Figure 5.14: Principle of auscultatory (Korotkoff's sounds) and oscillometric BP measurement methods [228].

PPG does not measure the blood pressure directly, it rather indicates the changes of the arterial volume change, which represents the basis for the blood pressure determination [228]. When the blood volume is constant, the pressure under the cuff is equal to the blood pressure value, because the applied pressure from outside the finger corresponds to the intra-arterial pressure [251].

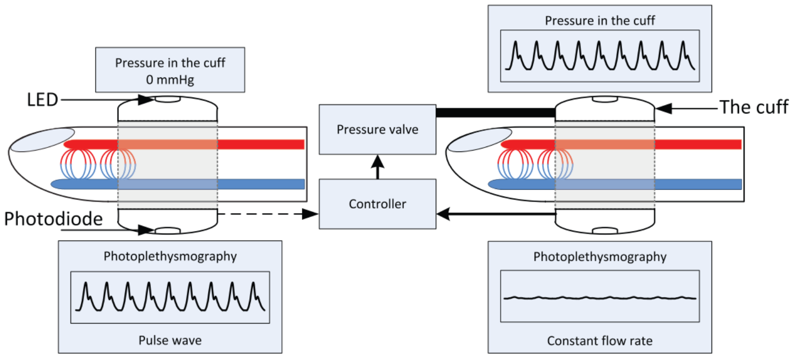

Figure 5.15: Principle of volume clamp method, where a low cuff-pressure causes a fully PPG signal (left), while a balanced pressure on the cuff leads to a constant PPG curve (right) [228].

Another possible way to determine the blood pressure is represented by the cuff-less method of measuring the PWV along the arterial tree and is often called ”Pulse transit time” method [228]. It builds the basis for the optical blood pressure estimation and will be discussed in the next section.

5.3 Optical Blood Pressure Estimation

In this section, common approaches of cuff-less and non-invasive blood pressure measurement methods are being described. They are based on optical detection of blood-pressure-related information, combined with mathematical models, which are using the described mechanical approaches of the last section. A general overview of the most commonly used methods to predict the blood pressure non-invasively, without the need of a cuff, is illustrated in Fig. 5.16, where next to the mentioned ”Time Delay” method, represented either by the delay between two PPG signals or between a PPG and an ECG signal, an analysis of the PPG waveform and other approaches leads to the resulting estimated blood pressure.

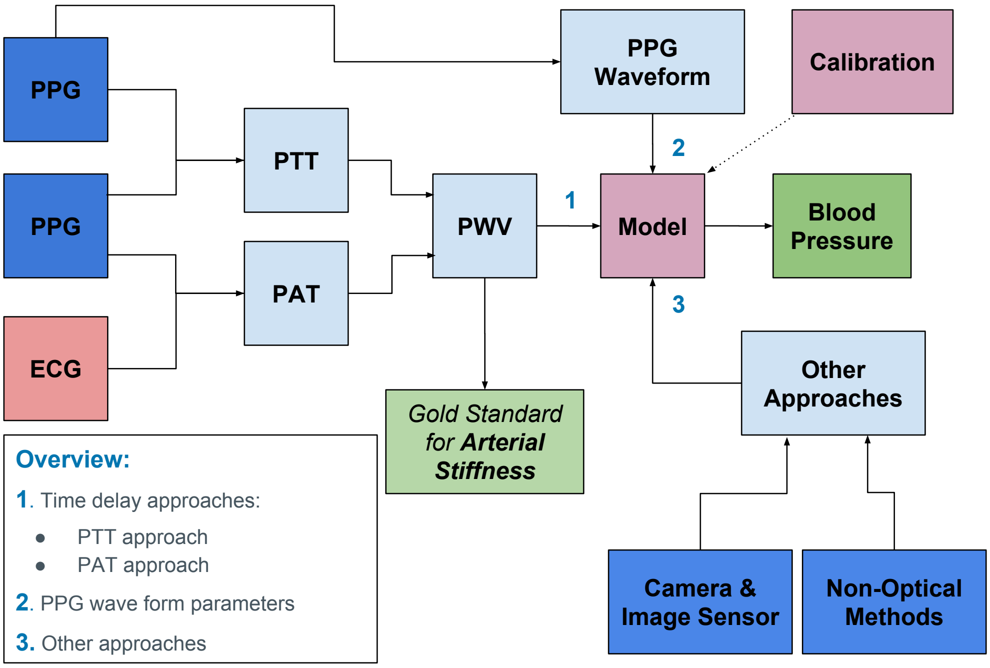

Figure 5.16: Overview of cuff-less and non-invasive blood pressure measurement.

5.3.1 Blood Pressure Estimation Models

A commonly used approach is based on the Hughes model [252], shown in Eq. 5.11, which relates the Young‘s modulus of a blood vessel E and E_0 (under non-pressure on the wall) with the pressure P in the vessel, which equals the desired blood pressure BP, and a constant α.

$$E = E_0 e^{\alpha P} = E_0 e^{\alpha \cdot BP} \tag{5.11}$$

Combining the Hughes model (Eq. 5.11) with the Moens-Korteweg equation (Eq. 5.8 (p. 120)) and the general definition of the PWV (Eq. 5.7 (p. 118)), leads to the resulting logarithmic blood pressure model in Eq. 5.12 [246]. In terms of general model descriptions, the logarithmic model is rewritten in Eq. 5.13, where a and b are subject-specific parameters, which are obtained by regression analysis [253]. As described later, the pulse transit time PTT is often misunderstood and wrongly interpreted, resulting in a mix-up and a surrogation by the pulse arrival time PAT. Thus, the term "Time Delay" was adapted from [253], which represents either the PTT or the PAT.

$$BP = -\frac{2}{\alpha}\ln PTT + \frac{1}{\alpha}\ln\frac{2r\rho L^2}{hE_0} \tag{5.12}$$

$$BP = a\ln(\text{Time Delay}) + b \tag{5.13}$$

A review of currently used BP estimation models was done by [253], where they introduced, next to the mentioned logarithmic model, four other general types of estimation models for the mathematical relationship between BP and a measured time delay. These models are summarized in Tab. 5.2. The linear model assumes a negligible change in artery thickness and diameter during pressure [254], while at the inverse squared model the artery is a rigid pipe, where the moving pressure wave can be written in terms of their kinetic energy, which depends on the PWV, the parameter $A = (0.6 \cdot \text{Subjects Height})^2\frac{\rho}{1.4}$, and B, which is determined by calibration [255]. This model was modified by [256], resulting in the modified inverse square model. The last mentioned model assumes an inverse relationship between the BP and the time delay [257]. Also, other approaches were mentioned, considering combinations with additional model parameters such as heart rate or PPG intensity ratio PIR, where the last one is a derivate from the PPG curvature.

Generally, the used model parameters are determined by using a calibration model with reference BP values, which are commonly measured with a gold standard method. All these calibration models translate the time delay or another BP-related parameter to BP, and are mainly based on the Moens-Korteweg equation, heuristic modeling with regression, or predictive modeling with data-driven methods like machine learning [262]. Nevertheless, other approaches estimate the blood pressure without the need of calibrated model parameter, resulting in a higher error.

Type	Equation	Source
Logarithmic model	$BP = a\ln(\text{Time Delay}) + b$	[197, 246, 258]
Linear model	$BP = a(\text{Time Delay}) + b$	[182, 254]
Inverse squared model	$BP = \frac{A}{\text{Time Delay}^2} + B$	[255]
Inverse squared model (modified)	$BP = a + (\frac{b}{\text{Time Delay}-c})^2$	[256]
Inverse model	$BP = \frac{a}{\text{Time Delay}} + b$	[257, 259–261]

Table 5.2: Overview of general BP models (adapted from [253]).

5.3.2 Pulse Transit Time (PTT) vs. Pulse Arrival Time (PAT)

The two terms pulse transit time (PTT) and pulse arrival time (PAT), which both indicate a time delay in the cardiac cycle, are often mixed up in literature and used the wrong way, resulting in a surrogation of the PTT by the PAT ([182, 246, 255, 262–265]).

The definition of the PTT is shown in Fig. 5.17, measured as the delay between the aortic valve opening (AO), derived from the seismocardiogramm (SCG), and the arrival of the pulse pressure wave on a distal artery, commonly the fingertip, while the PAT is defined as the distance between the R-peak of the ECG and the mentioned distal point [266]. It can be seen that the PTT and PAT are not equal, since a pre-ejection period (PEP) is also present at the PAT, but the PAT can be assumed as sum of PTT and PET (Eq. 5.14) [228, 267, 268].

$$PAT = PTT + PEP \tag{5.14}$$

Since both pulse times are commonly used in BP estimation, the study of [266] compared the use of the PTT and PAT on five healthy subjects in case of five minutes standing (REF) as well as five minutes pedaling at 100 W (R100), illustrated in Fig. 5.18. Additionally, the authors showed the relationship between PAT and PTT in case of pedaling, rated by their coefficient of determination after linear and parabolic regression, which is shown in Fig. 5.19. They concluded that the difference between PTT and PAT is subject-dependent and that a linear relationship between PAT and PTT could be strengthened by removing the fastest components of their variabilities. Moreover, it was mentioned that if there is an influence of the PEP on the PAT, it occurs most likely in the short term components of PAT variability.

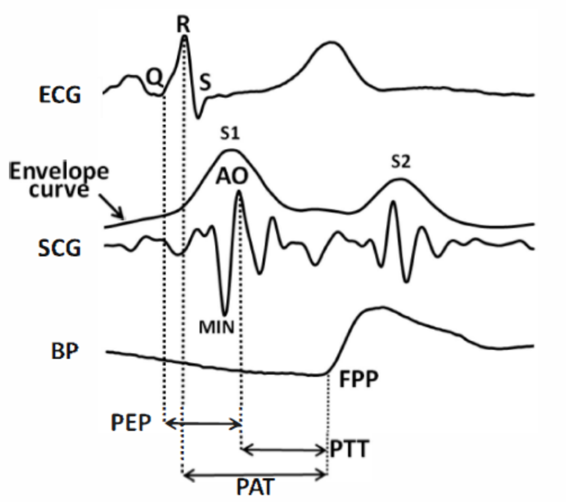

Figure 5.17: Definition of pulse times and time intervals [266].

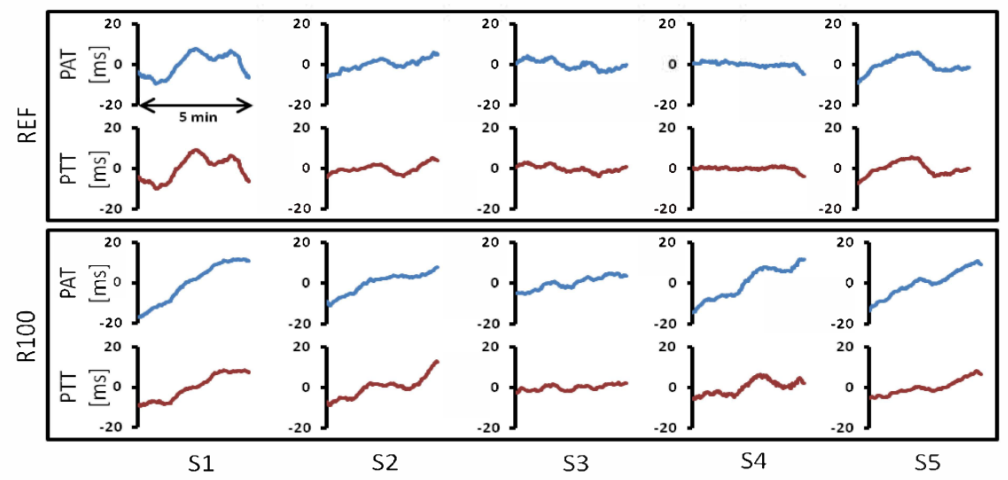

Figure 5.18: PAT and PTT from five subjects over a time of five minutes during resting (top) and pedaling (bottom) (mean value already removed) [266].

However, although the PTT and PAT can be perceived as equal, the major focus was kept on purely optical blood pressure approaches, which means BP prediction without the need of an ECG, and thus, the implementation of two PPG sensors over a known distance of a vessel.

5.3.3 Pulse Transit Time (PTT) Measurement

Since the PTT also describes the temporal offset between two PATs at two different locations along a blood vessel, shown in Fig. 5.20 [269], the measurement of two PPG signals

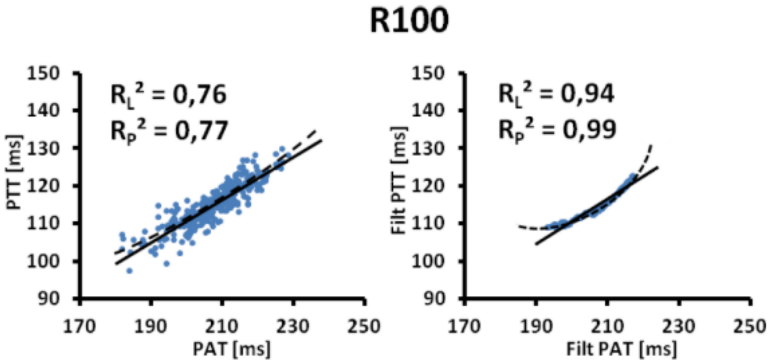

Figure 5.19: Relationship between PAT and PTT during pedaling before (left) and after (right) filtering with coefficient of determination computed by linear (R_L^2) and parabolic regression (R_P^2) [266].

along a known distance represents the basic idea of optical BP estimation. Thus, the principle of measuring a time delay between two distinct locations, separated by a distance and the further calculation of the PWV, can be realized by a dual-channel PPG and represents next to the PAT measurement, which needs an ECG as second input, a fully optical way to estimate the blood pressure. The basic idea of a BP sensor is shown in Fig. 5.21a, where a dual-channel PPG is integrated on a chip. For the determination of the PTT, the time delay between the two PPG signals would be measured as shown in Fig. 5.21b.

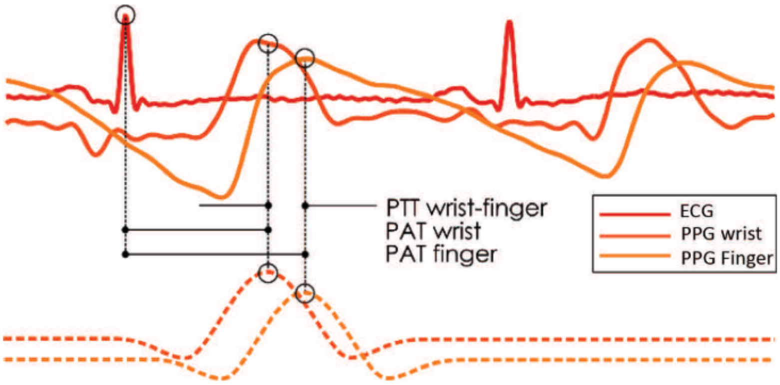

Figure 5.20: Comparison between PAT and PTT for optical blood pressure estimation [269].

In the study of [270], the PTT was measured by two PPG signals, which were separated 10 mm, shown in Fig. 5.22a. The sensor was placed on the radial artery of the index finger and the PTT of 13 healthy subjects was measured as well as the PWV was calculated as an average of ten cardiac cycles. They observed a minimum and maximum SD of 2.6 ms and

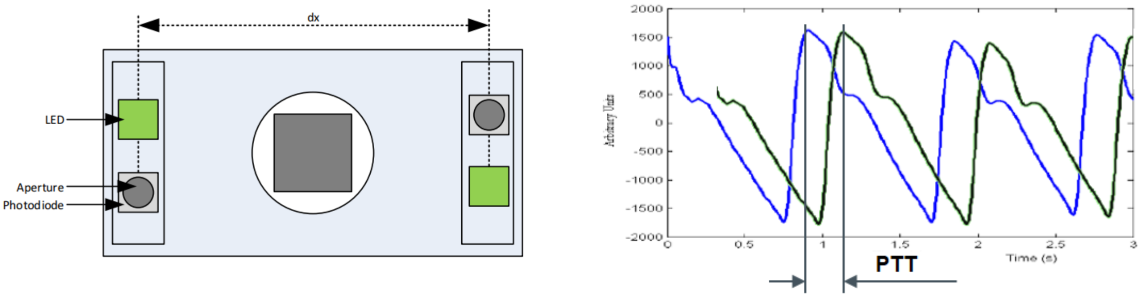

a) Dual-channel PPG on a chip. **b)** PTT determination.

Figure 5.21: Basic idea of BP sensor using dual-channel PPG.

0.4 ms respectively for a single volunteer. The mean PTT of all subjects was 10.1 ms and the calculated PWV was 1.1 m/s. The system was validated by a time-shifted sinusoids as input signal. The authors concluded that the circuit could response to small variation in PTT and that there is a possible use for continuous BP measurement as well as for monitoring of arterial stiffness.

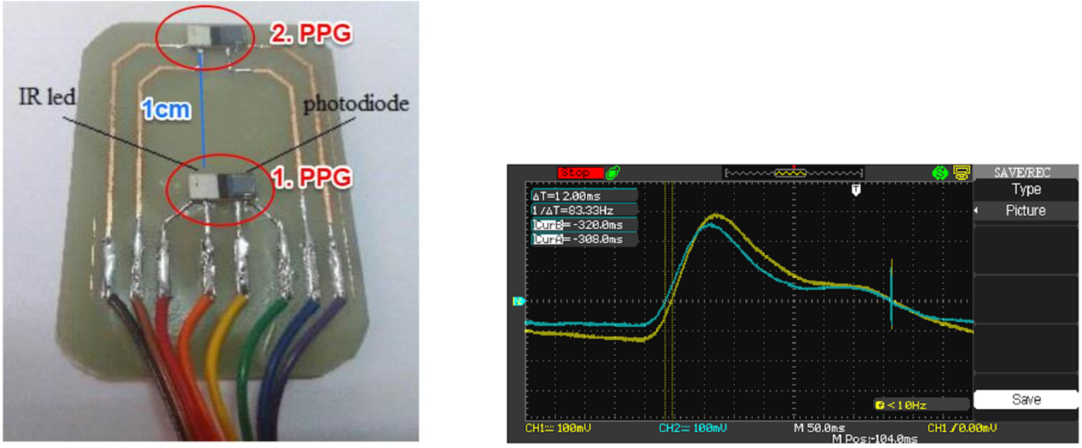

a) Dual-channel PPG. **b)** PTT measurement.

Figure 5.22: PTT measurement using dual-channel PPG (modified from [270]).

In another study, the authors [271] were determining the PTT in a similar way by measuring two PPG signals between a distance of 28 mm on the local carotid artery of ten healthy subjects. The design as well as the placement of the used PPG probe are illustrated in Fig. 5.23, and the used block diagram with the hardware and signal processing units is shown in Fig. 5.24. The resulting PTT curves of one subject are shown in Fig. 5.25, while the PWV of all subjects was measured with 2.64 ± 0.72 m/s as well as a maximum beat-to-beat variation of 16% was achieved. Again, the authors concluded a potential usage in

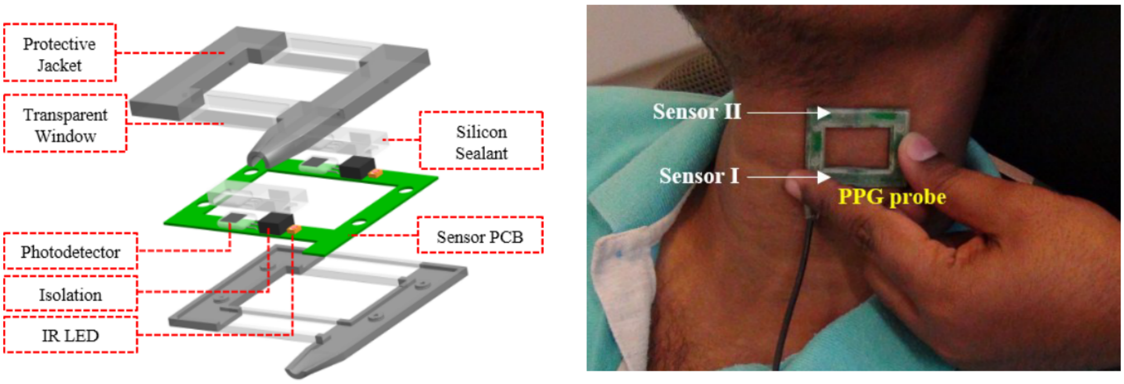

Figure 5.23: PTT measurement on local carotid artery using dual-channel PPG [271].

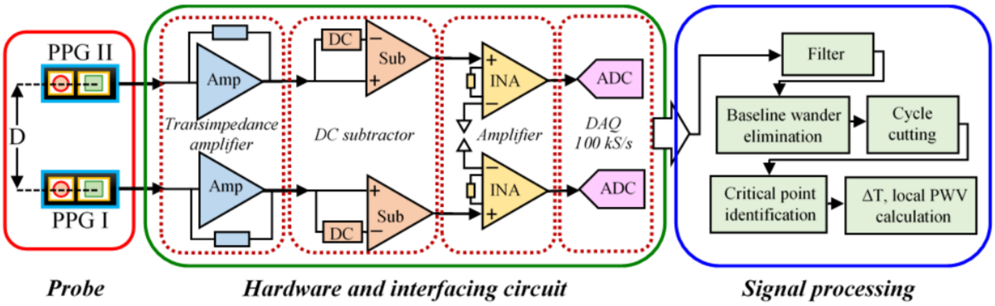

Figure 5.24: Block diagram of local PWV measurement [271].

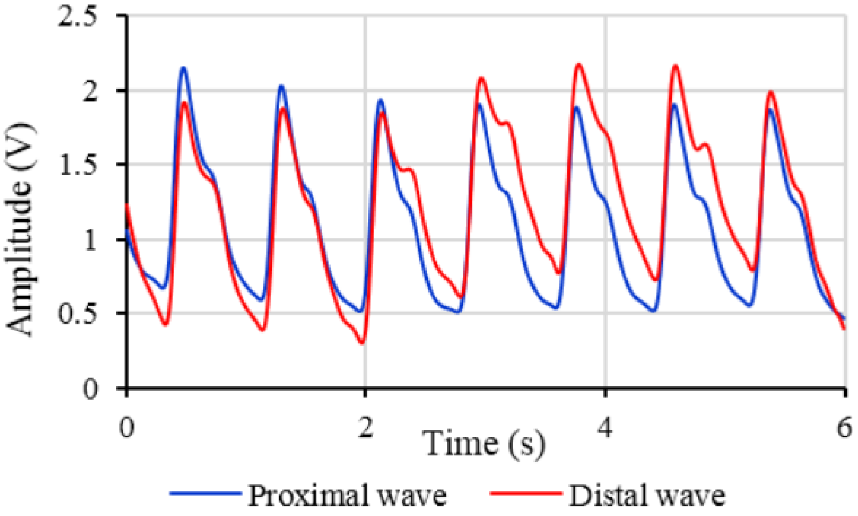

Figure 5.25: Dual-channel PPG of one subjects [271].

cuff-less BP measurement and its clinical application.

The authors of [272], presented a PPG probe, shown in Fig. 5.26, using a single infrared light source to measure the local PWV. A block diagram of their measurement process is illustrated in Fig. 5.27. They tested their approach in an in-vivo study with 35 volunteers where the local carotid PWV, the carotid-to-finger PWV as well as the PAT at the carotid artery were measured simultaneously. They mentioned a resulted accuracy of the proposed system with a repeatability, beat-to-beat variation of 4.15 % to 11.38 %, and reproducibility of measurement as correlation between two test trails of r = 0.96. Additionally, they mentioned that it was possible to detect high-fidelity BP signals (SNR $\approx$ 28 dB) from small sections of the carotid artery. The simultaneously measured PWV values were compared as marker of BP, where the proposed system has a slightly better performance in terms of SBP (r=0.74), DBP (r = 0.77), and MAP (r=0.78) tracking.

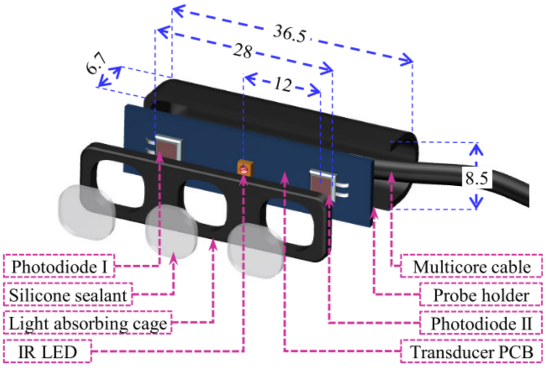

Figure 5.26: PPG transducer for PWV measurement (all dimensions in mm) [272].

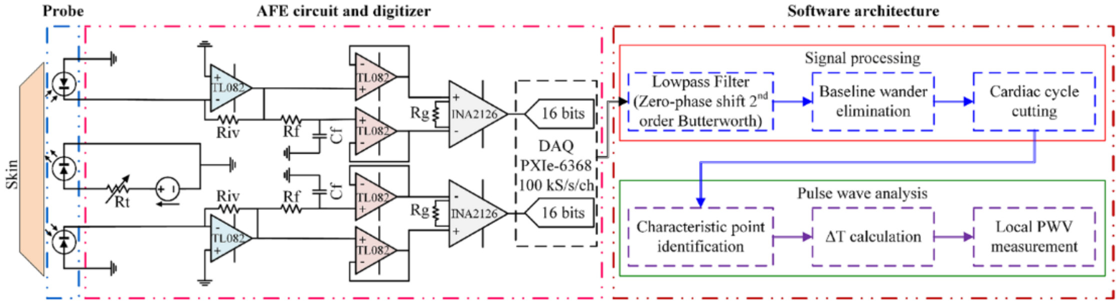

Figure 5.27: Block diagram of local PWV measurement [272].

The authors [273] tested PWV determination on the finger by using a Si PIN S8558 photodiode array (Hamamatsu Photonics, Japan), shown in Fig. 5.28, and measuring the PTT between the first and the last (16th) photo-diode with 625 nm and 880 nm LEDs as light source. They achieved a PWV of 1.1 ± 0.2 m/s in an in-vivo pilot study as baseline, where the applicability of the MPA in practice was illustrated by applying it on the right finger of a healthy subject and using the flow-mediated dilation (FMD) technique. In order to do this, the subject was sitting on a chair, while a BP cuff, placed on the upper arm, was inflated to 150 mmHg to block the blood flow to the lower arm, and released instantly after five minutes. The resulting pulse wave amplitude and PWV, averaged over each 30 s, are shown in Fig. 5.29. The resulted response of the pulse wave amplitude agreed with the used guidelines for ultrasound assessment of endothelial-dependent FMD of brachial artery from [274], resulting in an increase of the amplitude during the FMD. It was possible to measure the PWV with a maximum deviation of 3.0 %. Once again, a potential usage for local PWV was mentioned.

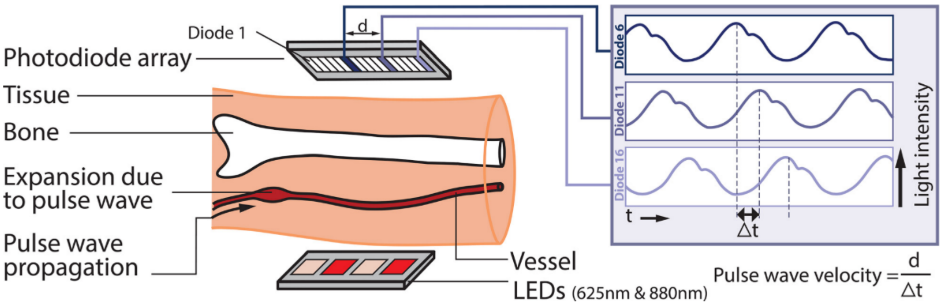

Fig. 1 Schematic overview of the MPA and calculation of the PWV

Figure 5.28: PWV measurement using multi-photodiode array (MPA) [273].

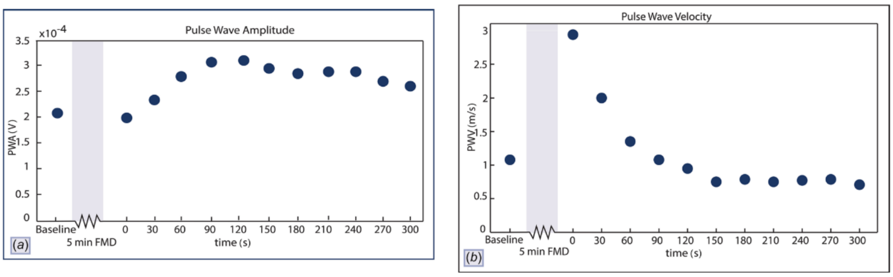

Figure 5.29: Pulse wave amplitude (left) and PWV (right) before and after FWD method (modified from [273]).

Considering non-optical approaches, the PTT was also measured by using a seismocardiogram (SCG) and an audio sensor [275, 276], a balistocardiogram (BSG) [276–279], and hall sensor devices [280] as second source next to the PPG sensor as well as with laser Doppler vibrometer [281].

5.4 Selected Methods of Optical Blood Pressure Estimation

In the study of [246], the logarithmic model was modified by adding the heart rate HR and the previous BP value BP_{n-1} as additional parameters. The resulting model is shown in Eq. 5.15, where the term PAT was used instead of the originally used PTT due to a wrong interpretation of the pulse transit time, since they used an ECG and a PPG for measurement. The parameters a, b, c, and d were calculated by using least square methods.

$$BP_n = a \ln PAT + b \cdot HR + c \cdot BP_{n-1} + d \tag{5.15}$$

The authors validated their method by using ECG, PPG, and BP data of six subjects from the MIMIC database, where the data was split into 10 equal sets. Nine sets were used for training and one set was used to test the regression model. The resulting estimated values for SBP and DPB as well as the estimation errors are illustrated in Fig. 5.30.

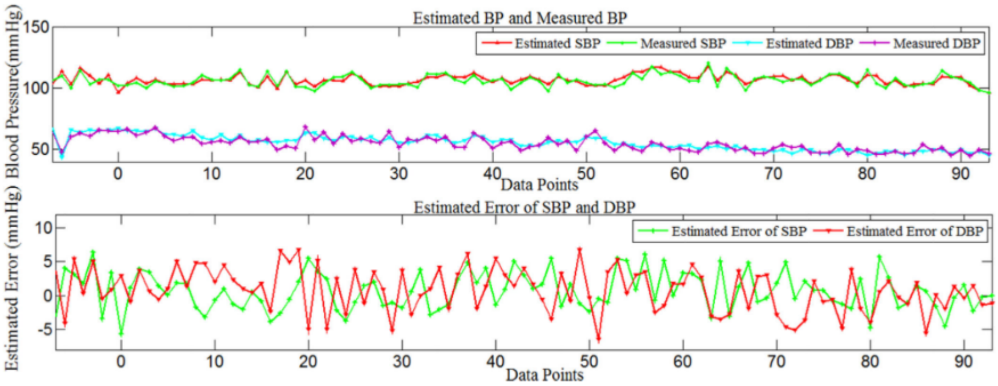

Figure 5.30: Measured and estimated SBP and DBP values as well as the estimation errors from [246].

Another usage of the logarithmic model (Eq. 5.12) was done by [197]. Since the authors were building a dual-channel PPG measurement system for in-vivo BP estimation, the term PTT was used in the right way. An overview of the equipment is shown in Fig. 5.31, where two PPG signals were measured on the forearm, separated by a distance of 17 cm. The used framework of their algorithm is shown in Fig. 5.32, where two PPG signals and three acceleration values were used for motion decision, which was finally used as input for singular spectrum analysis (SSA) to remove motion artifacts. Based on the determined peripheral PTT (PPTT) and the model parameter of the calibration model, the estimated

BP value was calculated. They used no continuous beat-to-beat BP monitoring, rather the calculated the average PTT over a minute. They tested their prediction on 30 healthy subjects, standing in five different arm positions and during walking, where an one-minute PPG was logged and a three minute rest was done between each position. The experiment was separated into calibration and validation, where the BP was calibrated in the first stage for each subject for three hours, and the validation was done four hours later for a two hour execution of the mentioned exercises. A performance comparison is illustrated in Fig. 5.33, showing the Pearson correlation coefficient (r = 0.75 for SBP and r = 0.78 for DPB) as well as the Bland-Altman plot between the estimated and reference BP value. The mean absolute difference (MAD) was 7.61 mmHg and 6.82 mmHg for SBP and DBP, respectively.

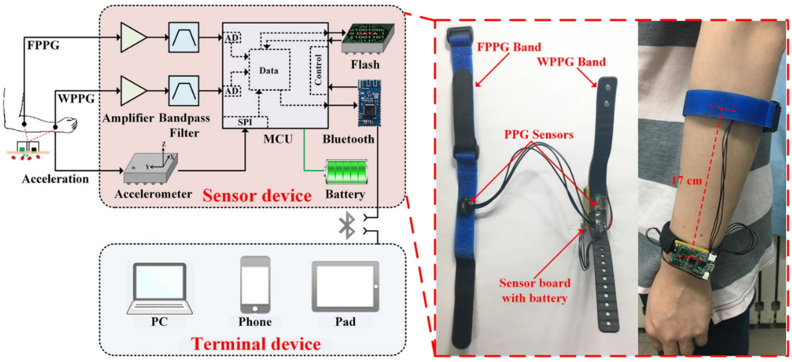

Figure 5.31: Dual-channel PPG for blood pressure estimation [197].

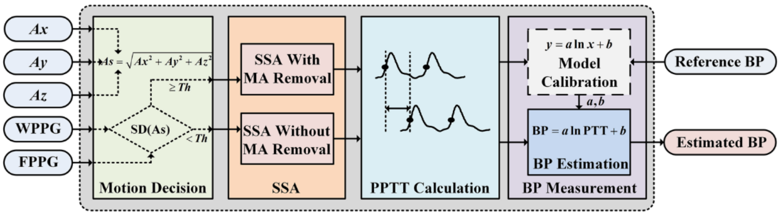

Figure 5.32: Framework of BP estimation algorithm [197].

A linear model approach was used in the study from [182]. The authors used four different wavelengths (IR (940 nm), yellow (590 nm), green (570 nm), and blue (470 nm)) for PPG (Fig. 5.34a) as well as an ECG signal as input for a multi-layer tissue model, which delivers the differential PTT ΔPTT, shown in Eq. 5.16, as a parameter of the estimation model for the SBP. The parameters k and b were obtained by linear regression, using a

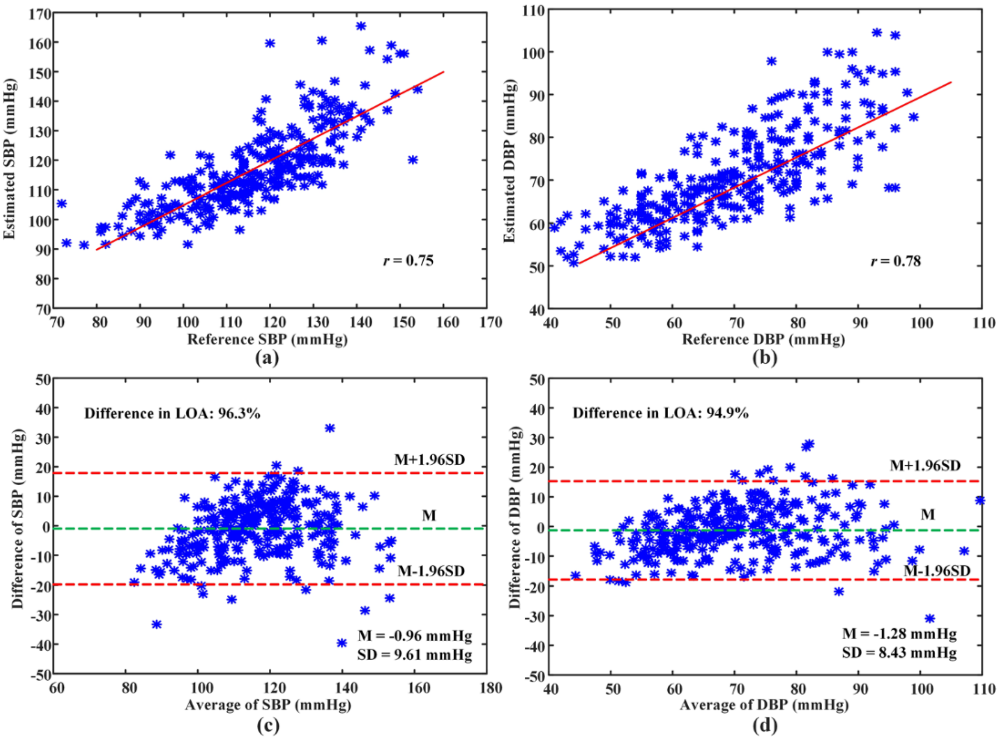

Figure 5.33: Pearson correlation (top) and Bland-Altman plot (bottom) between estimated and reference SBP (left) and DBP (right) of all subjects [197].

reference SBP.

$$\Delta SBP = k\Delta PTT + b \tag{5.16}$$

The tissue model was realized for two and for three layers, shown in Fig. 5.34b, and was used to extract arterial blood pulsation by considering the wavelength-dependency of light penetration in skin tissue, and thus, to remove the capillary pulsation, represented by short wavelengths, from the long wavelengths by using absorption weighting factors. An overview of this prediction method is illustrated in Fig. 5.35, where the general workflow (top) and the used signals (bottom) are linked with each other.

The model is based on the modified Beer-Lambert law (see Eq. 2.36, p. 21), where the authors approximate the differential path-length $L = \frac{\partial A_0}{\partial \mu_a}$ by the mean path-length of the diffusing photons, traveling from the source to the detector (Eq. 5.17). They assumed that the differential absorption coefficient $\Delta\mu_a(t)$ is proportional to the optical density, shown in Eq. 5.18, where i denotes the layer number, ΔC_i means the change of volume fraction of blood from the baseline state in layer i, and ε_b and ε_t represent the absorption coefficients

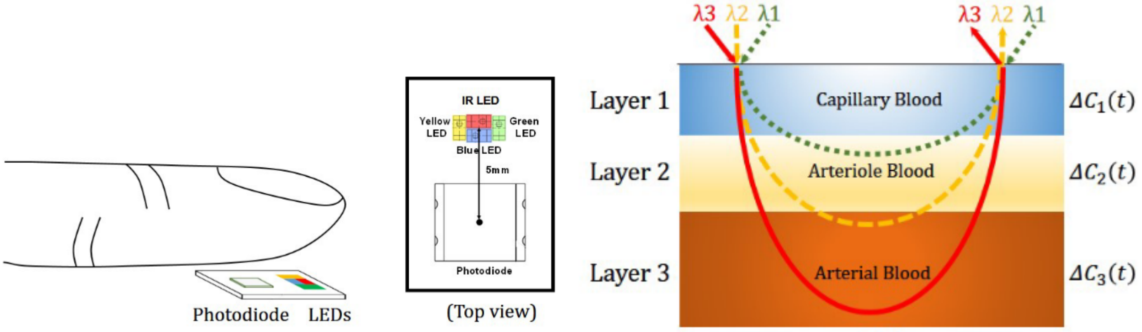

a) Multi-wavelength PPG probe. **b)** Multi-layer tissue model.

Figure 5.34: Multi-wavelength PPG for SBP estimation using four wavelengths and a multi-layer tissue model [182].

of the blood and the background tissue, respectively.

$$\Delta A(t) \approx L\Delta\mu_a(t) \tag{5.17}$$

$$\Delta\mu_{ai}(t) = (\varepsilon_b - \varepsilon_t)\Delta C_i(t) = \varepsilon'\Delta C_i(t) \tag{5.18}$$

$$\Delta A(t) = \sum_{i=1}^{N} K_i^{\lambda} L_i \varepsilon' \Delta C_i(t) \tag{5.19}$$

The general intensity variation for a N-layer tissue model is shown in Eq. 5.19, where K_i^{λ} means the depth proportion of each layer with a specific wavelength, and $K_i^{\lambda} = 1$ for layer 1 to N-1 and $0 \leq K_i^{\lambda} \leq 1$ for layer N. Thus, the short wavelengths might not travel through all layers. In case of a two-layer model, they assumed $K_2^{\lambda_1} \approx 0$ and $K_2^{\lambda_2} = 1$, resulting in Eq. 5.20, where W is a subject-dependent weighting factor delivered from calibration, since $\Delta A_{\text{diff}}(W,t) \propto \Delta C_2$. The solution for the three-layer model is shown in Eq. 5.21, resulting in two weighting factors (P, Q).

$$\Delta A_{\text{diff}}(W,t) = \Delta A^{\lambda_1}(t) - W\Delta A^{\lambda_2}(t)(t) \tag{5.20}$$

$$\Delta A_{\text{diff}}(P,Q,t) = \Delta A^{\lambda_3}(t) - P\Delta A^{\lambda_2}(t) - Q\Delta A^{\lambda_1}(t) \tag{5.21}$$

As shown in Fig. 5.35, the values for PTT can either be determined as difference between the reference signal (ECG) and the infra-red PPG (IR_PTT), or between the reference signal and the differential PPG (D_PTT), delivered from the multi-layer tissue model, where D2_PTT refers to the use of a two-layer and D3_PTT to a three-layer model. The optimal ability for BP tracking was achieved by using the combination of IR and green light for the two-layer model, and IR, yellow, and green for the model with three tissue layers. They tested their performance by comparing 20 subjects, using the three mentioned values of the PTT. The results are shown in Fig. 5.36, where values for MAD of 5.7 mmHg, 4.0 mmHg, and 2.9 mmHg were recorded for the use of IR_PTT, D2_PTT, and D3_PTT, respectively. The results show that the three-layer model had the best performance, but the authors mentioned that there might be a trade-off between accuracy and simplicity in practice. They also mentioned the possibility to use another pulsatile biosignal, originating from the heartbeat as reference signal, e.g. another PPG signal. In this case, the nomenclature would be correct, since in the previous case, again, the term PTT is wrongly used for meaning the PAT, which was not changed for a better clarity.

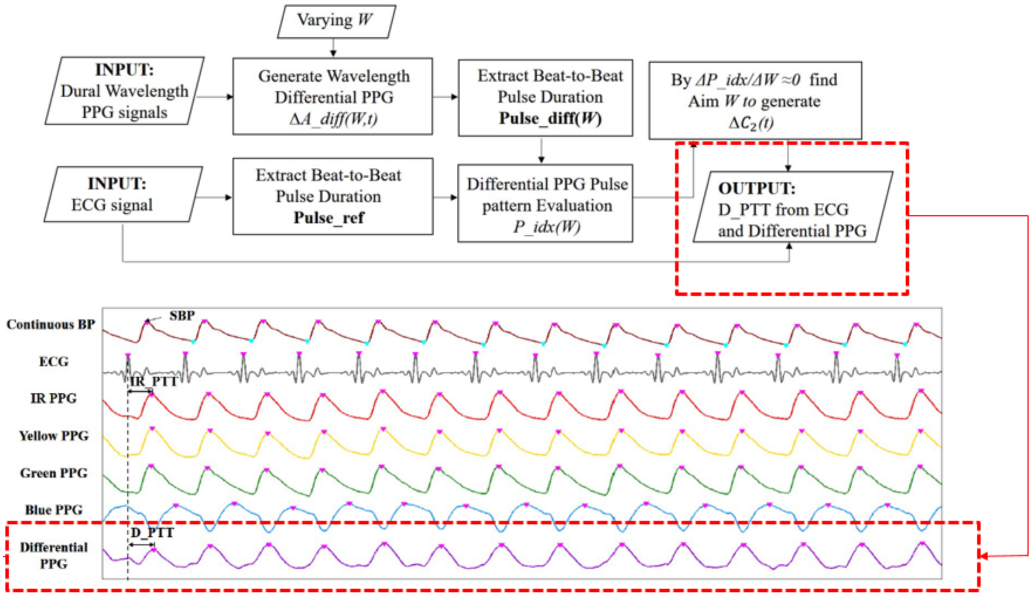

Figure 5.35: Overview of SBP prediction with multi-layer tissue model (modified from [182]).

The authors of [253] summarized 13 estimation algorithms, all based on the mentioned model types and each one applied at least one or more surveys with different time delays, where R^2 values from 0.02 to 0.97, between the predicted and the reference value were achieved. They took four algorithms, where each of them refers to one model type in Tab. 5.2, and compared them by using an online database as source for ECG, PPG, and BP. They showed that the additional consideration of the heart rate in the linear PAT-approach improved the efficiency of the model.

In the study of [262], a parameter called pressure intensity ratio PIR, was used next to PAT for the implementation of a squared BP estimation model, shown in Eq. 5.22 to

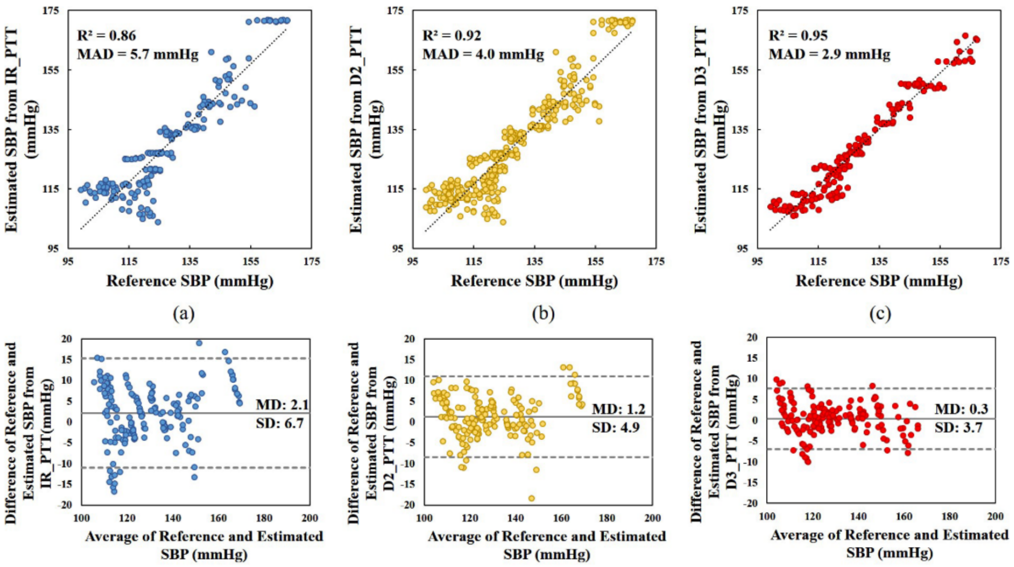

Figure 5.36: Coefficient of prediction R^2 (top) and Bland-Altman plot (bottom) of SBP estimation using IR (left), two-layer (middle) and three-layer tissue model (right) as second input signal [182].

Eq. 5.24 for the PP, SBP, and DBP, respectively. The mentioned parameter has been used in former studies [282, 283], reflecting arterial vasomotion and slow variations of the BP. The definition of the PIR is illustrated in Fig. 5.37, where this ratio is determined from the modified Beer-Lambert law (Eq. 5.25) and shown in Eq. 5.26, as ratio between the highest and the lowest light intensity.

$$PP = PP_0 \cdot \frac{PIR}{PIR_0} \cdot \left(\frac{PAT_0}{PAT}\right)^2 \tag{5.22}$$

$$SBP_i = MBP_0 \cdot \frac{PIR_0}{PIR_i} + \frac{2}{3}\frac{PIR_i}{PIR_0}\left(\frac{PAT_0}{PAT_i}\right)^2 \tag{5.23}$$

$$DBP_i = MBP_0 \cdot \frac{PIR_0}{PIR_i} - \frac{1}{3}\frac{PIR_i}{PIR_0}\left(\frac{PAT_0}{PAT_i}\right)^2 \tag{5.24}$$

$$I = I_0 e^{-(\varepsilon c V + S)} \tag{5.25}$$

$$\frac{I_L}{I_H} = e^{-\varepsilon c (V_s - V_d)} = e^{-\varepsilon c \pi D_0 (D_s - D_d)}$$

$$PIR = \frac{I_H}{I_L} = e^{k(D_s - D_d)} = e^{k\Delta d} \tag{5.26}$$

They validated their proposed algorithm as well as they did a comparison with other BP estimation methods over 5024 beats, from 33 (19 normotensive and 14 hypertensive) subjects according to the experiment protocol, shown in Fig. 5.38. The results are shown in Fig. 5.39 for both groups (hypertensive and normotensive group), while Fig. 5.40 shows the estimated BP of a single hypertensive subject.

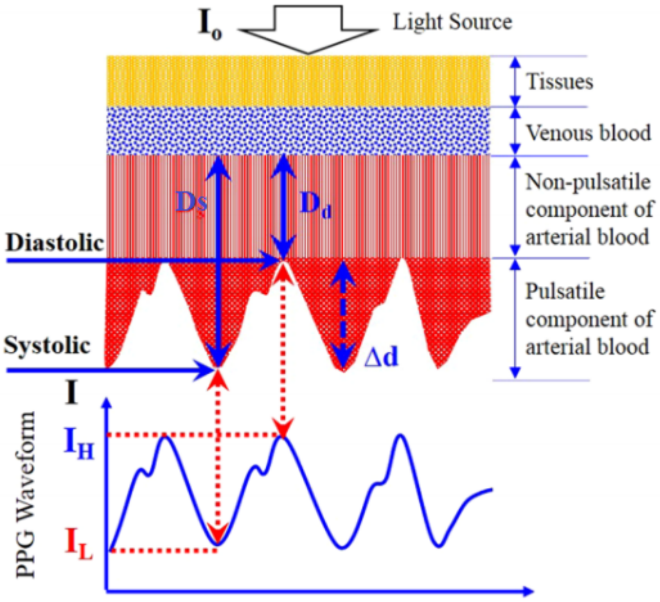

Figure 5.37: Definition of PPG intensity ratio (PIR) (modified from [262]).

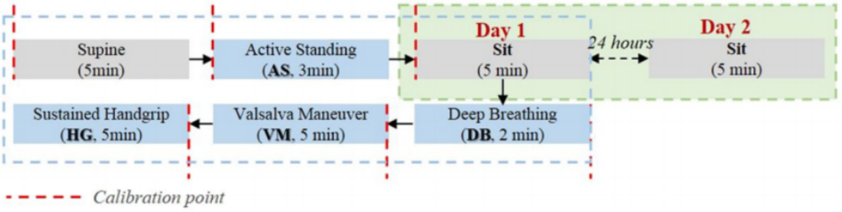

Figure 5.38: Experiment protocol of BP estimation using additional parameter PIR [262].

The authors compared their mentioned algorithm in terms of seven other estimation methods, which are summarized in Tab. 5.3, where the original nomenclature was adopted for a better understanding and ”Model 2” means the proposed method. An overall comparison is shown in Fig. 5.41, where the eight algorithms are being compared by their mean ± SD as well as their MAD. A differentiation between the normotensive and hypertensive group is illustrated in Fig. 5.42.

Several other approaches were developed in the past to predict the BP by using the mentioned ”Time Delay”, differing, next to the used estimation model, from the use of

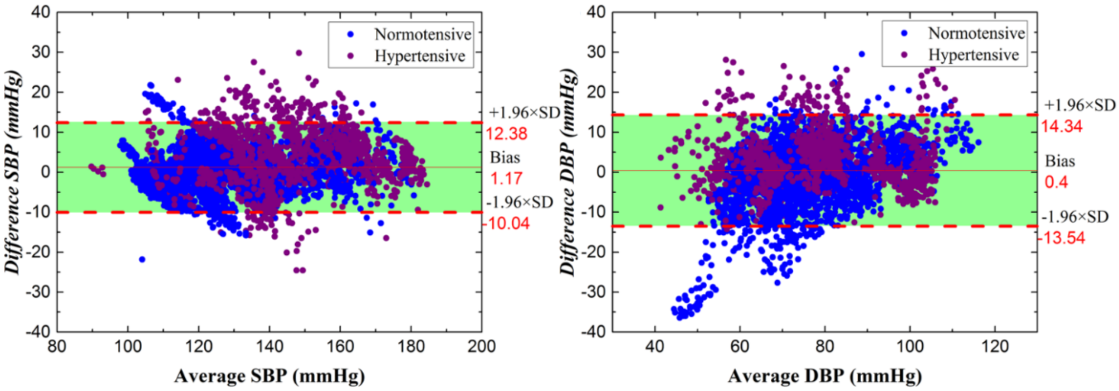

Figure 5.39: Bland-Altman plots of SBP (left) and DBP (right) estimation, using the additional model parameter PIR (modified from [262]).

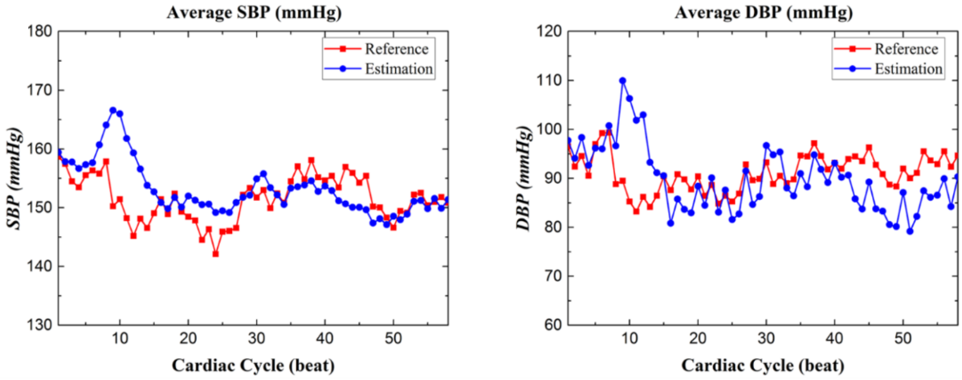

Figure 5.40: Estimated and reference BP (SBP(left), DPB(right)) of one hypertensive subject, seated at resting state (modified from [262]).

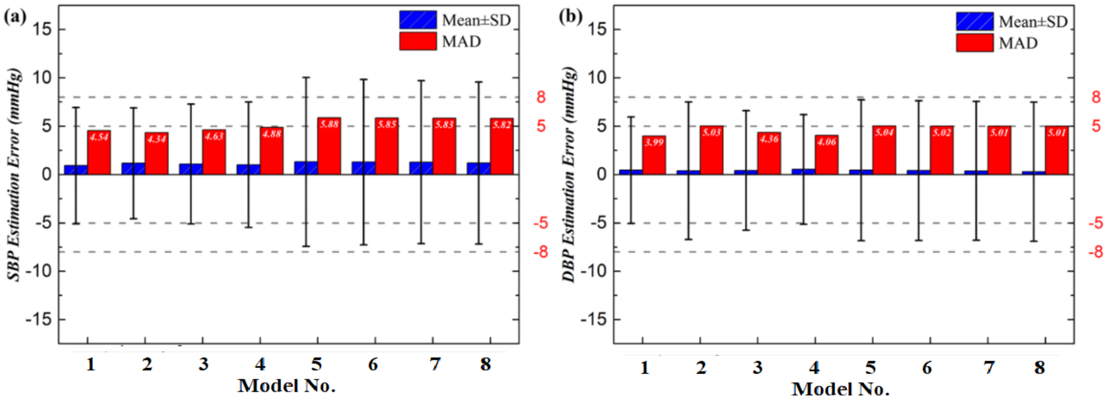

Figure 5.41: Overall comparison of performance of different BP estimation methods (Tab. 5.3) for SBP (left) and DPB (right) (modified from [262]).

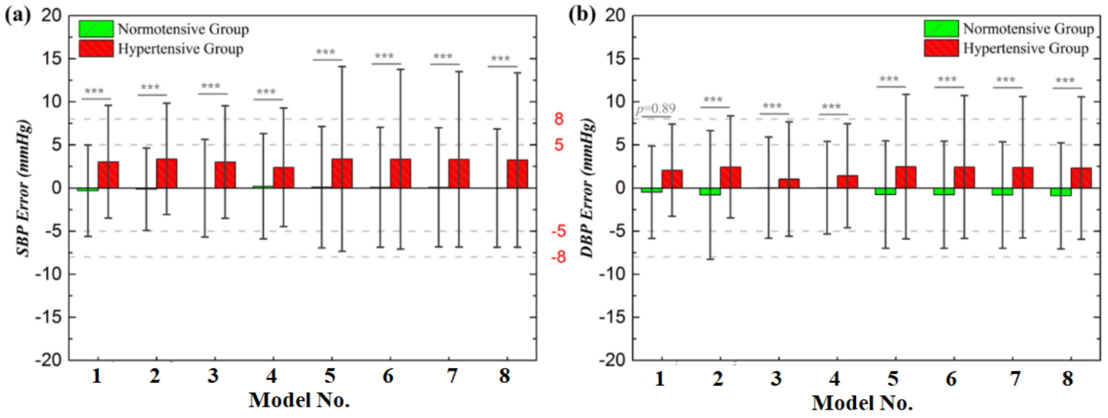

Figure 5.42: Performance of normotensive and hypertensive group for SBP (left) and DPB (right) of the eight mentioned BP estimation models (modified from [262]).

Model No.	DBP	SBP	Source
Model 1	$DPB + PP_0(\frac{PTT_0}{PTT})^2$	$DBP_0\frac{PIR_0}{PIR}$	[283]
Model 2	$MBP_0 \cdot \frac{PIR_0}{PIR_i} + \frac{2}{3}\frac{PIR_i}{PIR_0}\left(\frac{PAT_0}{PAT_i}\right)^2$	$MBP_0 \cdot \frac{PIR_0}{PIR_i} - \frac{1}{3}\frac{PIR_i}{PIR_0}\left(\frac{PAT_0}{PAT_i}\right)^2$	[262]
Model 3	$SBP_0 - \frac{2}{\gamma PTT_0}(PTT - PTT_0)$	$DBP_0 - \frac{2}{\gamma PTT_0}(PTT - PTT_0)$	[254]
Model 4	$DBP + PP_0(\frac{PTT_0}{PTT})^2$	$MBP_0 + \frac{2}{\gamma}\ln\frac{PTT_0}{PTT} - \frac{1}{3}PP_0(\frac{PTT_0}{PTT})^2$	[284]
Model 5	$aPTT + b$	$a'PTT + b'$	[182, 254]
Model 6	$a\ln(PTT) + b$	$a'\ln(PTT) + b'$	[197, 246, 258]
Model 7	$\frac{a}{PTT} + b$	$\frac{a'}{PTT} + b'$	[257, 259–261]
Model 8	$\frac{a}{PTT^2} + b$	$\frac{a'}{PTT^2} + b'$	[268]

Table 5.3: Eight BP estimation models for performance comparison (adapted from [262]).

different measurement sides, implementation, and realization. For example, the authors of [285] build a chair-based cuff-less BP monitor system, using ECG and PPG, integrated in the arm rest, and achieved MAD for SBP and DBP of 4.4 mmHg and 4.6 mmHg, respectively on a test of ten subjects. BP estimation was also done by using smartphone sensors, like camera and microphone [286]. Considering a camera as BP sensor, the author [287] used a color image sensor and monochromatic light sources to provide color imaging of the tissue, and estimated the BP by the use of an extended Windkessel model.

However, the reviewed methods represent an extract of the current optical BP estimation, where no single method outperform the others in a significant way, or by the possibility of BP prediction, without the need of calibration data, regardless, if the calibration is done by a reference method or by the use of a pre-trained model.

5.5 Discussion

The arterial blood pressure is a complex biosignal, depending on physiological and neurological parameters, which should be part of the estimation model. The most common approach is the mentioned ”Time-Delay” method, which either uses the distance between ECG and PPG (PAT) or between two PPGs (PTT). It was shown that both delays can be used to achieve similar results, but for a fully optical solution at least a dual-channel PPG sensor device is necessary.

The results from PTT measurement show that it is possible to measure the PTT, and thus, the local PWV over a small distance. The use of two or more PPG sensors could enable the possibility of a BP sensor in a relative small size for implantation in different devices for consumer and clinical applications. Additionally, it would eliminate the need of the ECG as second input and thus, provide a noninvasive and continuous measuring system, without the need of trained staff or expensive equipment [273]. The smallest reviewed distance was 10 mm, which leads to the conclusion that a PTT measurement on a chip, meaning a still smaller distance between light source and detector, might be difficult to realize. In case of the reviewed photodiode-array, the authors [273] mentioned that it was not possible to measure the PWV accurately, when sampling all 16 photodiodes, because the used sample frequency was too low for peak detection, even after interpolation. An accurate measurement of the PWV up to 45 m/s with a photo-diode array was possible, when using two photodiodes with a distance of 12 mm and a sample frequency of 125 kHz. When using four photodiodes spaced 4 mm apart, it was possible to accurately measure the PWV up to 25 m/s with a sample frequency of 62.5 kHz.

There are several issues, which make the ”Time Delay”-based BP estimation challenging, like the assumption of a tubular arterial system similar to central arterials, which is not holding because of the tapering of the peripheral branches [253] as well as the pressure amplification from heart to periphery [221]. Since a major amount of the optical BP estimations is based on the Moens-Korteweg equation, it should be keep in mind that there are several assumptions and limitations, like arteries treated as thin walled, deformations of the walls assumed as small, and artery wall modeled as Hookean solid, where, although these limitations, the Moens-Korteweg equation is useful and approximately correct as first-order treatment of elastic wave propagation problems [231, 288].

It was shown that PPG-based BP estimation could improve their performance by considering additional model parameters, like heart rate or vessel stiffness-related indices. The last one is also related to the age of the subject, which should be part of the model in any case, since many physiological parameters of the human body are rapidly changing with aging. Since the PTT and the PAT are just time indices, waveform morphology in combination with the time span of the PTT, meaning the time ratio from systole to diastole as well as from PPG cycle to diastolic duration, could also improve the performance of PPG-based BP estimation [263]. As mentioned in Sec. 4.3.1 (p. 83), the stiffness index SI is related to arterial stiffness, age, and PWV, which all should be considered in the BP estimation model, since they have direct influence on the BP prediction. It is generally known that the vascular properties are changing with the age. As summarized by [289], with aging, the Tunica intima is thickening, the Tunica media is decreasing elastin and increasing collagen, crosslinking and vascular smooth muscle cells, and the Tunica adventitia is increasing the collagen deposition. The so-called pressure index (PI) was developed by [220] as ratio between different PPG-curve sections, derived from first and second derivation of the PPG signal, and showing a correlation of r = 0.827 and r = 0.818 between the PI and SBP as well as between PI and PP, respectively, since they also demonstrated that there is a significant change between the normotensive and pre-hypertensive PPG waveform. Thus, the PPG curvature contains cardiovascular information, including vessel stiffness [220], and should be considered in the BP estimation model. Additionally, it should be mentioned that the reviewed PPG intensity ratio (PIR), introduced and applied by [262, 282, 283], is similar to the mentioned component ratio (CR), which represents the ratio of the AC-part and the whole signal PPG (Eq. 4.7, p. 89), since PIR equals the ratio of highest to lowest measured intensity (Eq. 5.26, p. 137), and considering that DC-part has the major amount of the whole PPG signal.

Most approaches of optical BP estimation use a calibration of the model parameter, meaning the adaption of the model to a particular user [290], but other predict the blood pressure optically without the need of calibrated values [291–293]. The authors of [292] compared five machine learning algorithms (linear regression, decision tree, support vector machine, AdaBost, random forest) to compare regression models by using PPG-shape features as well as ”Time delay”-parameters from the MIMIC II data base. They found that AdaBoost and random forest had the best performance, while linear regression had the worst one. According to them, their proposed algorithm is based on non-linear modeling and works properly, even without calibration, meaning a general pre-trained model without any modification for each individual. The authors of [290] presented a method to estimate the BP by using only ECG signals. They compared results of 51 subjects, using 3129 30-s ECG segments and seven extracted features, with and without applying calibration. Their results show that the MAE of 8.64 mmHg for SBP, 18.20 mmHg for DPB, and 7.72 mmHg for MAP without calibration was quite higher as in case of calibration with MAE of 7.72 mmHg for SBP, 9.45 mmHg for DBP, and 8.13 mmHg for MAP. In the study of [283], the authors found that heart diseases as well as the calibration interval can have an influence of the accuracy of the ”Time delay”-based BP estimation. They showed that the SBP estimation has a lower accuracy in patients with heart diseases than in healthy subjects, as well as they demonstrated that longer time intervals between calibration also lower the accuracy. Thus, the ”Time delay”-based BP estimation method requires an individual calibration by a reference method before use [283].

Since the vascular properties as well as the health state of an individual subjects can change over time, a general pre-trained model might be sufficient accurate for a healthy subject, but might not be for a patient of hypertension or other CVD. Although, also the case of hypertension can be included into the pre-trained model, it should be mentioned that there is a different performance between the BP estimation of healthy people and hypertension patients or other subjects with different CVD. Therefore, it should be differed between a personal health product for healthy people in everyday use and a diagnostic measurement system, which is needed in case of hypertension patients and which should be able to deliver diagnostic information about the cardiovascular state, without the need of previous provision of data, like age or hypertension grade. The current accuracy of the reviewed methods only fulfill the needs of the first application. Since the realization and implementation of blood pressure sensors differs a lot from clinical and consumer devices, it should be differentiated, which application area is concerned. Furthermore, the question is, is there a need for continuous BP monitoring for the healthy population or should the focus of further research be kept on the needs of CVD patients, which may have a higher requirement for long-time blood pressure monitoring.

Finally, it can be concluded that it is possible to predict a trend of the blood pressure level accurately enough to use changes as a warning as well as the continuous monitoring as an useful information in clinical environment [253]. Interferences by motion artifacts have a major impact on the performance of the BP estimation model [197], which leads to the conclusion that a removal of motion artifacts leads to a higher accuracy and better results, especially, in application fields such as sports or in everyday situations. As mentioned by [253], ”Time Delay”-based BP estimation devices have the capability to provide home-based monitoring, realized as a wearable device in combination with cloud-based server.

6 Conclusion

The field of biosignal acquisition is very complex and wide spread, where only a part is represented by spectral optical solutions. The present thesis has reviewed selected fields of biooptical applications, containing the measurement of three specific biosignals, named as blood glucose, heart rate, and blood pressure, where a focus has placed on the non-invasive in-vivo application of these signals. Moreover, biological and optical basics have been presented, building the basis for optical biosignal measurement, where the great variation of optical properties and behavior of human tissue has been demonstrated.

Biological tissues are mostly multi-layered and contain different components, which can influence the measurement unequally. The process of light and tissue interaction, especially by looking at the human skin, can be considered in different ways, but keeps concluding, that tissue is mostly a multi-scattering medium, which can interact with light in different depth due to its wavelength dependency. Thus, the possibility of spectral sensors, used in biomedical applications, has a huge potential to provide diagnostic information by each of the presented optical quantities.

In case of optical blood glucose determination, the spectral measurement in different wavelength regions has been reviewed, considering, next to absorption spectroscopy in near and mid-range infrared region, vibrational spectroscopy by relating the glucose concentration to the Raman shift. Also, the huge amount of other optical- and non-optical developed methods and devices has been demonstrated, concluding that a great general interest on a non-invasive way of blood glucose measurement exists. Today, no optical method for non-invasive blood glucose prediction is available on the market, although different approaches have a huge potential in detecting glucose trends, which often go along with a complex measurement equipment that might not be useful for the application of personal health. Moreover, already available minimal-invasive methods are an effective way for continuous glucose monitoring, which represent, next to also commonly researched non-optical methods, an alternative solution for the mentioned problem.

Regarding the detection of the heart rate, photoplethysmography (PPG) has been reviewed and represents the origin of different cardiovascular-related biosignals, where PPG itself stands for the pulse rate, which often represents an alternative to the heart rate, which is measured by ECG. Considering the spectral aspect of heart rate monitoring, care has been taken about the choice of the best wavelength, concluding the preference of green light, but in general, a dependency on the application persists. Additionally, the applications of heart rate variability and pulse oximetry have been discussed.

Based on PPG, optical blood pressure estimation has been evaluated, where different ways of modeling as well as physiological and biomechanical basics have been mentioned. Moreover, arterial stiffness, represented by pulse wave velocity (PWV), has also been discussed, showing a common interest in the pulse transit time (PTT) approach of optical blood pressure estimation, which has been reported as often being misused, instead of the pulse arrival time (PAT) approach, delivered from additional ECG measurement. Since the PTT itself can be detected only by PPG, a fully optical solution for blood pressure estimation is possible, where at least a trend of the blood pressure values can be predicted accurately enough for warnings, although several drawbacks must be improved in the future.

To sum up, depending on clinical or personal health applications, optical heart rate, and blood pressure measurement might deliver robust outcomes after the overcome of several drawbacks, while the future of optical non-invasive blood glucose monitoring is unclear due to its limitations and to the success of minimal-invasive methods.

Bibliography

[1] World Health Organization, “Cardiovascular diseases (CVDs) — (online accessed: 2018-10-03).” http://www.who.int/en/news-room/fact-sheets/detail/cardiovascular-diseases-(cvds), 2017.

[2] World Health Organization, “Global Report on Diabetes,” 2016.

[3] World Health Organization, “Questions and Answers on Hypertension — (online accessed: 2018-10-03).” https://www.who.int/features/qa/82/en/, 2015.

[4] B. Yu, D. G. Ferris, Y. Liu, and V. K. Nagarajan, “Emerging Optical Techniques for Detection of Oral , Cervical and Anal Cancer in Low-Resource Settings,” *Austin J Biomed Eng*, vol. 1, no. 2, 2014.

[5] L. Barnes, D. M. Heithoff, S. P. Mahan, G. N. Fox, A. Zambrano, J. Choe, L. N. Fitzgibbons, J. D. Marth, J. C. Fried, H. T. Soh, and M. J. Mahan, “Smartphone-based pathogen diagnosis in urinary sepsis patients.,” *EBioMedicine*, vol. 36, pp. 73–82, oct 2018.

[6] S. L. Jacques, “Optical properties of biological tissues: a review,” *Physics in Medicine and Biology*, vol. 58, pp. R37–R61, jun 2013.

[7] M. A. Farage, K. W. Miller, P. Elsner, and H. I. Maibach, “Structural Characteristics of the Aging Skin: A Review,” *Cutaneous and Ocular Toxicology*, vol. 26, no. 4, pp. 343–357, 2007.

[8] T. Vo-Dinh, *Biomedical photonics handbook*. CRC Press, 2003.

[9] S. L. Jacques and S. A. Prahl, “Introduction to Biomedical Optics (online accessed: 2017-10-06).” http://omlc.ogi.edu/classroom/ece532/.

[10] Encyclopædia Britannica Inc., “Anatomy - Tunica adventitia (online accessed: 2017-10-06).” https://www.britannica.com/science/tunica-adventitia.

[11] V. V. Tuchin, “Tissue Optics and Photonics: Light-Tissue Interaction,” *Journal of Biomedical Photonics & Engineering*, vol. 2, pp. 98–134, jun 2015.

[12] L. Fodor, Y. Ullmann, and M. Elman, “Light Tissue Interactions,” *Aesthetic Applications of Intense Pulsed Light*, pp. 11–20, 2011.

[13] E. Hecht, *Optics*. Pearson, 5th ed., 2016.

[14] M. Meinke, *Spektroskopische Bestimmung biophysikalischer Parameter humanen Blutes: Grundlagen und Anwendungen für das nicht-invasive Blutmonitoring*. Habilitation, 2007.

[15] R. P. Feynman, R. B. Leighton, and M. L. Sands, *The Feynman lectures on physics*. Addison-Wesley Pub. Co, 1963.

[16] P. Narkhede, S. Dhalwar, and B. Karthikeyan, "NIR Based Non-Invasive Blood Glucose Measurement," *Indian Journal of Science and Technology*, vol. 9, nov 2016.

[17] D. J. Faber, M. C. G. Aalders, E. G. Mik, B. A. Hooper, M. J. C. van Gemert, and T. G. van Leeuwen, "Oxygen Saturation-Dependent Absorption and Scattering of Blood," *Physical Review Letters*, vol. 93, p. 028102, jul 2004.

[18] D. Bohren, Craig F, Huffman, *Absorption and Scattering of Light by Small Particles*. 1983.

[19] A. Roggan, *Dosimetrie thermischer Laseranwendung in der Medizin : Untersuchung der optischen Gewebeeigenschaften und physikalisch -mathematische Modellentwicklung*. Ecomed, 1997.

[20] M. I. Mishchenko, L. D. Travis, and A. A. Lacis, "Scattering , Absorption , and Emission of Light by Small Particles," 2002.

[21] C. A. Bunge, R. Kruglov, and H. Poisel, "Rayleigh and Mie Scattering in polymer optical fibers," *Journal of Lightwave Technology*, vol. 24, pp. 3137–3146, aug 2006.

[22] L. Lelli, *Aerosols and Radiative Aspects in Clouds*. Lecture notes, University Bremen, 2014.

[23] G. F. Nataf, *New approaches to understand conductive and polar domain walls by Raman spectroscopy and low energy electron microscopy*. Phd thesis, Université Paris-Saclay, 2016.

[24] Chemistry Dictionary, "Definition of Absorption of Light (online accessed: 2017-10-06)." https://www.chemicool.com/definition/absorption_of_light.html.

[25] ANDOR, "What is ATR Spectroscopy? — Andor (online accessed: 2017-10-09)." http://www.andor.com/learning-academy/absorption-transmission-reflection-spectroscopy-an-introduction-to-absorption-transmission-reflection-spectroscopy.

[26] D. Perez-Guaita, S. Garrigues, M. De la, and Guardia, "Infrared-based quantification of clinical parameters," *TrAC Trends in Analytical Chemistry*, vol. 62, pp. 93–105, nov 2014.

[27] M. Monici, “Cell and tissue autofluorescence research and diagnostic applications,” *Biotechnology Annual Review*, vol. 11, pp. 227–256, jan 2005.

[28] J. Hegyi and V. Hegyi, “New Developments in Fluorescence Diagnostics,” in *Imaging in Dermatology*, pp. 89–94, Elsevier, 2016.

[29] LibreTexts (Physics), “Plane Electromagnetic Waves — (online accessed: 2018-06-18).” http://tinyurl.com/y92bqq54, 2018.

[30] Socratic, “What is polarized light? — (online accessed: 2018-06-19).” https://socratic.org/questions/58f0fd7e7c0149308e221579, 2018.

[31] V. V. Tuchin, “Polarized light interaction with tissues,” *Journal of Biomedical Optics*, vol. 21, p. 071114, apr 2016.

[32] V. V. Tuchin, “Light scattering study of tissues,” *Physics-Uspekhi*, vol. 40, pp. 495–515, may 1997.

[33] J. Yadav, A. Rani, V. Singh, and B. M. Murari, “Prospects and limitations of non-invasive blood glucose monitoring using near-infrared spectroscopy,” *Biomedical Signal Processing and Control*, vol. 18, pp. 214–227, apr 2015.

[34] L. C. Henyey and J. L. Greenstein, “Diffuse radiation in the Galaxy,” *The Astrophysical Journal*, vol. 93, p. 70, jan 1941.

[35] L. O. Reynolds and N. J. McCormick, “Approximate two-parameter phase function for light scattering,” *Journal of the Optical Society of America*, vol. 70, p. 1206, oct 1980.

[36] O. S. Khalil, “Spectroscopic and clinical aspects of noninvasive glucose measurements.,” *Clinical chemistry*, vol. 45, no. 2, pp. 165–77, 1999.

[37] J. Yadav, A. Rani, V. Singh, and B. M. Murari, “Near-infrared LED based non-invasive blood glucose sensor,” *2014 International Conference on Signal Processing and Integrated Networks (SPIN)*, pp. 591–594, 2014.

[38] J. Kottmann, J. M. Rey, and M. W. Sigrist, “Mid-infrared photoacoustic detection of glucose in human skin: Towards non-invasive diagnostics,” *Sensors (Switzerland)*, 2016.

[39] M. Brincat, Y. Muscat Baron, and R. Galea, “Estrogens and the skin,” *Climacteric*, vol. 8, pp. 110–123, jun 2005.

[40] S. M. Jackson, M. L. Williams, K. R. Feingold, and P. M. Elias, “Pathobiology of the stratum corneum.,” *The Western journal of medicine*, vol. 158, pp. 279–85, mar 1993.

[41] T. Biswas and T. Luu, “In vivo MR Measurement of Refractive Index, Relative

Water Content and T2 Relaxation time of Various Brain lesions With Clinical Application to Discriminate Brain Lesions," *ISPUB.COM The Internet Journal of Radiology*, vol. 13, no. 1, 2011.

[42] C. M. Gardner, "Transmission versus reflectance spectroscopy for quantitation," *Journal of Biomedical Optics*, vol. 23, p. 1, jan 2018.

[43] W. B. Baker, A. B. Parthasarathy, D. R. Busch, R. C. Mesquita, J. H. Greenberg, and A. G. Yodh, "Modified Beer-Lambert law for blood flow.," *Biomedical optics express*, vol. 5, pp. 4053–75, nov 2014.

[44] E. M. Buckley, A. B. Parthasarathy, P. E. Grant, A. G. Yodh, and M. A. Franceschini, "Diffuse correlation spectroscopy for measurement of cerebral blood flow: future prospects," *Neurophotonics*, vol. 1, p. 011009, jun 2014.

[45] S. Yu, M. Li, and L. Shi, "Chapter 6.3 Trust Establishment in Wireless Body Area Networks," in *Wearable Sensors*, pp. 475–491, 2014.

[46] K. Arasteh, H. Baenkler, and C. Bieber, *Innere Medizin*. Thieme, 2009.

[47] World Health Organization, "Definition and Diagnosis of Diabetes Mellitus and Intermediate Hyperglycemia," 2006.

[48] J. Šoupal, L. Petruželková, M. Flekač, T. Pelcl, M. Matoulek, M. Daková, J. Škrha, Š. Svačina, and M. Prázný, "Comparison of Different Treatment Modalities for Type 1 Diabetes, Including Sensor-Augmented Insulin Regimens, in 52 Weeks of Follow-Up: A COMISAIR Study," *Diabetes Technology & Therapeutics*, vol. 18, pp. 532–538, sep 2016.

[49] J. Yadav, A. Rani, V. Singh, and B. M. Murari, "Comparative Study of Different Measurement Sites Using NIR Based Non-invasive Glucose Measurement System," *Procedia Computer Science*, vol. 70, pp. 469–475, 2015.

[50] H. V. Dudukcu and T. Yildirim, "Noninvasive Glucose Measurement for Diabetes Mellitus Patients Mini Review," *Curr Trends Biomedical Eng & Biosci*, vol. 2, no. 3, 2017.

[51] J. Kollman and K.-H. Röhm, *Taschenatlas Biochemie des Menschen*. Thieme, 2009.

[52] L. Bellamy, J.-P. Casas, A. D. Hingorani, and D. Williams, "Type 2 diabetes mellitus after gestational diabetes: a systematic review and meta-analysis," *The Lancet*, vol. 373, pp. 1773–1779, may 2009.

[53] N. Ozana, N. Arbel, Y. Beiderman, V. Mico, M. Sanz, J. Garcia, A. Anand, B. Javidi, Y. Epstein, and Z. Zalevsky, "Improved noncontact optical sensor for detection

of glucose concentration and indication of dehydration level," *Biomedical Optics Express*, vol. 5, p. 1926, jun 2014.

[54] M. M. Gabir, R. L. Hanson, D. Dabelea, G. Imperatore, J. Roumain, P. H. Bennett, and W. C. Knowler, "The 1997 American Diabetes Association and 1999 World Health Organization criteria for hyperglycemia in the diagnosis and prediction of diabetes.," *Diabetes care*, vol. 23, pp. 1108–12, aug 2000.

[55] C. Higgins, "Measurement of circulating glucose: The problem of inconsistent sample and methodology (online accessed: 2018-08-27)." https://tinyurl.com/ycgh3gnk, 2008.

[56] B. Carstensen, J. Lindström, J. Sundvall, K. Borch-Johnsen, and J. Tuomilehto, "Measurement of blood glucose: comparison between different types of specimens," *Annals of Clinical Biochemistry*, vol. 45, pp. 140–148, mar 2008.

[57] E. Cengiz and W. V. Tamborlane, "A tale of two compartments: interstitial versus blood glucose monitoring.," *Diabetes technology & therapeutics*, vol. 11 Suppl 1, pp. S11–6, jun 2009.

[58] U. Larsson-Cohn, "Differences between Capillary and Venous Blood Glucose during Oral Glucose Tolerance Tests," *Scandinavian Journal of Clinical and Laboratory Investigation*, vol. 36, pp. 805–808, jan 1976.

[59] S. Colagiuri, A. Sandbaek, B. Carstensen, J. Christensen, C. Glumer, T. Lauritzen, and K. Borch-Johnsen, "Comparability of venous and capillary glucose measurements in blood.," *Diabetic medicine : a journal of the British Diabetic Association*, vol. 20, pp. 953–6, nov 2003.

[60] J. Roe, "Glucose Concentration Difference Between Arterial, Capillary, and Venous Blood. (online accessed: 2017-10-06)." https://www.bestthinking.com/articles/medicine/internal_medicine/hematology/glucose-concentration-difference-between-arterial-capillary-and-venous-blood.

[61] K. Kuwa, T. Nakayama, T. Hoshino, and M. Tominaga, "Relationships of glucose concentrations in capillary whole blood, venous whole blood and venous plasma," *Clinica Chimica Acta*, vol. 307, pp. 187–192, may 2001.

[62] A. Kulkarni, M. Saxena, G. Price, M. J. O'Leary, T. Jacques, and J. A. Myburgh, "Analysis of blood glucose measurements using capillary and arterial blood samples in intensive care patients," *Intensive Care Medicine*, vol. 31, pp. 142–145, jan 2005.

[63] B. Glassberg, "The arteriovenous difference in blood sugar content," *Archives of Internal Medicine*, vol. 46, p. 605, oct 1930.

[64] T. Shi, D. Li, G. Li, Y. Zhang, K. Xu, and L. Lu, “Modeling and Measurement of Correlation between Blood and Interstitial Glucose Changes,” *Journal of Diabetes Research*, vol. 2016, pp. 1–9, apr 2016.

[65] G. M. Steil, K. Rebrin, F. Hariri, S. Jinagonda, S. Tadros, C. Darwin, and M. F. Saad, “Interstitial fluid glucose dynamics during insulin-induced hypoglycaemia,” *Diabetologia*, vol. 48, pp. 1833–1840, sep 2005.

[66] N. S. Oliver, C. Toumazou, A. E. G. Cass, and D. G. Johnston, “Glucose sensors: a review of current and emerging technology,” *Diabetic Medicine*, vol. 26, no. 3, pp. 197–210, 2009.

[67] T. Siegmund, L. Heinemann, R. Kolassa, and A. Thomas, “Discrepancies Between Blood Glucose and Interstitial Glucose-Technological Artifacts or Physiology: Implications for Selection of the Appropriate Therapeutic Target.,” *Journal of diabetes science and technology*, vol. 11, no. 4, pp. 766–772, 2017.

[68] C. Scuffi, “Interstitium versus Blood Equilibrium in Glucose Concentration and its Impact on Subcutaneous Continuous Glucose Monitoring Systems,” *European Endocrinology*, vol. 10, no. 1, p. 36, 2014.

[69] A. Nawaz, P. Øhlckers, S. Sælid, M. Jacobsen, and M. Nadeem Akram, “Review: Non-Invasive Continuous Blood Glucose Measurement Techniques,” *Journal of Bioinformatics And Diabetes*, 2016.

[70] R. Pandey, S. K. Paidi, T. A. Valdez, C. Zhang, N. Spegazzini, R. R. Dasari, and I. Barman, “Noninvasive Monitoring of Blood Glucose with Raman Spectroscopy,” *Accounts of Chemical Research*, vol. 50, pp. 264–272, feb 2017.

[71] Ascensia Diabetes Care Switzerland AG, “Update zur ISO Norm 15197:2013 (online accessed: 2018-08-29).” https://www.ascensia-diabetes.ch/de/produkte/contour-next-blutzucker-messgeraete/iso-norm, 2017.

[72] Ascensia Diabetes Care Holdings AG, “Die DIN EN ISO-Norm 15197:2015 was ändert sich? (online accessed: 2018-08-29).” https://www.diabetes.ascensia.at/produkte/iso-norm-15197-2015/, 2016.

[73] J. M. Bland and D. G. Altman, “Statistical Methods for Assessing Agreement between two Methods of Clinical Measurement,” *The Lancet*, vol. 327, pp. 307–310, feb 1986.

[74] J. M. Bland and D. G. Altman, “Applying the right statistics: Analyses of measurement studies,” *Ultrasound in Obstetrics and Gynecology*, vol. 22, no. 1, pp. 85–93, 2003.

[75] J. L. Parkes, S. L. Slatin, S. Pardo, and B. H. Ginsberg, “A new consensus error grid to evaluate the clinical significance of inaccuracies in the measurement of blood glucose,” *Diabetes Care*, vol. 23, no. 8, pp. 1143–1148, 2000.

[76] D. C. Klonoff, “Point-of-Care Blood Glucose Meter Accuracy in the Hospital Setting,” *Diabetes Spectrum*, vol. 27, pp. 174–179, aug 2014.

[77] S. Haxha and J. Jhoja, “Optical Based Noninvasive Glucose Monitoring Sensor Prototype,” *IEEE Photonics Journal*, vol. 8, no. 6, 2016.

[78] A. K. Amerov, J. Chen, G. W. Small, and M. A. Arnold, “Scattering and Absorption Effects in the Determination of Glucose in Whole Blood by Near-Infrared Spectroscopy,” *Analytical Chemistry*, vol. 77, pp. 4587–4594, jul 2005.

[79] M. Goodarzi and W. Saeys, “Selection of the most informative near infrared spectroscopy wavebands for continuous glucose monitoring in human serum,” *Talanta*, vol. 146, pp. 155–165, 2016.

[80] K. Maruo and Y. Yamada, “Near-infrared noninvasive blood glucose prediction without using multivariate analyses: introduction of imaginary spectra due to scattering change in the skin,” *Journal of Biomedical Optics*, vol. 20, p. 047003, apr 2015.

[81] J. J. Burmeister, H. Chung, and M. A. Arnoldt, “Phantoms for Noninvasive Blood Glucose Sensing with Near Infrared Transmission Spectroscopy,” vol. 67, no. 1, pp. 50–55, 1998.

[82] S. Pan, H. Chung, M. A. Arnold, and G. W. Small, “Near-Infrared Spectroscopic Measurement of Physiological Glucose Levels in Variable Matrices of Protein and Triglycerides,” *Analytical Chemistry*, vol. 68, no. 7, pp. 1124–1135, 1996.

[83] Y. Yu, K. D. Crothall, L. G. Jahn, and M. A. DeStefano, “Laser diode applications in a continuous blood glucose sensor,” p. 268, jul 2003.

[84] W. Yang, N. Liao, H. Cheng, Y. Li, X. Bai, and C. Deng, “Determination of NIR informative wavebands for transmission non-invasive blood glucose measurement using a Fourier transform spectrometer,” *AIP Advances*, vol. 8, p. 035216, mar 2018.

[85] J. T. Alander, V. Bochko, B. Martinkauppi, S. Saranwong, and T. Mantere, “A Review of Optical Nondestructive Visual and Near-Infrared Methods for Food Quality and Safety,” *International Journal of Spectroscopy*, vol. 2013, no. May, pp. 1–36, 2013.

[86] R. L. van Veen, H. Sterenborg, A. Pifferi, A. Torricelli, and R. Cubeddu, “Determination of VIS- NIR absorption coefficients of mammalian fat, with time- and

spatially resolved diffuse reflectance and transmission spectroscopy," in *Biomedical Topical Meeting*, (Washington, D.C.), p. SF4, OSA, apr 2004.

[87] M. A. Arnold, L. Liu, and J. T. Olesberg, "Selectivity Assessment of Noninvasive Glucose Measurements Based on Analysis of Multivariate Calibration Vectors," tech. rep., 2007.

[88] J. Vessman, R. I. Stefan, J. F. van Staden, K. Danzer, W. Lindner, D. T. Burns, A. Fajgelj, and H. Müller, "Selectivity in analytical chemistry (IUPAC Recommendations 2001)," *Pure and Applied Chemistry*, vol. 73, pp. 1381–1386, aug 2001.

[89] X. Jintao, Y. Liming, L. Yufei, L. Chunyan, and C. Han, "Noninvasive and fast measurement of blood glucose in vivo by near infrared (NIR) spectroscopy," *Spectrochimica Acta - Part A: Molecular and Biomolecular Spectroscopy*, vol. 179, pp. 250–254, 2017.

[90] H. Arimoto, M. Tarumi, and Y. Yamada, "Instrumental Requirements for Non-Invasive Blood Glucose Measurement Using NIR Spectroscopy," *Optical Review*, vol. 10, pp. 161–165, may 2003.

[91] Y. Uwadaira, A. Ikehata, A. Momose, and M. Miura, "Identification of informative bands in the short-wavelength NIR region for non-invasive blood glucose measurement," *Biomedical Optics Express*, vol. 7, no. 7, p. 2729, 2016.

[92] M. R. Robinson, R. P. Eaton, D. M. Haaland, G. W. Koepp, E. V. Thomas, B. R. Stallard, and P. L. Robinson, "Noninvasive glucose monitoring in diabetic patients: a preliminary evaluation.," *Clinical chemistry*, vol. 38, pp. 1618–22, sep 1992.

[93] H. Heise, R. Marbach, T. Koschinsky, and F. Gries, "Noninvasive Blood Glucose Sensors Based on Near-Infrared Spectroscopy," *Artificial Organs*, vol. 18, pp. 439–447, jun 1994.

[94] J. Kay-Uwe, F. Christoph, D. Klaus, A. M. Ulrich, and M. Bernardo, "Application of near-infrared spectroscopy for non-invasive determination of blood/tissue glucose using neural networks," *Z. Phys. Chem.*, vol. 191, pp. 2179–2190, 1995.

[95] U. A. Müller, B. Mertes, C. Fischbacher, K. U. Jageman, and K. Danzer, "Non-invasive blood glucose monitoring by means of near infrared spectroscopy: methods for improving the reliability of the calibration models.," *The International journal of artificial organs*, vol. 20, pp. 285–90, may 1997.

[96] K. Danzer, C. Fischbacher, K. U. Jagemann, and K. J. Reichelt, "Near-infrared diffuse reflection spectroscopy for non-invasive blood-glucose monitoring," *LEOS Newslett*, vol. 12, no. 2, pp. 9–11, 1998.

[97] S. F. Malin, T. L. Ruchti, T. B. Blank, S. N. Thennadil, and S. L. Monfre, "Non-invasive prediction of glucose by near-infrared diffuse reflectance spectroscopy," *Clinical Chemistry*, vol. 45, no. 9, pp. 1651–1658, 1999.

[98] J. J. Burmeister and M. A. Arnold, "Evaluation of measurement sites for noninvasive blood glucose sensing with near-infrared transmission spectroscopy," *Clinical Chemistry*, vol. 45, no. 9, pp. 1621–1627, 1999.

[99] J. J. Burmeister, M. A. Arnold, and G. W. Small, "Noninvasive blood glucose measurements by near-infrared transmission spectroscopy across human tongues.," *Diabetes technology & therapeutics*, vol. 2, no. 1, pp. 5–16, 2000.

[100] S.-J. Yeh, C. F. Hanna, and O. S. Khalil, "Monitoring Blood Glucose Changes in Cutaneous Tissue by Temperature-modulated Localized Reflectance Measurements," tech. rep., 2003.

[101] K. Maruo, M. Tsurugi, J. Chin, T. Ota, H. Arimoto, Y. Yamada, M. Tamura, M. Ishii, and Y. Ozaki, "Noninvasive blood glucose assay using a newly developed near-infrared system," *IEEE Journal of Selected Topics in Quantum Electronics*, vol. 9, no. 2, pp. 322–330, 2003.

[102] C. AraujoAndrade, F. Ruiz, J. R. MartínezMendoza, and H. Terrones, "NonInvasive InVivo Blood Glucose Levels Prediction Using Near Infrared Spectroscopy," *AIP Conference Proceedings*, vol. 724, pp. 234–239, sep 2004.

[103] K. Xu, Q. Qiu, J. Jiang, and X. Yang, "Non-invasive glucose sensing with near-infrared spectroscopy enhanced by optical measurement conditions reproduction technique," *Optics and Lasers in Engineering*, vol. 43, pp. 1096–1106, oct 2005.

[104] C. D. Brown, H. T. Davis, M. N. Ediger, C. M. Fleming, E. L. Hull, and M. Rohrscheib, "Clinical Assessment of Near-Infrared Spectroscopy for Noninvasive Diabetes Screening," *Diabetes Technology & Therapeutics*, vol. 7, pp. 456–466, jun 2005.

[105] E. T. Ooi, X. Q. Zhang, J. H. Chen, P. H. Soh, K. Ng, and J. H. Yeo, "Noninvasive blood glucose measurement using multiple laser diodes," p. 64450K, feb 2007.

[106] C. S. Soh, X. Zhang, J. Chen, P. Raveendran, P. H. Soh, and J. H. Yeo, "Blood glucose prediction using neural network," vol. 6848, p. 68480B, International Society for Optics and Photonics, feb 2008.

[107] S. Liakat, K. A. Bors, L. Xu, C. M. Woods, J. Doyle, and C. F. Gmachl, "Noninvasive in vivo glucose sensing on human subjects using mid-infrared light," *Biomedical Optics Express*, vol. 5, p. 2397, jul 2014.

[108] G. B. Christison and H. A. MacKenzie, “Laser photoacoustic determination of physiological glucose concentrations in human whole blood,” *Medical & Biological Engineering & Computing*, vol. 31, pp. 284–290, may 1993.

[109] S. Liakat, K. A. Bors, T.-Y. Huang, A. P. M. Michel, E. Zanghi, and C. F. Gmachl, “In vitro measurements of physiological glucose concentrations in biological fluids using mid-infrared light,” *Biomedical Optics Express*, vol. 4, p. 1083, jul 2013.

[110] M. Pleitez, H. von Lilienfeld-Toal, and W. Mäntele, “Infrared spectroscopic analysis of human interstitial fluid in vitro and in vivo using FT-IR spectroscopy and pulsed quantum cascade lasers (QCL): Establishing a new approach to non invasive glucose measurement,” *Spectrochimica Acta Part A: Molecular and Biomolecular Spectroscopy*, vol. 85, pp. 61–65, jan 2012.

[111] S. Yoshida, M. Yoshida, M. Yamamoto, and J. Takeda, “Optical screening of diabetes mellitus using non-invasive Fourier-transform infrared spectroscopy technique for human lip,” *Journal of Pharmaceutical and Biomedical Analysis*, vol. 76, pp. 169–176, mar 2013.

[112] R. Kasahara, S. Kino, S. Soyama, and Y. Matsuura, “Noninvasive glucose monitoring using mid-infrared absorption spectroscopy based on a few wavenumbers,” *Biomedical Optics Express*, vol. 9, p. 289, jan 2018.

[113] S. Kino, S. Omori, T. Katagiri, and Y. Matsuura, “Hollow optical-fiber based infrared spectroscopy for measurement of blood glucose level by using multi-reflection prism,” vol. 7, no. 2, pp. 701–708, 2016.

[114] Y. Uwadaira and A. Ikehata, “Noninvasive Blood Glucose Measurement,” in *Nutritional and Therapeutic Interventions for Diabetes and Metabolic Syndrome*, pp. 489–504, Elsevier, 2018.

[115] J. Lambert, M. Storrie-Lombardi, and M. Borchert, *Measurement of Physiologic Glucose Levels Using Raman Spectroscopy in a Rabbit Aqueous Humor Model*, vol. 12. jan 1998.

[116] W.-C. Shih, K. L. Bechtel, and M. S. Feld, “Noninvasive Glucose Sensing with Raman Spectroscopy,” in *In Vivo Glucose Sensing*, pp. 391–419, Hoboken, NJ, USA: John Wiley & Sons, Inc., dec 2009.

[117] J. Shao, M. Lin, Y. Li, X. Li, J. Liu, J. Liang, and H. Yao, “In Vivo Blood Glucose Quantification Using Raman Spectroscopy,” *PLoS ONE*, vol. 7, p. e48127, oct 2012.

[118] M. J. Scholtes-Timmerman, S. Bijlsma, M. J. Fokkert, R. Slingerland, and S. J. Van Veen, “Raman spectroscopy as a promising tool for noninvasive point-of-care

glucose monitoring," *Journal of Diabetes Science and Technology*, vol. 8, no. 5, pp. 974–979, 2014.

[119] S. M. Lundsgaard-Nielsen, A. Pors, S. O. Banke, J. E. Henriksen, D. K. Hepp, and A. Weber, "Critical-depth Raman spectroscopy enables home-use non-invasive glucose monitoring," *PLOS ONE*, vol. 13, p. e0197134, may 2018.

[120] C. Chen, X.-L. Zhao, Z.-H. Li, Z.-G. Zhu, S.-H. Qian, A. Flewitt, C. Chen, X.-L. Zhao, Z.-H. Li, Z.-G. Zhu, S.-H. Qian, and A. J. Flewitt, "Current and Emerging Technology for Continuous Glucose Monitoring," *Sensors*, vol. 17, p. 182, jan 2017.

[121] J. Kim, A. S. Campbell, and J. Wang, "Wearable non-invasive epidermal glucose sensors: A review," *Talanta*, vol. 177, pp. 163–170, jan 2018.

[122] C. F. So, K. S. Choi, T. K. S. Wong, and J. W. Y. Chung, "Recent advances in noninvasive glucose monitoring," 2012.

[123] O. Abdallah, a. Bolz, J. Hansmann, H. Walles, and T. Hirth, "Design of a Compact Multi-Sensor System for Non-Invasive Glucose Monitoring Using Optical Spectroscopy," *Biomedical Engineering*, 2012.

[124] A. Sieg, "Noninvasive Glucose Monitoring by Reverse Iontophoresis in Vivo: Application of the Internal Standard Concept," *Clinical Chemistry*, vol. 50, pp. 1383–1390, jun 2004.

[125] M. X. Chu, K. Miyajima, D. Takahashi, T. Arakawa, K. Sano, S.-i. Sawada, H. Kudo, Y. Iwasaki, K. Akiyoshi, M. Mochizuki, and K. Mitsubayashi, "Soft contact lens biosensor for in situ monitoring of tear glucose as non-invasive blood sugar assessment," *Talanta*, vol. 83, no. 3, pp. 960–965, 2011.

[126] J. Kim, M. Kim, M.-S. Lee, K. Kim, S. Ji, Y.-T. Kim, J. Park, K. Na, K.-H. Bae, H. Kyun Kim, F. Bien, C. Young Lee, and J.-U. Park, "Wearable smart sensor systems integrated on soft contact lenses for wireless ocular diagnostics," *Nature Communications*, vol. 8, p. 14997, apr 2017.

[127] A. Caduff, E. Hirt, Y. Feldman, Z. Ali, and L. Heinemann, "First human experiments with a novel non-invasive, non-optical continuous glucose monitoring system," *Biosensors and Bioelectronics*, vol. 19, pp. 209–217, nov 2003.

[128] A. J. Bandodkar, W. Jia, C. Yardmc, X. Wang, J. Ramirez, and J. Wang, "Tattoo-Based Noninvasive Glucose Monitoring: A Proof-of-Concept Study," *Analytical Chemistry*, vol. 87, pp. 394–398, jan 2015.

[129] J. Yadav, A. Rani, V. Singh, and B. Mohan Murari, "Investigations on Multisensor-

Based Noninvasive Blood Glucose Measurement System," *Journal of Medical Devices*, vol. 11, p. 031006, jun 2017.

[130] I. Harman-Boehm, A. Gal, A. M. Raykhman, J. D. Zahn, E. Naidis, and Y. Mayzel, "Noninvasive Glucose Monitoring: A Novel Approach," *Journal of Diabetes Science and Technology*, vol. 3, pp. 253–260, mar 2009.

[131] Z. Geng, F. Tang, Y. Ding, S. Li, and X. Wang, "Noninvasive Continuous Glucose Monitoring Using a Multisensor-Based Glucometer and Time Series Analysis," *Scientific Reports*, vol. 7, p. 12650, dec 2017.

[132] C. D. Malchoff, K. Shoukri, J. I. Landau, and J. M. Buchert, "A Novel Noninvasive Blood Glucose Monitor," *Diabetes Care*, vol. 25, pp. 2268–2275, dec 2002.

[133] J. M. Buchert, "Thermal emission spectroscopy as a tool for noninvasive blood glucose measurements," vol. 5566, pp. 100–111, International Society for Optics and Photonics, aug 2004.

[134] A. Ghazaryan, M. Omar, G. J. Tserevelakis, and V. Ntziachristos, "Optoacoustic detection of tissue glycation.," *Biomedical optics express*, vol. 6, no. 9, pp. 3149–56, 2015.

[135] J. Kottmann, U. Grob, J. Rey, and M. Sigrist, "Mid-Infrared Fiber-Coupled Photoacoustic Sensor for Biomedical Applications," *Sensors*, vol. 13, pp. 535–549, jan 2013.

[136] M. A. Pleitez, T. Lieblein, A. Bauer, O. Hertzberg, H. von Lilienfeld-Toal, and W. Mäntele, "In Vivo Noninvasive Monitoring of Glucose Concentration in Human Epidermis by Mid-Infrared Pulsed Photoacoustic Spectroscopy," *Analytical Chemistry*, vol. 85, pp. 1013–1020, jan 2013.

[137] J. C. Pickup, F. Hussain, N. D. Evans, O. J. Rolinski, and D. J. Birch, "Fluorescence-based glucose sensors," *Biosensors and Bioelectronics*, vol. 20, pp. 2555–2565, jun 2005.

[138] E. A. Moschou, B. V. Sharma, S. K. Deo, and S. Daunert, "Fluorescence Glucose Detection: Advances Toward the Ideal In Vivo Biosensor," *Journal of Fluorescence*, vol. 14, pp. 535–547, sep 2004.

[139] R. Badugu, J. R. Lakowicz, and C. D. Geddes, "A glucose-sensing contact lens: from bench top to patient," *Current Opinion in Biotechnology*, vol. 16, pp. 100–107, feb 2005.

[140] Y. Beiderman, I. Horovitz, N. Burshtein, M. Teicher, J. Garcia, V. Mico, and Z. Zalevsky, "Remote estimation of blood pulse pressure via temporal tracking of re-

flected secondary speckles pattern.," *Journal of biomedical optics*, vol. 15, no. 6, p. 061707, 2010.

[141] Y. Beiderman, R. Blumenberg, N. Rabani, M. Teicher, J. Garcia, V. Mico, and Z. Zalevsky, "Demonstration of remote optical measurement configuration that correlates to glucose concentration in blood," *Biomedical Optics Express*, vol. 2, p. 858, apr 2011.

[142] K. V. Larin, M. S. Eledrisi, M. Motamedi, and R. O. Esenaliev, "Noninvasive blood glucose monitoring with optical coherence tomography: a pilot study in human subjects.," *Diabetes care*, vol. 25, pp. 2263–7, dec 2002.

[143] Y. T. Lan, Y. P. Kuang, L. P. Zhou, G. Y. Wu, P. C. Gu, H. J. Wei, and K. Chen, "Noninvasive monitoring of blood glucose concentration in diabetic patients with optical coherence tomography," *Laser Physics Letters*, vol. 14, p. 035603, mar 2017.

[144] R. Rawer, W. Stork, and C. F. Kreiner, "Non-invasive polarimetric measurement of glucose concentration in the anterior chamber of the eye," *Graefe's Archive for Clinical and Experimental Ophthalmology*, vol. 242, pp. 1017–1023, dec 2004.

[145] B. D. Cameron and Y. Li, "Polarization-Based Diffuse Reflectance Imaging for Noninvasive Measurement of Glucose," *Journal of Diabetes Science and Technology*, vol. 1, pp. 873–878, nov 2007.

[146] G. Purvinis, B. D. Cameron, and D. M. Altrogge, "Noninvasive polarimetric-based glucose monitoring: an in vivo study.," *Journal of diabetes science and technology*, vol. 5, pp. 380–7, mar 2011.

[147] M. F. Wood, N. Ghosh, X. Guo, and I. A. Vitkin, "Toward Noninvasive Glucose Sensing Using Polarizazion Analysis of Multiply Scattered Light," *Handbook of Optical Sensing of Glucose in Biological Fluids and Tissues Series in Medical Physics and Biomedical Engineering*, pp. 527–562, 2009.

[148] O. K. Cho, "Noninvasive Measurement of Glucose by Metabolic Heat Conformation Method," *Clinical Chemistry*, vol. 50, pp. 1894–1898, oct 2004.

[149] D. B. Sacks, M. Arnold, G. L. Bakris, D. E. Bruns, A. R. Horvath, M. S. Kirkman, A. Lernmark, B. E. Metzger, and D. M. Nathan, "Guidelines and Recommendations for Laboratory Analysis in the Diagnosis and Management of Diabetes Mellitus," *Clinical Chemistry*, vol. 57, pp. e1–e47, jun 2011.

[150] H. S. Kim, "Blood Glucose Measurement: Is Serum Equal to Plasma?," *Diabetes & Metabolism Journal*, vol. 40, p. 365, oct 2016.

[151] Y. Maeda, M. Sekine, and T. Tamura, "The advantages of wearable green reflected

photoplethysmography," *Journal of Medical Systems*, vol. 35, no. 5, pp. 829–834, 2011.

[152] R. Gajda, E. K. Biernacka, and W. Drygas, "Are heart rate monitors valuable tools for diagnosing arrhythmias in endurance athletes?," *Scandinavian Journal of Medicine & Science in Sports*, vol. 28, pp. 496–516, feb 2018.

[153] A. Shcherbina, C. Mattsson, D. Waggott, H. Salisbury, J. Christle, T. Hastie, M. Wheeler, and E. Ashley, "Accuracy in Wrist-Worn, Sensor-Based Measurements of Heart Rate and Energy Expenditure in a Diverse Cohort," *Journal of Personalized Medicine*, vol. 7, no. 2, p. 3, 2017.

[154] K. Bakhtiyari, N. Beckmann, and J. Ziegler, "Contactless heart rate variability measurement by IR and 3D depth sensors with respiratory sinus arrhythmia," *Procedia Computer Science*, vol. 109, pp. 498–505, 2017.

[155] A. Devon, "Heart rate vs. pulse: Are they the same or different? (online accessed: 2018-09-11)." https://www.belmarrahealth.com/heart-rate-vs-pulse-different/, 2017.

[156] LibreTexts (Biology), "The Cardiac Cycle — (online accessed: 2018-09-11)." https://tinyurl.com/yb6mjue5.

[157] S. Silbernagl and D. Agamemnon, *Taschenatlas Physiologie*. Thieme, 2012.

[158] American Heart Association Inc., "Target Heart Rates (online accessed: 2017-24-11)." http://www.heart.org/HEARTORG/HealthyLiving/PhysicalActivity/Target-Heart-Rates_UCM_434341_Article.jsp#.WhfXWVXiYkI.

[159] M. Lemay, M. Bertschi, J. Sola, P. Renevey, J. Parak, and I. Korhonen, "Chapter 2.3 Application of Optical Heart Rate Monitoring," in *Wearable Sensors*, pp. 105–129, 2014.

[160] M. Elgendi, "On the Analysis of Fingertip Photoplethysmogram Signals," *Current Cardiology Reviews*, vol. 8, pp. 14–25, jun 2012.

[161] J. Allen, "Photoplethysmography and its application in clinical physiological measurement," *Physiological Measurement*, vol. 28, pp. R1–R39, mar 2007.

[162] M. Elgendi, "Standard Terminologies for Photoplethysmogram Signals," *Current Cardiology Reviews*, vol. 8, pp. 215–219, sep 2012.

[163] T. Tamura, Y. Maeda, M. Sekine, and M. Yoshida, "Wearable Photoplethysmographic Sensors - Past and Present," *Electronics*, 2014.

[164] J. Webster, *Design of Pulse Oximeters*, vol. 19971023 of *Series in Medical Physics and Biomedical Engineering*. London: Taylor & Francis, 1st ed. ed., oct 1997.

[165] H. Asada, P. Shaltis, A. Reisner, Sokwoo Rhee, and R. Hutchinson, "Mobile monitoring with wearable photoplethysmographic biosensors," *IEEE Engineering in Medicine and Biology Magazine*, vol. 22, pp. 28–40, may 2003.

[166] B. J. . Onsson, C. Laurent, T. Skau, and L.-G. Lindberg, "A New Probe for Ankle Systolic Pressure Measurement Using Photoplethysmography (PPG)," *Annals of Biomedical Engineering*, vol. 33, no. 2, pp. 232–239, 2005.

[167] B. Jönsson, C. Laurent, M. Eneling, T. Skau, and L.-G. Lindberg, "Automatic Ankle Pressure Measurements Using PPG in Ankle-brachial Pressure Index Determination," *European Journal of Vascular and Endovascular Surgery*, vol. 30, pp. 395–401, oct 2005.

[168] A. A. Awad, A. S. Haddadin, H. Tantawy, T. M. Badr, R. G. Stout, D. G. Silverman, and K. H. Shelley, "The relationship between the photoplethysmographic waveform and systemic vascular resistance," *Journal of Clinical Monitoring and Computing*, vol. 21, pp. 365–372, nov 2007.

[169] S. C. Millasseau, R. P. Kelly, J. M. Ritter, and P. J. Chowienczyk, "Determination of age-related increases in large artery stiffness by digital pulse contour analysis," *Clinical Science*, vol. 103, pp. 371–377, 2002.

[170] J. Padilla, E. Berjano, J. Saiz, L. Facila, P. Diaz, and S. Merce, "Assessment of relationships between blood pressure, pulse wave velocity and digital volume pulse," *2006 Computers in Cardiology*, no. May 2014, pp. 893–896, 2006.

[171] L. Wang and Y. Zhang, "A novel photoplethysmogram index for total peripheral resistance after bicycle exercise," *Proc. of the 5th International Conference on Ubiquitous Healthcare, Pusan*, pp. pp. 175–6., 2008.

[172] L. Wang, E. Pickwell-MacPherson, Y. Liang, and Y. Zhang, "Noninvasive cardiac output estimation using a novel photoplethysmogram index," in *2009 Annual International Conference of the IEEE Engineering in Medicine and Biology Society*, vol. 2009, pp. 1746–1749, IEEE, sep 2009.

[173] R. D. Abbott, H. Petrovitch, B. L. Rodriguez, K. Yano, I. J. Schatz, J. S. Popper, K. H. Masaki, G. Ross, and J. Curb, "Ankle/brachial blood pressure in men >70 years of age and the risk of coronary heart disease," *The American Journal of Cardiology*, vol. 86, pp. 280–284, aug 2000.

[174] G. C. Leng, F. G. Fowkes, A. J. Lee, J. Dunbar, E. Housley, and C. V. Ruckley, "Use of ankle brachial pressure index to predict cardiovascular events and death: a cohort study.," *BMJ (Clinical research ed.)*, vol. 313, pp. 1440–4, dec 1996.

[175] S. H. Wild, C. D. Byrne, F. B. Smith, A. J. Lee, and F. G. R. Fowkes, "Low ankle-brachial pressure index predicts increased risk of cardiovascular disease independent of the metabolic syndrome and conventional cardiovascular risk factors in the Edinburgh Artery Study.," *Diabetes care*, vol. 29, pp. 637–42, mar 2006.

[176] T. Tigges, Z. Music, A. Pielmus, M. Klum, A. Feldheiser, O. Hunsicker, and R. Orglmeister, "Classification of morphologic changes in photoplethysmographic waveforms," *Current Directions in Biomedical Engineering*, 2016.

[177] K. Takazawa, N. Tanaka, M. Fujita, O. Matsuoka, T. Saiki, M. Aikawa, S. Tamura, and C. Ibukiyama, "Assessment of vasoactive agents and vascular aging by the second derivative of photoplethysmogram waveform.," *Hypertension (Dallas, Tex. : 1979)*, vol. 32, pp. 365–70, aug 1998.

[178] K. Takazawa, M. Fujita, K. Yabe, T. Sakai, T. Kobayashi, K. Maeda, Y. Yamashita, M. Hase, and C. Ibukiyama, *Clinical usefulness of the second derivative of a plethysmogram (acceleration plethysmogram)*, vol. 23. jan 1993.

[179] M. Elgendi, Y. Liang, and R. Ward, "Toward Generating More Diagnostic Features from Photoplethysmogram Waveforms," *Diseases*, vol. 6, p. 20, mar 2018.

[180] S. R. Alty, N. Angarita-Jaimes, S. C. Millasseau, and P. J. Chowienczyk, "Predicting arterial stiffness from the digital volume pulse waveform.," *IEEE transactions on bio-medical engineering*, vol. 54, pp. 2268–75, dec 2007.

[181] I. Imanaga, H. Hara, S. Koyanagi, and K. Tanaka, "Correlation between wave components of the second derivative of plethysmogram and arterial distensibility.," *Japanese heart journal*, vol. 39, pp. 775–84, nov 1998.

[182] J. Liu, B. P.-Y. Yan, W.-X. Dai, X.-R. Ding, Y.-T. Zhang, and N. Zhao, "Multi-wavelength photoplethysmography method for skin arterial pulse extraction," *Biomedical Optics Express*, vol. 7, p. 4313, oct 2016.

[183] Y. Yamakoshi, K. Matsumura, T. Yamakoshi, J. Lee, P. Rolfe, Y. Kato, K. Shimizu, and K.-i. Yamakoshi, "Side-scattered finger-photoplethysmography: experimental investigations toward practical noninvasive measurement of blood glucose," *Journal of Biomedical Optics*, vol. 22, p. 067001, jun 2017.

[184] J. Jihyoung Lee, K. Matsumura, K.-i. Yamakoshi, P. Rolfe, S. Tanaka, and T. Yamakoshi, "Comparison between red, green and blue light reflection photoplethysmography for heart rate monitoring during motion," in *2013 35th Annual International Conference of the IEEE Engineering in Medicine and Biology Society (EMBC)*, vol. 2013, pp. 1724–1727, IEEE, jul 2013.

[185] L. Yan, S. Hu, A. Alzahrani, S. Alharbi, P. Blanos, L. Yan, S. Hu, A. Alzahrani, S. Alharbi, and P. Blanos, "A Multi-Wavelength Opto-Electronic Patch Sensor to Effectively Detect Physiological Changes against Human Skin Types," *Biosensors*, vol. 7, p. 22, jun 2017.

[186] M. A. Pathak, K. Jimbow, G. Szabo, and T. B. Fitzpatrick, "Sunlight and Melanin Pigmentation," in *Photochemical and Photobiological Reviews*, pp. 211–239, Boston, MA: Springer US, 1976.

[187] T. B. Fitzpatrick, "The Validity and Practicality of Sun-Reactive Skin Types I Through VI," *Archives of Dermatology*, vol. 124, p. 869, jun 1988.

[188] J. D'Orazio, S. Jarrett, A. Amaro-Ortiz, and T. Scott, "UV Radiation and the Skin," *International Journal of Molecular Sciences*, vol. 14, pp. 12222–12248, jun 2013.

[189] B. A. Fallow, T. Tarumi, and H. Tanaka, "Influence of skin type and wavelength on light wave reflectance," *Journal of Clinical Monitoring and Computing*, vol. 27, pp. 313–317, jun 2013.

[190] L. Asare, E. Kviesis-Kipge, U. Rubins, O. Rubenis, and J. Spigulis, "Multi-spectral photoplethysmography technique for parallel monitoring of pulse shapes at different tissue depths," vol. 28, no. 2007, p. 80872E, 2011.

[191] L. Asare, E. Kviesis-Kipge, M. Ozols, J. Spigulis, and R. Erts, "Multi-spectral opto-electronic device for skin microcirculation analysis," *Lithuanian Journal of Physics*, vol. 52, no. 1, pp. 59–62, 2012.

[192] K. M. Warren, J. R. Harvey, K. H. Chon, and Y. Mendelson, "Improving pulse rate measurements during random motion using a wearable multichannel reflectance photoplethysmograph," *Sensors (Switzerland)*, vol. 16, no. 3, 2016.

[193] Y. Mendelson and B. Ochs, "Noninvasive pulse oximetry utilizing skin reflectance photoplethysmography," *IEEE Transactions on Biomedical Engineering*, vol. 35, no. 10, pp. 798–805, 1988.

[194] F. Huang, P. Yuan, and K. Lin, "Analysis of reflectance photoplethysmograph sensors," *World Academy of Science, . . .* , pp. 1266–1269, 2011.

[195] R.-C. Peng, X.-L. Zhou, W.-H. Lin, and Y.-T. Zhang, "Extraction of Heart Rate Variability from Smartphone Photoplethysmograms," *Computational and Mathematical Methods in Medicine*, vol. 2015, pp. 1–11, jan 2015.

[196] S. M. A. Salehizadeh, D. Dao, J. Bolkhovsky, C. Cho, Y. Mendelson, and K. H. Chon, "A Novel Time - Varying Spectral Filtering Algorithm for Reconstruction

of Motion Artifact Corrupted Heart Rate Signals During Intense Physical Activities Using a Wearable Photoplethysmogram Sensor," *Sensors*, vol. 16, no. 10, 2016.

[197] Y. Wang, Z. Liu, and S. Ma, "Cuff-less blood pressure measurement from dual-channel photoplethysmographic signals via peripheral pulse transit time with singular spectrum analysis," *Physiological Measurement*, vol. 39, p. 025010, feb 2018.

[198] H. Asada, Hong-Hui Jiang, and P. Gibbs, "Active noise cancellation using MEMS accelerometers for motion-tolerant wearable bio-sensors," in *The 26th Annual International Conference of the IEEE Engineering in Medicine and Biology Society*, vol. 3, pp. 2157–2160, IEEE, 2004.

[199] H. S. Shin, C. Lee, and M. Lee, "Adaptive threshold method for the peak detection of photoplethysmographic waveform," *Computers in Biology and Medicine*, vol. 39, pp. 1145–1152, dec 2009.

[200] F. Scholkmann, J. Boss, and M. Wolf, "An Efficient Algorithm for Automatic Peak Detection in Noisy Periodic and Quasi-Periodic Signals," *Algorithms*, vol. 5, pp. 588–603, nov 2012.

[201] M. Elgendi, I. Norton, M. Brearley, D. Abbott, and D. Schuurmans, "Detection of a and b waves in the acceleration photoplethysmogram.," *Biomedical engineering online*, vol. 13, p. 139, sep 2014.

[202] W. Zong, T. Heldt, G. Moody, and R. Mark, "An open-source algorithm to detect onset of arterial blood pressure pulses," in *Computers in Cardiology, 2003*, pp. 259–262, IEEE, 2003.

[203] D.-G. Jang, S. Park, M. Hahn, and S.-H. Park, "A Real-Time Pulse Peak Detection Algorithm for the Photoplethysmogram," *International Journal of Electronics and Electrical Engineering*, pp. 45–49, 2014.

[204] D.-G. Jang, U. Farooq, S.-H. Park, and M. Hahn, "A robust method for pulse peak determination in a digital volume pulse waveform with a wandering baseline.," *IEEE transactions on biomedical circuits and systems*, vol. 8, pp. 729–37, oct 2014.

[205] U. R. Acharya, K. P. Joseph, N. Kannathal, L. C. Min, and J. S. Suri, "Heart Rate Variability," in *Advances in Cardiac Signal Processing*, pp. 121–165, Berlin, Heidelberg: Springer Berlin Heidelberg, 2007.

[206] A. Alwosheel, A. Alasaad, and A. Alqaraawi, "Heart rate variability estimation in photoplethysmography signals using Bayesian learning approach," *Healthcare Technology Letters*, vol. 3, pp. 136–142, jun 2016.

[207] R. Mccraty and F. Shaffer, "Heart Rate Variability: New Perspectives on Physiolog-

ical Mechanisms, Assessment of Self-regulatory Capacity, and Health Risk," *Global Advances in Health and Medicine*, vol. 4, pp. 46–61, jan 2015.

[208] M. Malik, A. J. Camm, J. T. Bigger, G. Breithardt, S. Cerutti, R. J. Cohen, P. Coumel, E. L. Fallen, H. L. Kennedy, R. E. Kleiger, F. Lombardi, A. Malliani, A. J. Moss, J. N. Rottman, G. Schmidt, P. J. Schwartz, and D. H. Singer, "Heart rate variability. Standards of measurement, physiological interpretation, and clinical use. Task Force of the European Society of Cardiology and the North American Society of Pacing and Electrophysiology.," *European heart journal*, vol. 17, pp. 354–81, mar 1996.

[209] S. L. Raetz, C. A. Richard, A. Garfinkel, and R. M. Harper, "Dynamic Characteristics of Cardiac R-R Intervals during Sleep and Waking States," *Sleep*, vol. 14, pp. 526–533, nov 1991.

[210] T. Ziemssen, J. Gasch, and H. Ruediger, "Influence of ECG Sampling Frequency on Spectral Analysis of RR Intervals and Baroreflex Sensitivity Using the EUROBAVAR Data set," *Journal of Clinical Monitoring and Computing*, vol. 22, pp. 159–168, apr 2008.

[211] M. Nitzan, A. Romem, and R. Koppel, "Pulse oximetry: fundamentals and technology update," *Medical Devices: Evidence and Research*, vol. 7, p. 231, jul 2014.

[212] H. Lee, H. Ko, and J. Lee, "Reflectance pulse oximetry: Practical issues and limitations ," *ICT Express*, vol. 2, pp. 195–198, 2016.

[213] M. Nitzan, S. Noach, E. Tobal, Y. Adar, Y. Miller, E. Shalom, and S. Engelberg, "Calibration-Free Pulse Oximetry Based on Two Wavelengths in the Infrared A Preliminary Study," *Sensors*, vol. 14, pp. 7420–7434, apr 2014.

[214] E. M. Rodrigues, R. Godina, C. M. Cabrita, and J. P. Catalão, "Experimental low cost reflective type oximeter for wearable health systems," *Biomedical Signal Processing and Control*, vol. 31, pp. 419–433, jan 2017.

[215] J. Heerlein and T. Rügheimer, "Wearable-Medizintechnik: Lichtsensoren für die Selbstvermessung (online accessed: 2017-08-21)." http://www.elektroniknet.de/optoelektronik/lichtsensoren-fuer-die-selbstvermessung-113430.html.

[216] J. Moyle, *Principles and Practice Series: Pulse Oximetry, Revised Edition*. Wiley, 1998.

[217] H.-J. Priebe, "Pulse Oximetry, 2nd Edn," *British Journal of Anaesthesia*, vol. 89, pp. 802–803, nov 2002.

[218] M. Nitzan, A. Babchenko, B. Khanokh, and H. Taitelbaum, “Measurement of oxygen saturation in venous blood by dynamic near infrared spectroscopy,” *Journal of Biomedical Optics*, vol. 5, no. 2, p. 155, 2000.

[219] P. D. Mannheimer, J. R. Casciani, M. E. Fein, and S. L. Nierlich, “Wavelength Selection for Low-Saturation Pulse Oximetry,” vol. 44, no. 3, pp. 1–11, 1998.

[220] H. Shin and S. D. Min, “Feasibility study for the non-invasive blood pressure estimation based on ppg morphology: normotensive subject study,” *BioMedical Engineering OnLine*, 2017.

[221] S. Laurent, J. Cockcroft, L. Van Bortel, P. Boutouyrie, C. Giannattasio, D. Hayoz, B. Pannier, C. Vlachopoulos, I. Wilkinson, and H. Struijker-Boudier, “Expert consensus document on arterial stiffness: methodological issues and clinical applications,” *European Heart Journal*, vol. 27, pp. 2588–2605, sep 2006.

[222] F. U. Mattace-Raso, A. Hofman, G. C. Verwoert, J. C. Wittemana, I. Wilkinson, J. Cockcroft, C. McEniery, Yasmina, S. Laurent, P. Boutouyrie, E. Bozec, T. W. Hansen, C. Torp-Pedersen, H. Ibsen, J. Jeppesen, S. J. Vermeersch, E. Rietzschel, M. de Buyzere, T. C. Gillebert, L. van Bortel, P. Segers, C. Vlachopoulos, C. Aznaouridis, C. Stefanadis, A. Benetos, C. Labat, P. Lacolley, C. D. Stehouwer, G. Nijpels, J. M. Dekker, I. Ferreira, J. W. Twisk, S. Czernichow, P. Galan, S. Hercberg, B. Pannier, A. Guérin, G. London, J. Kennedy Cruickshank, S. G. Anderson, A. Paini, E. A. Rosei, M. L. Muiesan, M. Salvetti, J. Filipovsky, J. Seidlerova, and M. Dolejsova, “Determinants of pulse wave velocity in healthy people and in the presence of cardiovascular risk factors: establishing normal and reference values’,” *European Heart Journal*, vol. 31, pp. 2338–2350, oct 2010.

[223] J. Pietilä, S. Mehrang, J. Tolonen, E. Helander, H. Jimison, M. Pavel, and I. Korhonen, “Evaluation of the accuracy and reliability for photoplethysmography based heart rate and beat-to-beat detection during daily activities,” pp. 145–146, 2018.

[224] S. Akdemir Akar, S. Kara, F. Latifolu, and V. Bilgiç, “Spectral analysis of photoplethysmographic signals: The importance of preprocessing,” *Biomedical Signal Processing and Control*, vol. 8, pp. 16–22, jan 2013.

[225] A. Choi and H. Shin, “Photoplethysmography sampling frequency: pilot assessment of how low can we go to analyze pulse rate variability with reliability?,” *Institute of Physics and Engineering in Medicine Printed in the UK Physiol. Meas*, vol. 38, pp. 586–600, 2017.

[226] R. A. Payne, I. B. Wilkinson, and D. J. Webb, “Arterial stiffness and hypertension:

emerging concepts.," *Hypertension (Dallas, Tex. : 1979)*, vol. 55, pp. 9–14, jan 2010.

[227] C. M. McEniery, M. Spratt, M. Munnery, J. Yarnell, G. D. Lowe, A. Rumley, J. Gallacher, Y. Ben-Shlomo, J. R. Cockcroft, and I. B. Wilkinson, "An Analysis of Prospective Risk Factors for Aortic Stiffness in Men," *Hypertension*, vol. 56, pp. 36–43, jul 2010.

[228] L. Peter, N. Noury, and M. Cerny, "A review of methods for non-invasive and continuous blood pressure monitoring: Pulse transit time method is promising?," *IRBM*, vol. 35, pp. 271–282, oct 2014.

[229] B. Williams, G. Mancia, W. Spiering, E. Agabiti Rosei, M. Azizi, M. Burnier, D. L. Clement, A. Coca, G. de Simone, A. Dominiczak, T. Kahan, F. Mahfoud, J. Redon, L. Ruilope, A. Zanchetti, M. Kerins, S. E. Kjeldsen, R. Kreutz, S. Laurent, G. Y. H. Lip, R. McManus, K. Narkiewicz, F. Ruschitzka, R. E. Schmieder, E. Shlyakhto, C. Tsioufis, V. Aboyans, I. Desormais, and Authors/Task Force Members:, "2018 ESC/ESH Guidelines for the management of arterial hypertension: The Task Force for the management of arterial hypertension of the European Society of Cardiology and the European Society of Hypertension: The Task Force for the management of arterial h," *Journal of hypertension*, vol. 36, pp. 1953–2041, oct 2018.

[230] J. G. Betts, T. J. College, P. Desaix, J. E. Johnson, J. A. Wise, M. Womble, and K. A. Young, *Anatomy & Physiology*. OpenStax, Rice University, 2017.

[231] G. A. Holzapfel and R. W. Ogden, *Biomechanical modelling at the molecular, cellular, and tissue levels*. Springer, 2009.

[232] T. C. Gasser, R. W. Ogden, and G. A. Holzapfel, "Hyperelastic modelling of arterial layers with distributed collagen fibre orientations," *Journal of The Royal Society Interface*, vol. 3, pp. 15–35, feb 2006.

[233] G. A. Holzapfel, "Collagen in Arterial Walls: Biomechanical Aspects," in *Collagen* (P. Fratzl, ed.), no. January 2008, pp. 285–324, Boston, MA: Springer US, 2008.

[234] M. R. Roach and A. C. Burton, "The reason for the shape of the distensibility curves of arteries.," *Canadian journal of biochemistry and physiology*, vol. 35, pp. 681–90, aug 1957.

[235] P. C. Schönle, *A Power Efficient Spectrophotometry & PPG Integrated Circuit for Mobile Medical Instruments*. PhD thesis, 2017.

[236] G. A. Holzapfel, *Introduction of Biomechanics*. Lecture notes, Technical University Graz, 2012.

[237] S. R. Sharma, R. Poddar, P. Sen, and J. T. Andrews, “Effect of vitamin C on collagen biosynthesis and degree of birefringence in polarization sensitive optical coherence tomography (PS-OCT),” *African Journal of Biotechnology*, vol. 7, pp. 2049–2054, jun 2008.

[238] D. Knudson, *Fundamentals of Biomechanics*. Boston, MA: Springer US, 2nd ed., 2007.

[239] M. Catanho, M. Sinha, V. Vijayan, and V. Sinha, “Model of Aortic Blood Flow Using the Windkessel Eject,” tech. rep., BENG 21 - Mathematical Methods in Bioengineering, 2012.

[240] L. Hansen and W. Robert Taylor, “Is increased arterial stiffness a cause or consequence of atherosclerosis? HHS Public Access,” *Atherosclerosis*, vol. 249, pp. 226–227, 2016.

[241] G. F. Mitchell, “Arterial Stiffness and Hypertension: Chicken or Egg?,” *Hypertension*, vol. 64, pp. 210–214, aug 2014.

[242] G. F. Mitchell, N. Wang, J. N. Palmisano, M. G. Larson, N. M. Hamburg, J. A. Vita, D. Levy, E. J. Benjamin, and R. S. Vasan, “Hemodynamic Correlates of Blood Pressure Across the Adult Age Spectrum,” *Circulation*, vol. 122, pp. 1379–1386, oct 2010.

[243] G. F. Mitchell, S.-J. Hwang, R. S. Vasan, M. G. Larson, M. J. Pencina, N. M. Hamburg, J. A. Vita, D. Levy, and E. J. Benjamin, “Arterial Stiffness and Cardiovascular Events,” *Circulation*, vol. 121, pp. 505–511, feb 2010.

[244] T. Pereira, C. Correia, and J. Cardoso, “Novel Methods for Pulse Wave Velocity Measurement,” *Journal of Medical and Biological Engineering*, vol. 35, pp. 555–565, oct 2015.

[245] M. A. Darwich, F. Langevin, and K. Darwich, “Local Pulse Wave Velocity Estimation in the Carotids Using Dynamic MR Sequences,” *Journal of Biomedical Science and Engineering*, vol. 08, no. 04, pp. 227–236, 2015.

[246] R. Wang, W. Jia, Z.-H. Mao, R. J. Sclabassi, and M. Sun, “Cuff-free blood pressure estimation using pulse transit time and heart rate,” in *2014 12th International Conference on Signal Processing (ICSP)*, vol. 2014, pp. 115–118, IEEE, oct 2014.

[247] J. J. M. Westenberg, E. P. van Poelgeest, P. Steendijk, H. B. Grotenhuis, J. W. Jukema, and A. de Roos, “Bramwell-Hill modeling for local aortic pulse wave velocity estimation: A validation study with velocity-encoded cardiovascular magnetic resonance and invasive pressure assessment,” *Journal of cardiovascular magnetic*

resonance : official journal of the Society for Cardiovascular Magnetic Resonance, vol. 14, p. 2, jan 2012.

[248] J. C. Bramwell and A. V. Hill, "The Velocity of the Pulse Wave in Man," *Proceedings of the Royal Society B: Biological Sciences*, vol. 93, pp. 298–306, apr 1922.

[249] R. Kramme, ed., *Medizintechnik.* Springer Berlin Heidelberg, 2007.

[250] J. Penaz, "Photoelectric measurement of blood pressure, Volume and flow in the finger.," *Digest of the International Conference on Medicine and Biological Engineering*, p. 104, 1973.

[251] J. Fortin, W. Marte, R. Grüllenberger, A. Hacker, W. Habenbacher, A. Heller, C. Wagner, P. Wach, and F. Skrabal, "Continuous non-invasive blood pressure monitoring using concentrically interlocking control loops," *Computers in Biology and Medicine*, vol. 36, pp. 941–957, sep 2006.

[252] D. Hughes, "Measurements of Young's modulus of elasticity of the canine aorta with ultrasound," *Ultrasonic Imaging*, vol. 1, pp. 356–367, oct 1979.

[253] M. Sharma, K. Barbosa, V. Ho, D. Griggs, T. Ghirmai, S. Krishnan, T. Hsiai, J.-C. Chiao, and H. Cao, "Cuff-Less and Continuous Blood Pressure Monitoring: A Methodological Review," *Technologies*, vol. 5, no. 2, p. 21, 2017.

[254] W. Chen, I. T. Kobayashi, I. S. Ichikawa, Y. Takeuchi, and T. Togawa, "Continuous estimation of systolic blood pressure using the pulse arrival time and intermittent calibration," tech. rep., 2000.

[255] P. Fung, G. Dumont, C. Ries, C. Mott, and M. Ansermino, "Continuous Noninvasive Blood Pressure Measurement by Pulse Transit Time," 2004.

[256] T. Wibmer, K. Doering, C. Kropf-Sanchen, S. Rüdiger, I. Blanta, K. M. Stoiber, W. Rottbauer, C. Schumann, and T. Wibmer, "Pulse Transit Time and Blood Pressure During Cardiopulmonary Exercise Tests," *Physiol. Res*, vol. 63, pp. 287–296, 2014.

[257] L. A. Geddes, M. H. Voelz, C. F. Babbs, J. D. Bourland, and W. A. Tacker, "Pulse Transit Time as an Indicator of Arterial Blood Pressure," *Psychophysiology*, vol. 18, pp. 71–74, jan 1981.

[258] J. Proença, J. Muehlsteff, X. Aubert, and P. Carvalho, "Is Pulse Transit Time a good indicator of blood pressure changes during short physical exercise in a young population?," *2010 Annual International Conference of the IEEE Engineering in Medicine and Biology Society, EMBC'10*, pp. 598–601, 2010.

[259] H. T. Ma, “A Blood Pressure Monitoring Method for Stroke Management,” *BioMed Research International*, vol. 2014, pp. 1–7, aug 2014.

[260] R. Mukkamala, J.-O. Hahn, O. T. Inan, L. K. Mestha, C.-S. Kim, H. Toreyin, and S. Kyal, “Toward Ubiquitous Blood Pressure Monitoring via Pulse Transit Time: Theory and Practice,” *IEEE Transactions on Biomedical Engineering*, vol. 62, no. 8, pp. 1879–1901, 2015.

[261] M. Masè, W. Mattei, R. Cucino, L. Faes, and G. Nollo, “Feasibility of cuff-free measurement of systolic and diastolic arterial blood pressure,” *Journal of Electrocardiology*, vol. 44, pp. 201–207, mar 2011.

[262] X. Ding, B. P. Yan, Y.-T. Zhang, J. Liu, N. Zhao, and H. K. Tsang, “Pulse Transit Time Based Continuous Cuffless Blood Pressure Estimation: A New Extension and A Comprehensive Evaluation,” *Scientific Reports*, vol. 7, p. 11554, dec 2017.

[263] Y. Li, Z. Wang, L. Zhang, X. Yang, and J. Song, “Characters available in photoplethysmogram for blood pressure estimation: Beyond the pulse transit time,” *Australasian Physical and Engineering Sciences in Medicine*, vol. 37, no. 2, pp. 367–376, 2014.

[264] H. Gesche, D. Grosskurth, G. Küchler, and A. Patzak, “Continuous blood pressure measurement by using the pulse transit time: Comparison to a cuff-based method,” *European Journal of Applied Physiology*, vol. 112, no. 1, pp. 309–315, 2012.

[265] R. A. Payne, C. N. Symeonides, D. J. Webb, and S. R. J. Maxwell, “Pulse transit time measured from the ECG: an unreliable marker of beat-to-beat blood pressure.,” *Journal of applied physiology (Bethesda, Md. : 1985)*, vol. 100, pp. 136–41, jan 2006.

[266] E. Vaini, P. spero Lombardi, and M. Di Rienzo, “Aortic-Finger Pulse Transit Time vs. R-derived Pulse Arrival Time: a Beat-to-Beat Assessment,”

[267] G. Zhang, M. Gao, D. Xu, N. B. Olivier, and R. Mukkamala, “Pulse arrival time is not an adequate surrogate for pulse transit time as a marker of blood pressure,” *Journal of Applied Physiology*, 2011.

[268] J. Muehlsteff, X. L. Aubert, and M. Schuett, “Cuffless estimation of systolic blood pressure for short effort bicycle tests: The prominent role of the pre-ejection period,” *Annual International Conference of the IEEE Engineering in Medicine and Biology - Proceedings*, pp. 5088–5092, 2006.

[269] A.-G. Pielmus, M. Pflugradt, T. Tigges, M. Klum, A. Feldheiser, O. Hunsicker, and R. Orglmeister, “Novel computation of pulse transit time from multi-channel PPG

signals by wavelet transform," *Current Directions in Biomedical Engineering*, vol. 2, pp. 209–213, jan 2016.

[270] M. Lokharan, L. K. K. C, H. K. V, N. Kayalvizhi, R. Aryalekshmi, K. C. Lokesh Kumar, V. Harish Kumar, N. Kayalvizhi, and R. Aryalekshmi, *Measurement of Pulse Transit Time (PTT) Using Photoplethysmography*, vol. 61 of *IFMBE Proceedings*. Singapore: Springer Singapore, 2017.

[271] P. M. Nabeel, S. Karthik, J. Joseph, and M. Sivaprakasam, "Experimental Validation of Dual PPG Local Pulse Wave Velocity Probe," 2017.

[272] P. M. Nabeel, J. Jayaraj, and S. Mohanasankar, "Single-source PPG-based local pulse wave velocity measurement: a potential cuffless blood pressure estimation technique," *Physiological Measurement*, vol. 38, pp. 2122–2140, nov 2017.

[273] M. H. N. van Velzen, A. J. Loeve, E. G. Mik, and S. P. Niehof, "Design and Functional Testing of a Novel Blood Pulse Wave Velocity Sensor," *Journal of Medical Devices*, vol. 12, p. 011006, nov 2017.

[274] M. C. Corretti, T. J. Anderson, E. J. Benjamin, D. Celermajer, F. Charbonneau, M. A. Creager, J. Deanfield, H. Drexler, M. Gerhard-Herman, D. Herrington, P. Vallance, J. Vita, and R. Vogel, "Guidelines for the ultrasound assessment of endothelial-dependent flow-mediated vasodilation of the brachial artery: A report of the International Brachial Artery Reactivity Task Force," *Journal of the American College of Cardiology*, vol. 39, pp. 257–265, jan 2002.

[275] C. Yang and N. Tavassolian, "Pulse Transit Time Measurement Using Seismocardiogram, Photoplethysmogram, and Acoustic Recordings: Evaluation and Comparison," *IEEE Journal of Biomedical and Health Informatics*, vol. 2194, no. c, pp. 1–1, 2017.

[276] O. T. Inan, P.-F. Migeotte, K.-S. Park, M. Etemadi, K. Tavakolian, R. Casanella, J. Zanetti, J. Tank, I. Funtova, G. K. Prisk, and M. Di Rienzo, "Ballistocardiography and Seismocardiography: A Review of Recent Advances," *IEEE Journal of Biomedical and Health Informatics*, vol. 19, pp. 1414–1427, jul 2015.

[277] A. M. Carek and O. T. Inan, "Robust Sensing of Distal Pulse Waveforms on a Modified Weighing Scale for Ubiquitous Pulse Transit Time Measurement," *IEEE Transactions on Biomedical Circuits and Systems*, vol. 11, no. 4, pp. 765–772, 2017.

[278] D. Shao, F. Tsow, C. Liu, Y. Yang, and N. Tao, "Simultaneous Monitoring of Ballistocardiogram and Photoplethysmogram Using a Camera," *IEEE Transactions on Biomedical Engineering*, vol. 64, pp. 1003–1010, may 2017.

[279] C.-S. Kim, A. M. Carek, R. Mukkamala, O. T. Inan, and J.-O. Hahn, "Ballistocardiogram as Proximal Timing Reference for Pulse Transit Time Measurement: Potential for Cuffless Blood Pressure Monitoring HHS Public Access," *IEEE Trans Biomed Eng*, vol. 62, no. 11, pp. 2657–2664, 2015.

[280] D.-H. Nam, W.-B. Lee, Y.-S. Hong, and S.-S. Lee, "Measurement of Spatial Pulse Wave Velocity by Using a Clip-Type Pulsimeter Equipped with a Hall Sensor and Photoplethysmography," *Sensors*, vol. 13, pp. 4714–4723, apr 2013.

[281] Y. Li, P. Segers, J. Dirckx, and R. Baets, "On-chip laser Doppler vibrometer for arterial pulse wave velocity measurement," 2013.

[282] X.-R. Ding and Yuan-Ting Zhang, "Photoplethysmogram intensity ratio: A potential indicator for improving the accuracy of PTT-based cuffless blood pressure estimation," in *2015 37th Annual International Conference of the IEEE Engineering in Medicine and Biology Society (EMBC)*, vol. 2015, pp. 398–401, IEEE, aug 2015.

[283] X. Ding, Y. Zhang, and H. K. Tsang, "Impact of heart disease and calibration interval on accuracy of pulse transit timebased blood pressure estimation," *Physiological Measurement*, vol. 37, pp. 227–237, feb 2016.

[284] C. Poon and Y. Zhang, "Cuff-less and Noninvasive Measurements of Arterial Blood Pressure by Pulse Transit Time," in *2005 IEEE Engineering in Medicine and Biology 27th Annual Conference*, vol. 6, pp. 5877–5880, IEEE, 2005.

[285] Z. Tang, T. Tamura, M. Sekine, M. Huang, W. Chen, M. Yoshida, K. Sakatani, H. Kobayashi, and S. Kanaya, "A ChairBased Unobtrusive Cuffless Blood Pressure Monitoring System Based on Pulse Arrival Time," *IEEE Journal of Biomedical and Health Informatics*, vol. 21, pp. 1194–1205, sep 2017.

[286] A. Dias Junior, S. Murali, F. Rincon, and D. Atienza, "Methods for reliable estimation of pulse transit time and blood pressure variations using smartphone sensors," *Microprocessors and Microsystems*, vol. 46, pp. 84–95, oct 2016.

[287] Y. J. Segman, "New Method for Computing Optical Hemodynamic Blood Pressure," *Journal of Clinical & Experimental Cardiology*, vol. 7, no. 12, 2016.

[288] C. Ross Ethier and C. A. Simmons, *Introductory Biomechanics: From Cells to Organisms*. Cambridge University Press, 2007.

[289] M. C. Whitlock and W. G. Hundley, "Noninvasive Imaging of Flow and Vascular Function in Disease of the Aorta," *JACC: Cardiovascular Imaging*, vol. 8, pp. 1094–1106, sep 2015.

[290] M. Simjanoska, M. Gjoreski, M. Gams, and A. Madevska Bogdanova, "Non-

Invasive Blood Pressure Estimation from ECG Using Machine Learning Techniques," *Sensors*, vol. 18, p. 1160, apr 2018.

[291] M. Kachuee, M. M. Kiani, H. Mohammadzade, and M. Shabany, "Cuff-less high-accuracy calibration-free blood pressure estimation using pulse transit time," *2015 IEEE International Symposium on Circuits and Systems (ISCAS)*, no. 2, pp. 1006–1009, 2015.

[292] M. Kachuee, M. M. Kiani, H. Mohammadzade, and M. Shabany, "Cuffless Blood Pressure Estimation Algorithms for Continuous Health-Care Monitoring," *IEEE Transactions on Biomedical Engineering*, vol. 64, no. 4, pp. 859–869, 2017.

[293] F. Kern and S. Bernhard, "Beat-to-beat blood pressure measurement from instantaneous harmonic phase-shifts in non-invasive photoplethysmographic signals," *Current Directions in Biomedical Engineering*, vol. 3, no. 2, pp. 755–758, 2017.